



Ozone and carbon monoxide in the tropical troposphere, as seen by aircraft and satellite data; as seen by aircraft (IAGOS) and satellite (IASI) measurements

Maria Tsivlidou

► To cite this version:

Maria Tsivlidou. Ozone and carbon monoxide in the tropical troposphere, as seen by aircraft and satellite data; as seen by aircraft (IAGOS) and satellite (IASI) measurements. Climatology. Université Paul Sabatier - Toulouse III, 2023. English. NNT : 2023TOU30106 . tel-04266823

HAL Id: tel-04266823

<https://theses.hal.science/tel-04266823v1>

Submitted on 31 Oct 2023

HAL is a multi-disciplinary open access archive for the deposit and dissemination of scientific research documents, whether they are published or not. The documents may come from teaching and research institutions in France or abroad, or from public or private research centers.

L'archive ouverte pluridisciplinaire **HAL**, est destinée au dépôt et à la diffusion de documents scientifiques de niveau recherche, publiés ou non, émanant des établissements d'enseignement et de recherche français ou étrangers, des laboratoires publics ou privés.



THÈSE

En vue de l'obtention du

DOCTORAT DE L'UNIVERSITÉ DE TOULOUSE

Délivré par : *l'Université Toulouse 3 Paul Sabatier (UT3 Paul Sabatier)*

Présentée et soutenue le 06/03/2023 par :

Maria TSIVLIDOU

**L'ozone et le monoxyde de carbone dans la troposphère tropicale, vus
par les données aériennes (IAGOS) et satellitaires (IASI)**

JURY

VALÉRIE THOURET
SLIMANE BEKKI
GWENAËL BERTHET
JÉRÔME BRIOUDE
MARC MALLET
BASTIEN SAUVAGE
BRICE BARRET

Physicienne
Directeur de Recherche
Chargé de Recherche
Maître de conférences
Directeur de Recherche
Directeur
Co-directeur

Président du Jury
Rapporteur
Rapporteur
Rapporteur
Examineur
Membre du jury
Membre du jury

École doctorale et spécialité :

SDU2E : Océan, Atmosphère, Climat

Unité de Recherche :

Laboratoire d'Aérodynamique (UMR 5560)

Directeur(s) de Thèse :

Bastien SAUVAGE et Brice BARRET

Rapporteurs :

Slimane BEKKI, Gwenaël BERTHET et Jérôme BRIOUDE

Abstract

The overall objective of this thesis is to document the characteristics of ozone (O_3) and carbon monoxide (CO) distributions in the tropics and to characterise the tropical O_3 changes. To do so, we used aircraft (IAGOS) and satellite (IASI) data. The evaluation of IASI using IAGOS showed sensitivity of the O_3 change to: i) the sampling, and ii) the vertical sensitivity of the satellite. The best agreement between IASI and IAGOS was in the partial column (700–200 hPa), where IASI retrievals are the most sensitive to O_3 . The average partial column O_3 on a global scale increased by 0.4 DU (or 1.7 %) for 2018–2020 relative to 2008–2010, with the highest increase over South and SouthEast Asia (by 10 %).

Using the observational data in combination with model data (SOFT-IO), we document the characteristics of tropospheric O_3 and CO over the whole tropics for the last two decades. We explore the origin of the observed CO anomalies and investigate transport processes driving the tropical CO and O_3 distribution. Our study highlights the importance of anthropogenic emissions in the low troposphere, mostly over the northern tropics. The biomass burning contributions are dominant in the mid and upper troposphere when the fires are active. The highest O_3 and CO tropical maxima are observed over Africa in the low troposphere during the dry season (80 ppb of O_3 at 2.5 km and 850 ppb of CO at 0.3 km over Lagos), mostly due to local anthropogenic emissions (60 %). Africa is the most important region in terms of export of emissions in the tropical troposphere.

The second highest maxima are observed over Asia above the surface for CO, and in the free troposphere for O_3 , mostly due to local AN emissions. The only Asian cluster with O_3 maxima in the low troposphere is South China (75 ppb at 2.6 km) due to local AN and BB emissions. The impact of the Asian emissions in the low and mid troposphere is limited on a regional or local scale. In the upper troposphere, the export of Asian emissions intensifies, mostly towards Arabia and northern tropical Africa. Last, the smallest low tropospheric CO maxima are observed over Arabian and Eastern Africa, and South America, due to significantly lower CO emissions relative to the African and Asian ones.

Résumé

L'objectif global de cette thèse est de documenter les caractéristiques des distributions d'ozone (O_3) et de monoxyde de carbone (CO) dans les tropiques, et de caractériser les changements tropicaux de l' O_3 . Pour ce faire, nous avons utilisé des données aériennes (IAGOS) et satellitaires (IASI). L'évaluation de l'IASI à l'aide de IAGOS, a montré la sensibilité de la variation de O_3 à : i) l'échantillonnage, et ii) la sensibilité verticale du satellite. Le meilleur accord entre IASI et IAGOS était dans la colonne partielle (700–200 hPa), où les récupérations IASI sont les plus sensibles à O_3 . La moyenne de la colonne partielle de O_3 à l'échelle mondiale a augmenté de 0.4 DU (soit 1.7 %) pour 2018–2020 par rapport à 2008–2010, l'augmentation la plus importante ayant été enregistrée en Asie du Sud et du Sud-Est (de 10 %).

En utilisant les données d'observation en combinaison avec les données du modèle (SOFT-IO), nous documentons les caractéristiques de l' O_3 et du CO troposphériques sur l'ensemble des tropiques pour les deux dernières décennies. Nous explorons l'origine des anomalies de CO observées et étudions les processus de transport qui déterminent la distribution tropicale du CO et de l' O_3 . Notre étude souligne l'importance des émissions anthropiques dans la basse troposphère, principalement au-dessus des tropiques du nord. Les contributions de la combustion de la biomasse sont dominantes dans la troposphère moyenne et supérieure, lorsque les feux sont actifs. Les maxima tropicaux les plus élevés de O_3 et de CO sont observés au-dessus de l'Afrique dans la basse troposphère pendant la saison sèche (80 ppb de O_3 à 2.5 km et 850 ppb de CO à 0.3 km au-dessus de Lagos), principalement dus aux émissions anthropiques locales (60 %). L'Afrique est la région la plus importante en termes d'exportation des émissions dans la troposphère tropicale.

Les deuxièmes maxima les plus élevés sont observés au-dessus de l'Asie au-dessus de la surface pour le CO, et dans la troposphère libre pour O_3 , principalement en raison des émissions locales d'AN. Le seul groupe asiatique présentant des maxima de O_3 dans la basse troposphère est la Chine du Sud (75 ppb à 2.6 km), en raison des émissions locales de AN et BB. L'impact des émissions asiatiques dans la basse et moyenne troposphère est limité à l'échelle régionale ou locale. Dans la haute troposphère, l'exportation des émissions asiatiques s'intensifie, principalement vers l'Arabie et le nord de l'Afrique tropicale. Enfin, les plus petits

maxima de CO dans la basse troposphère sont observés au-dessus de l'Arabie, de l'Afrique de l'Est et de l'Amérique du Sud, en raison d'émissions de CO nettement inférieures à celles de l'Afrique et de l'Asie.

Acknowledgements

First, I would like to thank my thesis supervisors, Bastien and Brice, for their guidance and help during the completion of this thesis. Thank you for your time and patience during the past three years.

I would like to express my gratitude to the three reviewers of this thesis, Slimane Bekki, Gwenaël Berthet and Jérôme Brioude, for agreeing to evaluate my work and for providing comments which helped to improve this manuscript. Also, I would like to thank Valérie Thouret for being the president of the thesis jury, and Marc Mallet for being the examiner of my thesis.

I would also like to thank the IAGOS and IASI teams in LAERO, for their contribution to the quality of the data and the article, and for the constructive discussions. I extend my gratitude to Didier for kindly answering my questions related to nuwa.

Also, I wish to thank the fellow researchers in the LAERO, for the interesting discussions (and questions!) we had, the coffee and lunch breaks.

Further, I would like to thank my friends in Toulouse, back home in Greece and the rest of the world for making life more enjoyable. Thanks Xristina, Giannis X., Sofia, Maria, Florian, Svetlana, Laurent, Pierre, Azusa, and the many of you whom I may have forgotten. Special thanks to my dearest friends Camille and Joelle for making Toulouse feel a bit like home, for the support and the fun moments! Eirini, Gianni B. and Carlos thank you for the encouragement and the travelling adventures during the past years.

Last but not least, I wish to express my gratitude to my family in Greece that has been supporting me all these past years and helped me to achieve my goals.

Contents

Abstract	i
Abstract in french	iii
Acknowledgements	v
Table of Contents	vii
List of Figures	i
List of Tables	viii
Glossary	x
Acronyms	xiii
General Introduction	1
General Introduction in french	5
1 Ozone and Carbon monoxide in the Troposphere	10
1.1 Tropospheric ozone	10
1.1.1 Role and Significance	10
1.1.2 Sources and Sinks	11
1.1.3 Global budget	21
1.2 Carbon monoxide	23
1.2.1 Role and Significance	23
1.2.2 Sources and Sinks	23
1.2.3 Global Budget	25
2 Tropics: Tropospheric dynamics and precursor emissions	29
2.1 Tropospheric Dynamics	29
2.1.1 General Circulation	29
2.1.2 Variations of the General Circulation	33
2.2 Natural and Anthropogenic Sources	39
3 Data and Methods	49
3.1 IAGOS airborne observations	49

3.1.1	IAGOS instrumentation	51
3.1.2	Data quality	52
3.2	IASI spaceborne observations	56
3.3	SOFT-IO model	58
4	IASI validation with IAGOS	64
4.1	Validation of climatologies in the Upper Troposphere	66
4.2	Validation of tropospheric O ₃ change	74
4.3	Free tropospheric O ₃ change as seen by IASI	84
5	Tropical distributions	88
5.1	Introduction	88
5.2	Article	89
5.2.1	Introduction	91
5.2.2	Data and Methods	94
5.2.2.1	IAGOS observations	94
5.2.2.2	Data treatment	95
5.2.2.3	SOFT-IO model	96
5.2.2.4	IASI-SOFRID observations	99
5.2.3	Results	100
5.2.3.1	O ₃ and CO over the Northern and Southern Tropics	100
5.2.3.2	Regional characteristics of tropical O ₃ and CO	102
5.2.3.3	Control factors of tropical O ₃ and CO	119
5.2.4	Summary and conclusions	128
5.2.5	Appendix	131
5.2.5.1	SOFT-IO CO contributions	131
5.2.6	Supplement	139
5.2.6.1	CO emissions	139
6	Conclusions and Perspectives	144
6.1	Conclusions	144
6.2	Limitations and Perspectives	147
7	Conclusions and Perspectives in french	151
7.1	Conclusions in french	151
7.2	Limitations and Perspectives in french	154
	Bibliography	158

List of Figures

- 1.1 Cycling of HO_x and O_3 production in a polluted atmosphere. Source: Jacob (1999) 17
- 1.2 Isopleth (lines of constant value) plots for O_3 mixing ratios as a function of various initial VOCs and NO_x mixing ratios based on the EKMA (Empirical Kinetic Modelling Approach) model. Source: National Research Council (1991) 19
- 1.3 Present-day tropospheric O_3 budget terms based on models, and observations (where available). (a) The annual average O_3 burden, and annual total fluxes for (b) Chemical production and loss, (c) Dry deposition, and (d) Net stratospheric influx. Model results are shown as box-whisker plots, also indicating the median (horizontal line) and mean (filled circle) values of 50 models for the burden and 30 models for the fluxes (numbers of models indicated next to the boxes). Observation-based estimates for the burden are from Li1995 (Li (1995); after Wild (2007), FK1998 (Paul et al., 1998), Logan1999 (Logan et al., 1999), Ziemke2011 (after Ziemke et al. (2011)) and Osterman2008 (Osterman et al. (2008); range). Observation-based estimates for the net stratospheric influx are from MF1994 (Murphy and Fahey, 1994), Gettelman1997 (Gettelman et al., 1997), and Olsen2001 (Olsen et al., 2001). The error bars indicate their full uncertainty ranges. Source: Young et al. (2018) 22
- 1.4 Inversion-based estimates of global CO budget (Tg CO yr^{-1}). Source: Zheng et al. (2019). 27
- 2.1 Schematic of Hadley, Ferrel, and polar cell circulation. Source: NOAA 30
- 2.2 Schematic of Hadley cell circulation. Source: Fiehn (2017) 31
- 2.3 Position of the Intertropical convergence zone during January and July. Source: Yan (2005) 32
- 2.4 Top panel: Average conditions of ocean temperatures, rainfall, pressure, and winds over the Pacific Ocean during neutral conditions. Bottom panel: State of the ocean and the atmosphere during El Niño conditions. Source: NOAA image created by David Stroud 34
- 2.5 Transport pathways near the surface over the Indian Ocean during the Asian summer (left panel) and winter (right panel) monsoon. Source: Lawrence and Lelieveld (2010) 36
- 2.6 Schematic representation of the processes impacting MT and UT composition above the Middle East and Mediterranean during the Asian summer monsoon (July–August). Source: Dayan et al. (2017) 36

- 2.7 Monthly mean streamlines from the 2002 [ECMWF](#) analyses. (a) 250 hPa January, (b) 250 hPa July, (c) 650 hPa January, (d) 650 hPa July, (e) 850 hPa January, (f) 850 hPa July. The main dynamic African features are written in blue. The red line displays the [ITCZ](#) and the red points the position of the fires in January and July. Shaded areas indicate the [AEJ](#) location. Source: Sauvage et al. (2005) 37
- 2.8 Schematic of vertical section over South America during the South American Monsoon. Source: Climate Variability & Predictability Program (CLIVAR) (www.clivar.org) 38
- 2.9 Monthly mean emissions (in $\text{mg m}^{-2} \text{ day}^{-1}$) of isoprene (a) and monoterpenes (b) by the MEGAN model averaged for the period 1980–2010. Source: Sindelarova et al. (2014) 40
- 2.10 Monthly mean soil NO_x emissions (in kgN m^2) for January (a), April (b), July (c), and October (d) based on [MERRA-2](#) data averaged for the period 1980–2017. Source: Weng et al. (2020) 41
- 2.11 Seasonal mean global flash rate density constructed from individual observations made by the Lightning Imaging Sensor ([LIS](#)) on the Tropical Rainfall Measuring Mission ([TRMM](#)) satellite averaged for the period 1998–2003. Source: https://ghrc.nsstc.nasa.gov/lightning/data/data_lis_vhr-climatology.html 43
- 2.12 Climatological fields derived from the first 5 years of Terra MODIS fire observations for the period 2000–2005. (a) Mean annual fire pixel density, (b) month of maximum fire activity, and (c) length of the fire season. Source: Giglio et al. (2006) 45
- 2.13 Dominant fire type in each 0.5° grid cell based on carbon emissions. Source: Werf et al. (2010) 46
- 2.14 Relative contribution (%) from different regions to the average global total burned area and fire emissions of carbon, CO , and CH_4 for the period 1997–2009. The regions of interest correspond to Africa, Tropical Asia, and Tropical America. Source: Werf et al. (2010) 47
- 2.15 CEDS2 AN CO emissions (in $\text{kg m}^{-2} \text{ s}^{-1}$) averaged from 2000 to 2019. 48
- 3.1 Evolution of observations from programmes MOZAIC and CARIBIC to IAGOS: the aircraft represent the number of equipped units in operation. Observed parameters are indicated for the various evolution stages of the program. Source: www.iagos.org 50
- 3.2 Map of IAGOS flights per airline since 1994. Source: Blot et al. (2021) 51
- 3.3 IAGOS data flow. Source: Petzold et al. (2015) 53
- 3.4 Example of IAGOS O_3 data measured during a single flight from Atlanta to Frankfurt. Top panel: the trajectory of the aircraft. Middle panel: the evolution of the aircraft altitude (left); O_3 measurements (in ppb) during the ascent (middle) and descent (right) phase. Bottom: O_3 measurements (in ppb) during the cruise phase. Source: <https://www.iagos.org/> 55

3.5	IASI field of view. Source: https://www.eumetsat.int/iasi	56
3.6	Locations of tropical sites served by IAGOS, and geographical source regions used in SOFT-IO model. BONA: Boreal North America; TENA: Temperate North America; CEAM: Central America; NHSA: Northern Hemisphere South America; SHSA: Southern Hemisphere South America; EURO: Europe; MIDE: Middle East; NHAF: Northern Hemisphere Africa; SHAF: Southern Hemisphere Africa; BOAS: Boreal Asia; CEAS: Central Asia; SEAS: Southeast Asia; EQAS: Equatorial Asia; AUST: Australia and New Zealand.	59
3.7	Example of an individual IAGOS-CO and SOFT-IO contribution vertical profile during a single flight departing from Lagos on 2003-05-19 15:53:14. The purple line represents the observed CO mixing ratio, while the dashed line the background CO mixing ratio (in ppb) computed as explained in the text. The intermediate hatched part indicates the positive CO anomaly. The coloured part on the left shows the vertical distribution of CO contributions computed by SOFT-IO (in ppb). The geographic origin of CO emissions is indicated by the different colours, with the hatched part showing AN contribution, and the non-hatched part BB contribution.	61
3.8	Monthly mean UT (between 300–185 hPa) CO distributions measured by IAGOS for the period 2002–2020. The red boxes indicate the regions taken into account for the computation of the background CO mixing ratios.	62
4.1	IAGOS (at 300–185 hPa) (a–d) and IASI-SOFRID (at 290–220 hPa) (e–h) UT O ₃ mixing ratios averaged from 2008 to 2019 on a 1x1 grid. The boxes indicate the regions with the highest IAGOS coverage and are used for the computation of the meridional O ₃ and CO transects. The hatched part in the SOFRID map shows points where outgoing longwave radiation is lower than 220 W m^{-2} .	69
4.2	IAGOS (between 300–185 hPa) and IASI-SOFRID (between 290–220 hPa) monthly meridional transects of O ₃ over i) NATlantic, ii) Atlantic, iii) Africa iv) SAsia and v) SEAsia transects (The definition of the transects is given in Figs. 4.1 and 4.3). The shadowed part shows a range of \pm one standard deviation. The red line (and the right axis) represents the relative difference between SOFRID and IAGOS in %.	70
4.3	Same as Fig. 4.1 for CO.	72
4.4	Same as Fig. 4.2 for CO.	73
4.5	Number of IAGOS flights per month over Windhoek.	76
4.6	Number of IAGOS flights per month over South China.	77

- 4.7 Tropospheric column (1000–200 hPa) O₃ change in DU based on IAGOS (orange bars) daily measurements and IASI (blue bars): (a) monthly and (b) daily measurements when IAGOS data are available. The error bars correspond to the 90 % confidence intervals of the change. The Table in panel (b) shows the reference and modern periods taken into account for each site. 78
- 4.8 (a) Tropospheric column (1000–200 hPa) and (b) partial column (700–200 hPa) O₃ change in DU based on IAGOS (orange bars) and IASI (blue bars) daily measurements. The error bars correspond to the 90 % confidence intervals. The Table in panel (a) shows the reference and modern periods taken into account for each site. 81
- 4.9 IAGOS O₃ vertical distributions (in ppb) averaged for the reference period (blue line) and the modern period (red line). The shadowed part corresponds to ± 1 standard deviation. The time span of the two periods is annotated in the legend. 83
- 4.10 Partial column (700–200 hPa) O₃ change (in %) between the reference (2008–2010) and the modern period (2018–2020) based on SOFRID-O₃ retrievals. 85
- 5.1 Locations of tropical sites served by IAGOS, and geographical source regions used in SOFT-IO model. BONA: Boreal North America; TENA: Temperate North America; CEAM: Central America; NHSA: Northern Hemisphere South America; SHSA: Southern Hemisphere South America; EURO: Europe; MIDE: Middle East; NHAF: Northern Hemisphere Africa; SHAF: Southern Hemisphere Africa; BOAS: Boreal Asia; CEAS: Central Asia; SEAS: Southeast Asia; EQAS: Equatorial Asia; AUST: Australia and New Zealand. 99
- 5.2 IASI LT CO (between 900–700 hPa) (a) and MT O₃ (between 600–400 hPa) (b) mixing ratios averaged from 2008 to 2019 on a 1x1 grid. 101
- 5.3 Monthly mean LT CO distributions (a–d), MT O₃ distributions (e–h), UT CO distributions based on IASI (i–l) and IAGOS (q–t), UT O₃ distributions based on IASI (m–p) and IAGOS (u–x). 103
- 5.4 IAGOS monthly mean O₃ (panel 1) and CO (panel 2) vertical distributions for the African clusters and sites. The annotated numbers correspond to the number of flights per month, given in the same colour as in the legend. The shadowed part corresponds to \pm one standard deviation. The location of the clusters and sites is displayed in Fig. 5.1. Vertical distribution of CO contributions (in ppb), averaged over all the positive CO anomalies observed in the IAGOS vertical profile (panels 3 to 5). The geographic origin of CO emissions is indicated by the different colours, with the hatched part showing AN contribution, and the non-hatched part BB contribution. Note that the source region where the site belongs is indicated by the colour of the box. 105

5.5	Mean SOFT-IO contributions (in ppb), averaged over all the positive CO anomalies for the tropical sites (Caracas, Lagos, Central Africa, South China, and Bangkok) for low (a), mid (b), and upper (c) troposphere. The geographic CO origin of CO is indicated by the colours, for the AN (hatched) and BB (unhatched) contributions. Each pie corresponds to a different month and each group of four pies refers to a different site (see panel b).	106
5.6	Same as Fig. 5.4 for the Asian clusters.	111
5.7	Same as Fig. 5.4 for the South American clusters.	114
5.8	Same as Fig. 5.4 for the Arabian and Eastern African clusters.	117
5.9	O ₃ (a) and CO (b) annual maximum (higher bar) and minimum (lower bar) mixing ratio observed over the tropical clusters. The annotated number on top of each bar indicates the altitude (in km) of the observed annual maximum/minimum mixing ratio. The colour in the bar indicates the month of the maximum/minimum.	121
5.10	Transport of CO (AN+BB) emissions from the African, South American and Asian source regions towards the 20 tropical sites taken into account for this study. The colour bar shows the amount of CO transported in ppb.	123
5.11	Mean AN (a–d) and BB (e–h) contributions in ppb over the tropical upper troposphere (300–185 hPa) from 2002–2019.	127
5.12	Same as Fig. 5.4 (panel 3) for CO contributions over Sahel (1), Gulf of Guinea (2), Madras (3), Hyderabad (4), Ho Chi Minh City (5), Gulf of Thailand (6) and Manila (7).	131
5.13	Same as Fig. 5.5 for CO contributions over Windhoek, Addis Ababa, Khartoum, Jeddah and Gulf of Thailand.	132
5.14	Same as Fig. 5.5 for CO contributions over Madras, Mumbai, Hyderabad, Ho Chi Minh City and Manila.	133
5.15	Mean CO contribution (in ppb) per source region in the tropical UT (300–185 hPa) averaged from 2002–2019 for January. The hatched part indicates BB as the dominant source of CO.	134
5.16	Same as Fig. 5.15 for April.	135
5.17	Same as Fig. 5.15 for July.	136
5.18	Same as Fig. 5.15 for October.	137
5.19	GFAS BB CO emissions (in $kg\ m^{-2}\ s^{-1}$) averaged from 2003 to 2017.	139
5.20	CEDS2 AN CO emissions (in $kg\ m^{-2}\ s^{-1}$) averaged from 2000 to 2019.	140
5.21	ECMWF Reanalysis 5th Generation (ERA5) wind vectors at 850 (a–d), 550 (e–h) and 250 (i–l) hPa averaged from 2008 to 2020 at 0.25x0.25° resolution.	141

List of Tables

1.1	Average CO budget in (10^3 Tg CO yr ⁻¹) during 2000–2017 based on Zheng et al. (2019).	26
4.1	Statistics of the comparison between IAGOS and IASI-SOFRID monthly O ₃ /CO meridional UT transects for the period 2008–2019. The Pearson correlation coefficient (R), the bias (in %), and the root-mean-square of the relative difference (RMSD) (in %) are given.	67
4.2	Mean statistics of the comparison between IAGOS and IASI-SOFRID monthly O ₃ and CO meridional UT transects. The correlation coefficient and the mean bias (in %) are given.	71
4.3	IAGOS, IASI-monthly and IASI-daily tropospheric (1000–200 hPa) O ₃ change (in DU) between the reference and the modern period. The mean indicates the mean O ₃ change between the two periods. Numbers in bold correspond to statistically significant O ₃ changes. The CI stands for the 90 % confidence interval of the change. The insignificant changes with respect to the 90 % confidence intervals are indicated as NS.	79
4.4	O ₃ change (in DU) based on IAGOS and IASI daily measurements (these results are also displayed in Figure 4.8). From left to right, tropospheric column (1000–200 hPa) and partial tropospheric column (700–200 hPa) O ₃ change between the reference and the modern periods. The mean indicates the mean O ₃ change between the two periods. Numbers in bold correspond to statistically significant O ₃ changes. The CI stands for the 90 % confidence interval of the change. The insignificant changes with respect to the 90 % confidence intervals are indicated as NS.	82
5.1	Field campaigns providing <i>in situ</i> gas and aerosol measurements in the tropics.	93
5.2	Description of individual sites and clusters used in this study. The location of the sites is displayed in Fig. 5.1	97
5.3	Annual mean LT CO and O ₃ mixing ratio (in ppb) over the Northern Tropics (0–25° N), Southern Tropics (0–25° S), Northern Africa (10° W–12.5° E; 0–12.5° N), Southern Africa (10–35° E; 2.5–20° S), East Asia (92.5–110° E; 10–27° N) and South America (35–50° W; 0–20° S) based on IASI data (Fig. 5.2).	101

- 5.4 Total (AN + BB) CO emission rates (in $10^{-10} \text{ kg m}^{-2} \text{ s}^{-1}$) based on CEDS2 and GFAS emission inventories over West Africa (10° W– 12.5° E; 0 – 12.5° N), Central Africa (10 – 35° W; 2.5 – 20° S), East Asia (92.5 – 110° E; 10 – 27° N), Maritime Continent (93 – 121° E; 10° S– 10° N), South Brazil (35 – 50° W; 0 – 20° S) and Arabia and Eastern Africa (30 – 60° E; 5 – 25° N). 121

Glossary

CH₄ Methane.

CO Carbon Monoxide.

CO₂ Carbon Dioxide.

H Hydrogen.

H₂O Water.

H₂O₂ Hydrogen Peroxide.

HNO₃ Nitric acid.

HO₂ Hydroperoxyl Radical.

HO_x Hydrogen Oxide Radicals.

LiNO_x Lightning-induced NO_x.

M Third body.

nm Nanometers.

NO Nitric Oxide.

NO₂ Nitrogen Dioxide.

NO_x Nitrogen Oxides.

NO_y Reactive Nitrogen Compounds.

O Atomic Oxygen.

O₂ Dioxygen.

O₃ Tropospheric Ozone.

O(¹D) Oxygen atom in its excited state.

O(³P) Oxygen atom in its ground state.

OH Hydroxyl Radical.

ppb Parts per billion.

RH Hydrocarbons.

RO Organic Oxy Radical.

RO₂ Organic Peroxy Radical.

VOCs Volatile Organic Compounds.

Acronyms

ACCENT Atmospheric Composition Change: the European Network of excellence.

ACCMIP Atmospheric Chemistry and Climate Model Intercomparison Project.

AEA Arabia and Eastern Africa.

AEJ Africa Easterly Jet.

AMA Asian monsoon Anticyclone.

AN Anthropogenic.

AUST Australia.

BB Biomass burning.

BOAS Boreal Asia.

BONA Boreal North America.

CARIBIC Civil Aircraft for the Regular Investigation Based on an Instrument Container.

CEAM Central America.

CEAS Central Asia.

CEDS2 Community Emissions Data System.

CNES Centre National d'Etudes Spatiales.

CNRS Centre National de la Recherche Scientifique.

CTM Chemistry Transport Model.

D Loss due to depositions to the surface.

DU Dobson units.

ECMWF European Center for Medium Range Weather Forecasts.

ENSO El Niño Southern Oscillation.

EQAS Equatorial Asia.

EUMETSAT European Organization for the Exploitation of Meteorological Satellites.

EURO Europe.

FLEXPART FLEXible PARTicle dispersion model.

FT Free troposphere.

GCHP GEOS-Chem High Performance.

GFAS Global Fire Assimilation System.

IAGOS In-service Aircraft for a Global Observing System.

IASI Infrared Atmospheric Sounding Interferometer.

ITCZ Intertropical Convergence Zone.

L Chemical loss.

LIS Lightning Imaging Sensor.

LT Lower troposphere.

MERRA-2 Modern-Era Retrospective analysis for Research and Applications, Version 2.

MetOp Meteorological operational satellite.

MIDE Middle East.

MLS Microwave Limb Sounder.

MODIS Moderate Resolution Imaging Spectroradiometer.

MOPITT Measurements Of Pollution In The Troposphere.

MOZAIC Measurements of OZone and water vapor by in-service AIRbus airCRAFT.

MT Mid troposphere.

NH Northern Hemisphere.

NHAF Northern Hemisphere Africa.

NHSA Northern Hemisphere South America.

NWP Numerical Weather prediction.

OMI Ozone Monitoring Instrument.

OPE Ozone production efficiency.

P Chemical production.

PBL Planetary Boundary layer.

R Pearson correlation coefficient.

RMSD Root-mean-square of the the relative difference.

S Stratosphere-troposphere exchange.

SASTA South Atlantic Subtropical Anticyclone.

SEAS South East Asia.

SH Southern Hemisphere.

SHAF Southern Hemisphere Africa.

SHSA Southern Hemisphere South America.

SOFRID Software for a Fast Retrieval of IASI Data.

SOFT-IO SOft attribution using FlexparT and carbon monoxide emission inventories for
In-situ Observation database.

TEJ Tropical Easterly Jet.

TENA Temperate North America.

TIR Thermal Infrared.

TOAR-I Tropospheric Ozone Assessment Report, Phase I.

TOAR-II Tropospheric Ozone Assessment Report, Phase II.

TRMM Tropical Rainfall Measuring Mission.

TTL Tropical Tropopause layer.

UKMO UK Met Office.

USD United States dollar.

UT Upper troposphere.

UTLS Upper troposphere lower stratosphere.

WAM West African Monsoon.

WHO World Health Organization.

General Introduction

Tropospheric ozone (O_3) and carbon monoxide (CO) are key components in the atmosphere due to their role in air quality, atmospheric chemistry, and climate. O_3 impacts the oxidative capacity of the troposphere as a major source of hydroxyl radicals (OH), and the climate as a powerful greenhouse gas in the upper troposphere (IPCC, 2021). Also, O_3 close to the surface harms human health and vegetation growth (Jerrett et al., 2009). O_3 is mostly produced photochemically by emissions of precursors, such as CO and Volatile Organic Compounds (VOCs), in the presence of nitrogen oxides (NO_x) (Logan et al., 1981). It is a secondary pollutant, with a relatively short lifetime (typically hours in the BL and approximately 22 days in the free troposphere (FT); Stevenson et al., 2006), thus its control factors are difficult to identify. Its distribution in the troposphere is driven by: (anthropogenic and natural) emissions of precursors (Monks et al., 2015) followed by photochemical production and destruction, stratosphere-to-troposphere exchange (Stevenson et al., 2013), dynamical processes which redistribute air masses rich or poor in O_3 and precursors (Wild et al., 2004), and depositional and photochemical processes destroying O_3 (Monks et al., 2015).

CO influences the oxidative capacity of the troposphere, as it is the main sink OH (Lelieveld et al., 2016), and thus the climate through an enhancement of the lifetime of methane (CH_4) (Seinfeld and Pandis, 1998), the second most important greenhouse gas (IPCC, 2021). Also, its oxidation contributes to an increase in carbon dioxide (CO_2) and O_3 (Myhre et al., 2013), which are greenhouse gases (IPCC, 2021). CO is produced by primary sources (e.g. surface emissions from anthropogenic (AN) and biomass burning (BB) combustion), and by secondary sources (e.g. oxidation of VOCs). The relation between the observed O_3 and CO is useful to constrain our understanding of the factors controlling O_3 (Voulgarakis et al., 2011). Due to its long lifetime, CO is considered a pollution tracer of combustion products (Logan et al., 1981) which emit O_3 precursors. A correlation between O_3 and CO was observed in aged pollution and BB plumes (e.g. Parrish et al., 1993; Jaffe and Wigder, 2012), indicating that a region has experienced photochemical O_3 production from its precursors (including CO) (Voulgarakis et al., 2011 and references therein). The O_3 - CO anti correlation close to the surface indicates deposition and O_3 destruction. Also, the O_3 - CO relation extends into the FT and on intercontinental scales, reflecting the mixing of air masses and chemistry (e.g. Andreae et al., 1994). When stratospheric intrusions occur, O_3 and CO are anti correlated, as stratospheric air is rich in O_3 and poor in CO (e.g. Parrish et al., 1998). Thus, the O_3 - CO relation is useful to constrain O_3 sources and transport.

The tropics are of particular interest regarding tropospheric O_3 and CO . They combine: i)

intense photochemistry due to high solar radiation and humidity, ii) large active natural sources (biomass burning, lightning, and soil emissions) of O_3 precursors (e.g. Sauvage et al., 2007b; Ziemke et al., 2009), iii) large ozone net production potential because deep convection can transport chemical species in the upper troposphere (UT), where their lifetime is increased due to lack of surface deposition and dilution with unpolluted background (Pickering et al., 1995), and iv) dynamic processes capable of redistributing chemical species in a regional and global scale (Zhang et al., 2016). Thus, the tropics are a region where O_3 production is favoured.

Recent studies (e.g. Zhang et al., 2016; Gaudel et al., 2018; 2020) have shown increasing tropospheric O_3 burden in the second half of the 20th century mostly due to the increase of precursors in the tropical regions. However, uncertainties remain in the detection of global tropospheric O_3 trends. Ozonesondes provide measurements in the troposphere, but they are limited by the low sampling frequency and their sparse spatial coverage (Tarasick et al., 2019). Satellite instruments provide measurements of tropospheric O_3 with high spatial and temporal resolution and on a global scale. However, satellite-detected O_3 trends are less certain due to inconsistencies among different satellite products (Gaudel et al., 2018). Therefore, it is necessary to validate satellite-detected trends using in situ observations to rely on satellites for O_3 trend detection.

Despite their inconsistencies, the different satellites agree on a tropospheric O_3 increase over the tropics (Gaudel et al., 2018). Several studies tend to confirm this increase (e.g. Zhang et al., 2016; Ziemke et al., 2019) but they are mostly based on model simulations, sparse ground observations, or satellite data with little consistency, and it is not clear what can cause such O_3 increase. Therefore, further in situ measurements are needed to study the composition of the tropical troposphere, to better constraint models, validate satellite retrievals, and reduce the uncertainties in the quantification of O_3 and CO trends and source attribution over the tropics.

Despite the importance of the tropics in O_3 and CO production, the tropical troposphere is little documented in comparison with the northern mid-latitudes. Measurements of tropical O_3 and CO are available by satellite observations, but they have a coarse vertical resolution (e.g. Barret et al., 2008; Thompson et al., 2001). Measurements provided by campaigns offer limited spatial and temporal coverage. The Southern Hemisphere ADDitional OZone Sounding (SHADOZ) program (Thompson et al., 2003a) provides long-term O_3 observations over the tropics using ozonesondes since 1998. Even though these measurements offered a better understanding of the vertical distribution of tropical O_3 , they are mostly limited to remote observing sites such as Ascension and Reunion Island. In addition, it is difficult to provide additional constraints regarding the relation between O_3 and CO in the tropics, due to a lack of simultaneous CO in situ observations.

The overall objective of this thesis is to characterise the tropical O_3 changes and to document

the characteristics of O_3 and CO climatologies in the tropical troposphere.

Infrared Atmospheric Sounding Interferometer (IASI)-Software for a Fast Retrieval of IASI Data (SOFRID) (Barret et al., 2011; De Wachter et al., 2012) retrievals provide measurements of O_3 and CO on a global scale and with an almost daily revisit. Previous studies have validated IASI products (Barret et al., 2020; De Wachter et al., 2012), but they do not focus on the tropical region due to the limited available in situ observations. The radiative forcing of O_3 is particularly important in the tropical UT (Chen et al., 2007). Therefore, it is important to document the ability of IASI to document the characteristics of O_3 and its precursor CO in this layer independently. In addition, to reduce the uncertainties of O_3 trends by IASI, it is necessary to determine the impact of the vertical sensitivity of IASI upon the documented trends.

The IAGOS (In-service Aircraft for a Global Observing System; (Marenco et al., 1998; Petzold et al., 2015; Thouret et al., 2022) program has provided continuous and consistent O_3 (Thouret et al., 1998; Blot et al., 2021) and CO (Nédélec et al., 2015) observations over the tropics since 1994 and 2002 respectively. It measures vertical profiles over remote (e.g. Madras) and megacities (e.g. Lagos, Hong Kong), along with the lower part of the upper tropical troposphere. Previous studies have documented the tropical composition over Africa (Sauvage et al., 2005; Sauvage et al., 2007a; Sauvage et al., 2007d; Lannuque et al., 2021), South America (Yamasoe et al., 2015) and South Asia (Sahu et al., 2014; Sheel et al., 2014). However, they are focused on specific regions of the tropics and have limited temporal coverage, especially for CO as fewer measurements were available at this time. Thus, the O_3 and CO distributions and their interlocking in the entire tropics are still not well documented.

The **SOft attribution using FlexparT and carbon monoxide emission inventories for In-situ Observation database (SOFT-IO)** model (Sauvage et al., 2017) has been developed to supplement the analysis of the IAGOS dataset by estimating AN and BB contributions to the observed CO measurements. These measurements, along with the SOFT-IO output allow us to trace the CO origin, and establish connections with the O_3 origin over the tropics.

The first part of this thesis is mostly focused on the O_3 trends over the tropics. First, we use IAGOS vertical profiles to evaluate tropospheric O_3 trends from IASI. This way, we prove that we can rely on IASI for trend detection, and we can take advantage of its continuous measurements (in time and space) to assess the O_3 evolution in the tropics. Then, the IASI evaluated trends are compared with O_3 trends available in the bibliography.

The second part of the thesis is focused on the O_3 and CO climatologies over the tropics. First, the IASI O_3 and CO retrievals are evaluated in the tropical UT, using IAGOS cruise measurements. After, the global distributions provided by IASI are analysed to complement the O_3 and CO distributions provided by IAGOS. They are used to document the spatial extent of pollution plumes and explore intercontinental transport patterns. We also take

advantage of the fine vertical resolution of IAGOS to assess the characteristics and seasonal variability of O_3 and CO over the tropical troposphere. Using SOFT-IO, we explore the origin of the observed CO anomalies and investigate transport processes driving the CO and O_3 distribution in the tropics. The questions we address in this part are:

- Where are the maxima and minima of O_3 and CO recorded in the tropics? What is their seasonal variation?
- Where does CO come from to form these maxima (anthropogenic or biomass burning)?
- Which region contributes the most to the export of CO in the tropical troposphere?

The manuscript is organised as follows. [Chapter 1](#) provides information about O_3 and CO. We explain their role and significance in the troposphere, their main sources and sinks, as well as their global budget. [Chapter 2](#) focuses on the region of interest, the tropics. We describe the particularities of the tropospheric dynamics in the tropics, and the natural and anthropogenic sources of precursors located in the region. [Chapter 3](#) provides detailed information about the observational (IAGOS and IASI) and modelled based (SOFT-IO) datasets used in this thesis. In [Chapter 4](#), we present the two quality assessments of IASI retrievals using IAGOS measurements for the evaluation of: i) the UT CO and O_3 climatologies, and ii) the tropospheric O_3 trends. In the last part of this chapter, we present the characteristics of the tropical O_3 trends as seen by IASI. [Chapter 5](#) provides the analysis of the climatologies of O_3 and CO over the tropical troposphere based on IAGOS and IASI data. In addition, the sources of observed CO are explored with SOFT-IO. Last, in [Chapter 6](#) we summarise the main results of the thesis, and we discuss possible perspectives of this work.

General Introduction in French

L’ozone troposphérique (O_3) et le monoxyde de carbone (CO) sont des composants clés de l’atmosphère en raison de leur rôle dans la qualité de l’air, la chimie atmosphérique et le climat. O_3 a un impact sur la capacité d’oxydation de la troposphère en tant que source majeure de radicaux hydroxyles (OH), et sur le climat en tant que puissant gaz à effet de serre dans la haute troposphère (IPCC, 2021). De plus, l’ O_3 proche de la surface a un impact négatif sur la santé humaine et la croissance de la végétation (Jerrett et al., 2009). L’ O_3 est principalement produit photochimiquement par les émissions de précurseurs, tels que le CO et les composés organiques volatils (VOCs), en présence d’oxydes d’azote (NO_x) (Logan et al., 1981). C’est un polluant secondaire, avec une durée de vie relativement courte (typiquement quelques heures dans le BL et environ 22 jours dans la troposphère libre (FT) ; Stevenson et al., 2006), donc ses facteurs de contrôle sont difficiles à identifier. Sa distribution dans la troposphère est déterminée par : les émissions (anthropiques et naturelles) de précurseurs (Monks et al., 2015) suivies d’une production et d’une destruction photochimique, les échanges stratosphère-troposphère (Stevenson et al., 2013), les processus dynamiques qui redistribuent les masses d’air riches ou pauvres en O_3 et en précurseurs (Wild et al., 2004), et les processus de dépôt et photochimiques entraînant la destruction de O_3 (Monks et al., 2015).

Le CO influence la capacité d’oxydation de la troposphère, qui est le principal puits de OH (Lelieveld et al., 2016), et donc le climat par le biais d’une augmentation de la durée de vie du méthane (CH_4) (Seinfeld and Pandis, 1998), le deuxième plus important gaz à effet de serre (IPCC, 2021). De plus, son oxydation contribue à une augmentation du dioxyde de carbone (CO_2) et de l’ O_3 (Myhre et al., 2013), qui sont des gaz à effet de serre (IPCC, 2021). Le CO est produit par des sources primaires (par exemple, les émissions de surface provenant de la combustion anthropique (AN) et de la combustion de la biomasse (BB)), et par des sources secondaires (par exemple, l’oxydation des COV). La relation entre l’ O_3 observé et le CO est utile pour contraindre notre compréhension des facteurs contrôlant l’ O_3 (Voulgarakis et al., 2011). En raison de sa longue durée de vie, le CO est considéré comme un traceur de pollution des produits de combustion (Logan et al., 1981) qui émettent des précurseurs de O_3 . Une corrélation entre l’ O_3 et le CO a été observée dans des panaches de pollution et de BB âgés (Parrish et al., 1993; Jaffe and Wigder, 2012), ce qui indique qu’une région a connu une production photochimique d’ O_3 à partir de ses précurseurs (dont le CO) (Voulgarakis et al., 2011 et références y afférentes). L’anticorrélation O_3 - CO près de la surface indique un dépôt et une destruction de O_3 . De plus, la relation O_3 - CO s’étend dans la FT et à des échelles intercontinentales, reflétant le mélange des masses d’air et de la chimie (par exemple

Andreae et al., 1994). Lorsque des intrusions stratosphériques se produisent, O_3 et CO sont anti corrélés, car l'air stratosphérique est riche en O_3 et pauvre en CO (e.g. Parrish et al., 1998). Ainsi, la relation O_3 -CO est utile pour contraindre les sources et le transport de O_3 .

Les tropiques présentent un intérêt particulier pour l' O_3 et le CO troposphériques. Elles combinent : i) une photochimie intense due à un rayonnement solaire et à une humidité élevés, ii) d'importantes sources naturelles actives (combustion de la biomasse, foudre et émissions dans le sol) de précurseurs de l' O_3 (par exemple Sauvage et al., 2007b; Ziemke et al., 2009), iii) un grand potentiel de production nette d'ozone car la convection profonde peut transporter les espèces chimiques dans la haute troposphère (UT), où leur durée de vie est accrue en raison de l'absence de dépôt en surface et de la dilution avec le fond non pollué (Pickering et al., 1995), et iv) des processus dynamiques capables de redistribuer les espèces chimiques à l'échelle régionale et mondiale (Zhang et al., 2016). Ainsi, les tropiques sont une région où la production de O_3 est favorisée.

Des études récentes (par exemple, Zhang et al., 2016 ; Gaudel et al., 2018 ; 2020) ont montré une augmentation de la charge troposphérique en O_3 dans la seconde moitié du 20ème siècle, principalement due à l'augmentation des précurseurs dans les régions tropicales. Toutefois, des incertitudes subsistent dans la détection des tendances mondiales de l' O_3 troposphérique. Les ozonosondes fournissent des mesures dans la troposphère, mais elles sont limitées par la faible fréquence d'échantillonnage et leur couverture spatiale clairsemée (Tarasick et al., 2019). Les instruments satellitaires fournissent des mesures de l' O_3 troposphérique avec une haute résolution spatiale et à l'échelle mondiale. Cependant, les tendances de l' O_3 détectées par satellite sont moins certaines en raison des incohérences entre les différents produits satellitaires (Gaudel et al., 2018). Il est donc nécessaire de valider les tendances détectées par satellite à l'aide d'observations in situ afin de pouvoir se fier aux satellites pour la détection des tendances de l' O_3 .

En dépit de leurs incohérences, les différents satellites s'accordent sur une augmentation de l' O_3 troposphérique sur les tropiques (Gaudel et al., 2018). Plusieurs études tendent à confirmer cette augmentation (par exemple Zhang et al., 2016; Ziemke et al., 2019) mais elles sont pour la plupart basées sur des simulations de modèles, des observations au sol éparses ou des données satellitaires peu cohérentes, et on ne sait pas clairement ce qui peut provoquer une telle augmentation de O_3 . Il est donc nécessaire d'effectuer d'autres mesures in situ afin d'étudier la composition de la troposphère tropicale, de mieux contraindre les modèles, de valider les données récupérées par satellite et de réduire les incertitudes dans la quantification des tendances de l' O_3 et du CO et l'attribution des sources au-dessus des tropiques.

Malgré l'importance des tropiques dans la production de O_3 et de CO, la troposphère tropicale est peu documentée par rapport aux moyennes latitudes du nord. Des mesures de l' O_3 et du CO tropicaux sont disponibles par des observations satellitaires, mais elles ont

une résolution verticale grossière : [par exemple] [barret2008, thompson2001tropical]. Les mesures fournies par les campagnes offrent une couverture spatiale et temporelle limitée. Le programme Southern Hemisphere ADDitional OZone Sounding (SHADOZ) (Thompson et al., 2003a) fournit des observations à long terme de O_3 au-dessus des tropiques en utilisant des ozonesondes depuis 1998. Bien que ces mesures aient permis de mieux comprendre la distribution verticale de l' O_3 tropical, elles sont pour la plupart limitées à des sites d'observation éloignés tels que l'Ascension et l'île de la Réunion. De plus, il est difficile de fournir des contraintes supplémentaires concernant la relation entre O_3 et CO dans les tropiques, en raison d'un manque d'observations simultanées de CO in situ.

L'objectif global de cette thèse est de caractériser les changements tropicaux de O_3 , et de documenter les caractéristiques des climatologies de O_3 et de CO dans la troposphère tropicale.

L'interféromètre de sondage atmosphérique infrarouge (IASI)-Software for a Fast Retrieval of IASI Data (SOFRID) (Barret et al., 2011; De Wachter et al., 2012) fournit des mesures de O_3 et de CO à l'échelle mondiale et avec une revisite presque quotidienne. Des études précédentes ont validé les produits IASI (Barret et al., 2020; De Wachter et al., 2012), mais elles ne se concentrent pas sur la région tropicale en raison du nombre limité d'observations in situ disponibles. Le forçage radiatif de O_3 est particulièrement important dans l'UT tropicale (Chen et al., 2007). Il est donc important de documenter la capacité de l'IASI à documenter indépendamment les caractéristiques de O_3 et de son précurseur CO dans cette couche. En outre, afin de réduire les incertitudes des tendances de O_3 par IASI, il est nécessaire de déterminer l'impact de la sensibilité verticale de IASI sur les tendances documentées.

Le programme IAGOS (In-service Aircraft for a Global Observing System ; (Marenco et al., 1998; Petzold et al., 2015; Thouret et al., 2022) a fourni des observations continues et cohérentes de O_3 (Thouret et al., 1998; Blot et al., 2021) et de CO (Nédélec et al., 2015) au-dessus des tropiques depuis 1994 et 2002 respectivement. Il mesure les profils verticaux au-dessus des villes éloignées (par exemple Madras) et des mégapoles (par exemple Lagos, Hong Kong), ainsi que la partie inférieure de la haute troposphère tropicale. Des études antérieures ont documenté la composition tropicale au-dessus de l'Afrique (Sauvage et al., 2005; Sauvage et al., 2007c; Sauvage et al., 2007d; Lannuque et al., 2021), de l'Amérique du Sud (Yamasoe et al., 2015) et de l'Asie du Sud (Sahu et al., 2014; Sheel et al., 2014). Cependant, elles se concentrent sur des régions spécifiques des tropiques et ont une couverture temporelle limitée, notamment pour le CO car moins de mesures étaient disponibles à cette époque. Ainsi, les distributions de O_3 et de CO et leur imbrication dans l'ensemble des tropiques ne sont pas encore bien documentées.

Le modèle **SOft attribution using FlexparT and carbon monoxide emission inventories for In-situ Observation database (SOFT-IO)** (Sauvage et al., 2017) a été développé pour compléter

l'analyse du jeu de données IAGOS en estimant les contributions AN et BB aux mesures de CO observées. Ces mesures, ainsi que la sortie de SOFT-IO nous permettent de tracer l'origine du CO, et d'établir des connexions avec l'origine de O₃ au-dessus des tropiques.

La première partie de cette thèse est principalement axée sur les tendances de l'O₃ au-dessus des tropiques. Tout d'abord, nous utilisons les profils verticaux de IAGOS pour évaluer les tendances de l'O₃ troposphérique provenant de IASI. De cette façon, nous prouvons que nous pouvons compter sur IASI pour la détection des tendances, et nous pouvons tirer profit de ses mesures continues dans le temps et l'espace afin d'évaluer l'évolution de l'O₃ dans les tropiques. Les tendances évaluées par IASI sont comparées aux tendances de l'O₃ disponibles dans la bibliographie.

La deuxième partie de la thèse se concentre sur les climatologies de l'O₃ et du CO au-dessus des tropiques. Tout d'abord, les extractions IASI de O₃ et de CO sont validées dans l'UT tropicale, en utilisant les mesures de la croisière IAGOS. Ensuite, la distribution globale fournie par IASI est analysée pour compléter la distribution de O₃ et de CO fournie par IAGOS. Elles sont utilisées pour documenter l'étendue spatiale des panaches de pollution, et explorer les modèles de transport intercontinentaux. Nous profitons également de la fine résolution verticale de IAGOS pour évaluer les caractéristiques et la variabilité saisonnière de O₃ et de CO au-dessus de la troposphère tropicale. En utilisant SOFT-IO, nous explorons l'origine des anomalies de CO observées et nous étudions les processus de transport qui déterminent la distribution du CO et de l'O₃ dans les tropiques. Les questions que nous abordons dans cette partie sont :

- Où sont les maxima et minima de O₃ et de CO enregistrés dans les tropiques ? Quelle est leur variation saisonnière ?
- D'où vient le CO pour former ces maxima (anthropique ou combustion de la biomasse) ?
- Quelle région contribue le plus à l'exportation de CO dans la troposphère tropicale ?

Le manuscrit est organisé comme suit. [Chapter 1](#) fournit des informations sur l'O₃ et le CO. Nous expliquons leur rôle et leur importance dans la troposphère, leurs principales sources et leurs principaux puits, ainsi que leur bilan global. [Chapter 2](#) se concentre sur la région qui nous intéresse, les tropiques. Nous décrivons les particularités de la dynamique de la troposphère dans les tropiques, et les sources naturelles et anthropiques de précurseurs situées dans la région. [Chapter 3](#) fournit des informations détaillées sur les jeux de données d'observation (IAGOS et IASI) et de modélisation (SOFT-IO) utilisés dans cette thèse. Dans le chapitre [Chapter 4](#), nous présentons les deux évaluations de la qualité des récupérations IASI en utilisant les mesures IAGOS pour l'évaluation de : i) les climatologies UT CO et O₃, et ii) les tendances de l'O₃ troposphérique. Dans la dernière partie de ce chapitre, nous présentons les caractéristiques des tendances de l'O₃ tropical telles qu'elles sont observées par IASI. [Chapter 5](#) fournit l'analyse des climatologies de O₃ et de CO au-dessus de la

troposphère tropicale sur la base des données IAGOS et IASI. En outre, les sources du CO observé sont explorées avec SOFT-IO. Enfin, dans [Chapter 6](#) nous résumons les principaux résultats de la thèse, et nous discutons des perspectives possibles de ce travail.

CHAPTER 1

Ozone and Carbon monoxide in the Troposphere

In this chapter, we give some general information about O_3 (Section 1.1) and CO (Section 1.2), which are key components in the Earth's atmosphere. In Section 1.1, we begin explaining the role of O_3 in the atmosphere (Section 1.1.1) to clarify the scientific interest in this atmospheric compound. This is followed by a description of its main sources and sinks in the troposphere (Section 1.1.2), and its global budget (Section 1.1.3). Similarly in Section 1.2, we provide information about the role of CO (Section 1.2.1), its main sources and sinks (Section 1.2.2), as well as our current knowledge about its global budget (Section 1.2.3).

1.1 Tropospheric ozone

1.1.1 Role and Significance

O_3 is one of the most important trace gases in the atmosphere, with both positive and negative impacts on the environment.

O_3 plays a key role in the oxidation capacity of the atmosphere as a major source of OH. Trace gases, such as CO and CH_4 , are removed from the atmosphere mainly due to oxidation by OH. The oxidation in the troposphere is important because: i) the troposphere contains 85 % of the total atmospheric mass, and ii) most of the emissions of the trace gases are located at the surface (Jacob, 1999).

In the UT, O_3 acts as a greenhouse gas, as it absorbs IR radiation emitted by the surface and traps heat in the troposphere. O_3 is the third most powerful greenhouse gas, after CO_2 and CH_4 , contributing to global warming and climate change (Myhre et al., 2013). According to IPCC (2021), the control of short-lived climate pollutants such as O_3 , along with the reduction in CO_2 emissions are necessary steps to limit global warming within 1.5 ° since pre-industrial times.

In the boundary layer, O_3 is considered a toxic and harmful pollutant for humans, as it can cause respiratory problems (Monks et al., 2015). Long-term exposure can be related to premature deaths due to respiratory diseases (Jerrett et al., 2009). To protect public health, the World Health Organization (WHO) has suggested Air quality guidelines, which provide limit values for specific air pollutants. Currently, the Air quality guideline for O_3

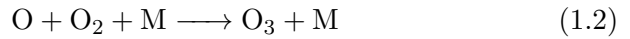
recommends an 8 h value of $100 \mu\text{g m}^{-3}$ for short-term exposure, and a peak season¹ value of $60 \mu\text{g m}^{-3}$ for long-term exposure (WHO, 2021).

Boundary-layer O_3 can also damage trees and vegetation, and reduce crop production by affecting photosynthesis and the growth of plants (Monks et al., 2015). The latter can have a serious impact on the economy on a regional and global scale. Many crops, such as wheat and rice, are sensitive or moderately sensitive to O_3 (Mills et al., 2007). The crop production loss due to exposure to O_3 globally is estimated to be 79–121 million tonnes, which translates to United States dollar (USD) 11–18 billion on an annual basis (Avnery et al., 2011). Over two states of India, the crop loss due to O_3 was estimated to be USD 6.5 billion in 2012–2013, and USD 3.7 billion in 2013–2014 (Sinha et al., 2015). On a national scale, the crop loss in India would be enough to feed approximately 94 million people living below the poverty limit (Ghude et al., 2014).

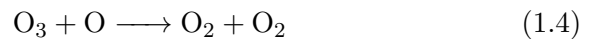
1.1.2 Sources and Sinks

O_3 is found in trace amounts in the Earth’s atmosphere, peaking in the stratospheric layer (approximately 90 %) (Jacob, 1999). Stratospheric O_3 absorbs the harmful UV radiation from the Sun (100–400 nm) and is substantial for maintaining life on Earth. On the other hand, tropospheric O_3 is a greenhouse gas and a harmful pollutant (see Section 1.1.1).

O_3 is produced naturally in the atmosphere according to a cycle of reactions, the so-called Chapman cycle (Chapman, 1930). The cycle is initiated by the photolysis of oxygen molecules (O_2) at wavelengths less than 242 nm (Equation 1.1). The produced atomic oxygen (O) reacts rapidly with O_2 in the presence of a stable third body, M (usually N_2 or O_2) to form a molecule of O_3 (Equation 1.2).



Equations 1.1 and 1.2 result in O_3 production, however, UV radiation can also dissociate O_3 to form O (Equation 1.3). O_3 is also destroyed by reaction with O to reform O_2 (Equation 1.4). O_2 rapidly leads to O_3 formation as the Equation 1.2 is a very fast reaction.



¹Average of daily maximum 8-hour mean O_3 concentration in the six consecutive months with the highest six-month running average O_3 concentration.

The Chapman cycle (Equations 1.1–1.4) is not dominant in the troposphere, because of the limited levels of UV radiation at wavelengths <242 nm (because of the UV absorption by O_3 in the stratosphere) available for the dissociation of O_2 into atomic oxygen (Equation 1.1). In the troposphere, O_3 is formed by a similar mechanism, but the source of the atomic oxygen is different: the photolysis of NO_2 in the visible range of solar radiation.

O_3 – NO_x cycle

The formation of tropospheric O_3 is realised in catalytic cycles. One important ingredient is the presence of NO_x : nitric oxide (NO) and nitrogen dioxide (NO_2). NO_2 is photolyzed in the atmosphere (at wavelengths <424 nm) and produces an O atom, which recombines with O_2 to form O_3 (Equations 1.5 and 1.2). However, without any other compound involved, NO will react with O_3 and destroy the O_3 formed by NO_2 photolysis (Equation 1.6).



Consequently, Equations 1.5, 1.2, and 1.6 are a sink and a source of O_3 in the troposphere. This cycle of reactions does not lead to a net gain or loss of O_3 but maintains photochemical equilibrium between O_3 , NO , and NO_2 , the so-called null cycle. This indicates that for O_3 production in the troposphere, another source of NO_2 in addition to Equation 1.6 is required.

During the nighttime, in the absence of solar radiation, the NO_2 photolysis (Equation 1.5) no longer occurs. Alternatively, NO_2 reacts with O (Equation 1.7). Therefore, NO_2 is destroyed, producing NO which reacts with O_3 (Equation 1.6). Therefore, during nighttime the null cycle is disturbed, leading to a net O_3 destruction.



Hydroxyl Radical

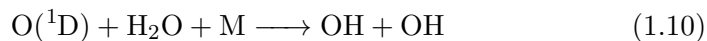
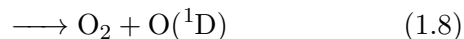
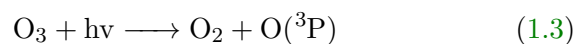
The null cycle described above can be disturbed by the peroxy radicals (HO_2) organic peroxy radicals (RO_2 , where R denotes an organic group) reactions with NO (Equations 1.11 and 1.20), as we will see later. These reactions allow the conversion of NO to NO_2 without O_3 destruction. The highly reactive HO_2 and RO_2 result from the oxidation of VOCs by OH.

The OH production in the troposphere is initiated by the photolysis of O_3 . O_3 photolysis can lead to the formation of an oxygen atom in its ground state ($O(^3P)$) (Equation 1.3) or an oxygen atom in its excited state ($O(^1D)$) (Equation 1.8).

- In the case $O(^3P)$ is formed, the ground state oxygen recombines with O_2 (Equation 1.2) to reproduce O_3 . As a result, there is no net production or destruction of O_3 .

- In the case $O(^1D)$ is formed, the excited oxygen atom can follow two main pathways. Firstly, it can collide with a third body, M (usually N_2 and O_2) which removes the energy from the excited atom and converts it back to its ground state $O(^3P)$ (Equation 1.9). As mentioned before, the O atom can react with O_2 to reform O_3 , resulting in a null cycle for O_3 .

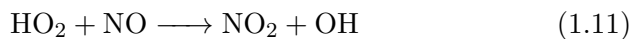
Secondly, the excited oxygen atom can react with water (H_2O) to form OH (Equation 1.10).



Initially, it was assumed that the formation of OH does not occur in the troposphere because the required UV radiation is absorbed by O_3 in the stratosphere. However, it turns out that there is a small wavelength interval between 300 and 320 nm where there is the possibility of OH production in the troposphere. Despite the less available light in the troposphere than in the stratosphere, the troposphere holds more H_2O . As a result, more of $O(^1D)$ can produce OH by Equation 1.10.

The fraction of $O(^1D)$ atoms that form OH depends on the concentration of H_2O . Typically, in the marine boundary layer, about 10 % of the $O(^1D)$ leads to OH formation (Monks, 2005). Equations 1.8 and 1.10 are the primary source of OH in the troposphere.

Another reaction pathway leading to OH formation is the reaction of NO with the hydroperoxyl radical (HO_2), to form NO_2 and OH (Equation 1.11). The production of NO_2 by Equation 1.11 will result in a net production of O_3 as the conversion of NO to NO_2 occurs without any consumption of O_3 .

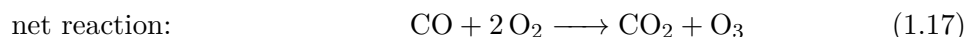
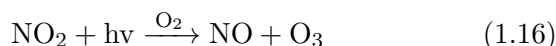
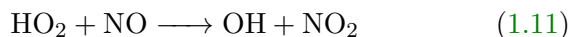
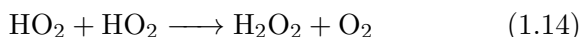
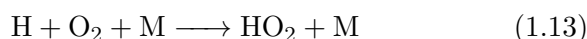
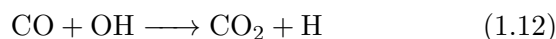


The main sink of OH is the oxidation of other trace gases in the troposphere such as CO and CH_4 . As we will see later, these oxidation processes can also lead to the production of peroxy radicals, contributing to additional NO_2 production by oxidation of NO , and thus further O_3 production. In polluted regions, another important sink of OH is the loss to NO_2 .

CO oxidation mechanism

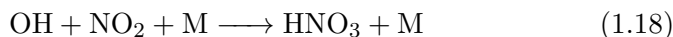
The CO oxidation mechanism initiates an O_3 producing cycle which is summarised in Equation 1.17. The individual reaction steps are presented in Equations 1.12–1.16. The

reaction of CO with OH produces an H atom (Equation 1.12), which rapidly reacts with O₂ to form the HO₂ radical (Equation 1.13). This HO₂ enters the O₃ production via interaction with the NO_x cycle discussed above. Without any O₃ being consumed and thus omitting Equation 1.6, the equilibrium between NO and NO₂ in Equations 1.5 and 1.6 is disturbed and shifted towards NO₂. The photolysis of NO₂ produces O atoms and leads to O₃ formation. The equilibrium established by the rapid photochemical cycling between NO_x and O₃ will thus react by increasing the O₃ concentration. The production of O₃ in this cycle occurs because the oxidation of NO to NO₂ is done by the HO₂ radical (Equation 1.11).



The fact that OH is not consumed, but is used as a catalyst as it is re-formed by the reaction HO₂ with NO (Equation 1.11), is particularly important for atmospheric chemistry. During the 1970s, scientists were concerned that the increasing emissions of CO from fossil fuel burning could result in the poisoning of the atmosphere, as all the available OH could be used up, leading to insufficient cleansing of the atmosphere.

Finally, the termination of the chain occurs when OH and NO₂ react to produce nitric acid according to the following reaction:



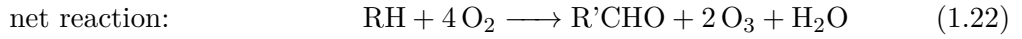
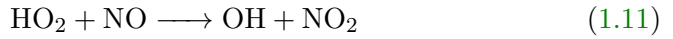
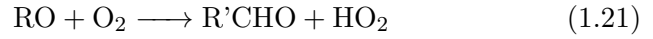
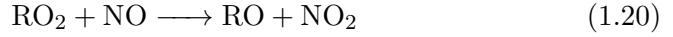
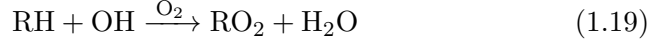
This reaction is a sink for both hydrogen oxide radicals (HO_x) and NO_x.

Hydrocarbons oxidation mechanism

The hydrocarbons (RH, where R denotes an organic group) oxidation mechanism initiates an O₃ producing cycle which is summarised in Equation 1.22. The individual reaction steps are presented in the equations below (Equations 1.19–1.21, 1.11, 1.5, and 1.2). The reaction of RH with OH produces RO₂ (Equation 1.19) which reacts with NO to form NO₂ and an organic oxy radical, RO (Equation 1.20). The produced NO₂ participated in the production of O₃, as we can see in the equations below (Equations 1.5 and 1.2).

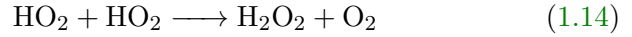
The produced RO radical reacts with O₂ to form carbonyl compounds (R'CHO) (Equa-

tion 1.21) which can either photolyze to form HO_x or react with OH to continue the chain propagation.



The reaction chain is terminated by the loss of the HO_x radicals. This loss can occur following these main reaction pathways:

- HO_2 may react with themselves instead of with NO to produce peroxides and other oxygenated compounds. The most important process is the self-reaction of HO_2 :



- Another sink of HO_x radicals is the oxidation of NO_2 by OH:



- Last, HO_2 may react with RO_2 :

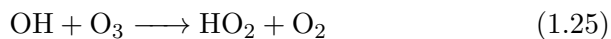
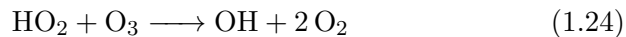


The nitric acid (HNO_3) molecules are photolyzed to form NO_x at a local scale. Similar to hydrogen peroxide (H_2O_2), HNO_3 is scavenged in and below clouds which remove it from the atmosphere. These species can also be removed by dry deposition. In the lower troposphere (LT), HNO_3 is a sink for NO_x and HO_x , and H_2O_2 is a sink for HO_x .

Photochemical destruction

The chemical destruction of O_3 in the troposphere is mainly caused by O_3 photolysis (Equation 1.3), which results in OH formation in the presence of water vapour (Equation 1.10). The chemical destruction of O_3 is larger in the LT due to the higher water vapour concentrations (Monks et al., 2015).

O₃ can also be destroyed through the reactions:



In urban regions, the high concentration of NO close to the surface results in reduced O₃ mixing ratios. The reaction of NO with O₃ (Equation 1.6) is known as chemical O₃ titration and is typically short-lived. This is because the formed NO₂ leads to further O₃ formation after its transport to cleaner environments in terms of NO concentration (Monks et al., 2015).

O₃ production regimes

The reactions relevant to the cycling of HO_x and the formation of O₃ are summarised below:

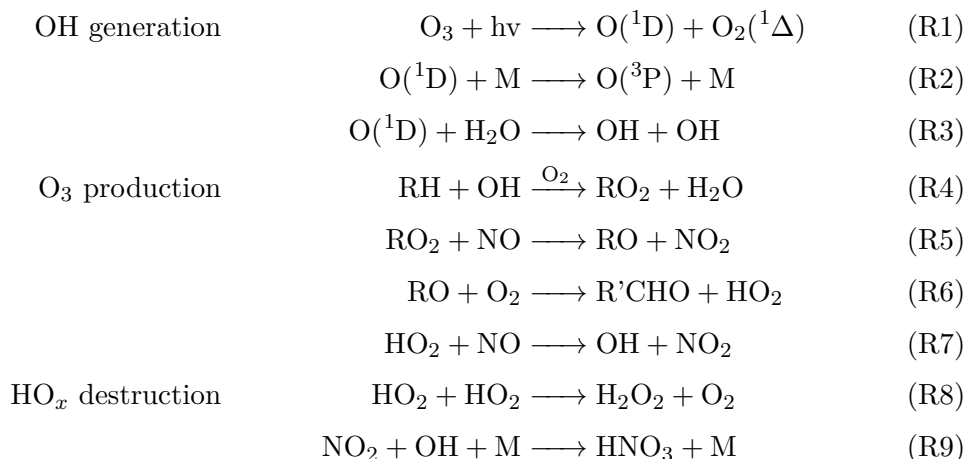


Figure 1.1 displays the diagram of the O₃ production mechanism based on the reactions above. After one chain propagation cycle (R4–R7), two molecules of O₃ are formed, in the steps (R5) and (R7).

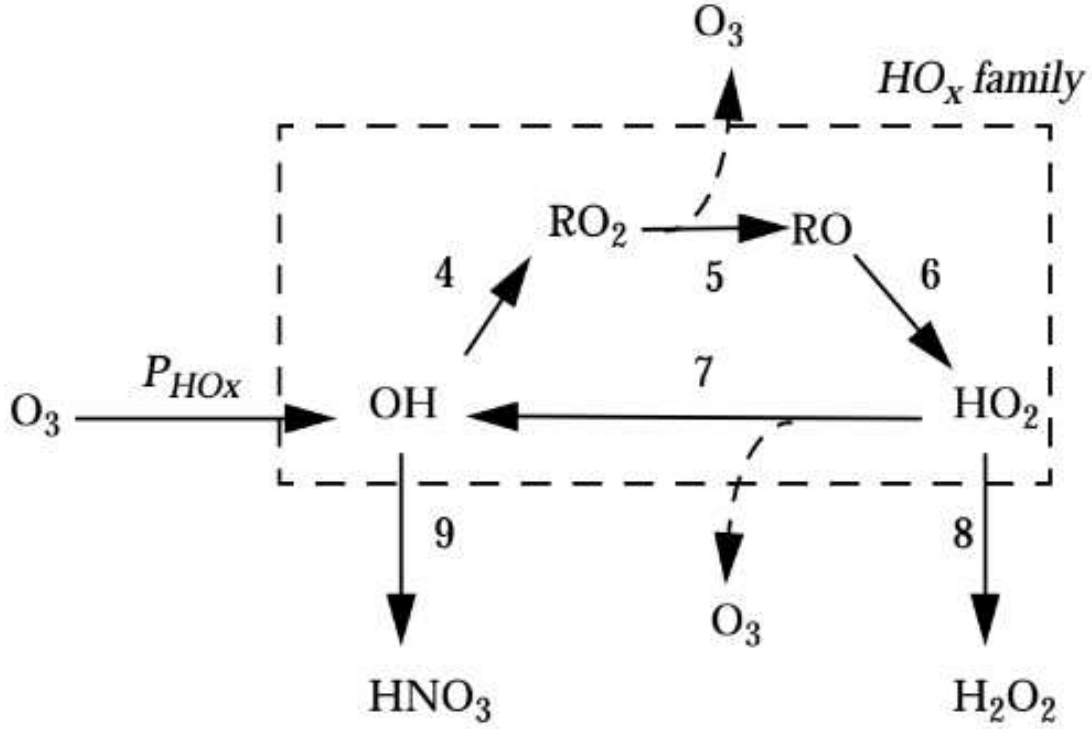


Figure 1.1: Cycling of HO_x and O₃ production in a polluted atmosphere. Source: Jacob (1999)

As discussed in Jacob (1999), we can assume efficient chain propagation in a polluted atmosphere, which yields to $\text{rate(R4)} = \text{rate(R5)} = \text{rate(R6)} = \text{rate(R7)}$. The rate of O₃ production is:

$$P_{O_3} = k_5[RO_2][NO] + k_7[HO_2][NO] = 2k_7[HO_2][NO] \quad (1.26)$$

The efficient cycle also yields to a steady state for OH. This means that the production of OH from (R7) is in balance with its loss from (R4):

$$[OH] = \frac{k_7[HO_2][NO]}{k_4[NO]} \quad (1.27)$$

The steady state of the HO_x family, yields to:

$$P_{HO_x} = k_8[HO_2]^2 + k_9[NO_2][OH][M] \quad (1.28)$$

- When the NO_x concentrations are low: The rate(R8) is much larger than the rate(R9). This means that the second term on the right-hand side of Equation 1.28 can be

neglected. Inserting the latter in Equation 1.26 leads to:

$$P_{O_3} = 2k_7 \sqrt{\frac{P_{HO_x}}{k_8}} [NO] \quad (1.29)$$

Consequently, the O_3 production rate, P_{O_3} , increases linearly with $[NO]$ but is independent of hydrocarbons. This case is known as the NO_x -limited regime because the O_3 production rate is limited by the NO_x supply.

- When the NO_x concentrations are high: The rate(R8) is much smaller than the rate(R9). In this case, the first term on the right-hand side of the Equation 1.28 can be neglected, leading to:

$$[OH] = \frac{P_{HO_x}}{k_9[NO_2][M]} \quad (1.30)$$

Inserting the latter in the Equation 1.27, yields to:

$$[HO_2] = \frac{P_{HO_x} k_4 [RH]}{k_7 k_9 [NO][NO_2][M]} \quad (1.31)$$

Using the latter in Equation 1.26 gives:

$$P_{O_3} = \frac{2k_4 P_{HO_x} [RH]}{k_9 [NO_2][M]} \quad (1.32)$$

In Equation 1.32, the O_3 production rate, P_{O_3} , increases linearly with $[RH]$ and decreases inversely with $[NO_2]$. This case is known as the VOC-limited regime because the O_3 production rate is limited by the VOCs supply.

Figure 1.2 displays the results of a simple box model (EKMA) which estimated the O_3 concentrations produced from various initial VOCs and NO_x concentrations. The simulated O_3 concentrations were later tested with environmental chamber data. The Figure shows the maximum O_3 isopleths (in ppm) as a function of VOCs (in ppmC) and NO_x (in ppm) concentrations. It also shows three lines denoting different VOCs to NO_x ratios (4/1, 8/1, and 15/1). The ratio of VOCs to NO_x concentrations plays a key role in the rate of O_3 production and it is used for the differentiation between the two O_3 production regimes (VOC- and NO_x -limited regimes). According to the EKMA method, a VOCs/ NO_x ratio of about 8/1 is optimal for O_3 production (Figure 1.2). The VOC-limited regime occurs when the VOCs/ NO_x ratio is smaller than 8/1, whereas the NO_x -limited regime occurs when the VOCs/ NO_x ratio is larger than 8/1.

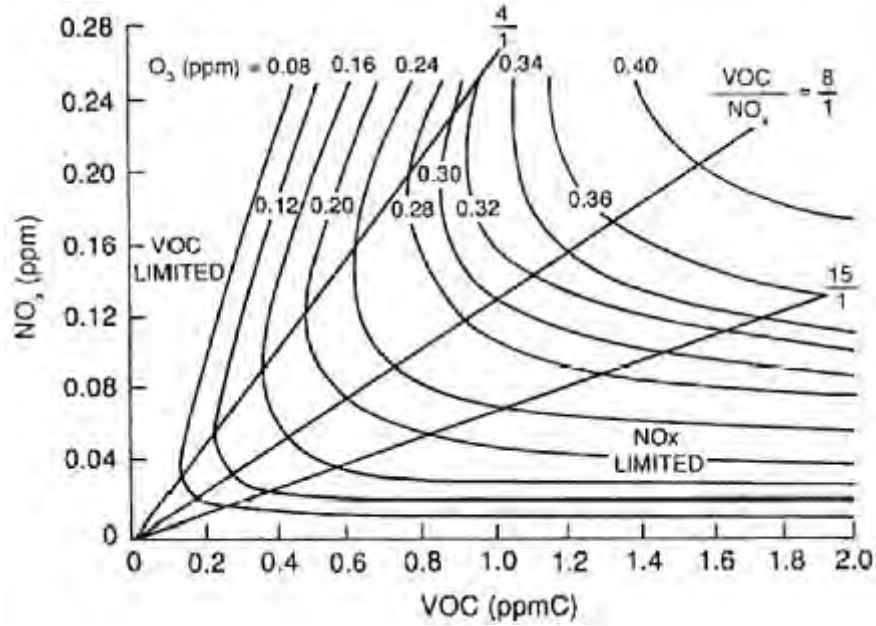


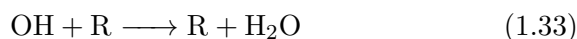
Figure 1.2: Isopleth (lines of constant value) plots for O_3 mixing ratios as a function of various initial VOCs and NO_x mixing ratios based on the EKMA (Empirical Kinetic Modelling Approach) model. Source: National Research Council (1991)

Figure 1.2 displays the non-linear dependency of O_3 on the concentration of its precursors. Under a high VOCs/ NO_x ratio (NO_x -limited regime; at the right side of the ridge line in Figure 1.2), decreasing NO_x concentration either at constant VOCs concentrations or coupled with decreasing VOCs concentrations leads to decreased peak concentrations of O_3 . At the NO_x -limited regime, the limiting factor of O_3 production is the NO_x cycle. This is because the intensity of the NO_x cycle is weaker than the one of the RO_x cycle, under the short NO_x supply characterising this regime. The high abundances of HO_2 and RO_2 react with NO to convert it to NO_2 (Equations 1.11 and 1.20). The only important source of O_3 is the photolysis of NO_2 which produces an O atom. This atom reacts with O_2 to form O_3 (Equations 1.5 and 1.2). Therefore, the decrease in the available NO_x leads to a decrease in O_3 . In contrast, O_3 production is not sensitive to declines in VOCs concentration at constant NO_x or the VOCs composition.

Under a low VOCs/ NO_x ratio (VOC-limited regime; at the left side of the ridge line in Figure 1.2), the decrease in VOCs concentrations at constant NO_x concentrations results in lower peak concentrations of O_3 . Similarly, decreases in O_3 concentrations can be achieved by decreasing VOCs and NO_x proportionally and simultaneously. On the other hand, decreasing NO_x concentrations while keeping the VOCs concentrations constant under this regime leads to increased peak O_3 concentrations, until the ridge line is reached and O_3 concentration starts decreasing. This increase of O_3 with decreasing NO_x under some conditions, results from the complex chemistry in the VOCs- NO_x - O_3 system.

According to Monks (2005), the propensity for O_3 formation in the troposphere depends

strongly on the chain length of the cycle, which is the number of free radical propagated cycles before termination. Consequently, the O_3 production efficiency becomes a balance between the propagation of the free radical interconversion cycle versus the rate of termination of the cycle. Under the VOC-limited regime, the competing chain propagation and termination reactions are:



where Equation 1.33 will lead to O_3 production and Equation 1.18 will lead to the termination of the HO_x chemistry. In practice, because of the high abundance of NO_x characterising this regime, as NO_x increases, the rate of the termination reaction (Equation 1.18) increases, removing both HO_x and NO_x and thus limiting the OH - HO_2 cycle. As a result, as NO_x decreases more OH is available to react with VOCs leading to O_3 production. Also, O_3 is removed through the process of NO titration (Equation 1.6), even though during the day O_3 is reformed after the photolysis of NO_2 (Equations 1.5 and 1.2).

As discussed earlier, the VOCs oxidation mechanism produces additional free radicals (e.g. Equation 1.21) that can either photolyze to form HO_x or react with OH to contribute to O_3 formation. Therefore, declining VOCs under a VOC-limited regime reduces the production of these radicals, leading to smaller abundances of RO_2 and HO_2 radicals and thus to lower rates of NO to NO_2 conversion (Equations 1.11 and 1.20).

In the case of much higher NO levels, such as over polluted urban regions, O_3 production is limited by Equation 1.6 and thus the system falls into a NO_x -titrated regime.

The understanding of the different O_3 regimes is essential for controlling O_3 levels in different regions. Because the dependency of O_3 production on precursor emissions is different between the different regimes, studies are required to establish efficient policies for O_3 reduction.

O_3 production efficiency

The **Ozone production efficiency (OPE)** is defined as the total number of O_3 molecules produced per unit of NO_x emitted. It is used as a measure for the chain length of O_3 production by NO_x .

Assuming a steady state for NO_x , efficient HO_x cycling, and loss of NO_2 only by reaction with OH :

$$OPE = \frac{P_{O_3}}{L_{NO_x}} = \frac{2k_7[HO_2][NO]}{k_9[NO_2][OH]} = \frac{2k_4[RH]}{k_9[NO_2]} \quad (1.34)$$

Deposition

Another sink of O_3 in the troposphere is the dry deposition on the Earth's surface, under reactions with organic material (Jacob, 1999). According to Monks et al. (2015), the main depositional sinks at the surface are: i) the stomatal uptake by plants, ii) the non-stomatal uptake, iii) solar radiation and surface temperature, iv) the in-canopy chemistry, and v) the uptake to water.

The non-stomatal uptake refers to deposition over the external surfaces of vegetation such as leaf surfaces and soil. Due to its high reactivity, O_3 deposition is affected by the temperature. For instance, considering the non-stomatal uptake as the thermal decomposition of O_3 at the surface, it increases with increasing temperature.

As mentioned before, in urban areas, O_3 is removed by the chemical O_3 titration due to high NO levels close to the surface (Equation 1.6). Similar removal of O_3 due to reaction with NO can happen in rural environments for instance due to NO emissions from soils. Concerning the deposition to water surfaces, it is found to be generally small. Its role in O_3 removal increases in case other reactive compounds are found in the water.

O_3 vertical profile and lifetime

Generally, O_3 profiles display the classical increase from the surface to the mid troposphere (MT). According to Jacob et al. (1996), this is because the role of photochemistry changes from a net sink to a net source of O_3 above 6km, depending on the NO_x concentration. The photochemical O_3 destruction dominates the LT (Archibald et al., 2020) where water vapour concentrations are high, and in highly polluted regions where there is direct removal by reaction with NO -titration (Monks et al., 2015). The vegetation can also act as a rapid sink for O_3 via dry deposition (Cros et al., 2000). The lack of these sinks in the FT, coupled with lower water vapour concentrations, leads to an increase of O_3 with altitude (Archibald et al., 2020). NO_x emitted by lightning can also increase O_3 mixing ratios in the MT and UT (Barret et al., 2010).

The presence of O_3 sinks in the surface result in a relatively short lifetime of O_3 (typically hours). In contrast, the absence of sinks in the FT leads to an increased lifetime in the order of several weeks (Stevenson et al., 2006). This time is long enough to allow the transport of O_3 on an intercontinental scale. In addition, there is the transport of NO_x and HO_x reservoirs (such as H_2O_2 and HNO_3 ; see above) that can produce NO_x and HO_x again in the subsidence zones and contribute to O_3 formation. Thus, pollution due to high O_3 levels is not limited to an urban scale but also occurs on an intercontinental scale due to transport (Akimoto, 2003).

1.1.3 Global budget

The global tropospheric O_3 burden is defined as the mass of O_3 in the troposphere. The O_3 budget is defined by four main terms: i) chemical production (**P**), ii) chemical loss (**L**), iii) loss due to depositions to the surface (**D**), and iv) a net influx resulting from the

stratosphere–troposphere exchange (S). To understand the interplay between O_3 sources and sinks, as well as their impact on O_3 burden, atmospheric chemistry models are used (Archibald et al., 2020).

Figure 1.3 displays the global O_3 burden, and the aforementioned terms computed by the models taking part in the European Union project Atmospheric Composition Change: the European Network of excellence (ACCENT) (Stevenson et al., 2006), and the Atmospheric Chemistry and Climate Model Intercomparison Project (ACCMIP) (Young et al., 2013), and single model studies (Myhre et al., 2013). Figure 1.3 displays a significant range of burden terms calculated by the different models. This indicates the levels of uncertainties in our understanding of the global O_3 . The burden ranges by a factor of approximately 1.5, the chemical terms by a factor of 2, and the S and D by a factor of 3.

In the last 60 years, our knowledge related to tropospheric O_3 has improved significantly. However, uncertainties remain regarding the quantification of processes controlling O_3 , due to its complex chemistry.

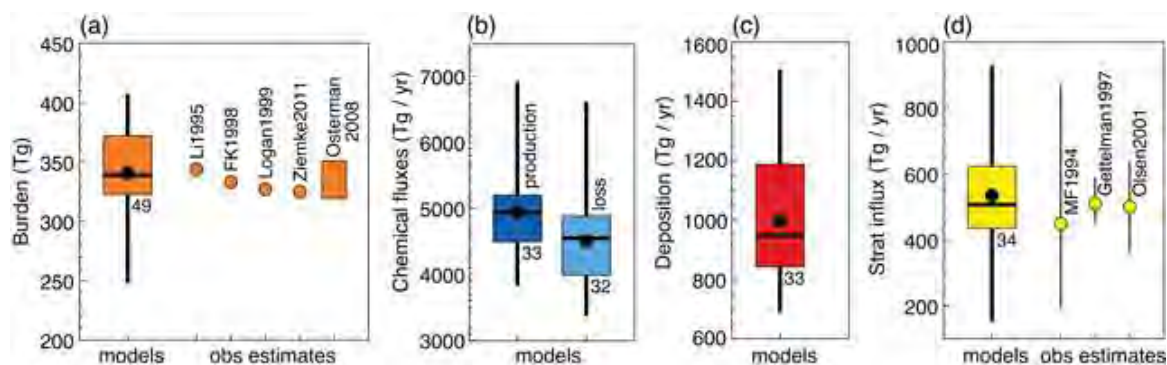


Figure 1.3: Present-day tropospheric O_3 budget terms based on models, and observations (where available). (a) The annual average O_3 burden, and annual total fluxes for (b) Chemical production and loss, (c) Dry deposition, and (d) Net stratospheric influx. Model results are shown as box–whisker plots, also indicating the median (horizontal line) and mean (filled circle) values of 50 models for the burden and 30 models for the fluxes (numbers of models indicated next to the boxes). Observation-based estimates for the burden are from Li1995 (Li (1995); after Wild (2007), FK1998 (Paul et al., 1998), Logan1999 (Logan et al., 1999), Ziemke2011 (after Ziemke et al. (2011)) and Osterman2008 (Osterman et al. (2008); range). Observation-based estimates for the net stratospheric influx are from MF1994 (Murphy and Fahey, 1994), Gettelman1997 (Gettelman et al., 1997), and Olsen2001 (Olsen et al., 2001). The error bars indicate their full uncertainty ranges. Source: Young et al. (2018)

Recent studies (Gaudel et al., 2018; 2020; Zhang et al., 2016) have shown increasing tropospheric O_3 burden in the second half of the 20th century. Satellite observations from the Ozone Monitoring Instrument (OMI) and Microwave Limb Sounder (MLS) sensors (Ziemke et al., 2019) and simulations from the GEOS–Chem chemical transport model (Zhang et al., 2016; 2021) display the highest O_3 burden increase in the tropical region – mostly over India, East Asia, and SouthEast Asia. Most studies tend to confirm an increase of

O₃ in the tropics but they are mostly based on model simulations, sparse ground observations, or satellite data with little consistency, and it is not clear what can cause such an O₃ increase.

Another obstacle to the quantification of the global O₃ burden is the lack of global observations (Gaudel et al., 2018). The current global O₃ monitoring network is unevenly distributed and covers only approximately 25 % of the globe (Tarasick et al., 2019). For this reason, the global O₃ distribution and sources remain uncertain due to inadequate observations in the remote FT, especially over developing countries in the tropics (Gaudel et al., 2018; Tarasick et al., 2019).

1.2 Carbon monoxide

1.2.1 Role and Significance

CO is an atmospheric trace gas that plays a significant role in air quality, atmospheric chemistry, and climate. Higher levels of CO close to the surface can lead to serious health problems (Raub and Benignus, 2002). The reaction of CO with OH (Section 1.1.2) is the main sink of OH, accounting for 40 % of the annual OH loss in a nonpolluted troposphere (Lelieveld et al., 2016). As a result, the variability of CO directly impacts the OH concentration. OH is considered the cleansing agent of the atmosphere (Logan et al., 1981), as mentioned previously. Consequently, CO directly impacts the oxidation capacity of the atmosphere due to the feedback between CO and OH.

The reaction mechanism for CO destruction indicates that enhanced levels of CO in the troposphere lead to lower OH concentrations available for reaction with other greenhouse gases such as CO₂ and CH₄ (Myhre et al., 2013). A consequence of declined OH levels in the atmosphere is the enhancement of the lifetime of CH₄ (Seinfeld and Pandis, 1998), the second most important greenhouse gas, after CO₂ (IPCC, 2021). According to the Intergovernmental Panel on Climate Change (IPCC), the global warming potential of CH₄ ranges between 84–87 when considering its impact over 20 years, and between 28–36 when considering its impact over 100 years relative to CO₂ (IPCC, 2021). In addition, CO's oxidation produces CO₂ and O₃ which are also greenhouse gases (IPCC, 2021). Thus, CO is considered an indirect short-lived climate forcer (IPCC, 2021).

CO is mainly produced by incomplete combustion processes (Granier et al., 2011). Because of its relatively long lifetime, CO concentrations in the troposphere are strongly influenced by transport processes. As a result, it is considered a powerful pollution tracer of combustion processes (Logan et al., 1981; Crutzen and Andreae, 1990) which emit O₃ precursors (i.e., NO_x, VOCs, CO). Its global distribution provides information about the transport pathways of pollution at a hemispheric scale.

1.2.2 Sources and Sinks

CO production is based on primary (e.g. emitted directly into the atmosphere) and secondary (e.g. formed by reactions in the atmosphere) sources. The main primary sources are located

at the Earth's surface and include anthropogenic incomplete combustion of carbon-based materials such as fossil fuels and biofuels (Hoesly et al., 2018), biomass burning (Van Der Werf et al., 2017), vegetation (Bruhn et al., 2013) and the ocean (Conte et al., 2019). The most important secondary CO sources are the oxidation of CH₄ and other VOCs, which result in CO chemical production.

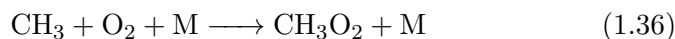
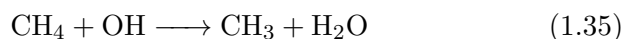
Primary Sources

Anthropogenic emissions depend on several factors such as the fuel type, fuel amount, and combustion technology. Biomass burning emissions are initiated by humans (e.g. for land cleaning purposes) or by natural causes (e.g. due to lightning in fire-prone areas like forests). The intensity of the fires and the CO emissions depends on the climate conditions (for instance drought conditions during El Niño intensify fires over Indonesia; Ravindrababu et al., 2019), and are enhanced or suppressed by human activities (e.g. deforestation activities can intensify fires). The CO production efficiency in the fires depends on factors such as the type of burning area (e.g. savanna or peat fires). More discussion about the anthropogenic and biomass burning emissions follows in Section 2.2. Smaller CO contributions originate directly from plant leaves and marine biogeochemical cycles, with much smaller annual variations than the ones from anthropogenic and biomass burning emissions (Zheng et al., 2019).

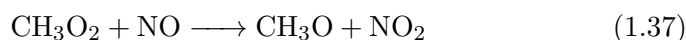
Secondary sources

The CH₄ oxidation mechanism is one of the major natural chemical sources of CO. Under high NO_x levels, the oxidation of CH₄ results in the rapid production of CH₂O, without involving any intermediates. Then the CH₂O is likely to photolyze or react with OH, resulting in CO production.

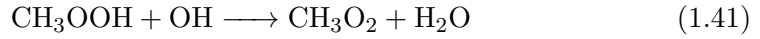
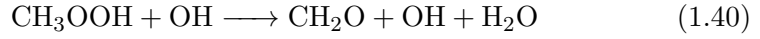
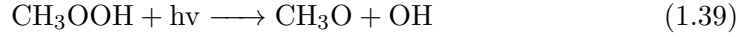
In contrast, under low NO_x levels, the CH₄ oxidation leads to the production of CH₂O via CH₃OOH, a relatively long-lived intermediate. Then, it can photolyze or react with OH, to produce CH₂O and CO. These processes are described by the following reactions:



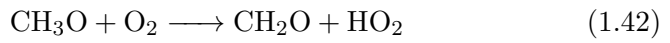
The dominant sinks of CH₃O₂ (methyl peroxy radical) are the reactions with NO and HO₂:



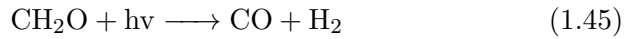
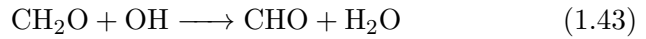
Then, the CH₃OOH (methyl hydroperoxide) can either photolyze or react with OH :



The CH_3O (methoxy radical) produced by Equations 1.37 and 1.39 reacts fast with O_2 :



Formaldehyde (CH_2O) produced by Equations 1.40 and 1.42 can either react with OH or photolyze:



The CHO radical produced by Equations 1.43 and 1.44 reacts rapidly with O_2 to produce CO:



Other non-methane VOCs, emitted by vegetation and react with OH, are converted to oxygenated compounds and then partly to CO. Their biogenic emissions can vary depending on climate and land use changes (Zheng et al., 2019).

Sinks

The main sink of CO is the oxidation with OH (see Section 1.1.2), with a smaller contribution from dry deposition (IPCC, 2021). CO deposits on sea ice, snow, soil, vegetation, and structures and dissolution in surface water. However, because it is relatively insoluble, its dissolution rate is low (Jacobson, 2012).

1.2.3 Global Budget

Despite the significant role of CO in climate and air quality, there are still large uncertainties in the global CO budget for both its sources and sinks. Using an inverse method (e.g. constrain an atmospheric model by Measurements Of Pollution In The Troposphere (MOPITT) CO observations to estimate its sources and sinks), Zheng et al. (2019) reported the global

budget of CO during 2000–2017, as seen in Table 1.1. According to their computations, the direct emissions and the chemical production contribute roughly equally to the global CO sources (1.4 and 1.2×10^3 Tg CO yr⁻¹ respectively), in agreement with IPCC (2021). The main surface sources originate from anthropogenic and biomass burning emissions (0.7 and 0.5×10^3 Tg CO yr⁻¹ respectively), while the biogenic and oceanic sources represent the 15 % of the surface emissions. The oxidation of CH₄ is the main chemical production source accounting for 75 % of the secondary CO sources.

Table 1.1: Average CO budget in (10^3 Tg CO yr⁻¹) during 2000–2017 based on Zheng et al. (2019).

	(10^3 Tg CO yr ⁻¹)
Sources	
Anthropogenic	0.7
Biomass burning	0.5
Ocean	0.02
Biogenic	0.2
Sub-total direct sources	1.4
Methane oxidation	0.9
NMVOCs oxidation	0.3
Sub-total chemical oxidation	1.2
Total sources	2.6
Sinks	
OH reaction	2.6

Figure 1.4 displays inversion-based estimates of the global CO budget (Tg CO yr⁻¹) based on several studies. All these studies, including Zheng et al. (2019) and Table 1.1, tend to agree on the estimate of the global CO sources. However, they disagree on the proportion of CO produced: i) by surface emissions and by chemical production, and ii) by oxidation of CH₄ and by oxidation of VOCs. In addition, the CO production by the oxidation of VOCs shows a large spread among the different studies, indicating high uncertainties in the estimations.

Study	Constraint	Period ^a	Run ^b	A ^c	BB ^d	O ^e	B ^f	DE ^g	CH ₄ ^h	VOC ⁱ	C ^j	Source ^k	Sink ^l
Müller et al. (2018)	IASI	2013	STD	511	320	98 ^m		929	718	733	1451	2381	
			HN	617	352	107		1076	820	815	1635	2711	
			LN	436	294	91		821	644	674	1318	2139	
			HS	564	354	108		1026	816	813	1629	2655	
			LS	478	293	90		861	648	671	1319	2180	
Jiang et al. (2017)	MOPITT v6	2001–2015	Column	499	287								
			Profile	541	322								
			Lower profile	581	345								
Gaubert et al. (2017)	MOPITT v5	2002–2013	Reanalysis						782	468	1250		2226
Yin et al. (2015)	MOPITT v6	2002–2011	TransCom INCA					1444			1199	2642	2668
								1540			1226	2765	2794
Park et al. (2015)	δ ¹⁸ O	2004		716	377	20	97	1210	919	454	1373	2583	
Fortems-Cheiney et al. (2012)	OMI, MOPITT v4, WDCGG	2005–2010						1434			1101	2535	2546
Fortems-Cheiney et al. (2011)	MOPITT v4	2000–2009						1412					
Kopacz et al. (2010)	Multiple satellites	MAY 2004 to APR 2005						1350			1507	2857	
Stavrakou and Müller (2006)	MOPITT v3	MAY 2000 to APR 2001	GFED-Grid	664	450	20	199	1333	761	813	1574	2907	
			GFED-Region-Monthly	685	434	20	200	1339	772	794	1566	2905	
			GFED-Region-Annual	675	412	20	186	1293	770	798	1568	2861	
			POET-Grid	688	404	20	195	1307	755	798	1553	2860	
				841	563				394				
Arellano et al. (2006)	MOPITT v3	APR 2000 to MAR 2001											
Arellano et al. (2004)	MOPITT v3	2000	Column	844–	508–				767	175–		2388	
				923	579					209			
			500 mb	782–	531–				767	148–		2363	
				899	633					192			
			700 mb	884–	486–				767	207–		2450	
				960	573					235			
Péron et al. (2004)	MOPITT	APR 2000 to MAR 2001		683	408		183	1274			1650	2924	2630

^a: Year of the data. If data of multiple years are provided, the annual average are presented in the table.

^b: The label of inversion run defined in each paper.

^c: Anthropogenic emissions; ^d: Biomass burning emissions; ^e: Oceanic emissions; ^f: Biogenic emissions; ^g: surface direct emissions from the sum of anthropogenic, biomass burning, oceanic, and biogenic sources; ^h: CO from the oxidation of CH₄; ⁱ: CO from the oxidation of NMVOCs; ^j: chemical production of CO from the sum of CH₄ and NMVOCs oxidation; ^k: CO total source; ^l: CO total sink; ^m: The sum of oceanic and soil emissions are presented in Müller et al. (2018).

Figure 1.4: Inversion-based estimates of global CO budget (Tg CO yr⁻¹). Source: Zheng et al. (2019).

Except for inversion-based estimations, global chemistry transport models are used to simulate the CO concentrations and estimate the global CO burden and budget. The overall performance of the global models is discussed in IPCC (2021). Generally, they capture the spatial distribution of the observed CO concentrations but they show regional biases up to 50 % (IPCC, 2021 and references therein). For instance, models are persistently biased low in the Southern hemisphere, and biased high in the tropics, particularly over polluted regions such as India and East Asia. The estimations of the simulated global CO burden by global models lie in the range of the one estimated from data assimilation techniques. For instance, CO emissions from anthropogenic sources are estimated to range between 450 and 600 TgCO yr⁻¹ (Lannuque et al., 2021), which is comparable to the CO emissions from

biomass burning sources, estimated between 350 and 600 TgCO yr⁻¹ (Van Der Werf et al., 2017). The global chemical oxidation sources from CH₄ and VOCs oxidation are estimated between 600–1000 and 450–1200 TgCO yr⁻¹, respectively (Stein et al., 2014). Nevertheless, the large spread across the models is driven by uncertainties in both CO sources and sinks, particularly those related to the chemical production of CO from MNVOCs oxidation and loss due to the reaction with OH (IPCC, 2021).

CHAPTER 2

Tropics: Tropospheric dynamics and precursor emissions

In [Chapter 2](#), we focus on the region of interest, the tropics which is a key region for O_3 photochemistry and CO. We start by explaining the govern dynamics ([Section 2.1](#)), and the natural and anthropogenic sources ([Section 2.2](#)) located in the region.

The tropical zone can be defined in several ways, such as by meteorological characteristics (e.g. location of the subtropical jets), climatic elements (e.g. precipitation rates), or by geographical extent. Following the latter way, in the [Tropospheric Ozone Assessment Report, Phase II \(TOAR-II\)](#)(<https://igacproject.org/activities/TOAR/TOAR-II>) Ozone and Precursors in the Tropics working group, the tropics are defined between 20° S and 20° N. In our study, we consider the extended area between 25° S and 25° N, to investigate interactions of pollution and the transport of air masses between the tropics and the subtropics.

Because of its location close to the equator, the tropical troposphere receives up to twice as much solar radiation as the extratropics. Also, the tropical stratospheric O_3 layer is 60 % of the one at mid-latitudes (Peters, [2002](#)). For these reasons, the amount of energy to drive photochemistry and processes such as convection and evaporation, is greater than in the extratropics. Due to high temperatures and evaporation, the tropics are characterised by high humidity, which promotes the production of OH radicals. Consequently, there are favourable conditions for converting NO into NO_2 without consuming O_3 . Therefore, the combination of high solar radiation and humidity favours O_3 production in the tropical troposphere.

2.1 Tropospheric Dynamics

2.1.1 General Circulation

The uneven heating of the Earth by the Sun at different latitudes is the main driver of the global scale atmospheric circulation (Seinfeld and Pandis, [1998](#)). Even though the total energy received by the Earth is in balance with the total energy emitted back to space, this is not true for every region of the Earth. The tropics receive more energy from the Sun than is emitted back to space, whereas the polar regions receive less energy than they emit. This

is because of i) the decline in solar radiation to the polar regions during winter, and ii) the high surface albedo in the polar regions.

The redistribution of energy from regions with energy excess towards the regions with energy deficit is mainly achieved by atmospheric motions. Because the Earth is rotating and thus these motions are affected by the Coriolis force, the air cannot flow directly from the equator to the pole and back. Instead, the circulation of the atmosphere can be explained by a simplified three-cell model consisting of: 1) the Hadley cell in the equatorial region, 2) the Ferrel cell in the mid-latitudes, and 3) the polar cell at high latitudes (Figure 2.1).

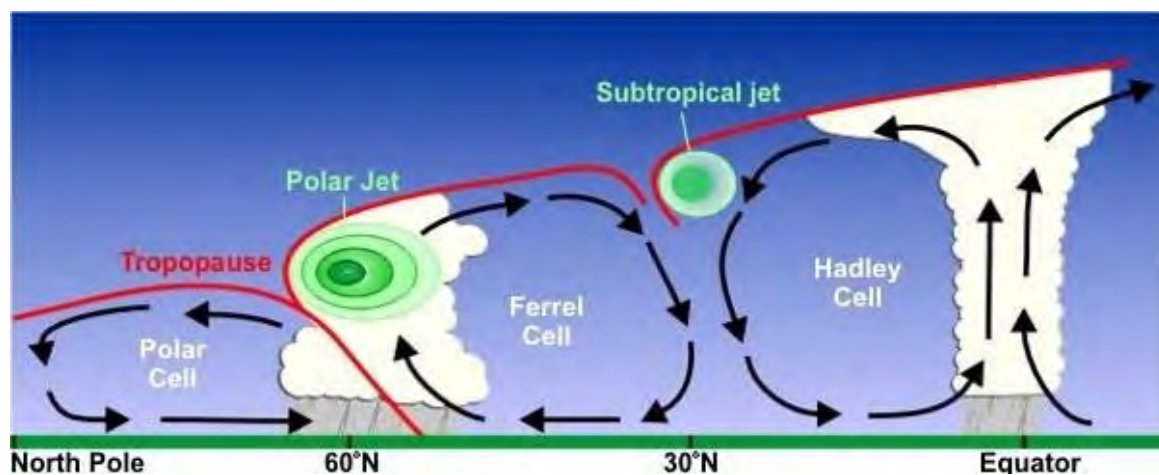


Figure 2.1: Schematic of Hadley, Ferrel, and polar cell circulation. Source: NOAA

Hadley Circulation

The Hadley cell is characterised by rising air at the equator, moving polewards in the tropical UT and descending due to adiabatic cooling at the subtropics, and moving equatorwards at the surface (Figs. 2.1 and 2.2). Air over the equator rises because it is warm and moist. At the tropical tropopause layer (TTL), the atmosphere is stable and the upward motion is suspended. The air that does not enter the stratosphere, converges, cools as it moves northwards (southwards), and sinks at around 30 °latitude. While sinking, the air warms by compression. At the surface, to conserve mass, some of the sinking air moves equatorwards, and is deflected to the right (resp. left) in the NH (resp. SH) due to the Coriolis force. As a result, on both sides of the equator, there is a region where the wind blows from east to west (easterlies). This region is known as the trade wind belt (Seinfeld and Pandis, 1998) (Figure 2.2).

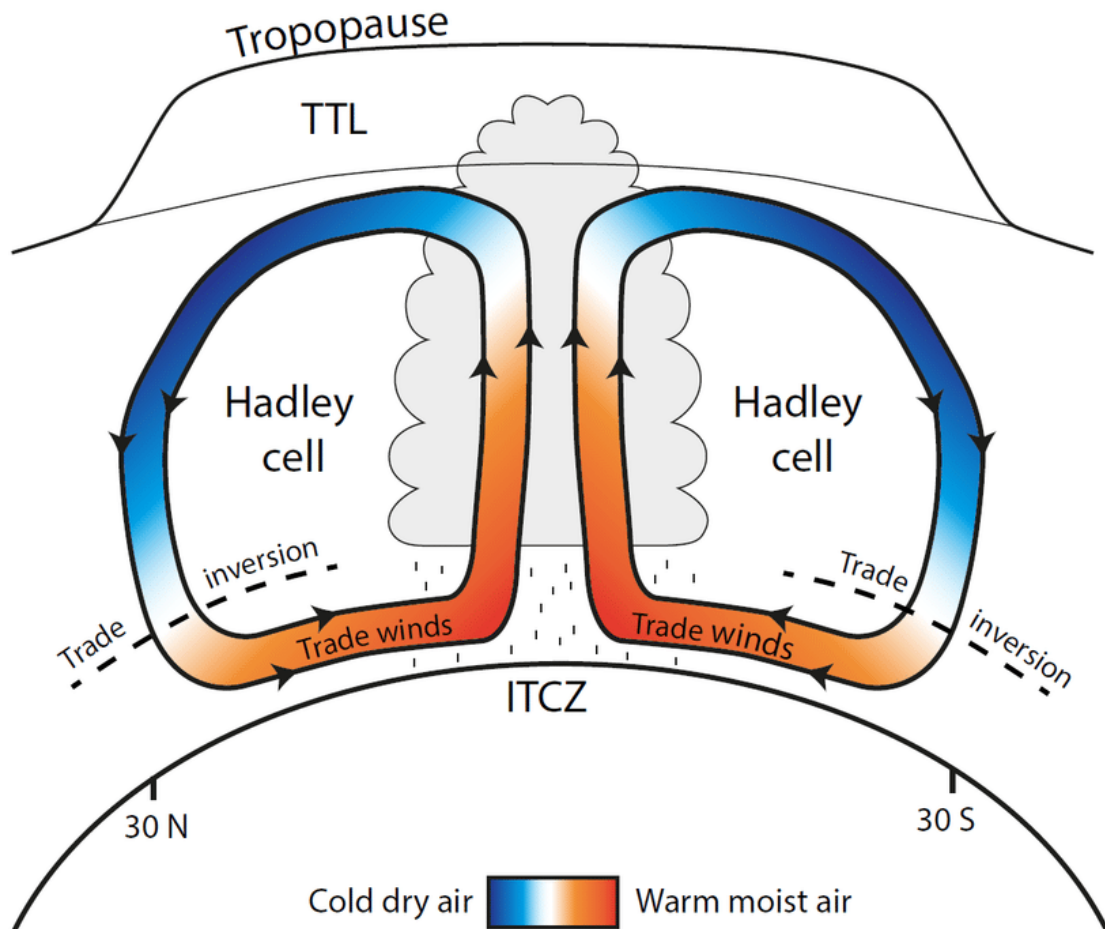


Figure 2.2: Schematic of Hadley cell circulation. Source: Fiehn (2017)

Intertropical Convergence Zone

Near the equator, northeasterlies from the NH converge with southeasterlies from the SH in a region known as the Intertropical Convergence Zone (ITCZ) (Figure 2.2). In reality, the ITCZ follows the location of the thermal equator. As a result, its location varies with the season, shifting northwards in summer and southward during winter (Figure 2.3). Because the ITCZ is associated with convective clouds and heavy rainfall, it causes the alteration of rainy and fire seasons in the tropics.

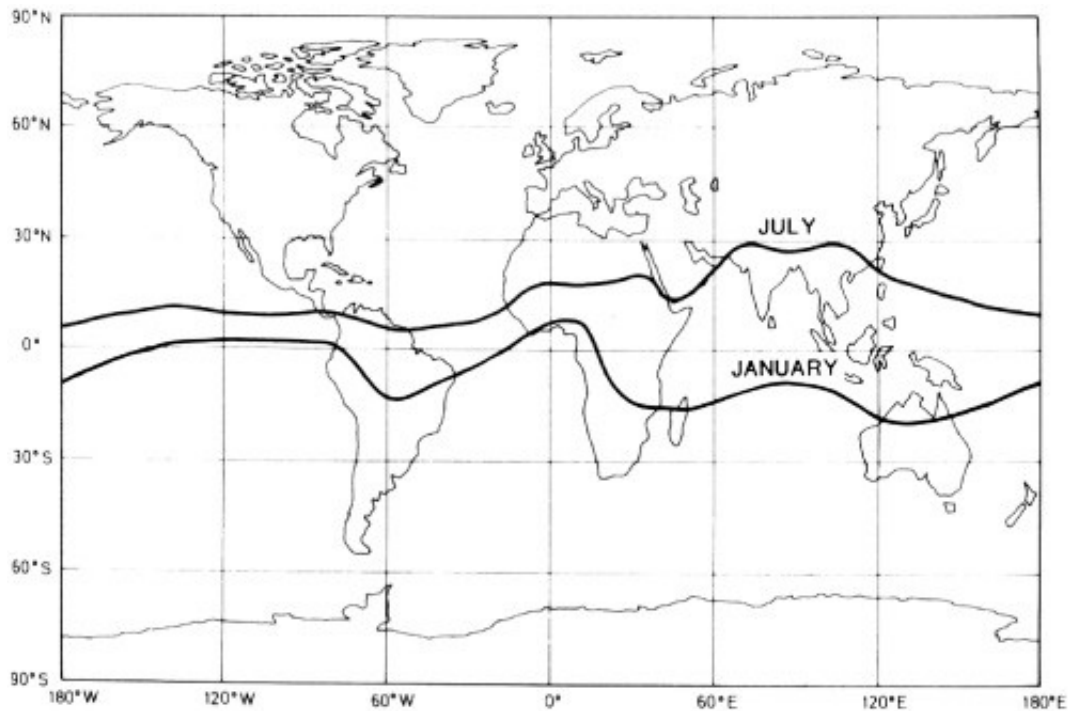


Figure 2.3: Position of the Intertropical convergence zone during January and July. Source: Yan (2005)

Subtropical jet

When the upper poleward branch of the Hadley cell induces air in the UT, the subtropical jet develops (Figure 2.1). In contrast to the surface trades winds, the subtropical jet has weak meridional components relative to the zonal ones. This is because as the UT air moves away from the equator, it increasingly comes under the influence of the Coriolis force, and air deflects toward the right (resp. left) in the NH (resp. SH). As a result, the upper circulation in the low latitudes becomes increasingly westerly at a distance from the equator.

Walker circulation

In the proximity of the equator with the absence of the Coriolis force, a thermodynamic circulation develops in the zonal and vertical directions (Figure 2.4 top panel). The so-called Walker circulation is driven by differences in surface temperature and the resulting pressure gradients over the western and eastern tropical Pacific Ocean. During normal (average) conditions over the Pacific Ocean, trade winds blow westwards along the equator, moving warm water from South America towards Asia (Figure 2.4 top panel). A westerly flow develops in the UT, while convection and rainfall occur mostly over SouthEast Asia. El Niño and La Niña are two climate patterns that disturb these normal conditions (more details follow later).

Dynamical processes in the tropics are of great importance because they are capable of redistributing polluted air masses at regional (Barret et al., 2008; Sauvage et al., 2005) and

global scales (Zhang et al., 2016). Zhang et al. (2016) highlighted the dominant role of emissions from the tropics and subtropics to the global O_3 burden, due to convection, along with strong reaction rates and NO_x sensitivity in these regions. Observations and models (e.g. Cooper et al., 2012; Cooper et al., 2015) have associated emission increases in Asia with increasing O_3 above western North America. Other studies have found that BB products from South America and Africa contribute to an O_3 enhancement over South Atlantic. As discussed by Barret et al. (2016), convective transport can affect the O_3 distribution by vertical mixing. O_3 -poor masses from the LT, where the O_3 lifetime is short (Section 1.1.2), are uplifted in the UT, where it is long. Due to mass conservation, the O_3 -rich air masses from the UT are transported to the LT, by subsidence. The effect of this air-mass exchange between the LT and UT leads to a decline in UT O_3 and the tropospheric O_3 lifetime and burden. Over polluted regions, such as Asia, the convective uplifting of O_3 precursors, and the emitted during convective storms increase the O_3 production in the MT and UT. However, convective clouds reduce the available solar radiation and thus the tropospheric photochemical activity. These effects cause lower mid-tropospheric O_3 mixing ratios over South Asia, compared to regions with higher solar radiation and downwind transport of O_3 , such as Africa and the Middle East.

2.1.2 Variations of the General Circulation

El Niño Southern Oscillation

In addition to the typical circulation patterns, there are some seasonal and non-seasonal atmospheric motions in the tropics, which impact the O_3 distribution. The non-seasonal variations include the El Niño Southern Oscillation (ENSO) cycle, which is the reverse of the Walker circulation every few years and is associated with ocean and atmosphere interaction. El Niño and La Niña are the warm and cool phases of ENSO.

During an El Niño event, warmer water than the average extends to the east (Figure 2.4 bottom panel). The overlying air warms and thus rises, leading to a low-pressure system. In turn, the water, and consequently the overlying air, is relatively cooler above SouthEast Asia. This leads to less rising motions and a higher pressure system above SouthEast Asia. The pressure changes induce changes in the wind patterns. During an El Niño event, the trade winds over the Pacific are less strong, the precipitation rates are lower than the average over Indonesia and stronger than the average over the Central or Eastern Pacific. The La Niña pattern (Fig. not shown) shows the opposite effects of the El Niño. Cooler water temperatures over the West Coast of America lead to stronger trade winds. Lower (resp. higher) than the average pressure over Western Pacific (resp. Central and Eastern Pacific) results in increased (resp. decreased) rainfall in that region. Consequently, drier than the average conditions are induced over South America.

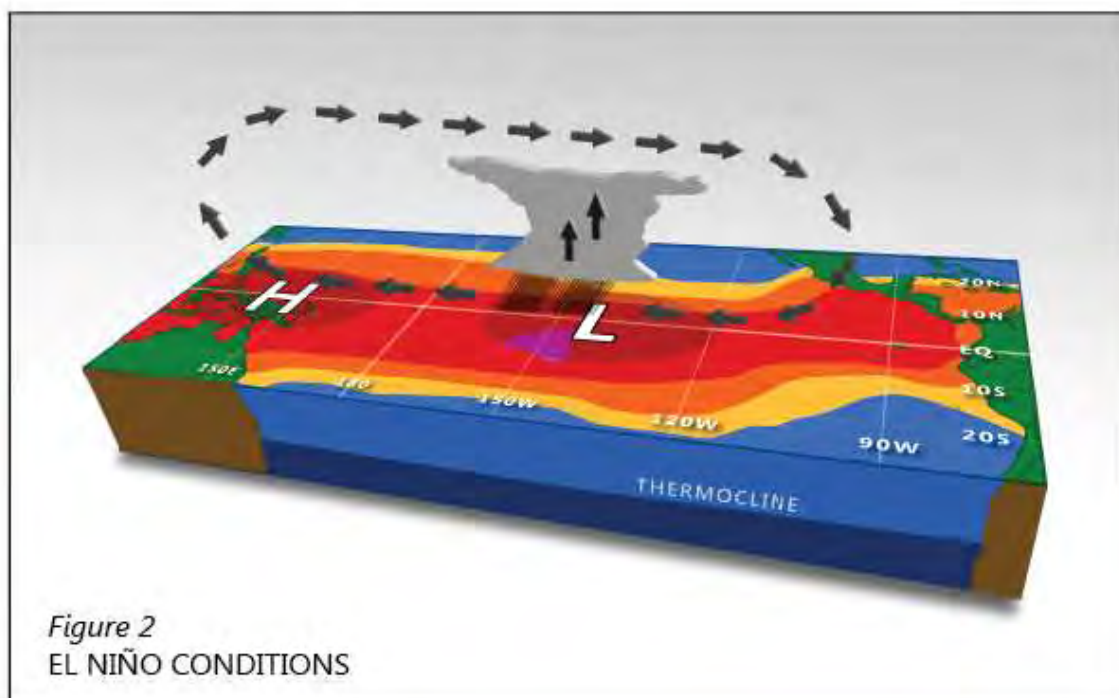
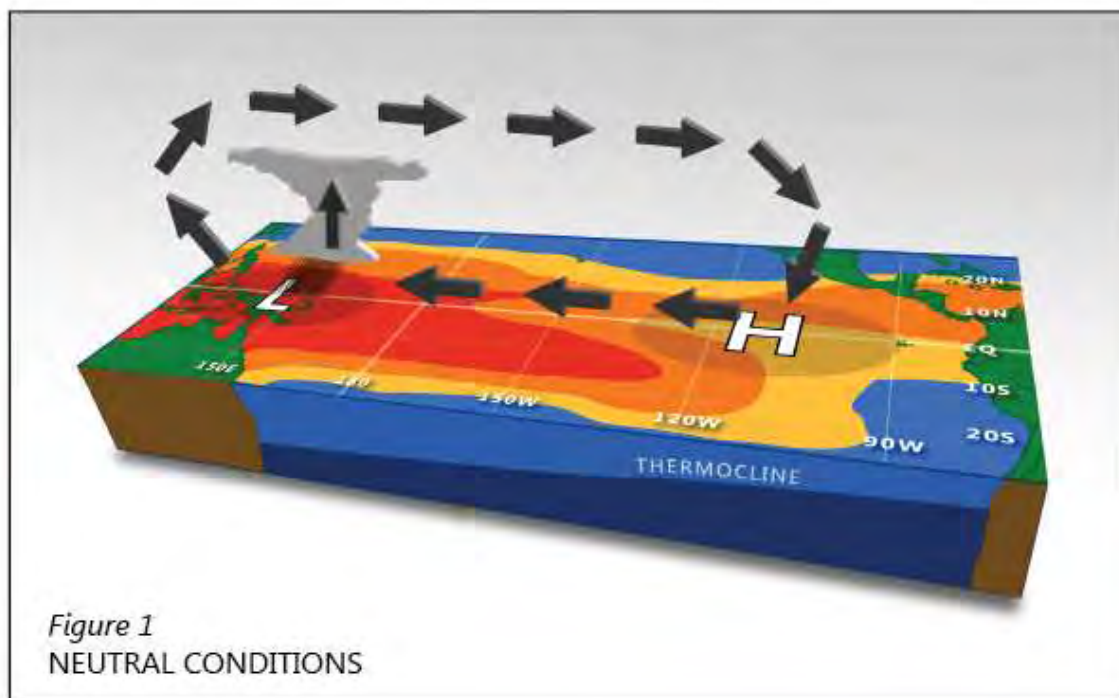


Figure 2.4: Top panel: Average conditions of ocean temperatures, rainfall, pressure, and winds over the Pacific Ocean during neutral conditions. Bottom panel: State of the ocean and the atmosphere during El Niño conditions. Source: NOAA image created by David Stroud

The El Niño and La Niña events occur every two to seven years, and last nine to 12 months approximately. The strongest El Niño events were observed during 1997/1998 (Huijnen

et al., 2016) followed by 2015/2016 (Ravindrababu et al., 2019). Several studies (e.g. Ziemke et al., 2010; Leventidou et al., 2016) have examined the impact of ENSO on tropospheric O_3 . Because the El Niño event induces drier conditions than the average over SouthEast Asia, the fire activities over the regions are found to be amplified (e.g. Ravindrababu et al., 2019). As a result, El Niño has an impact on emissions of trace gases, including O_3 .

Monsoons

The main synoptic seasonal pattern in the tropics is the monsoon, which is related to the seasonal transition of prevailing winds and precipitation. The monsoons are characterised by rainy summers with onshore flow and drier winters with offshore flow. The changes in the low-level wind flow are associated with the changes in the thermal contrast between the land and the ocean. During summer, the air over the land is warmer and more unstable than the air over the nearby oceanic regions. As a result, lower pressure occurs over land and higher pressure occurs over the oceanic regions. This pressure pattern causes low-level moist air to converge onto the land, resulting in increased precipitation. During winter, the temperature contrast, and thus the low-level wind flow is reversed, leading to drier conditions over land. Several regions show monsoon characteristics: Western Africa, Asia, Northern Australia, South America, and North America. In this chapter, we will give some further information about the monsoon systems in tropical regions (West Africa, Asia, and South America).

Asia

During winter (October to March), the prevailing northerly wind brings dry and cool weather conditions over Asia (Fig. 2.5 right panel). The prevailing southwesterly (resp. westerlies) during the East Asian (resp. South Asian) summer monsoon (Fig. 2.5 left panel) brings clean and moist ocean air to East Asia (resp. Indian subcontinent), enhances cloud covers and precipitations. Satellite and in situ observations have shown a decrease in tropospheric O_3 in South and SouthEast Asia from May to August with the evolution of the Asian Summer Monsoon. This decrease is associated either with reduced photochemistry production of O_3 or transport of O_3 -poor oceanic air masses. At the same time, the Asian monsoon Anticyclone (AMA) dominates the circulation in the upper levels of the troposphere (Barret et al., 2008; Park et al., 2007). Figure 2.6 displays the transport processes developed during the Asian summer monsoon:

1. LT air masses impacted by surface Asian emissions are captured in the Asian monsoon.
2. They are convectively uplifted in the UT by the Asian monsoon
3. and are trapped in the AMA circulation in the UT.
4. South of AMA, strong westward winds, the Tropical Easterly Jet (TEJ), are responsible for the long-range transport of Asian polluted air masses towards Northern Africa and the Middle East (Barret et al., 2008).

5. Subsiding air masses result in the build-up of pollutants in the MT above the Middle East and Mediterranean (Dayan et al., 2017).

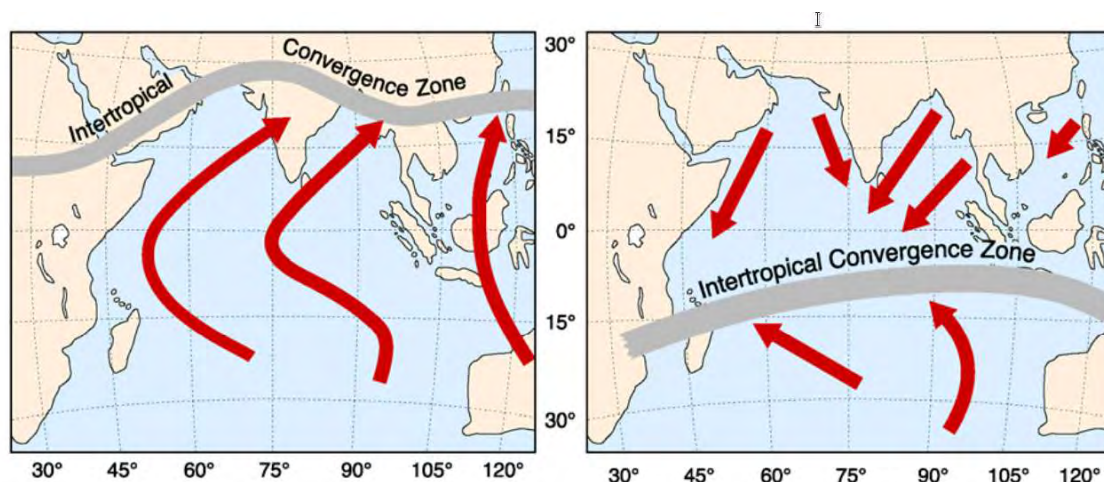


Figure 2.5: Transport pathways near the surface over the Indian Ocean during the Asian summer (left panel) and winter (right panel) monsoon. Source: Lawrence and Lelieveld (2010)

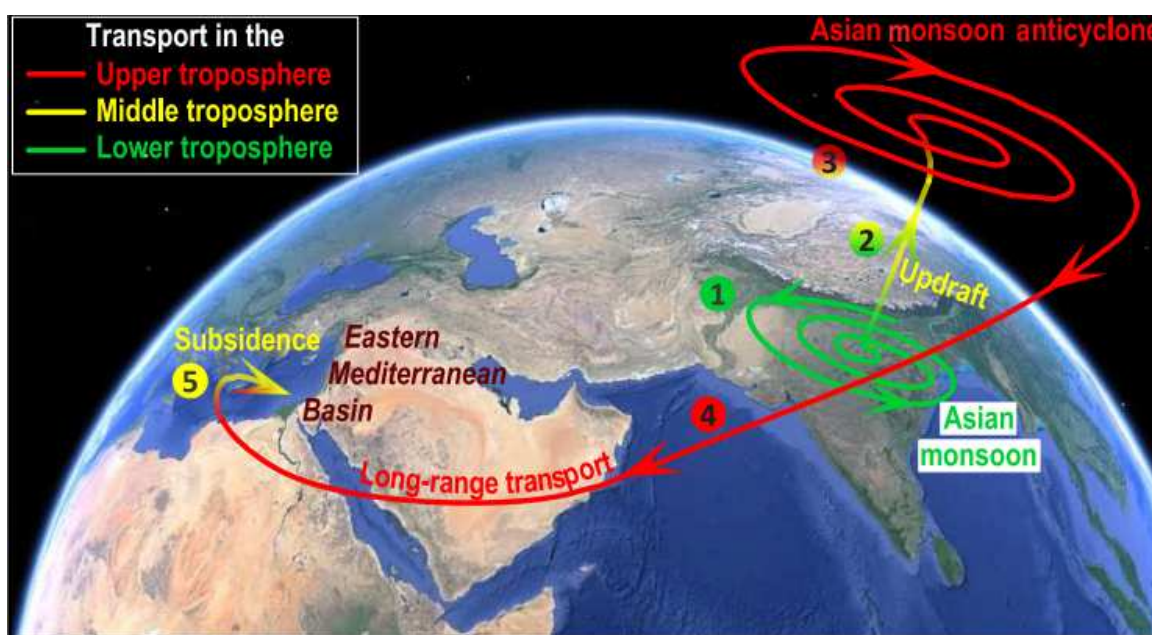


Figure 2.6: Schematic representation of the processes impacting MT and UT composition above the Middle East and Mediterranean during the Asian summer monsoon (July–August). Source: Dayan et al. (2017)

Africa

Similarly, over Africa, the West African Monsoon (WAM) wind flows from the southwest and converges with the northeasterly trade wind (Harmattan) in the ITCZ (Figs. 2.7, 2.3). Sauvage et al. (2007d) suggested an uplift of O_3 -poor masses from the LT in the ITCZ where

O_3 is produced due to the photochemical production of precursors produced by lightning or coming from the surface, in the upper branches of the Hadley circulation (Fig. 2.2). During the NH monsoon season in Africa, BB products originating from the south of ITCZ are transported to the ITCZ (Sauvage et al., 2005; Sauvage et al., 2007a) and impact the atmospheric composition in the African UT.

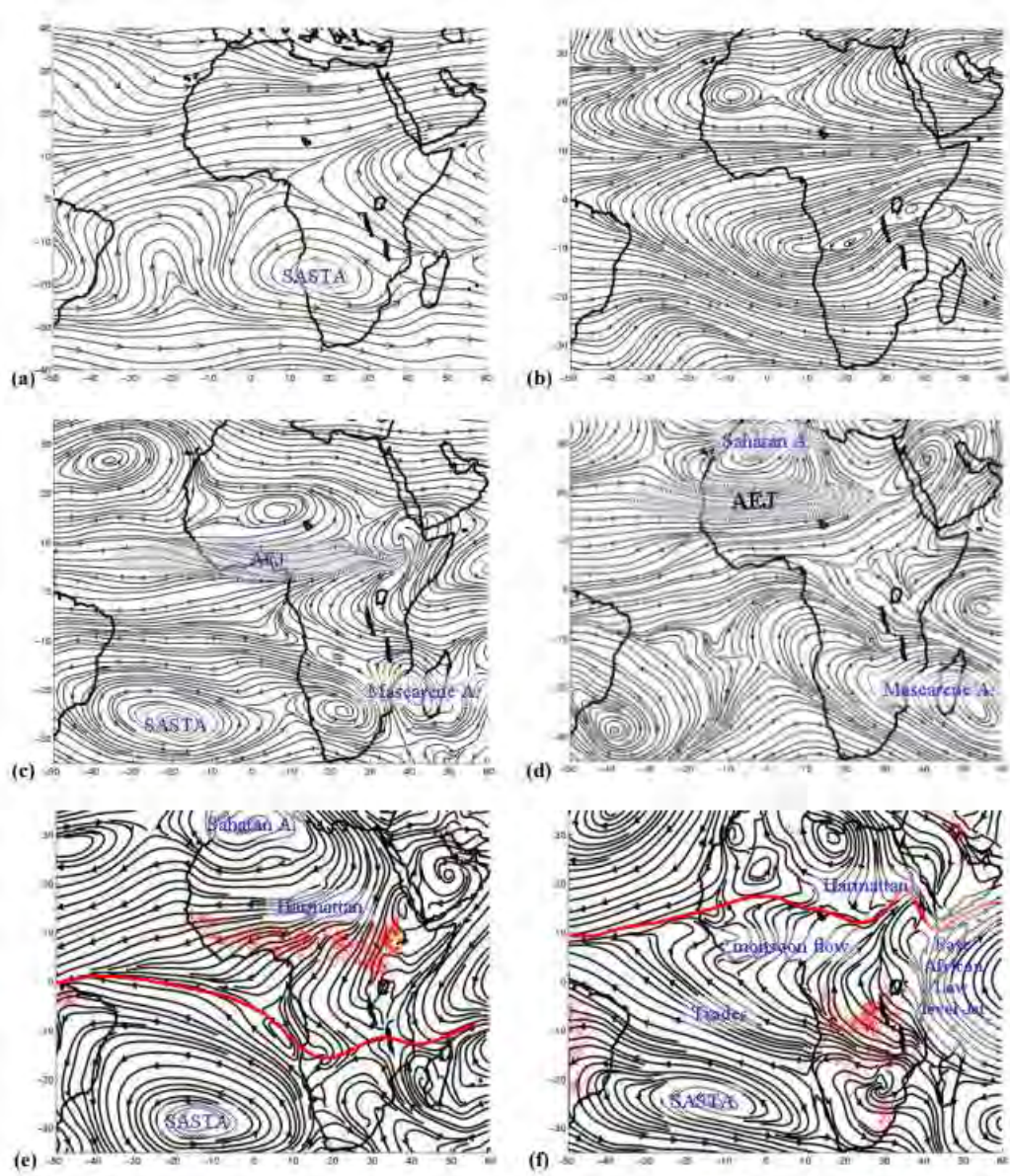


Figure 2.7: Monthly mean streamlines from the 2002 ECMWF analyses. (a) 250 hPa January, (b) 250 hPa July, (c) 650 hPa January, (d) 650 hPa July, (e) 850 hPa January, (f) 850 hPa July. The main dynamic African features are written in blue. The red line displays the ITCZ and the red points the position of the fires in January and July. Shaded areas indicate the AEJ location. Source: Sauvage et al. (2005)

The thermal difference between the warm Sahara desert and the cold Gulf of Guinea results

in a low tropospheric flow, the Africa Easterly jet (AEJ) (Figure 2.7). The AEJ develops in the pressure range of 700–650 hPa and may be the birthplace of easterly waves which show maximum from May to October (Sauvage et al., 2005). At higher altitudes (500 hPa), there are two anticyclones: the Saharan Anticyclone (centered at 15°N–10°E) and the South Atlantic Subtropical Anticyclone (SASTA; centered at 30°S–15°W) (Figure 2.7), which contribute to a stable trade-wind inversion and a highly stratified atmosphere.

East Africa is also affected by the ITCZ, however because of the different topography and the influence of the Indian Ocean, the area is impacted by different regimes relative to West Africa. For instance, the circulation is affected by: the East Africa low-level jet originating at the northeastern tip of Madagascar; and the TEJ which prevails in the UT (Figure 2.7).

South America

The main features related to the South American Monsoon system are displayed in Figure 2.8. The topography of South America, and more particularly the Andes mountains and the Amazon basin, play a significant role in the South American monsoon system (Silva and Kousky, 2012). During austral summer, there is a low-level wind that flows over the land (easterly). The Andes mountains act as a barrier to this easterly flow and deflect it towards the south, over western Brazil, Bolivia, and Paraguay (Silva and Kousky, 2012). During summertime, the intense convection above the land results in the development of an UT anticyclone, the so-called Bolivian High (Figure 2.8). The air is rising over the land and sinks over the Pacific and Atlantic oceans. These oceanic regions are associated with the absence of deep convection and the development of an upper-tropospheric cyclonic circulation.

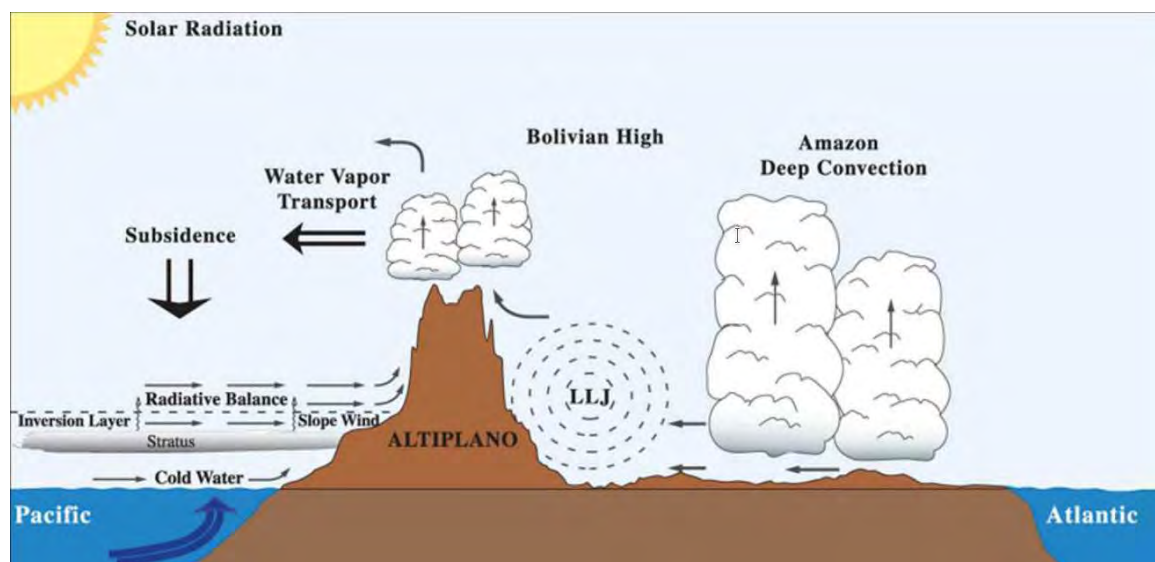


Figure 2.8: Schematic of vertical section over South America during the South American Monsoon. Source: Climate Variability & Predictability Program (CLIVAR) (www.clivar.org)

2.2 Natural and Anthropogenic Sources

In the tropics, natural sources (soils, lightning, and biomass burning emissions) are active, and emit O_3 precursors such as CO, NO_x , and VOCs. In addition, anthropogenic emissions have been constantly increasing, causing critical pollution and air quality issues.

Vegetation

Vegetation emits a large amount of VOCs. According to bottom-up estimates, biogenic VOCs emissions account for more than 80% of the total global VOCs input (Olivier and Berdowski, 2001). Because of their high reactivity, biogenic VOCs can impact tropospheric chemistry immediately after they are emitted. They lead to O_3 production (resp. destruction) in high (resp. low) NO_x levels (see Section 1.1.2). Biogenic VOCs emissions are mostly controlled by temperature because of the nature of photosynthesis (Lu et al., 2019b). The exponential increase of these emissions with increasing temperature has been recognised as the main driver of the positive correlation between O_3 and temperature, especially in urban areas where NO_x concentrations are high (Lu et al., 2019c).

The release of VOCs in the atmosphere, along with their impact on photochemistry is favoured in the tropics due to the high solar radiation and humidity. More than 70% of the total global biogenic VOCs flux occurs in the tropics, with significant emissions from the leaves of plants (Karl et al., 2007). Figure 2.9 displays the monthly mean emissions of isoprene (a) and monoterpenes (b). According to Sindelarova et al. (2014), the annual total biogenic VOCs emission are estimated equal to 760 Tg (C) yr^{-1} , mainly consisting of isoprene (70 %) and monoterpenes (11 %). Figure 2.9 displays the highest biogenic VOCs emissions over the tropics, especially over the Amazon forest in South America.

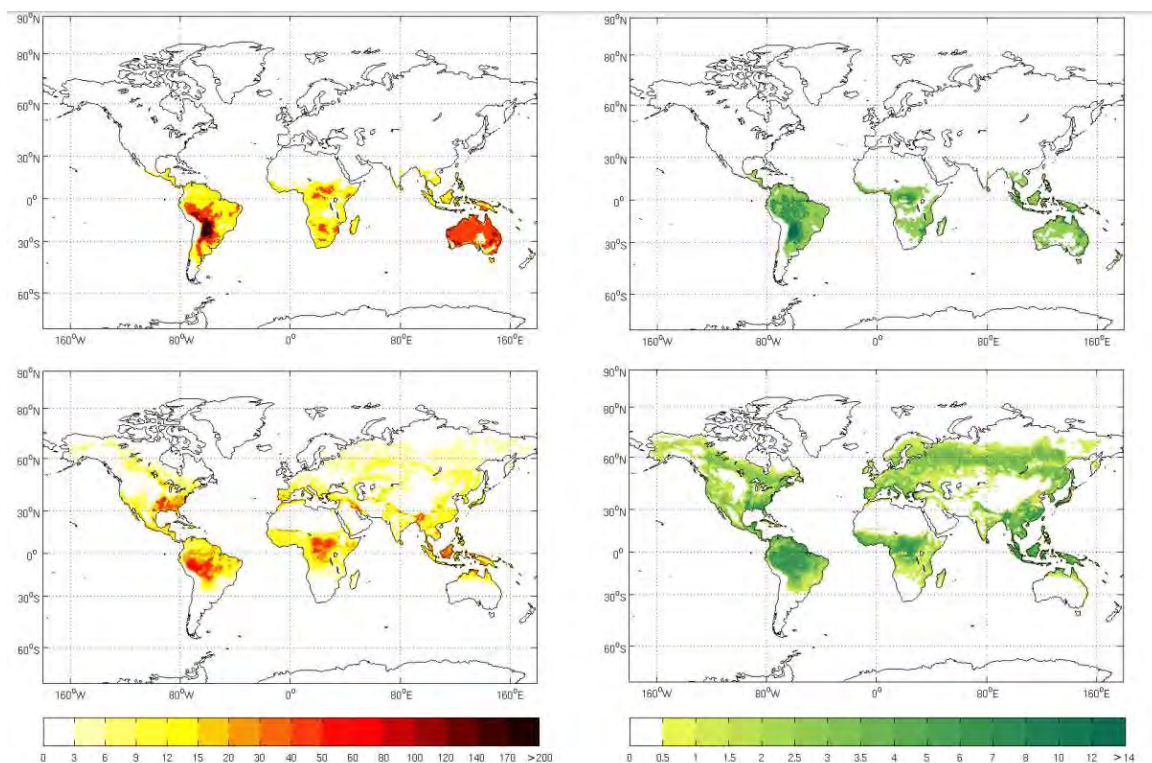


Figure 2.9: Monthly mean emissions (in $\text{mg m}^{-2} \text{ day}^{-1}$) of isoprene (a) and monoterpenes (b) by the MEGAN model averaged for the period 1980–2010. Source: Sindelarova et al. (2014)

As discussed by Hanif et al. (2021) and references therein, the remote tropical forest has been exploited, and the pristine forest is lost because of deforestation, industrial logging activities, and fires to obtain land for agricultural use. When the pristine forest is converted to agricultural land, it is often replaced with high VOCs emitting cash crops like oil palms in Southern China and Southeast Asia. Thus, any change in the factors affecting VOCs emissions (e.g. temperature) is expected to affect the VOCs levels in the tropical atmosphere.

Soil NO_x emissions

As discussed in Section 1.1.2, NO_x play a key role in atmospheric chemistry by catalysing O_3 production. Soil emissions can release NO_x due to microbial activities (e.g. nitrification), contributing to approximately 10–15 % of the present-day global NO_x emissions (Vinken et al., 2014). However, the estimates of soil emissions remain highly uncertain (Vinken et al., 2014).

The main control factors of soil NO_x emissions are the soil nitrogen content, and climate and soil conditions such as temperature and soil moisture (Vinken et al., 2014). Approximately 70 % of global soil emissions are emitted in the tropics (Yienger and Levy, 1995). Figure 2.10 displays the monthly mean soil NO_x emissions averaged for the period 1980–2017. It is obvious that the highest NO_x soil emissions on an annual scale occur over the tropics. As

reported by Weng et al. (2020), the shifting of the emissions from the NH to the SH follows the seasonal variations of the temperature. The peak of the emissions is observed over regions with intense agricultural activities such as the Ganges River Basin of India (Weng et al., 2020).

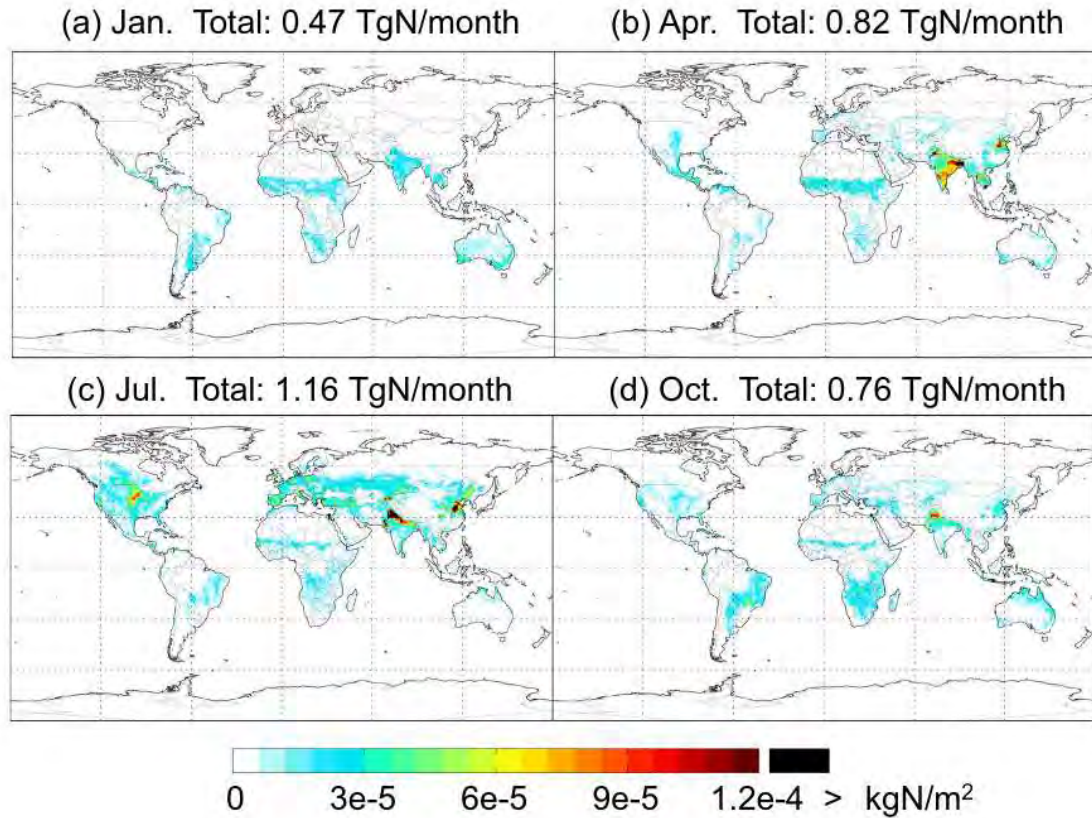


Figure 2.10: Monthly mean soil NO_x emissions (in kgN m^2) for January (a), April (b), July (c), and October (d) based on MERRA-2 data averaged for the period 1980–2017. Source: Weng et al. (2020)

Previous studies have also found large pulses of soil NO_x emissions at the beginning of the wet season, following the dry season. For instance, observations from GOME showed enhanced NO_2 columns during the rainy season over West African Sahel due to emissions from nitrogen accumulated in soils during the dry season (Jaeglé et al., 2004). The beginning of rains activates the bacterial nitrification leading to significant release of NO which is rapidly converted into NO_2 in the atmosphere via oxidative processes. The enhanced NO_x concentrations from the moist soil contribute to an O_3 increase over West African Sahel during the West African monsoon season (Saunio et al., 2009). After excess nitrogen is consumed, wet season NO emissions decrease and contribute less to the local O_3 mixing ratio (Adon et al., 2010).

Lightning NO_x emissions

Thunderstorm lightning is another major source of NO_x . Lightning-induced NO_x (LiNO_x) sources are considered one of the largest global natural NO_x sources in the atmosphere (Galloway et al., 2004), and the largest source in the UT. However, it is complicated to determine the global LiNO_x amount (Schumann and Huntrieser, 2007; Miyazaki et al., 2017) because they cannot be measured directly. Thus, the magnitude and distribution of LiNO_x remain highly uncertain (Schumann and Huntrieser, 2007).

Figure 2.11 displays the seasonal mean global flash rate density averaged for the period 1998–2003 based on satellite observations. It is obvious that the highest lightning activity is observed over the region of the tropics, especially in Africa. The most intense lighting activity, and thus LiNO_x sources, are found in the location of the ITCZ (Section 2.1) (Christian et al., 2003). The direct emissions of NO_x in the UT are of particular importance for O_3 production. This is because of: i) longer lifetimes of NO_x and O_3 (Jacob et al., 1996), and ii) increased OPE at higher altitudes, due to low OH abundances and high NO to NO_2 ratios (Equation 1.34) (Sauvage et al., 2007b). Several studies have highlighted the role of LiNO_x on UT tropical O_3 . For instance, Liaskos et al. (2015) found that a decline in LiNO_x from 5 to $2.5 \text{ Tg(N) yr}^{-1}$ leads to a significant reduction of UT O_3 in the tropics, up to 40–60 %. Using tagged traces from different NO_x sources, Grewe (2007) found that lightning contributed 40 % of O_3 and 70 % of reactive nitrogen compounds (NO_y) in the tropical UT, while Lelieveld and Dentener (2000) found a 50 % contribution of lightning to the UT tropical O_3 . Using the GEOS-chem model, Sauvage et al. (2007b) found that lightning is the main contributor to tropical tropospheric O_3 , accounting for more than 28 % of the tropical tropospheric O_3 burden on an annual average. The contribution of biomass burning, fossil fuels, and soils are 4 to 6 times smaller, even though the strength of the sources are similar. This is because of the increased OPE with altitude.

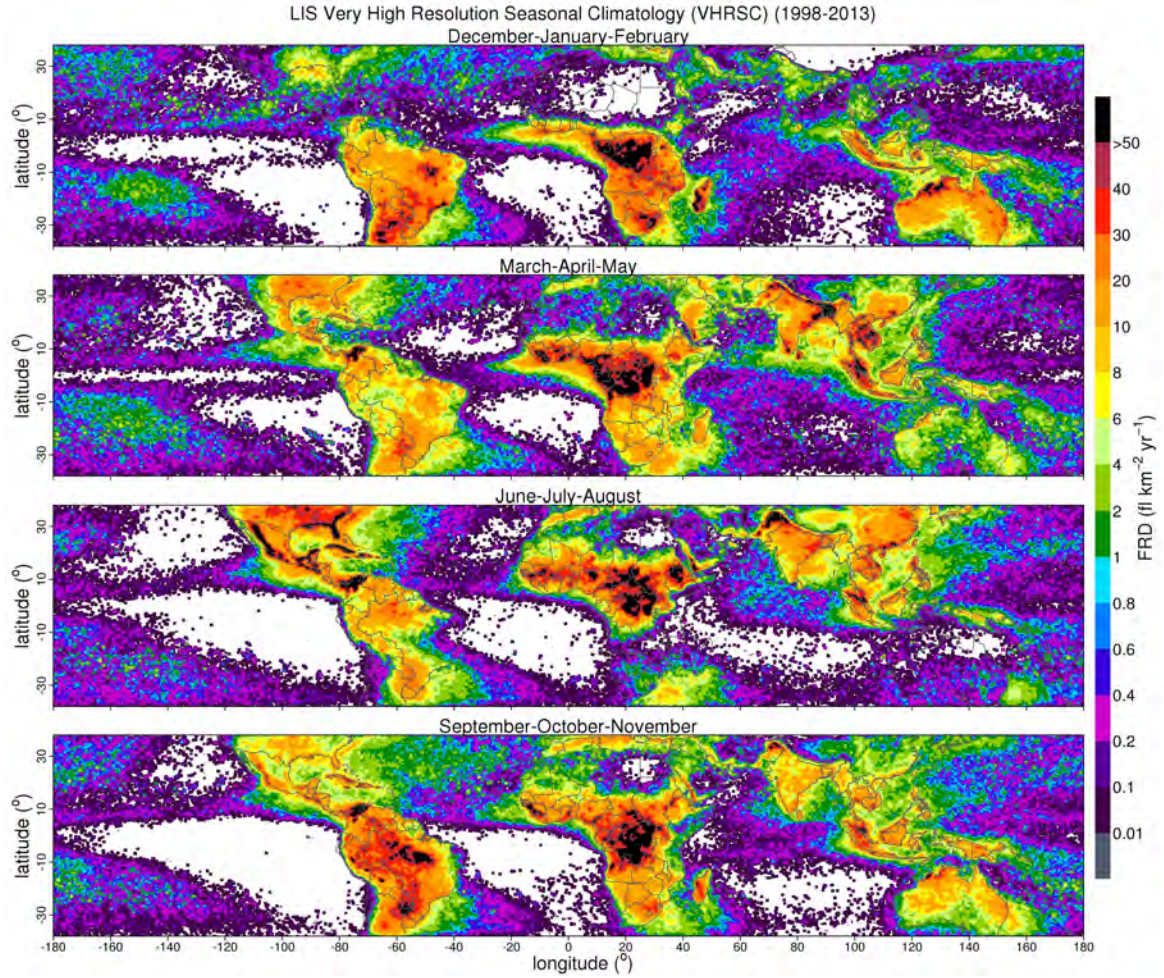


Figure 2.11: Seasonal mean global flash rate density constructed from individual observations made by the Lightning Imaging Sensor (LIS) on the Tropical Rainfall Measuring Mission (TRMM) satellite averaged for the period 1998–2003. Source: https://ghrc.nsstc.nasa.gov/lightning/data/data_lis_vhr-climatology.html

Stratosphere to troposphere exchange

Stratosphere-to-troposphere exchange is considered another natural O_3 source, with a primary impact in the UT, and a smaller one in the surface O_3 levels (Lelieveld et al., 2009). Dry, O_3 -rich air from the stratosphere is transported to the troposphere during the so-called stratospheric intrusions (Danielsen, 1968). This natural O_3 source is quite uncertain (Stohl et al., 2013), and has been found to contribute to tropospheric O_3 5–7 times less than the photochemical production by precursors (Young et al., 2013). Also, stratospheric intrusions impact mostly O_3 abundances in the mid-latitudes during spring, and show minor effects on tropical O_3 levels.

Biomass burning

BB activities are associated with naturally occurring wildfires, and with human-induced fires for several purposes, such as deforestation and cleaning of land for agricultural use,

control of pests and weeds, removal of litter, and energy production for cooking, heating, and fuel (Crutzen and Andreae, 1990). These type of fires are intentionally set on an annual basis during the dry season over tropical regions such as Africa, Asia, and South America (Ziemke et al., 2009). Because of the rapid increase of population in the tropics, these fires contribute to the clearing of the land for human and industrial expansions.

BB emissions are a significant source of O_3 and precursors such as CO and NO_x . Using OMI/MLS measurements for the period 2004–2008, Ziemke et al. (2009) found that BB in the tropics (South America, western Africa, and Indonesia) caused an 8–10 ppb O_3 enhancement over mean values of 35–55 ppb during August–November on a global scale. They also found that BB shows a rather regional impact on O_3 abundance, near the burning regions and mostly in the LT (within 3 km above the fires). In addition to O_3 enhancement, BB emissions are responsible for a 7–9 % and a 30–40 % increase in NO_x and CO respectively, during the peak fire season.

Even though BB play an important role in O_3 and precursors budget in the troposphere, uncertainties remain in the estimation of their emissions. The uncertainties are related to uncertainties on burned area, fuel load, emissions factors, and fire injection heights (Monks et al., 2015). Information about the spatial and temporal occurrence of fires is provided by satellites, with rather limited accuracy (e.g. Giglio and Kendall, 2004). In the tropics, the sparse fire monitoring system makes it difficult to acquire additional quantitative information related to local fires. The amount of fuel load and combustion factors in the models are estimated by ecosystem models or empirical formulas depending on fuel characteristics such as fire type and moisture (Monks et al., 2015). This results in high spatial and temporal variations of the emissions factors, and thus large uncertainties in the emission estimation.

Figure 2.12a displays the mean annual fire pixel density based on Terra MODIS fire observations for the period 2000–2005. It is obvious that the highest fire pixel density occurs over the tropics, especially over NH Africa, followed by South America and Asia. The peak month of the fire activity and the duration of the fire season is displayed in Figure 2.12b and c, respectively. The fires over the aforementioned tropical regions last for approximately three months (Figure 2.12c), which corresponds to the dry season of each hemisphere. The seasonal pattern of the fires differs for the tropical regions (Figure 2.12b) because the dry and rainy seasons are controlled by the positions of the ITCZ (Figure 2.7, Section 2.1). Consequently, the fires in the NH are active during the boreal winter, when the ITCZ is located further south (Figure 2.3). The fire activities over NH Africa peak in January, while over NH South America and Central Asia during March (Fig. 2.12b). During boreal summer, the ITCZ mitigates northwards (Figure 2.3), resulting in dry conditions over the SH. As a result, the fires are moving towards the south over SH Africa (peaking during July and September), SH South America (peak in September), and SouthEast and Equatorial Asia (peak in February and October) (Fig. 2.12a and b).

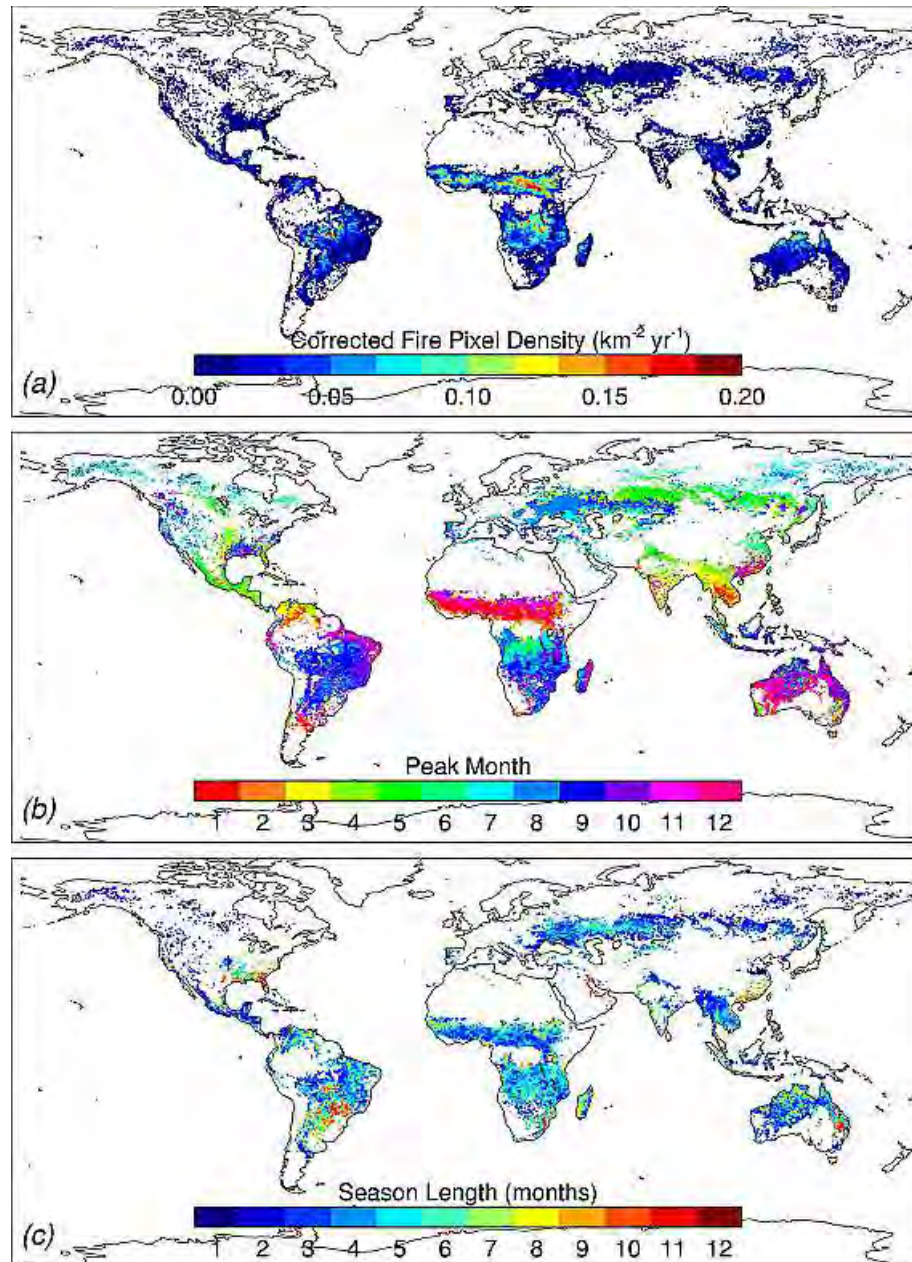


Figure 2.12: Climatological fields derived from the first 5 years of Terra MODIS fire observations for the period 2000–2005. (a) Mean annual fire pixel density, (b) month of maximum fire activity, and (c) length of the fire season. Source: Giglio et al. (2006)

In addition to the varying seasonal pattern, the tropical regions are characterised by different types of fires, as displayed in Figure 2.13. Savanna fires are dominant over Africa and SH South America. In contrast, deforestation fires mostly occur over Amazonia and South East Asia, and agriculture fires over India.

The different types of fires have an impact on the amount of CO emitted from each region. Interestingly, the NH African fires in January correspond to 72 % of the global burned area,

whereas the NH Asian fires only to 2.5 % (Figure 2.14). However, both regions contribute significantly to the global CO concentrations (44 % for Africa and 22 % for Asia) because of more complete oxidation, and thus reduced CO production, over grass fires (African savannas), relative to fires in forests and peat-lands (deforestation and peat-land fires over Asia) (Werf et al., 2010).

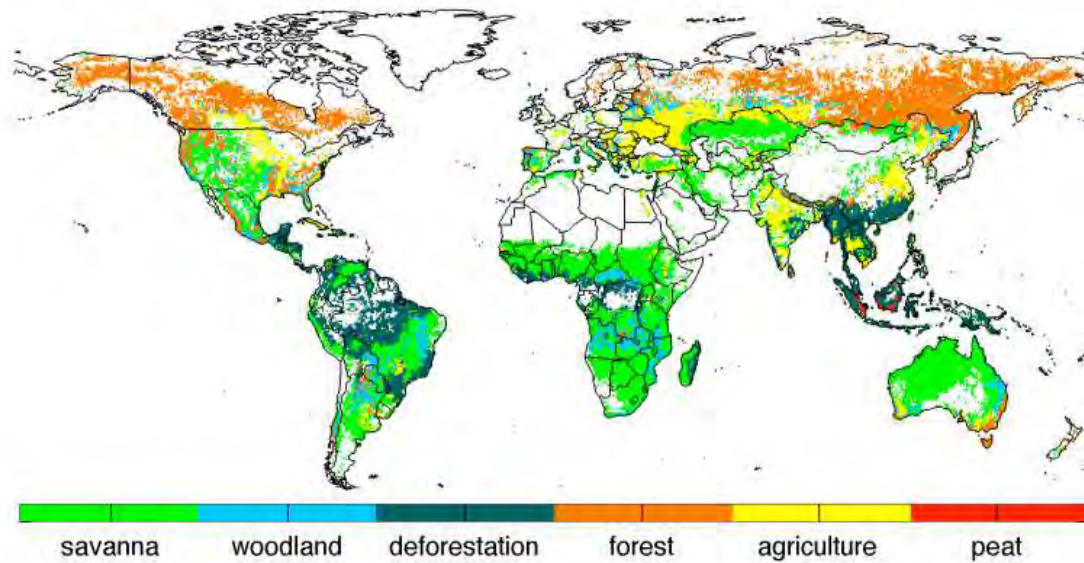


Figure 2.13: Dominant fire type in each 0.5° grid cell based on carbon emissions. Source: Werf et al. (2010)

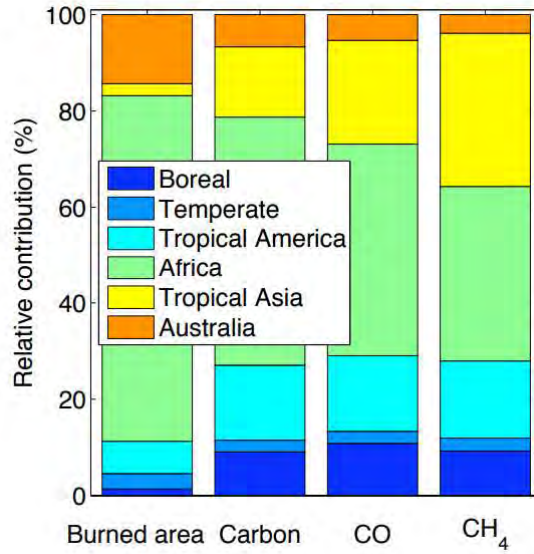


Figure 2.14: Relative contribution (%) from different regions to the average global total burned area and fire emissions of carbon, CO, and CH₄ for the period 1997–2009. The regions of interest correspond to Africa, Tropical Asia, and Tropical America. Source: Werf et al. (2010)

Recent studies have shown decreasing global trends of BB (e.g. Andela et al., 2017). This is in accordance with long-term trends of BB over some tropical regions. For instance, the decrease in BB CO emissions in South America (Andela et al., 2017; Deeter et al., 2018) is due to the long-term declining deforestation rates, especially over forested areas ($\approx 54\%$) and over savanna and shrublands ($\approx 39\%$) (Naus et al., 2022). The decline of BB emissions over NH Africa is attributed to the reducing BB area extent (Hickman et al., 2021) since 2005.

Anthropogenic emissions

Tropics hosted 40 % of the global population in 2014. Projections reveal that the percentage will increase to 50 % by 2050. This is because the tropics are associated with rapid rates of increasing population, especially over Africa. AN emissions are related to emissions of precursors such as CO, NO_x, and VOCs, and thus are expected to modify the O₃ burden.

Figure 2.15 displays the tropical AN emissions from Community Emissions Data System (CEDS2) emission inventory averaged for the period 2000–2019. In contrast to BB, AN emissions show rather weak seasonal variability over the tropics. They also show some characteristics which depend on the region. Concerning Africa, the rapid growth over megacities, such as Lagos, is responsible for increasing emissions from diffuse and inefficient combustion sources (Marais and Wiedinmyer, 2016). This increase is mostly attributed to the growing residential source mainly for cooking and heating (Zheng et al., 2019), but also to traffic emissions (related to a large number of two-stroke vehicles, poor fuel quality, and poorly-maintained engines) (Assamoi and Lioussé, 2010).

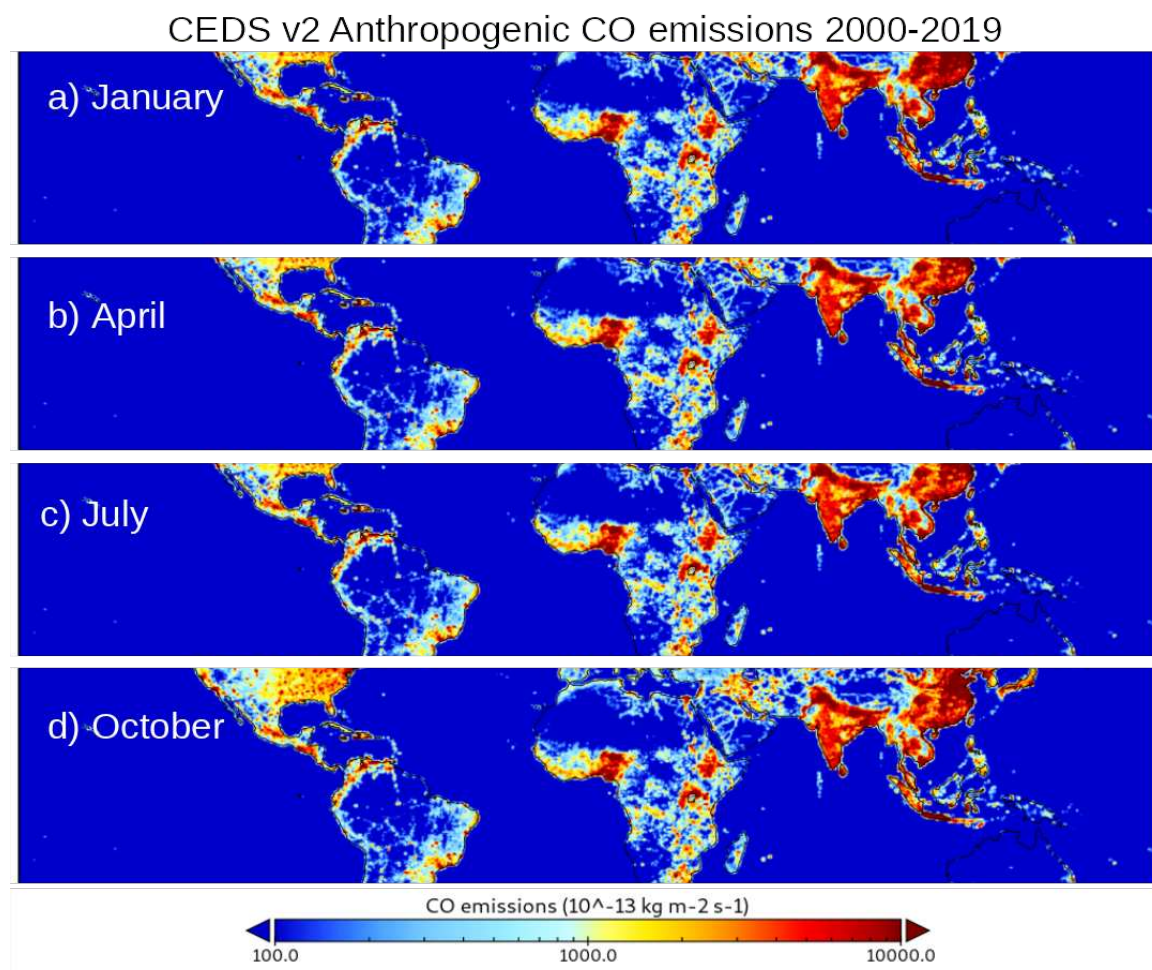


Figure 2.15: CEDS2 AN CO emissions (in $\text{kg m}^{-2} \text{ s}^{-1}$) averaged from 2000 to 2019.

In contrast, Eastern China has had one of the largest decreases in CO emissions (Hedelius et al., 2021) due to technological changes with improved combustion efficiency and emission control measures (Zheng et al., 2018b). Using MOPITT data for the period 2002–2018, Buchholz et al. (2021) found the largest reduction in CO concentrations over China. This reduction is attributed to declines in local CO emissions since 2002, related to replacing residential coal use with electricity and natural gas, and to the implementation of Clean Air Policies (A et al., 2017) around 2010. In India, on the other hand, there are no regulations on the emissions. Previous studies have already reported increasing CO emissions over India from 1996–2015, due to several factors such as increases in residential and agricultural sources (Pandey et al., 2014), and power production and transport activities (Sadavarte and Venkataraman, 2014).

Concerning South America, the strongest AN emissions are found over megacities such as São Paulo and Rio de Janeiro. Martins and Andrade (2008) identified vehicular emission as the main source of O_3 precursors in the boundary layer of these cities.

CHAPTER 3

Data and Methods

In this chapter, we describe the datasets and methods used in our analysis. We start by introducing the **IAGOS** (Section 3.1) airborne in situ data, and the **IASI SOFRID** spaceborne data (Section 3.2). We continue with a brief description of the model-based data provided by the **SOFT-IO** tool (Section 3.3).

3.1 IAGOS airborne observations

IAGOS (Petzold et al., 2015; www.iagos.org) is a European research infrastructure with the objective to monitor the atmospheric chemical composition on a global scale, using commercial aircraft. It delivers in situ measurements of trace gases (O_3 and water vapour since 1994 (Thouret et al., 1998; Helten et al., 1999), CO since 2001 (Nedelec et al., 2003), NO_y between 2001 and 2005 (e.g. Gressent et al., 2014), and more recently NO_x , CH_4 , CO_2 , and cloud particles, see <https://www.iagos.org/iagos-data/>), along with meteorological parameters (temperature and winds).

Its operation began in 1994 under the name **Measurements of OZone and water vapor by in-service AIrbus airCraft** (**MOZAIC**) (Marenco et al., 1998), a collaborative effort between the European aircraft manufacturer Airbus and the **Centre National de la Recherche Scientifique** (**CNRS**). Its initial purpose was to investigate the potential growing impact of the aeronautical industry on climate (Blot et al., 2021). At the time, 5 aircraft were equipped with sensors (Figure 3.1).

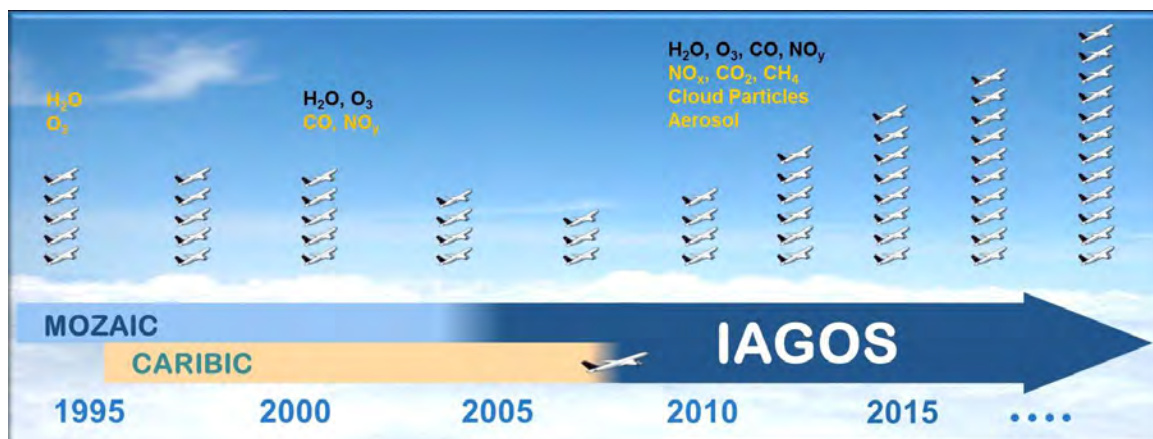


Figure 3.1: Evolution of observations from programmes MOZAIC and CARIBIC to IAGOS: the aircraft represent the number of equipped units in operation. Observed parameters are indicated for the various evolution stages of the program. Source: www.iagos.org

At about the same time (in 1997), the **Civil Aircraft for the Regular Investigation Based on an Instrument Container (CARIBIC)** program (Brenninkmeijer et al., 1999) was launched in Germany, with a similar principle but complementary role to **MOZAIC**. In **MOZAIC**, the measurements were taken automatically during every flight of the long-range aircraft. In **CARIBIC**, a wide variety of species (approximately 100) were measured, including the ones measured by **MOZAIC**, from one single aircraft. The instruments were loaded into the cargo compartment of the aircraft once per month, for four intercontinental flights.

Since the merge of these programs in 2008, their database are known as **IAGOS-CORE** and **IAGOS-CARIBIC**. In the present study, we consider them as a unique database (hereinafter referred to as **IAGOS**), as the **IAGOS** and its predecessors provide consistent O_3 and CO measurements (Nédélec et al., 2015; Blot et al., 2021).

Even though its operation was originally planned to last for a few years, the long-term support from the French and German ministries of research, the European Union (EU Framework Program funding), and the participating airlines have allowed **IAGOS** to equip 17 aircraft in 25 years (nine retired) (Blot et al., 2021), providing a significant amount of measurements, at cruising altitude (9–12 km; 300–185 hPa), and during takeoffs and landings in the proximity of the airport. Since 1994, **IAGOS** has accomplished more than 60 000 flights, and approximately 120 000 profiles over 338 sites around the globe (Figure 3.2), which leads to about 3.5 million points of observations (Blot et al., 2021).

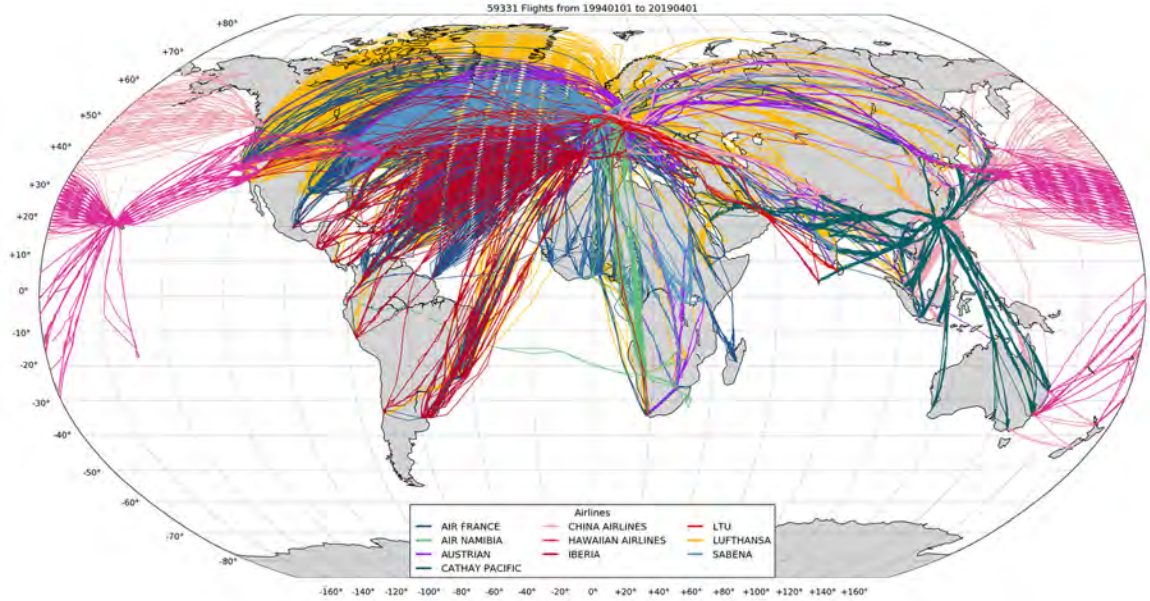


Figure 3.2: Map of IAGOS flights per airline since 1994. Source: Blot et al. (2021)

IAGOS has a central role in the global observing system, as it provides long-term measurements of high accuracy and density throughout the troposphere and the lower stratosphere. Therefore, **IAGOS** has been used to: i) assess statistically robust climatologies and trend analysis (e.g. Cohen et al., 2018; Gaudel et al., 2020), ii) validate chemical transport models (e.g. Sauvage et al., 2007c; Gressent et al., 2016), as well as satellite observations (e.g. De Wachter et al., 2012).

3.1.1 IAGOS instrumentation

IAGOS-CORE measurements are collected by sets of instruments (packages). The main package abroad for all aircraft is Package1, which is developed by CNRS. Package1 is in charge of the O_3 and CO measurements, the data acquisition system, and the interface that collects aircraft parameters (e.g. position and speed of the aircraft, ambient meteorological data) (Nédélec et al., 2015). Package2 includes instruments for measuring greenhouse gases (e.g. CO_2 and CH_4), NO_x , NO_y , or aerosol particle properties, and is optionally deployed on the aircraft. Here, we focus on Package1 instrumentation for O_3 and CO , which provide the measurements taken into account for this study. Further details on Package2 can be found in Petzold et al. (2015).

O_3 and CO measurements are based on optical instruments, which measure the absorption of sampled air at different wavelengths. Two samples are used: one with ambient air containing O_3 (resp. CO), and one with zero O_3 (resp. CO) air (removed by MnO_3 and Sofnocat filters respectively). Auxiliary measurements of temperature and pressure make it possible to automatically deduce a mixing ratio.

O_3 (resp. CO) is measured using a dual-beam ultraviolet absorption monitor at 254 nm

(infrared analyser at $4.6\ \mu\text{m}$) with an accuracy of 2 ppb (resp. 5 ppb), a precision of 2 % (resp. 5 %), and a time resolution of 4 (resp. 30) seconds (Thouret et al., 1998; Nédélec et al., 2003). Considering the maximum aircraft speed ($15\ \text{m s}^{-1}$ during ascend/descend; $250\ \text{m s}^{-1}$ during the cruise), the time resolution of the instruments corresponds to a maximum vertical resolution of 60 m (resp. 450 m) and a horizontal resolution of 1 km (resp. 7.5 km) for O_3 (resp. CO).

In IAGOS-CARIBIC, O_3 is measured with a combination of a dry chemiluminescence detector and a UV absorption spectrometer, with accuracy and precision of 0.5 ppb and 1 % (Zahn et al., 2012). The time response is 4 seconds in the case of UV absorption, or 0.2 s in the case of chemiluminescence (Zahn et al., 2012). CO is measured by a vacuum UV fluorescence, with an accuracy of less than 2 ppb, precision of 1–2 ppb, and time response of 2 seconds (Scharffe et al., 2012).

3.1.2 Data quality

To ensure their quality, IAGOS data are subject to several validation and calibration processes. For in-flight calibration (on the ground and during the cruise every two hours), an O_3 generator is used to expose the instruments in different O_3 concentration levels (0, 100, 500 ppb of O_3 , with a margin error of 15–20 %). This process aims to detect possible instrument drifts (Nédélec et al., 2015).

For post-flight calibration, an O_3 and CO laboratory calibration is performed by CNRS, before and after each Package1 operations period (normally 6 months). The calibration is done by comparing Package1 with a reference instrument, and for several concentrations levels (for O_3 : 0, 50, 100, 200, 300, 500, and 800 ppbv; for CO : 0, 250, 500, 750, 1000, and 1500 ppbv) to check the instrument linearity within 1% for O_3 , and 2% for CO .

Another way to check the consistency between the instruments is by comparing flights that landed or took off at the same site in less than 3h (Nédélec et al., 2015).

IAGOS data are controlled by a central computer. In real-time, the measurements are assigned to flight parameters (such as the position of the aircraft), by the computer onboard the aircraft. Then, they are sent to the central computer, where they are subject to validation processes (Figure 3.3). These validated data are sent to operational users (e.g. Copernicus). Data fully validated and calibrated are stored in the database. In this final stage, they include auxiliary data (such as potential vorticity) calculated from the European Center for Medium Range Weather Forecasts (ECMWF) operational fields, interpolated along IAGOS trajectories. Further information about the auxiliary data will be given in Section 3.3.

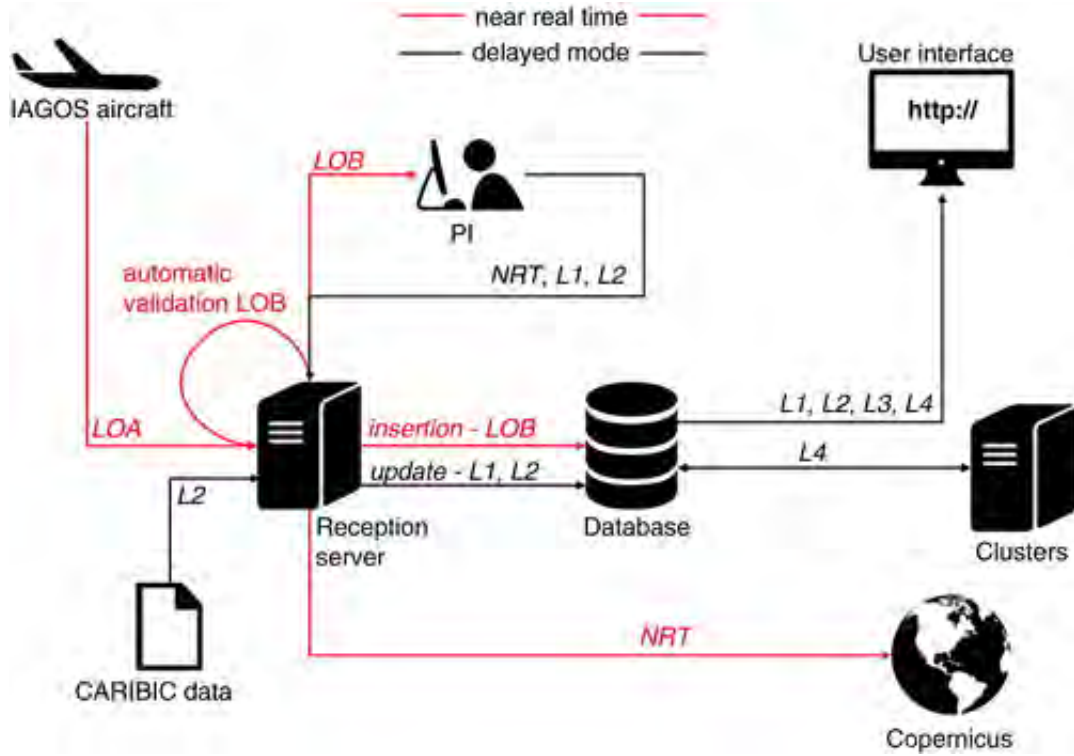


Figure 3.3: IAGOS data flow. Source: Petzold et al. (2015)

Figure 3.4 displays an example of a single IAGOS flight and the acquired O_3 measurements during ascend/descend and cruise phases. CO measurements are collected similarly. As discussed in Petetin et al. (2018a), the IAGOS profiles during ascend/descend are: i) slanted and not strictly vertical, ii) collected close to international airports, in the vicinity of large cities, and iii) along flight corridors frequently visited by other aircraft. Because of this specificity of the IAGOS measurements, the influence of the local pollution on the IAGOS measurements needed to be examined, especially close to the surface, where CO is emitted.

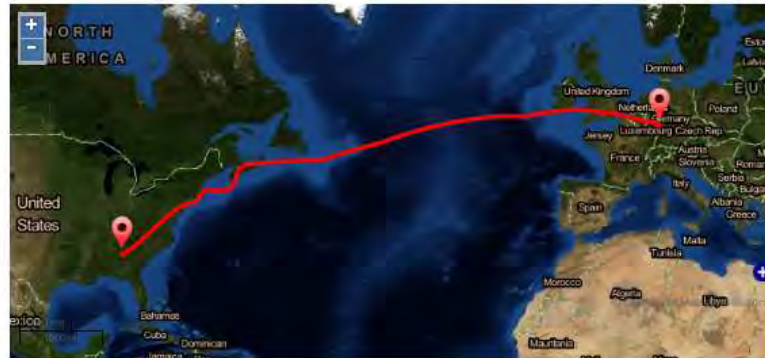
Several studies have compared IAGOS O_3 measurements with radiosondes and surface stations to assess the representativeness of IAGOS measurements (e.g. Thouret et al., 1998; Tanimoto et al., 2015). The most recent one was made by Petetin et al. (2018a), who compared O_3 and CO IAGOS measurements with nearby surface stations (from the local Air Quality monitoring network) and more distant regional surface stations (from the Global Atmospheric Watch network) for the period 2002–2012. Results indicate that the IAGOS O_3 and CO measurements close to the surface are not strongly impacted by local emissions due to airport activities. Comparisons between IAGOS and the surrounding urban background stations showed similar O_3 and CO characteristics close to the surface, in terms of mixing ratio, seasonality, and trends. Better agreement in higher altitudes indicates larger representativeness of the IAGOS measurements.

In this study, we use validated and calibrated IAGOS O_3 and CO observations during ascend

and descent, to document vertical profiles over the tropics (between 25° S and 25° N), since 1994 and 2002 respectively. For the same period, cruise data are used to study the (lower part of) UT tropical composition. Previous studies have used IAGOS data to document the tropical composition over Africa (Sauvage et al., 2005; Sauvage et al., 2007a; Sauvage et al., 2007d; Lannuque et al., 2021), South America (Yamasoe et al., 2015) and South Asia (Sahu et al., 2014; Sheel et al., 2014). However, their analysis is focused on a regional scale, with limited temporal coverage, especially for CO as fewer measurements were available at that time. In this study, we will analyse the tropical composition using IAGOS as a unified and consistent dataset for the entire tropics, as a globe. This way, we aim to bridge the gap of knowledge concerning the O₃ and CO distributions and their interlocking in the entire tropics which are still not well documented.

Flight information

Name : 2011080222382635
 Departure Airport : Atlanta (ATL)
 Departure Date : 2011-08-02
 22:38:26
 Arrival Airport : Frankfurt (FRA)
 Arrival Date : 2011-08-03 07:25:51



Parameter to plot

O3_PM

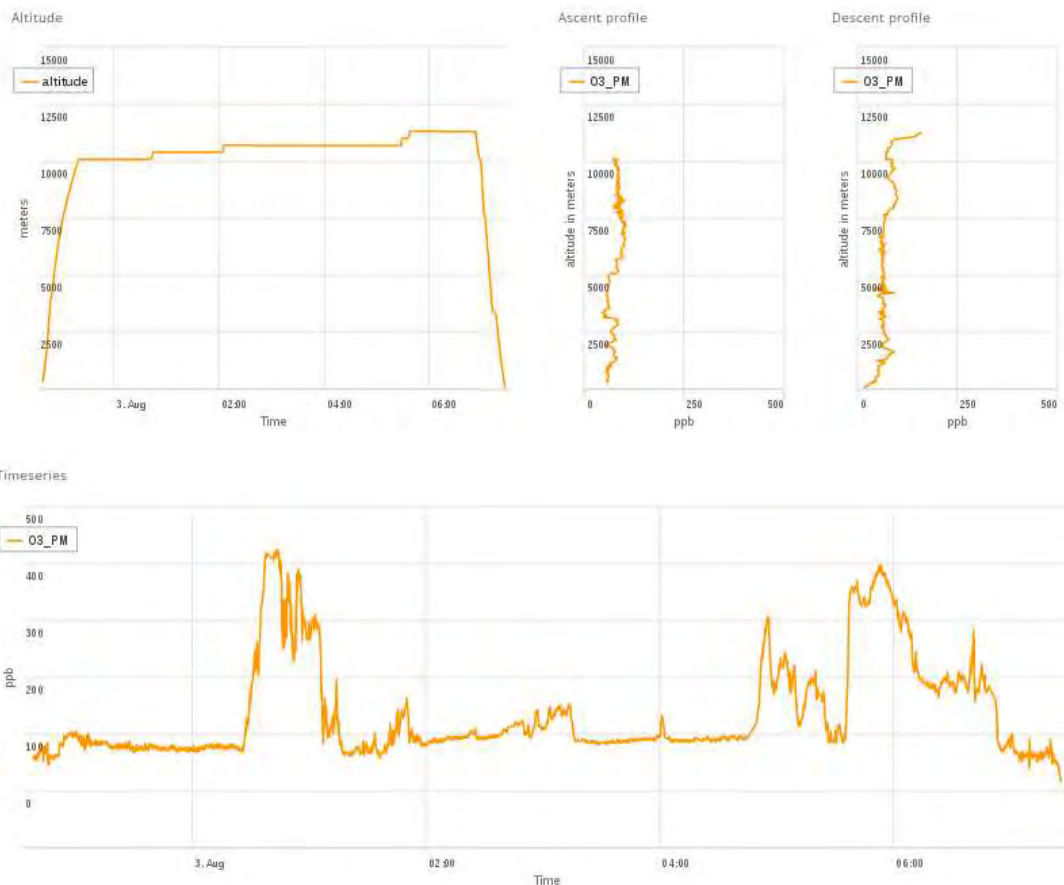


Figure 3.4: Example of IAGOS O_3 data measured during a single flight from Atlanta to Frankfurt. Top panel: the trajectory of the aircraft. Middle panel: the evolution of the aircraft altitude (left); O_3 measurements (in ppb) during the ascent (middle) and descent (right) phase. Bottom: O_3 measurements (in ppb) during the cruise phase. Source: <https://www.iagos.org/>

3.2 IASI spaceborne observations

The **IASI**, developed by **Centre National d'Etudes Spatiales (CNES)** in collaboration with the **European Organization for the Exploitation of Meteorological Satellites (EUMETSAT)**, is the main payload instrument of the **MetOp**–A, B, and C satellites launched in 2006, 2012 and 2018. **IASI** measures temperature and humidity, allowing improvements to **Numerical Weather prediction (NWP)**. In addition, it provides information on several atmospheric components such as O_3 (Eremenko et al., 2008; Barret et al., 2011; Boynard et al., 2016), CO (George et al., 2009; De Wachter et al., 2012) and N_2O (Barret et al., 2021), allowing the monitoring of the atmospheric composition on a global scale.

IASI is a Fourier transform spectrometer that measures the infrared radiation emitted by the Earth and its atmosphere, from a low altitude (817 km) sun-synchronous polar orbit. It has a spectral resolution of 0.25 cm^{-1} from 645 to 2760 cm^{-1} wave number region. Its field of view and a 2200 km swath (**Figure 3.5**) allows global coverage twice daily, at 9:30 and 21:30 local solar time. Each instantaneous field of view consists of a 2×2 circular pixel, with a diameter of 12 km at nadir (**Figure 3.5**).

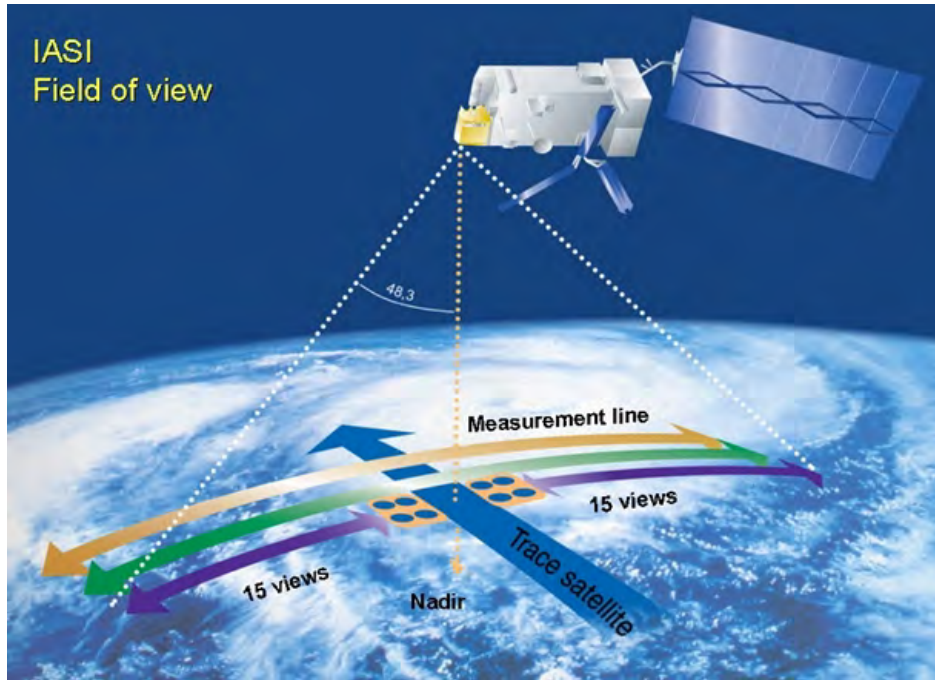


Figure 3.5: IASI field of view. Source: <https://www.eumetsat.int/iasi>

The O_3 and CO retrievals used in this study are performed with the **Software for a Fast Retrieval of IASI Data (SOFRID)** (Barret et al., 2020; De Wachter et al., 2012), developed at LAERO. SOFRID is based on the RTTOV radiative transfer model developed jointly by ECMWF, Météo-France, and **UK Met Office (UKMO)** (Matricardi et al., 2004; Saunders et al., 2018). The retrievals are performed with the **UKMO 1D-Var** algorithm developed by the **UKMO** (Pavelin et al., 2008) which uses the optimal estimation method (Rodgers,

2000). Briefly, this method combines measurements and a priori information to constrain the retrievals where the sensitivity is low. The a priori information represents the best knowledge of the state vector (e.g. the retrieved profile) at the moment of the measurement.

SOFRID-O₃ vertical profiles are retrieved from radiances in the 980–1100 cm^{−1} spectral window encompassing the 9.6 μm O₃ absorption band (Barret et al., 2020), while the SOFRID-CO profiles in 2143–2181 cm^{−1} spectral window (De Wachter et al., 2012). Both vertical profiles are retrieved on 43 fixed pressure levels from the surface up to 0.1 hPa.

As discussed in Clerbaux et al. (2009), nadir looking **Thermal Infrared (TIR)** instruments like IASI can measure atmospheric radiation down to the Earth’s surface, during cloud-free conditions. When properties such as ground emissivity, surface, and atmospheric temperatures are known at the location of the measurements, the profiles of species such as O₃ and CO can be retrieved. However, the presence of clouds can modify the optical path and thus affect the radiance signal recorded by the instrument. For this reason, it is important to apply a cloud filter and consider only the measurements not (or little) impacted by clouds. Details on the cloud filter applied to IASI data can be found in Barret et al. (2011) and De Wachter et al. (2012). Briefly, based on the AVHRR¹-derived fractional cloud cover from the IASI **EUMETSAT** L2 products, only pixels with a cloud fraction between 0 and 25 % are taken into account. For pixels with unavailable cloud fraction, the retrieved surface temperature at 11μm (T11) and 12μm (T12) IASI channels are compared to the ECMWF surface temperature. When the difference between T12 and the ECMWF surface temperature is larger than 10 K or when the difference between T11 and T12 is larger than ±10 K, the pixel is removed because it is considered contaminated by clouds.

De Wachter et al. (2012) validated SOFRID-CO relative to **IAGOS** CO profiles for the 2008–2009 period. They showed that IASI provides two independent pieces of information in the lower (surface–480 hPa) and upper troposphere (480–225 hPa), with retrieval errors of less than 21% and 10%, respectively. IASI captures the seasonal variability of CO over the tropics (Windhoek) and the mid-latitudes (Frankfurt) in the lower and upper troposphere in good agreement relative to **IAGOS**, as indicated by the large correlation coefficients (0.85 and 0.70 respectively). At Windhoek, SOFRID-CO is biased low in the lower troposphere and upper troposphere by 13 ± 20 % and 4 ± 12 % respectively.

SOFRID-O₃ v3.5 retrievals use a dynamical a priori profile based on latitude, season, and tropopause height (Barret et al., 2020). In the tropics, where the surface temperature, thermal contrast, and tropopause height are the highest, SOFRID-O₃ retrievals allow two independent pieces of information, one in the troposphere and one in the **Upper troposphere lower stratosphere (UTLS)** (Barret et al., 2020). Comparisons with ozonesonde measurements for the period 2008–2017, showed that SOFRID-O₃ is biased low in the tropical troposphere

¹Advanced Very High Resolution Radiometer.

and UTLS, by 3 ± 16 % and 12 ± 33 % respectively in the Northern Tropics (0 – 30°N), and by 8 ± 14 % and 21 ± 30 % in the Southern Tropics (0 – 30°S) (Barret et al., 2020). Comparisons between SOFRID- O_3 retrievals using dynamical a priori profiles instead of a single a priori profile showed improvements (e.g. a general increase in the correlation coefficients and the amplitude of the retrieved variability) mostly in the troposphere. The change of the a priori profile leads to minor differences in the UTLS, indicating the highest sensitivity of IASI to this layer (Barret et al., 2020).

We use monthly averaged SOFRID-CO and O_3 retrievals on a $1^\circ \times 1^\circ$ grid from 2008–2019. We focus on pressure levels corresponding approximately to the independent pieces of information, and on daytime measurements when larger thermal contrast between the surface and the atmosphere results in increased sensitivity of the instrument (Clerbaux et al., 2009).

SOFRID- O_3 and CO retrievals have been widely used to offer a better understanding of the atmospheric composition over tropical regions such as Asia (e.g. Barret et al., 2011; Safieddine et al., 2016), Africa (e.g. Barret et al., 2008; Lannuque et al., 2021) or South America (e.g. Yamasoe et al., 2015). However, these studies are either focused on: i) a rather continental scale (e.g. Barret et al., 2011), ii) a specific tropospheric layer (e.g. Lannuque et al., 2021), and/or iii) a specific season (e.g. Safieddine et al., 2016).

Even though satellite-retrieved observations offer better spatial and temporal coverage than in situ measurements, they provide limited information on the vertical. In situ IAGOS measurements are considered more accurate and with a finer vertical resolution. Thus, the combination of the two observing systems provides an opportunity to better characterise the tropical O_3 and CO distributions and their variabilities from the lower troposphere to the UTLS.

3.3 SOFT-IO model

The SOFT-IO tool (Sauvage et al., 2017; <http://dx.doi.org/10.25326/2>) has been developed to investigate the origin of the observed IAGOS-CO, by coupling FLEXible PARTicle dispersion model (FLEXPART) 20-days backward transport simulations with emission inventories. For each point of the IAGOS trajectory, SOFT-IO estimates the CO contribution coming from 14 different geographical regions (see Fig. 3.6), for AN and BB origin separately. We use the CEDS2 AN emission inventory (McDuffie et al., 2020) and the Global Fire Assimilation System (GFAS) BB emission inventory (Kaiser et al., 2012) which include fire injection heights, to discriminate sources of CO anomalies over different regions of interest. For the calculations, BB emissions are updated daily, due to their strong variability. The AN emissions, which show weaker temporal variability, are updated monthly. The meteorological fields are based on $1^\circ \times 1^\circ$ ECMWF analysis and forecast with a time resolution of 6 and 3h respectively (with a preference to analysis over forecast).

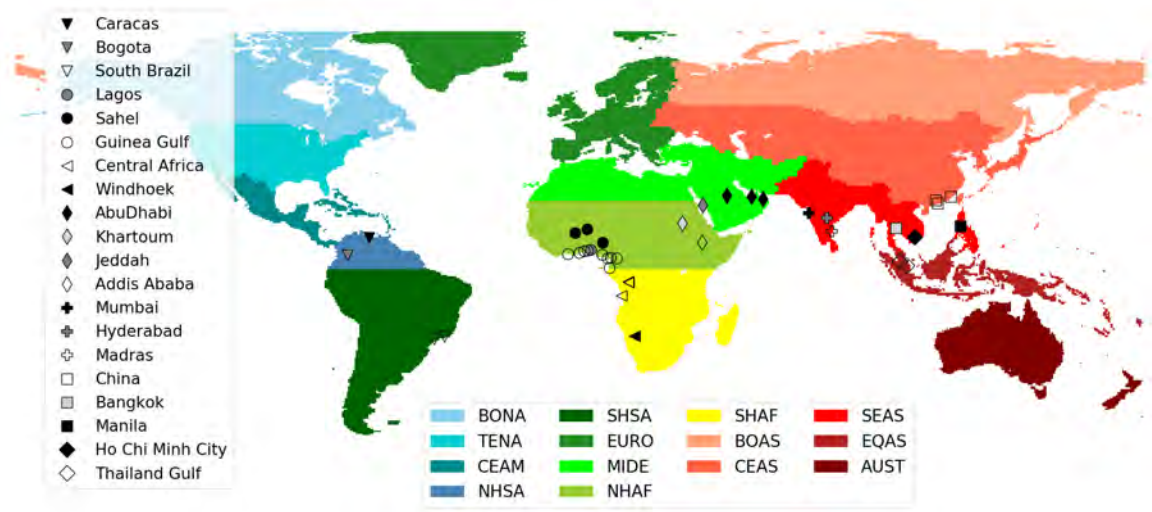


Figure 3.6: Locations of tropical sites served by *IAGOS*, and geographical source regions used in *SOFT-IO* model. *BONA*: Boreal North America; *TENA*: Temperate North America; *CEAM*: Central America; *NHSA*: Northern Hemisphere South America; *SHSA*: Southern Hemisphere South America; *EURO*: Europe; *MIDE*: Middle East; *NHAF*: Northern Hemisphere Africa; *SHAF*: Southern Hemisphere Africa; *BOAS*: Boreal Asia; *CEAS*: Central Asia; *SEAS*: Southeast Asia; *EQAS*: Equatorial Asia; *AUST*: Australia and New Zealand.

FLEXPART (Stohl et al., 2005) is a Lagrangian particle dispersion model which is used to simulate a variety of atmospheric transport processes. Lagrangian dispersion models typically excel in accurately representing the differential advection, in contrast to global Eulerian models that struggle to capture intercontinental pollution transport effectively (Eastham et al., 2017). Moreover, Lagrangian models offer this advantage while maintaining a significantly lower computational cost. Specifically, these models can reconstruct small-scale atmospheric composition structures using large-scale global meteorological data. As a result, the model outputs comparable to high-resolution in situ observations (Pisso et al., 2009) such as *IAGOS* (Sauvage et al., 2017). In our case, we use *FLEXPART* in a backward mode (in time) to determine the history of air parcels affecting a measurement site. Joined with emissions inventories, *FLEXPART* is capable of describing the origin of the observed CO for 20 days before the observation. The 20-day time period is sufficient to capture the transport of pollution at a hemispheric scale in the mid-latitudes (e.g. Cristofanelli et al., 2013).

The CO contributions computed by *SOFT-IO* refer to primary CO sources (e.g. AN and BB emissions) which are directly released on the surface. This tool does not calculate the background CO. The background CO can be emitted by primary sources older than 20 days, and by secondary sources such as oxidation of methane and VOCs. The secondary formation of CO is considered a rather slow photochemical process. Thus, the secondary CO is not expected to accumulate on the surface, as there is sufficient time for the redistribution of the air masses in the troposphere. Similarly, for the same reason, the aged air affected by

primary sources is considered well-mixed in the troposphere.

The photochemical lifetime of CO due to oxidation by OH is approximately 1 to 2 months (Edwards et al., 2004). Therefore, it is possible to link elevated CO mixing ratios (with respect to a seasonal background mixing ratio) at an observing site with emission sources without simulating the atmospheric chemistry (Sauvage et al., 2017).

In addition, the 20-days time period is longer than the lifetime of polluted plumes in the FT, as the typical time scale for mixing in the troposphere is estimated to be shorter than 10 days (Pisso et al., 2009). Consequently, SOFT-IO is capable to link air masses anomalies such as CO elevated levels with the region of the emissions (Sauvage et al., 2017).

Figure 3.7 displays one example of an individual vertical profile of IAGOS and SOFT-IO contributions during a single flight departing from Lagos on 19 May 2003. The Figure shows the absolute contributions computed by SOFT-IO. In our study, we focus on the SOFT-IO contributions to the positive CO anomalies over a site. A CO anomaly is defined as the positive difference between the observed and the background CO mixing ratio (see Figure 3.7). The background CO mixing ratio represents a reference value, not affected by surface emission or pollution events. For this reason, it is computed as the monthly climatological median CO of a remote area away from polluted regions, in the upper troposphere (300–185 hPa, during the whole study period 2002–2020) (Figure 3.8).

The areas selected for the computation of the background CO mixing ratio are displayed in Figure 3.8. The box on the left (resp. right) located over the remote tropical Atlantic (resp. Pacific) is used to compute the background CO mixing ratio over the South American (resp. Asian) clusters. The box over NH Africa (resp. SH Africa) is used for the respective African clusters as they are located upwind of the local AN and BB (resp. BB) local emissions. The background CO mixing ratio is computed for every month (January, April, July, and October) to take into account the seasonal variations of the observed CO mixing ratio, as illustrated in Figure 3.8.

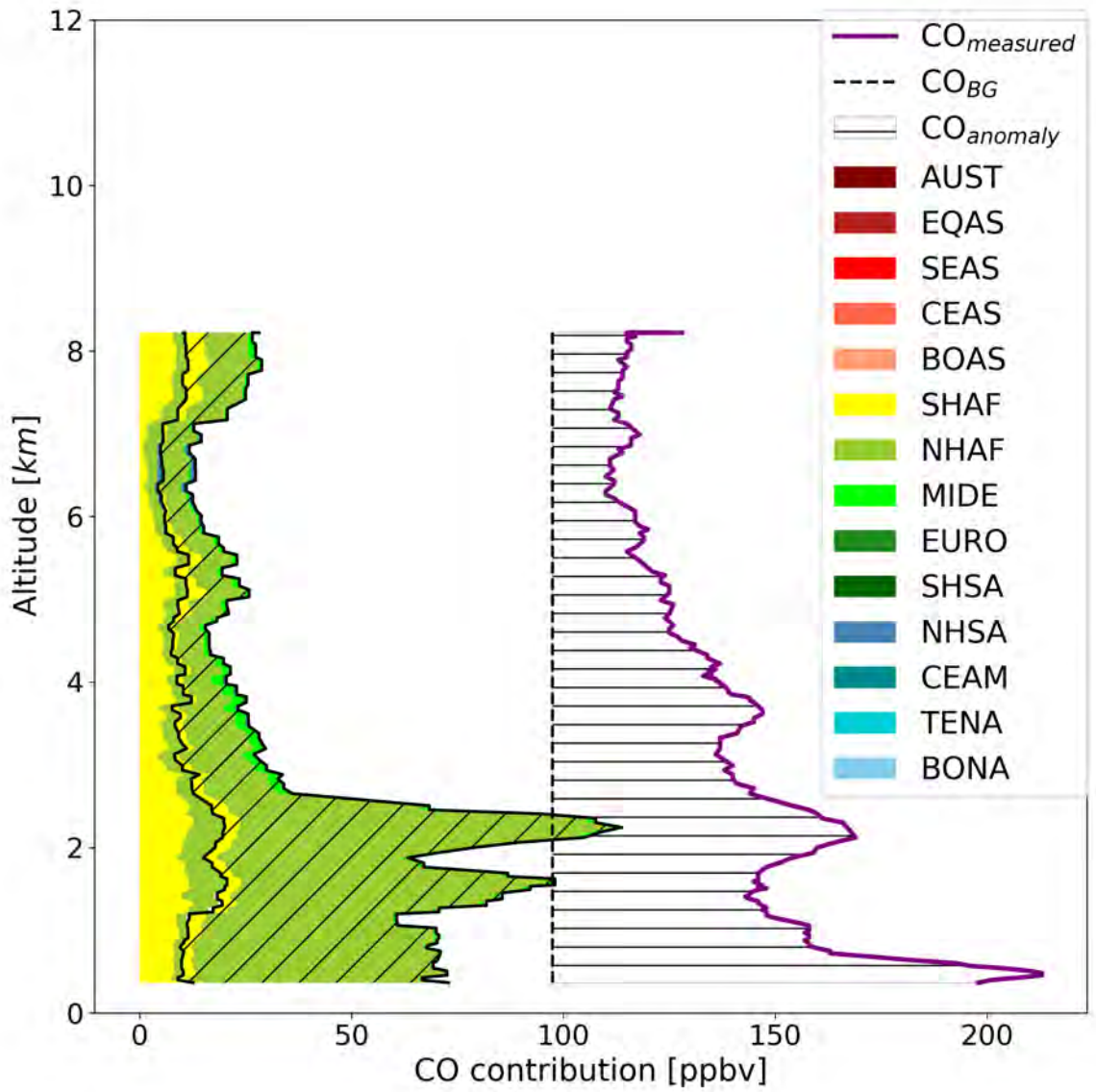


Figure 3.7: Example of an individual IAGOS-CO and SOFT-IO contribution vertical profile during a single flight departing from Lagos on 2003-05-19 15:53:14. The purple line represents the observed CO mixing ratio, while the dashed line the background CO mixing ratio (in ppb) computed as explained in the text. The intermediate hatched part indicates the positive CO anomaly. The coloured part on the left shows the vertical distribution of CO contributions computed by SOFT-IO (in ppb). The geographic origin of CO emissions is indicated by the different colours, with the hatched part showing AN contribution, and the non-hatched part BB contribution.

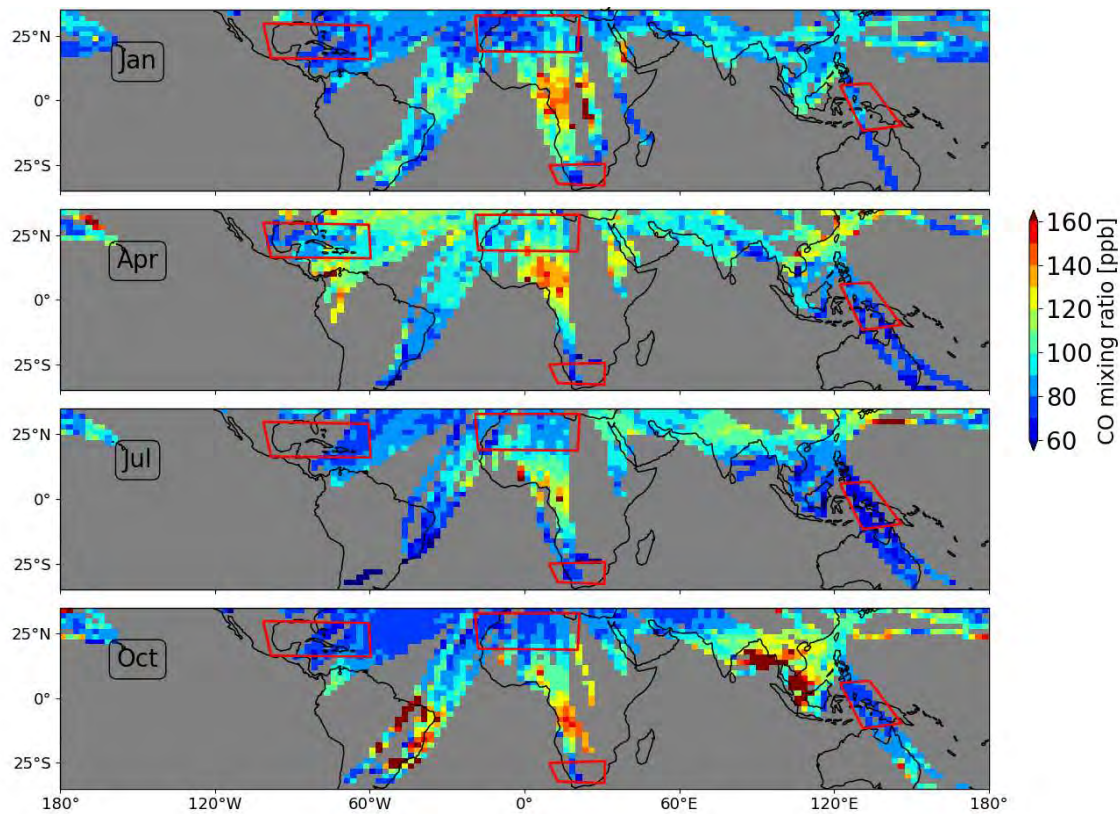


Figure 3.8: Monthly mean UT (between 300–185 hPa) CO distributions measured by IAGOS for the period 2002–2020. The red boxes indicate the regions taken into account for the computation of the background CO mixing ratios.

To investigate the sensitivity of our analysis to the selection of the background CO mixing ratio, we followed an alternative method to compute the latter. In this method, we chose a specific background CO for each site and month, computed as the median CO mixing ratio in the 540–300 hPa pressure range (approximately 6–10km) for each monthly mean vertical profile. We select this pressure range to limit the influence of surface emissions on the CO mixing ratio. The analysis of the CO anomalies based on the two different background CO definitions showed similar origin and CO contributions for the different sites. Thus, we conclude that our method is robust and independent of the selection of the background CO mixing ratio.

The absolute contributions estimated by **SOFT-IO** can be subject to biases and uncertainties mainly induced by uncertainties in emissions inventories or difficulties in the representation of processes such as deep convection, by the **FLEXPART** model or **ECMWF** analyses. Sauvage et al. (2017) validated **SOFT-IO** performance against IAGOS CO observations for several regions and tropospheric levels. Results show **SOFT-IO**’s capability to detect more than 95 % of the observed CO anomalies over most of the regions, without any strong dependence on altitude or region of the CO plume. **SOFT-IO** captures the intensity of CO anomalies with a bias lower than 10–15 ppb for most of the regions and tropospheric levels. The bias is

higher in extreme pollution events and might be related to uncertainties in the emissions inventories.

The main advantage of SOFT-IO is that it can be used as complementary material to analyse in-depth a global and long-term observational database like IAGOS. Knowing the origin of the air sampled over one region can lead to a better understanding of dynamical processes affecting the atmospheric composition on a regional or even a global scale. In addition, the synergy between SOFT-IO and IAGOS-CO observations offers the opportunity to validate emission inventories relative to observations on a global scale. This way, a significant reduction in the uncertainties of emissions inventories can be achieved leading to better representation of the atmospheric composition by global atmospheric models.

Previous studies (e.g. Lannuque et al., [2021](#); Petetin et al., [2018b](#)) have used SOFT-IO to track back the sources of CO measured by IAGOS, but on a rather limited spatial extent. Petetin et al. ([2018b](#)) studied the CO origin over small geographical areas (vertical profiles at different sites such as Windhoek and Japan), while Lannuque et al. ([2021](#)) focused on the African upper troposphere. In this study, we will use the SOFT-IO output for CO source attribution in the entire tropics, over the whole troposphere.

CHAPTER 4

IASI validation with IAGOS

Upper tropospheric O₃ and CO climatologies

As discussed before (Sections 1.1.1, 1.2.1), O₃ and CO are harmful pollutants, strongly impacting the oxidizing capacity of the troposphere and influencing the climate in a direct (for O₃) and indirect (for O₃ and CO) way. Through its reaction with OH, CO enhances the lifetime of CH₄, which is a greenhouse gas. Also, CO oxidation results in production of CO₂ and O₃, which are also greenhouse gases. O₃ is a short-lived climate forcer (IPCC, 2021) whose increase during the 20th century has contributed to global warming (Shindell et al., 2006). The radiative forcing of O₃ is particularly significant in the tropical UTLS (Chen et al., 2007). Therefore, it is important to document the characteristics of O₃ and its precursor CO as accurately as possible over the tropical UTLS.

The relatively long lifetime of CO makes it an ideal tracer to study the long-range transport of pollution (Logan et al., 1981). The lifetime of tropospheric O₃ varies with altitude and ranges from 1–2 days in the BL to several weeks in the FT (Stevenson et al., 2006). Thus, O₃ in the FT can be transported intercontinentally (Monks et al., 2015), influencing air quality from a local to a hemispheric scale. The tropics are associated with strong (natural and anthropogenic) surface emissions which emit large amounts of O₃ precursors, including CO (Section 2.2). Deep convection is particularly active over the tropics (Andreae et al., 2001), due to their proximity to the ITCZ (Section 2.1), and it plays a significant role in the transport of precursors from the surface to higher altitudes. In addition, the dynamic impacts of the monsoon systems (e.g. Randel et al., 2010; Barret et al., 2016) can contribute to the uplift of surface air masses to the UTLS. These dynamic processes can favour the redistribution of tropical air masses on an intercontinental scale (Zhang et al., 2016). Therefore, it is necessary to study tropical O₃ and CO in the UTLS across this range of scales. This information can be provided by satellite observations.

IASI-SOFRID retrievals provide O₃ and CO measurements since 2008 with a high spatial and temporal resolution (Section 5.2.2.4). Previous studies have validated IASI-SOFRID O₃ (Barret et al., 2020) and CO retrievals (De Wachter et al., 2012), but without spanning the whole tropics due to the lack of available in situ observations. These studies used vertical profiles from ozonesondes (Barret et al., 2020) and IAGOS (De Wachter et al., 2012), which

offer rather limited spatial coverage and are not indicative of the whole tropical UTLS. The validation study over the tropics is particularly interesting as cloud formation is associated with the ITCZ and might affect the measurements from space. SOFRID-O₃ retrievals have been validated for a long period (2008–2017) (Barret et al., 2020). An issue that was raised in this study was a systematic underestimation of O₃ by IASI in the tropical UTLS, with a bias of -12 % (resp. -21 %) in the northern (resp. southern) tropics. On the other hand, SOFRID-CO retrievals have been only validated at the beginning of the IASI period and in a very short time frame (2008–2009) (De Wachter et al., 2012).

In this context, in Section 4.1, the UT O₃ and CO mixing ratios from IAGOS and IASI-SOFRID are compared to evaluate the ability of IASI to document the UT O₃ and CO spatiotemporal variations over the tropics and subtropics. For the validation of IASI-SOFRID, it is necessary to include the subtropics (between 25° S–34° S and 25° N–34° N) to better assess the shift of O₃/CO mixing ratios between the troposphere in the tropics and the stratosphere in the subtropics.

Tropospheric O₃ trends

Several studies use in situ aircraft data (e.g. Gaudel et al., 2020; Wang et al., 2022) and ozonesondes (e.g. Thompson et al., 2021; Christiansen et al., 2022) for the detection of tropospheric O₃ trends. However, these observations are sparse in time and space (Tarasick et al., 2019). Thus, it is difficult to establish straightforward trends for O₃ using in situ measurements. On the other hand, satellite instruments provide measurements of tropospheric O₃ with high spatial and temporal resolution on a global scale. Nevertheless, in the frame of the Tropospheric Ozone Assessment Report, Phase I (TOAR-I), Gaudel et al. (2018) pointed out global uncertainties in the recent tropospheric O₃ trends by satellites due to inconsistencies among the different products. In their study, they computed O₃ trends based on five satellite products, which do not agree in magnitude and sign. UV sounders show mainly positive trends (e.g. Ziemke et al., 2019), in contrast to IR sounders which show mainly negative trends (Wespes et al., 2017). The reasons for the discrepancies among the satellite products are still unknown and require further investigation.

The determination of O₃ trends based on satellite retrievals can have uncertainties due to time-varying biases in the instruments, or by time-dependent corrections in the retrievals. The low vertical sensitivity of the sensor can also affect the trend estimation. Understanding the contributions of instrument biases and the limited vertical sensitivity to the uncertainties in the trends requires validation using in situ measurements. In this frame, we use IAGOS vertical profiles to validate tropospheric O₃ trends from SOFRID. The aim is to evaluate possible drifts of SOFRID-O₃ and determine the impact of the vertical sensitivity of IASI upon the documented trends.

One of the objectives of the TOAR-II satellite working group is to resolve the reasons for the trend differences among the satellite products. Our evaluation study aims to document

the impact of the sampling of IAGOS and the vertical sensitivity of IASI to the trend computations, as mentioned before. This can offer some discussion for the satellite group, as the UV and IR measurements are characterised by different sampling and vertical sensitivities that are expected to affect the trend estimation (Gaudel et al., 2018).

Last, in Section 4.3 we discuss the O₃ change as seen by IASI. The periods we account for the change are the 3-year periods with the maximum separation during the IASI period (2008–2010 and 2018–2020).

4.1 Validation of climatologies in the Upper Troposphere

The comparison between IAGOS and SOFRID is made for O₃ and CO monthly meridional averages for areas where IAGOS has the highest coverage (transects) (black boxes in Fig. 4.3), in the UT for the period 2008–2019. Some statistical indicators are computed for the transects and the for the whole region (34° S–34° N):

1. the mean relative difference $\frac{SOFRID-IAGOS}{IAGOS}$ (bias)
2. the root-mean-square of the relative difference $\sqrt{\frac{\sum(SOFRID-IAGOS)^2}{\text{Number of measurements}}}$ (RMSD)
3. the Pearson correlation coefficient (R)

These statistics are based on 1 latitudinal degree bins of the monthly meridional means along the transects.

For O₃, on average we find a correlation coefficient of 0.70 with a not significant positive bias of $9 \pm 18\%$ (Table 4.1), in contrast with Barret et al. (2020) (bias of -12 ± 33 (resp. -21 ± 30) in the NH tropics (resp. SH tropics) compared to sondes in the UTLS from 2008 to 2017). The differences in the mean bias with our study can be related to: i) the different validation method, ii) the different definition of the tropics (0–30° N/S for Barret et al. (2020) and iii) of the UTLS (300–150 hPa). For their validation, Barret et al. (2020) used vertical profiles over 11 tropical sites, which cover a relatively small area of the tropics. The lower bias of IASI in our study highlights the ability of IASI to capture large-scale features of O₃ in the tropical UTLS.

Concerning O₃-SOFRID v1.6 retrievals, previous studies have found a correlation coefficient of 0.95 (resp. 0.80) and biases of $10 \pm 10\%$ (resp. $17.5 \pm 20\%$) compared to O₃ sondes in the UTLS (resp. Barret et al., 2011; Dufour et al., 2012). The similar bias between the two SOFRID-O₃ versions highlights the sensitivity of IASI in the UTLS, as its performance is slightly affected by changing the a priori profile. In addition, it shows that the overestimation of SOFRID-O₃ v1.6 in the UTLS is not caused by the use of a single a priori profile biased towards mid-latitudes, where O₃ increases sharply above 290 hPa due to the low tropopause height, as suggested by Emili et al. (2014). Concerning the different transects, correlation coefficients range from 0.66 to 0.84 (Table 4.1) indicating high consistency between IAGOS

Table 4.1: Statistics of the comparison between IAGOS and IASI-SOFRID monthly O₃/CO meridional UT transects for the period 2008–2019. The Pearson correlation coefficient (R), the bias (in %), and the root-mean-square of the relative difference (RMSD) (in %) are given.

Transect	O ₃		CO	
	R	Bias ± RMSD	R	Bias ± RMSD
NAtlantic	0.84	6 ± 18	0.90	0 ± 6
Atlantic	0.66	20 ± 27	0.75	-2 ± 7
Africa	0.66	17 ± 28	0.88	-9 ± 11
SEAsia	0.78	-3 ± 18	0.62	-3 ± 7
SAsia	0.68	12 ± 21	0.80	-1 ± 6
Tropics+Subtropics	0.70	9 ± 18	0.75	-6 ± 10

and SOFRID spatiotemporal variabilities. For all the transects except over SEASia, SOFRID overestimates O₃ UT concentrations.

Figure 4.1 displays IAGOS and SOFRID UT O₃ averaged over the 2008–2019 period. SOFRID-O₃ v3.5 retrieval uses a dynamical a priori profile, which takes the pixel location, time, and tropopause height into account (Barret et al., 2020), (Sect. Section 3.2). The stripes along the 10° latitude bands are due to the use of a dynamical a priori profile and indicate a discontinuity between two adjacent latitude bands with different a priori profiles. Nevertheless, the stripes are a minor issue as the use of a dynamical a priori profile largely improves the retrieved O₃ profiles in terms of variability and correlation coefficients in most latitude bands, relative to the previous version which uses a climatological a priori profile (Barret et al., 2020).

SOFRID-O₃ qualitatively captures the transition from low tropical UT O₃ to high extratropical UTLS O₃ in good agreement with IAGOS observations where available. The ability of SOFRID to detect this O₃ gradient was already highlighted by Barret et al. (2016) concerning the low O₃ concentrations in the Asian Monsoon Anticyclone (AMA). Furthermore, SOFRID-O₃ (Fig. 4.1e, 4.1g and 4.1h) clearly captures the tropical O₃ wave-one pattern (Thompson et al., 2003b; Sauvage et al., 2006) with maxima (resp. minima) concentration over the Southern Atlantic (resp. Western Pacific) with the largest concentrations in October over the Southern Atlantic. This is in agreement with the sparse IAGOS data recorded close to the coast of Brazil and southern Africa in October (Fig. 4.1d).

The ability of SOFRID to detect the transition from low to high O₃ from the tropics to the mid-latitudes is clear on the different latitudinal transects displayed in Fig. 4.2. For the

transects extending to 30° N or more (NAtlantic, Atlantic, SAsia, and Africa), the transition between low UT tropical and high extra tropical UTLS O_3 is coincidentally detected by IAGOS and SOFRID resulting in high correlation coefficients. It is noteworthy that the SOFRID O_3 -increases between 20 and 25° N are stronger than IAGOS ones resulting in a bias increasing northward (up to approximately 30° N). This can be explained by the differences between the two observing systems. IAGOS is a straightforward *in situ* observation at a precise altitude. SOFRID retrievals provide one piece of information in the broad UTLS region (see Barret et al., 2016 and 2020). This means that in the tropics, with a high altitude tropopause, SOFRID UTLS retrieval corresponds to UT tropical air masses and low O_3 . In the extratropics where the tropopause altitude sharply decreases with latitude, SOFRID smoothes the O_3 profiles between the LS with high concentrations and the UT with low concentrations causing an increasing positive bias with IAGOS (up to 80 % over Africa). Similarly, in July the tropopause altitude is the highest over SAsia, and the O_3 precursors trapped in the AMA lead to high O_3 production. The maximum altitude seems too high to be seen by IAGOS, contrary to SOFRID. The same reason may be responsible for the underestimation of low (below 50 ppb) UT tropical O_3 by SOFRID (see in particular NAtlantic in January and April, Atlantic and SAsia in April, and SEAsia all year long). SOFRID UT O_3 is sensitive to O_3 up to the top of the Tropical Tropopause Layer with O_3 concentrations lower than at the IAGOS cruise altitude. Interestingly, in some cases (see NAtlantic in July, SAsia all months except July), the northward increase of the bias up to 25° N is followed by a decrease beyond 30° N. This might be related to the use of a different a priori profile in the latitude band above 30° N (Fig. 4.1). Consequently, it highlights the improvement of the retrieval by taking into account a tropopause-related a priori profile.

Concerning Africa (Fig. 4.2iii) an anomalous negative bias is found for each month around 20° N. We suspect that this bias is related to retrieval problems in the presence of desert ground with sand emissivity interfering with the O_3 signature (Boynard et al., 2018). In the Saharan region, the number of good pixels is lower than in the remaining part of the African transect (the average number of pixels is approximately 2 % of the average in the rest latitudinal bins) and the SOFRID data are less trustworthy.

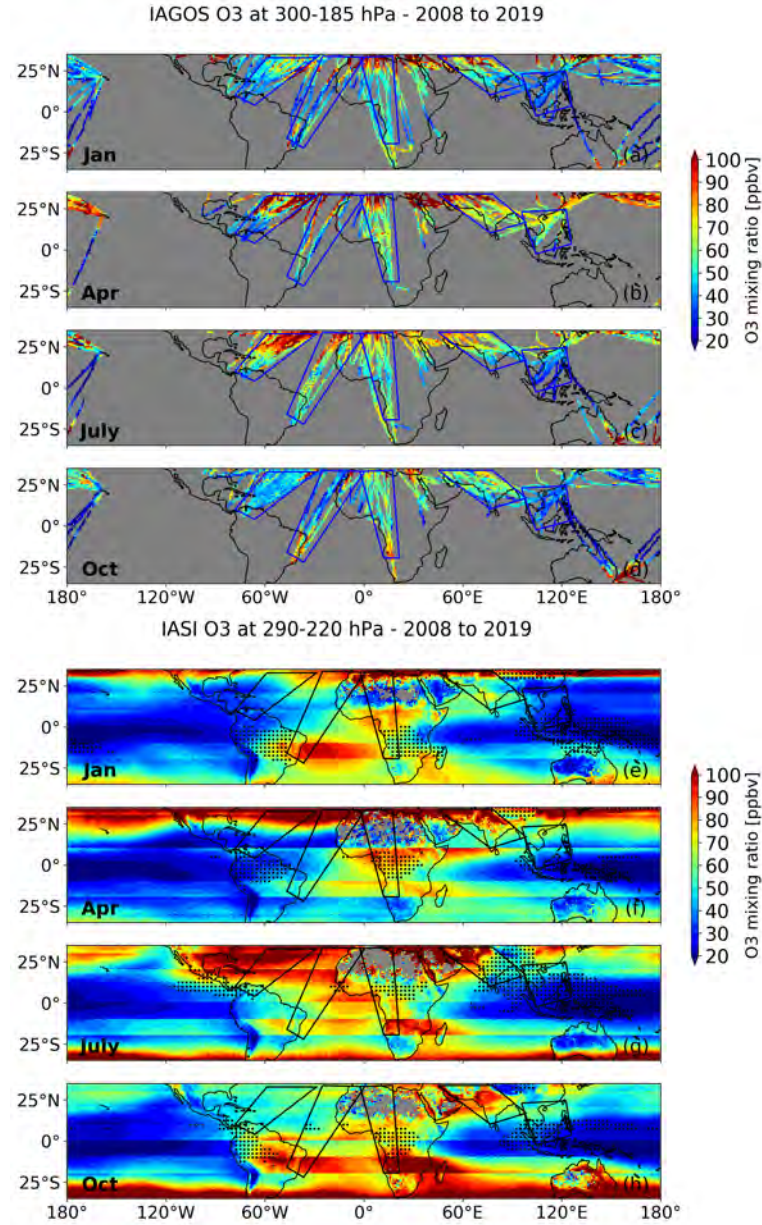


Figure 4.1: IAGOS (at 300–185 hPa) (a–d) and IASI-SOFRID (at 290–220 hPa) (e–h) UT O₃ mixing ratios averaged from 2008 to 2019 on a 1x1 grid. The boxes indicate the regions with the highest IAGOS coverage and are used for the computation of the meridional O₃ and CO transects. The hatched part in the SOFRID map shows points where outgoing longwave radiation is lower than 220 W m^{-2} .

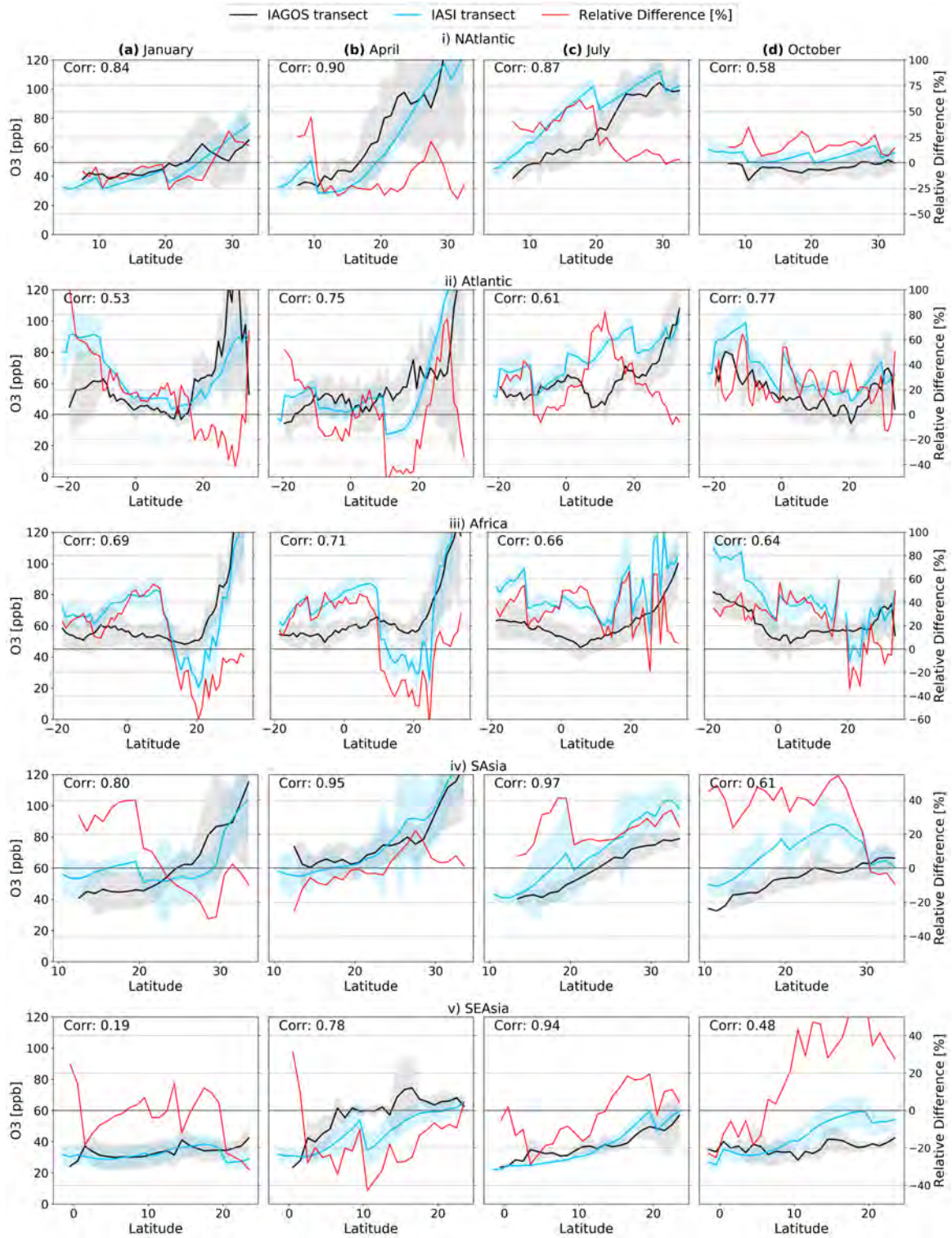


Figure 4.2: IAGOS (between 300–185 hPa) and IASI-SOFRID (between 290–220 hPa) monthly meridional transects of O_3 over i) NATlantic, ii) Atlantic, iii) Africa iv) SAsia and v) SEAsia transects (The definition of the transects is given in Figs. 4.1 and 4.3). The shadowed part shows a range of \pm one standard deviation. The red line (and the right axis) represents the relative difference between SOFRID and IAGOS in %.

Table 4.2: Mean statistics of the comparison between IAGOS and IASI-SOFRID monthly O₃ and CO meridional UT transects. The correlation coefficient and the mean bias (in %) are given.

	NAtlantic		Atlantic		Africa		SEAsia		SAsia	
O ₃	R	Bias	R	Bias	R	Bias	R	Bias	R	Bias
January	0.84	-5	0.53	16	0.69	10	0.19	-3	0.80	7
April	0.90	-13	0.75	0	0.71	11	0.78	-17	0.95	0
July	0.87	26	0.61	26	0.66	35	0.94	-3	0.97	24
October	0.58	17	0.77	25	0.64	25	0.48	20	0.61	33
CO	R	Bias	R	Bias	R	Bias	R	Bias	R	Bias
January	0.50	2.5	0.88	2	0.94	-6	-0.07	2	0.96	4
April	0.86	-6	0.59	0.5	0.95	-10	0.84	-2	0.73	3
July	0.91	3	0.81	1	0.96	-6	0.92	-1	0.96	0
October	0.97	1	0.84	-6	0.94	-4	0.20	-15	0.92	-1

Comparisons between SOFRID-CO and IAGOS show an overall good agreement, with a high average correlation coefficient of 0.75 and a mean negative bias of 6 ± 10 % (Table 4.1). All transects display high correlation coefficients (0.75–0.90) except SEAsia one, and negative biases from 0 up to 9 %. Over Africa, the seasonal CO maxima shifting from the South during boreal summer to the north during boreal winter are clearly detected by SOFRID coincidentally with IAGOS as can be seen on the maps from Fig. 4.3 and more clearly on the latitudinal transects from Fig. 4.4. Significant correlations coefficients (≥ 0.94 , Table 4.2) highlight the consistency of the two datasets and their in-phase variability. The African maxima are underestimated by up to 20 ppb (20 %) by SOFRID.

Over the Atlantic, the CO latitudinal variability is also well captured by SOFRID relative to IAGOS with in particular a persistent weak maximum corresponding to the Transatlantic transport of African (January–April) and South American (July) BB around the Equator (Figs. 4.3 a to c, 4.3 e to g, and 4.4 panels iia to iic). In October the maximum from both SOFRID and IAGOS has shifted towards 10° S and the coast of Brazil (Fig. 4.3d) due to the intense BB activity in northern Brazil and the transport of AN emissions from Boreal Africa towards the equator. Over the Atlantic, the SOFRID bias remains within the (-30; 30) % range with a 2 % average (see Table 4.2) except for the October Brazilian maximum.

Over Africa and the Atlantic, the most significant underestimation of SOFRID-CO occurs around the latitudinal maxima. This discrepancy can be attributed to the different nature of the observing systems. To retrieve CO, the true profile is presented on a (satellite)

pressure grid with coarse vertical resolution. Thus, some characteristics of the true profile are smoothed in the retrieved one (Rodgers, 2000). SOFRID-CO in the UT is a weighted mean over a 6-km layer, where the maxima are smoothed due to lower CO levels included in this broad layer.

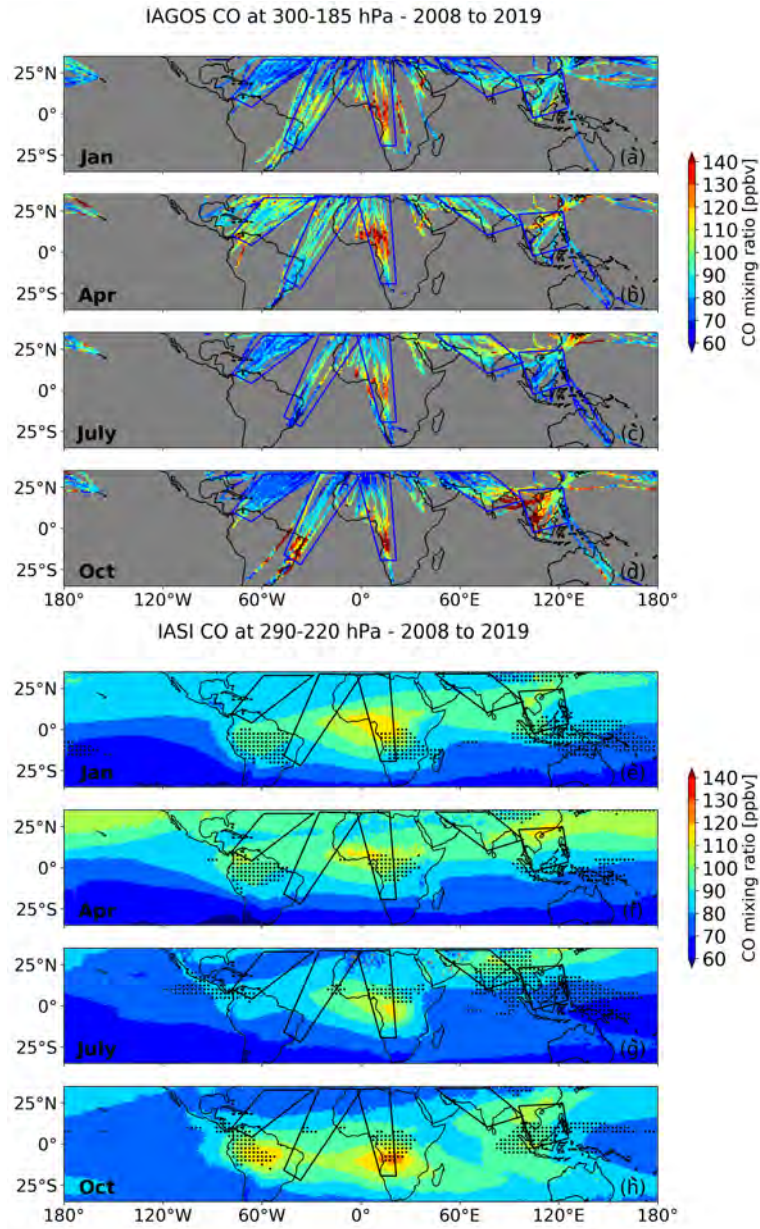


Figure 4.3: Same as Fig. 4.1 for CO.

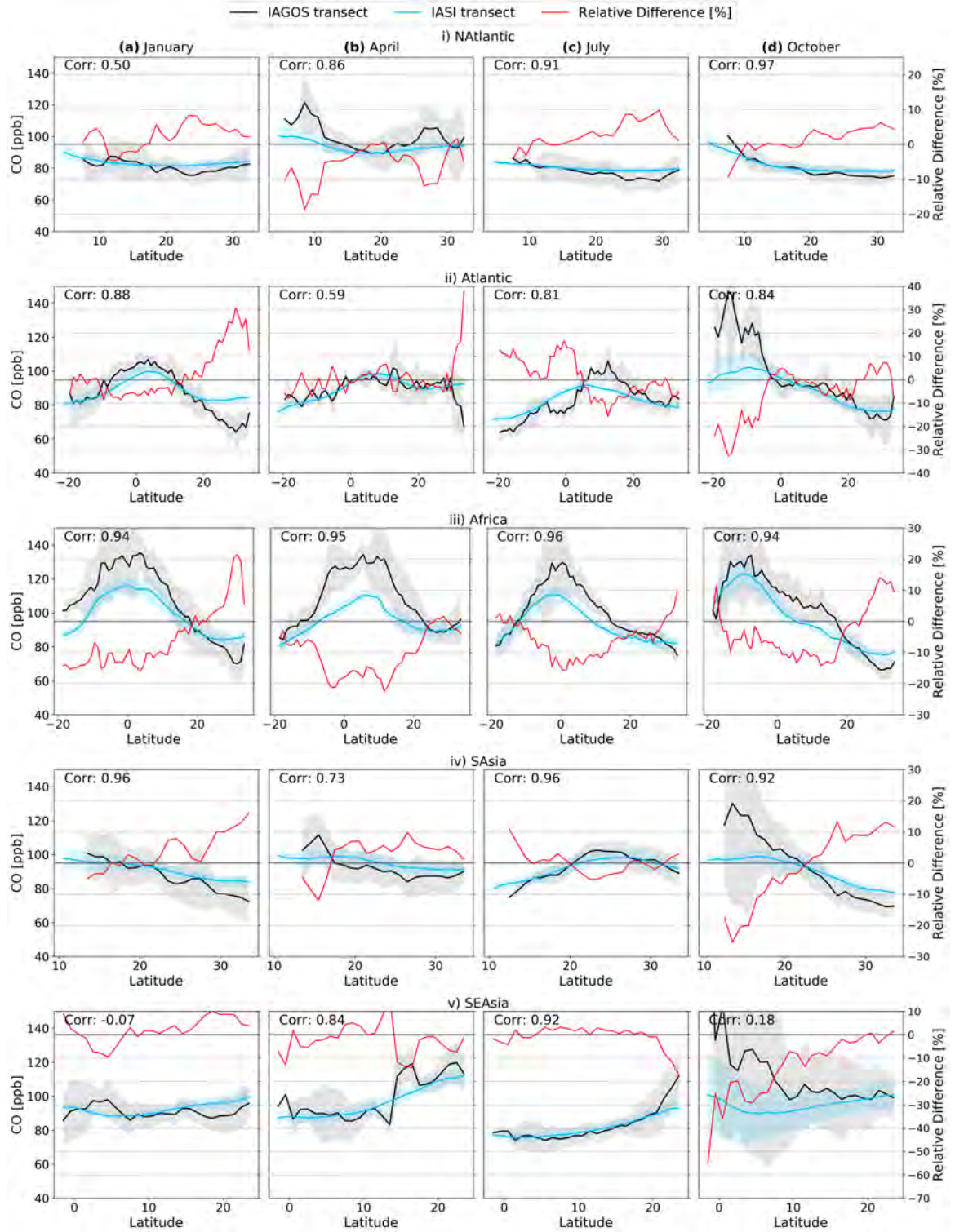


Figure 4.4: Same as Fig. 4.2 for CO.

Concerning Asia, SOFRID and IAGOS both document the springtime CO maximum over East Asia and its export over the Pacific (Fig. 4.3b and 4.3f). The largest CO concentrations (130–140 ppb) from South China to Indonesia are observed by IAGOS in October (Fig. 4.3d).

This seasonal maximum is also captured by SOFRID but with a weaker amplitude (100–110 ppb) (Fig. 4.3h).

Over SAsia, the SOFRID and IAGOS transects are in very good agreement (Fig. 4.4iv) with correlation coefficients between 0.73 and 0.96 and mean biases within the (-20; 35) % range (2 % on average see Table 4.2) except in October south of 20° N. For SEAsia, the agreement is a bit lower with larger biases (5 % on average) and some months with low correlation coefficients (-0.07 in January and 0.20 in October).

To investigate further the largest discrepancies in October, motivated by the high interannual variability of IAGOS, we compared IAGOS and SOFRID on an annual basis. The agreement between SOFRID and IAGOS is good for all the available years, except for 2015 when IAGOS detects CO mixing ratios up to 250 ppb (Fig. not shown). This maximum is attributed to severe fire activities over South East Asia, amplified by dry conditions induced by 2015–2016 El Niño (Ravindrababu et al., 2019) – the largest since 1997/1998 (Huijnen et al., 2016). SOFRID is capable of capturing the positive southward zonal CO gradient in 2015 (especially over SEAsia where CO increases from 100 to 150 ppb). Excluding the 2015–flights with CO outliers from the climatology, results in overall higher correlation coefficients (0.99 (resp. 0.60)) and significantly smaller negative biases (less than 2.5 % over SAsia (resp. SEAsia)). Thus, the detection of lower CO levels by SOFRID is likely related to the proximity of the IAGOS aircraft to intense fire events.

To summarise, the comparison between IAGOS and SOFRID showed that the performance of the latter is improved for low levels of CO, whereas high levels are often biased low (African and Brazilian seasonal maximum).

High O₃ levels towards the extratropics are overestimated, while low levels (below 50 ppb) are underestimated. These discrepancies are mainly due to differences in the nature of the observing systems. The smoothing of the O₃ and CO profile due to the coarser resolution of the satellite explained part of the discrepancies. Another difference between the systems is that IAGOS sees the lower part of the UT in the tropics and subtropics, while IASI is more sensitive to the UTLS in the extratropics, and the TTL in the tropics. However, overall IAGOS and SOFRID meridional transects and maps are fairly consistent in the qualitative representation of O₃ and CO patterns in the tropical UT. SOFRID captures well the seasonal variability of O₃ and CO in the tropical UT, and the minima and maxima are well collocated relative to IAGOS. Thus, SOFRID data are useful to complement IAGOS observations and give an insight into the spatial extent of pollution plumes, as well as intercontinental transport patterns.

4.2 Validation of tropospheric O₃ change

In principle, the trend detection of an atmospheric tracer is based on a regression model accounting for the sources of its variability. In the case of O₃ (e.g. Chang et al., 2021), the time series is decomposed into several components according to the equation below:

$$\text{observations} = \text{seasonal cycle} + \text{trend} + \text{covariates} + \text{residual error} \quad (4.1)$$

The first three terms refer to the seasonal pattern of O₃, the long-term change, and some external variability, such as ENSO, which impact O₃ variability. The residual error refers to the model error and/or the remaining unexplained variability of the observations. The quantification of the attribution of O₃ variability to these factors is measured by regression coefficients.

Several regression methods have been developed for the analysis of time series and trends of trace gases. The selection of the appropriate technique is critical for robust trend computations (Chang et al., 2021). Concerning datasets with continuous measurements (e.g. satellites with daily global coverage such as IASI), the appropriate method for the O₃ trends detection (as well as the other regression coefficients) is based on least squares linear regression (e.g. Gaudel et al., 2018; Ziemke et al., 2019; Wespes et al., 2017). On the other hand, the quantile regression method, predicts trends for a distribution by taking into consideration the quantiles of the distribution instead of the condition means. An advantage of this method is that it can tolerate missing values and outliers. As a result, this method is appropriate for trend detection from sparse datasets in time and space such as IAGOS (e.g. Gaudel et al., 2020; Wang et al., 2022) and ozonesondes (e.g. Christiansen et al., 2022).

As IASI provides continuous measurements, while IAGOS provides measurements with some gaps in space and time, the trend detection should be based on the method which is the most appropriate for each case. The comparison of the trends computed by different methods is rather complicated, as questions would continue to arise, such as how much of the difference in the trends is due to the differences in the statistical method used. To deal with this problem, we decided to follow a simple but straightforward method to evaluate the O₃ change in the troposphere. The O₃ change is defined as the difference in the tropospheric O₃ column between a reference and a modern period. This evaluation study aims to investigate the ability of IASI to capture the O₃ change in the tropospheric column, as its vertical resolution (vertical resolution of approximately 6km; Barret et al., 2016) is limited compared to in situ observations like IAGOS (vertical resolution of 30 m for O₃ Thouret et al., 1998).

For this study, the tropospheric column is defined in the 1000–200 hPa pressure range. The upper limit of 200 hPa is applied because the high tropopause altitude characterising the tropics (at about 150–50 hPa (about 12–18 km); Gettelman et al., 2002) is higher than the IAGOS cruise altitude (at about 300–185 hPa (9–12 km); see Section 3.1), and thus IAGOS cannot sample the tropospheric column up to the tropopause, like IASI. As mentioned in Section 5.2.2.4, IASI measurements are available on a global scale with an almost daily revisit since 2008. IAGOS O₃ measurements are available for the period 1994–2019, but they depend on the flight schedule of the aircraft. For this reason, IAGOS data are available for different time ranges depending on the site. Thus, the reference and modern periods for

our computations are adjusted to the availability of IAGOS measurements and might vary among the sites.

Figures 4.5 and 4.6 shows the number of flights per month over Windhoek and South China sites, respectively. In the first case (Figure 4.5), the reference period is 2008–2009, while the modern period is 2011–2012. In the second case (Figure 4.6), when the time span of the available data is rather limited, the reference period corresponds to the year 2011, while the modern period to the year 2016.

For all the cases, to assess the statistical significance of the change between the reference and the modern period, we provide the 90% confidence intervals of the difference between the two means, using Welch t-test against the null hypothesis of no change between the two periods. We apply Welch’s t-test, as it is suitable for distribution with unequal sample sizes (Welch, 1947).

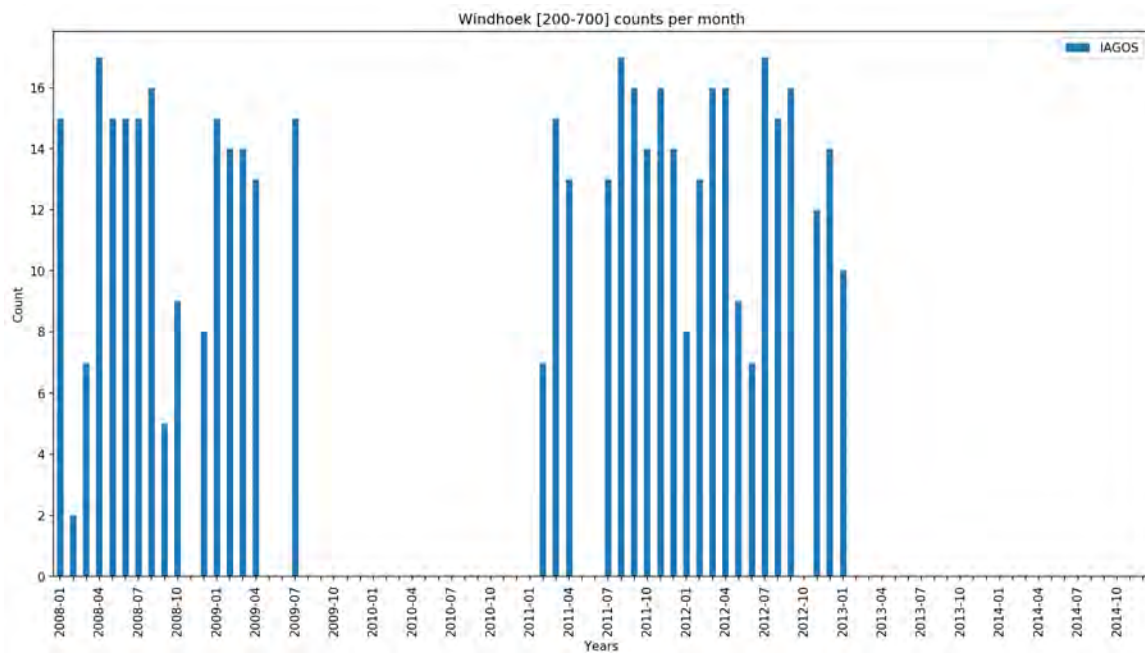


Figure 4.5: Number of IAGOS flights per month over Windhoek.

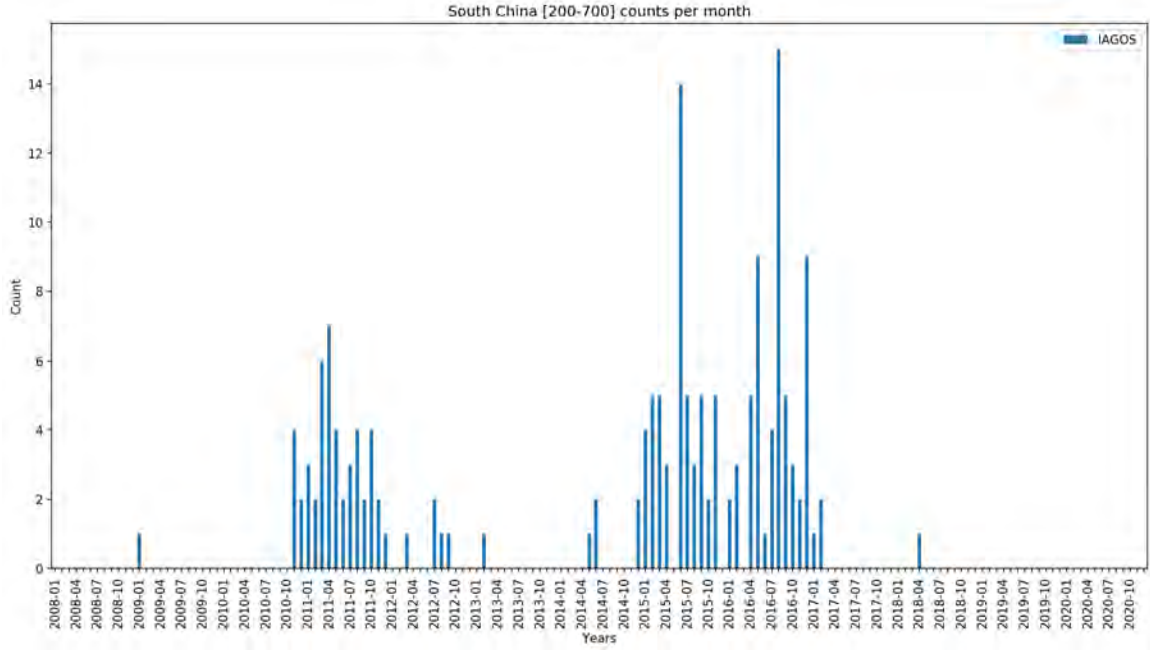
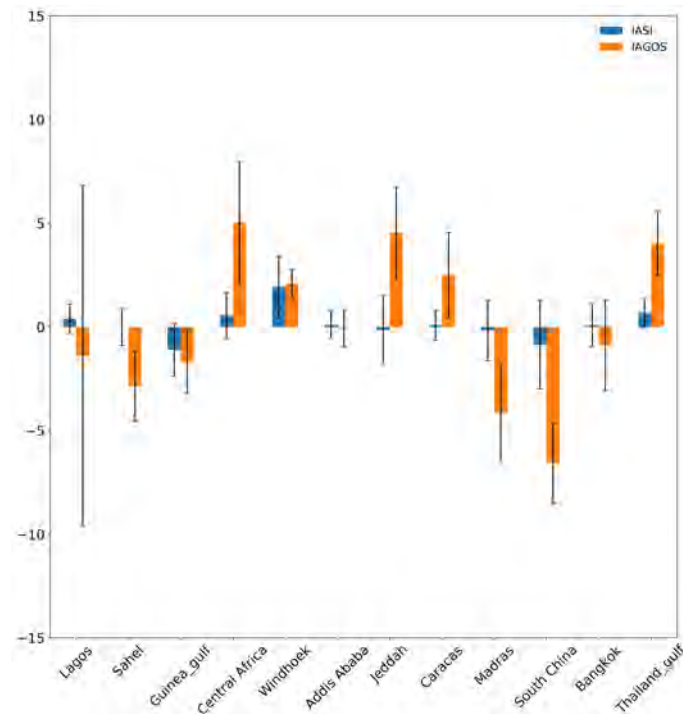


Figure 4.6: Number of IAGOS flights per month over South China.

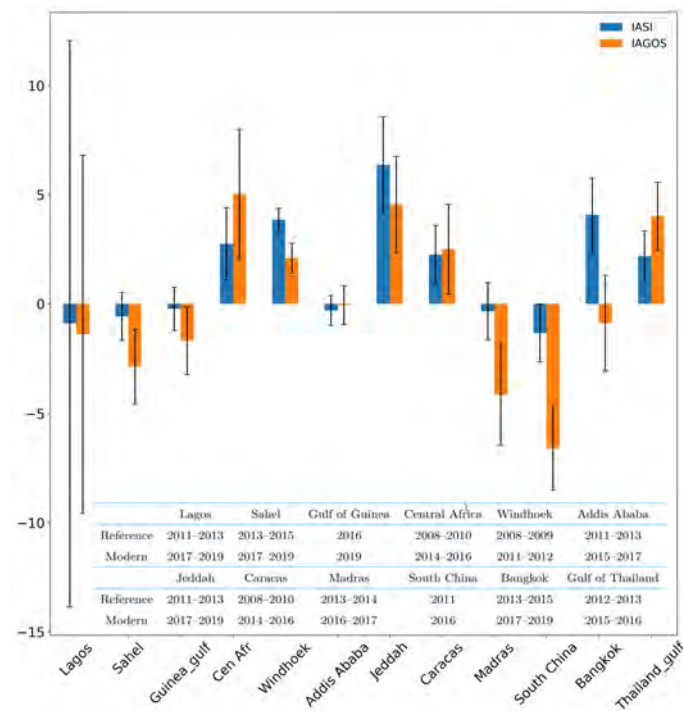
This limitation of IAGOS data should be taken into account in the interpretation of the results. Due to the different definitions of modern and reference periods for each site, it is not possible to assess the O₃ change in the tropics as a whole. However, this method is beneficial for the objectives of the evaluation study, as it can offer insight into the impact of the sensitivity of IASI on the observed O₃ change.

Impact of Sampling

Figure 4.7 displays the tropospheric column O₃ change in Dobson units (DU) for IAGOS and IASI. For the IASI computations in panel a, we account for all the monthly measurements (IASI-monthly), while in panel b we account only for the days when IAGOS data are available (IASI-daily). For both panels, IAGOS computations are based on the daily measurements, when available. The Table included in panel b shows the time range of the periods accounted for each site. For clarity reasons, the results of Figure 4.7 are also summarised in Table 4.3.

O₃ change (DU)

(a) IASI-monthly, and IAGOS data



(b) IASI-daily and IAGOS data

Figure 4.7: Tropospheric column (1000–200 hPa) O₃ change in DU based on IAGOS (orange bars) daily measurements and IASI (blue bars): (a) monthly and (b) daily measurements when IAGOS data are available. The error bars correspond to the 90 % confidence intervals of the change. The Table in panel (b) shows the reference and modern periods taken into account for each site.

Table 4.3: IAGOS, IASI-monthly and IASI-daily tropospheric (1000–200 hPa) O₃ change (in DU) between the reference and the modern period. The mean indicates the mean O₃ change between the two periods. Numbers in bold correspond to statistically significant O₃ changes. The CI stands for the 90 % confidence interval of the change. The insignificant changes with respect to the 90 % confidence intervals are indicated as NS.

Site	IAGOS		IASI-monthly		IASI-daily		Periods	
	mean	CI	mean	CI	mean	CI	Reference	Modern
Lagos	-1.5	NS	0.4	NS	-1	NS	2011–2013	2017–2019
Sahel	-3	[-4.5; -1]	0	NS	-0.5	NS	2013–2015	2017–2019
Guinea G.	-1.5	[-3; -0.14]	-1	NS	-0.2	NS	2016	2019
Cen. Africa	5	[2; 8]	0.5	NS	3	[1; 4.5]	2008–2010	2014–2016
Windhoek	2	[1.5; 3]	2	[1.5; 3]	4	[3; 4.5]	2008–2009	2011–2012
Addis Ababa	0	NS	0	NS	0	NS	2011–2013	2015–2017
Jeddah	4.5	[2.5; 6.5]	0	NS	6	[4; 8.5]	2011–2013	2017–2019
Caracas	2.5	[0.5; 4.5]	0	NS	2.5	[1; 3.5]	2008–2010	2014–2016
Madras	-4	[-6.5; -2]	0	NS	-0.5	NS	2013–2014	2016–2017
South China	-6.5	[-8.5; -4.5]	-1	NS	-1.5	[-2.5; -0.01]	2011	2016
Bangkok	-1	NS	0	NS	4	[2.5; 6]	2013–2015	2017–2019
Thailand G.	4	[2.5; 5.5]	0.5	NS	2	[1; 3.5]	2012–2013	2015–2016

Based on the IASI-monthly data (Figure 4.7 a and Table 4.3 IASI-monthly), the O₃ changes over the tropospheric column are nonsignificant for all the sites, except Windhoek where a positive change is observed (mean change of approximately 2 DU). The mean of the majority of the nonsignificant changes tends to be zero (Sahel, Addis Ababa, Caracas, Madras, and Bangkok), with fewer positive (over Lagos, Central Africa, and the Gulf of Thailand with mean change ranging between 0.4 and 0.5 DU) and negative (over the Gulf of Guinea and South China with a mean change of approximately -1 DU) changes. In contrast to IASI-monthly, according to IAGOS data, the majority of the sites show significant O₃ changes (Figure 4.7 a and Table 4.3 IAGOS). The positive mean changes (Central Africa, Windhoek, Jeddah, Caracas, and the Gulf of Thailand) are in the range between 2 and 5 DU, while the negative mean changes (Sahel, Gulf of Guinea, Madras and South China) range between -6.5 and -1.5 DU.

The comparisons of the O₃ change between IASI-monthly and IAGOS show important differences for the majority of the sites (except Windhoek). However, we should keep in mind that IAGOS data are sparse in time relative to the IASI measurements which are provided on a daily frequency. To have a fair comparison between IAGOS and IASI, we should account for the days when IAGOS measurements are available for both datasets. For instance, the only good agreement between IASI-monthly and IAGOS is observed over Windhoek, where

the frequency of IAGOS measurements is the highest over the tropical sites. To assess the impact of the sampling issues, we continue with comparing the O_3 change based only on the days where IAGOS provides measurements (Figure 4.7 b and Table 4.3 IASI-daily).

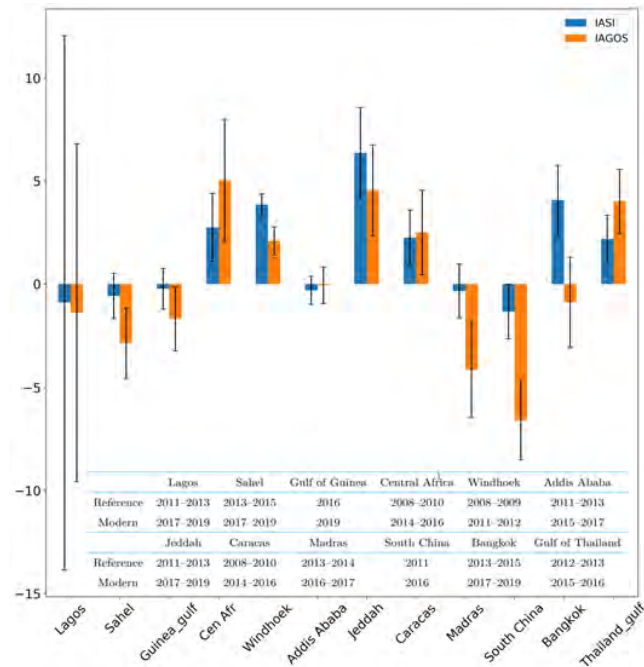
When the IASI-daily data are taken into account seven sites show statistically significant O_3 changes (Central Africa, Windhoek, Jeddah, Caracas, South China, Bangkok, and the Gulf of Thailand). In all these sites, except South China, the O_3 change is positive, in the range between 2 and 6 DU. For all these cases (except for Bangkok), there is a good agreement (in sign and magnitude) between IASI-daily changes and IAGOS. The agreement between IAGOS and IASI is improved when the comparison is focused on the specific days when IAGOS data are available (except for Bangkok).

Improvement in the agreement is observed over Lagos, Sahel, and Madras, even though the IASI change is nonsignificant both for IASI-daily and IASI-monthly data. Nevertheless, the mean O_3 change is positive based on IASI-monthly over Lagos and negative based on IASI-daily measurements, in agreement with the negative mean IAGOS change. For the other two cases, the almost zero change becomes negative, as observed by IAGOS. The agreement between IAGOS and IASI-daily is rather poor over Bangkok where IAGOS captures a (nonsignificant) negative change, while IASI exhibits a (significant) positive change. Further discussion about this discrepancy will follow later.

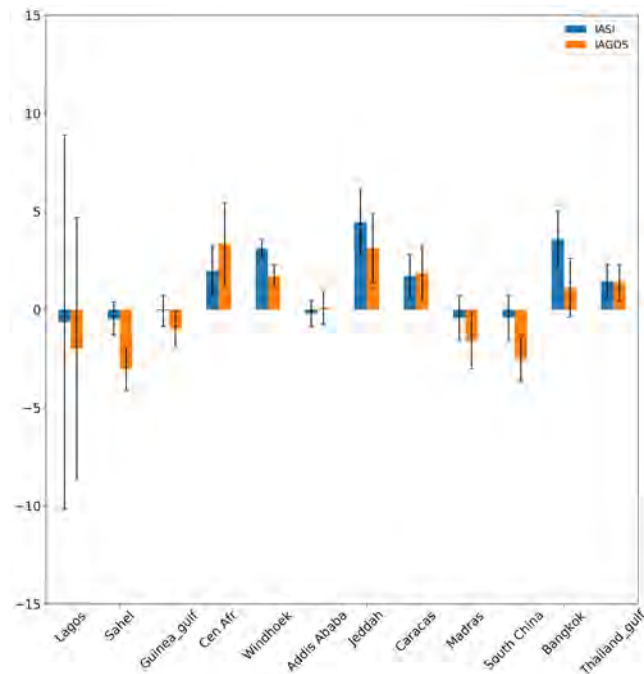
The comparison between IASI-monthly and IASI-daily and/or IAGOS changes shows that the O_3 change is sensitive to the sampling. This identifies a limitation in computing O_3 changes (or trends) based on IAGOS because its limited sampling in the tropics (relative to Europe and North America) can affect the sign and the significance of the observed O_3 change.

Impact of vertical sensitivity

Figure 4.8 displays: (a) the tropospheric column O_3 change, and (b) the partial column O_3 change (in DU) for IAGOS and IASI-daily. We validate IASI relative to IAGOS in the partial column between 700–200 hPa, where the IASI retrievals are the most sensitive to O_3 (Dufour et al., 2012). For clarity reasons, the numbers displayed in Figure 4.8 (means and confidence intervals of the O_3 change) are also provided in Table 4.4. Note that the results referring to the tropospheric O_3 changes based on IASI-daily and IAGOS data (Figure 4.8a and Table 4.4) are the same as in the previous section (Figure 4.7a and Table 4.3). We present them again to make the comparison between the two tropospheric columns more clear.

O₃ change (DU)

(a) Tropospheric column (1000–200 hPa)



(b) Partial column (700–200 hPa)

Figure 4.8: (a) Tropospheric column (1000–200 hPa) and (b) partial column (700–200 hPa) O₃ change in DU based on IAGOS (orange bars) and IASI (blue bars) daily measurements. The error bars correspond to the 90 % confidence intervals. The Table in panel (a) shows the reference and modern periods taken into account for each site.

As discussed before, based on IAGOS data, we observe statistically significant tropospheric O₃ changes for the majority of the sites (Figure 4.8a and Table 4.4). Focusing on the partial column (Figure 4.8b and Table 4.4), the statistically significant changes remain, however, their magnitude is smaller than over the tropospheric column. The positive changes range between 1.5 and 3 DU, while the negative ones are between -3 and -1 DU.

Table 4.4: O₃ change (in DU) based on IAGOS and IASI daily measurements (these results are also displayed in Figure 4.8). From left to right, tropospheric column (1000–200 hPa) and partial tropospheric column (700–200 hPa) O₃ change between the reference and the modern periods. The mean indicates the mean O₃ change between the two periods. Numbers in bold correspond to statistically significant O₃ changes. The CI stands for the 90 % confidence interval of the change. The insignificant changes with respect to the 90 % confidence intervals are indicated as NS.

Site	Tropospheric column				Partial column				Periods	
	IAGOS		IASI-daily		IAGOS		IASI-daily		Reference	Modern
	mean	CI	mean	CI	mean	CI	mean	CI		
Lagos	-1.5	NS	-1	NS	-2	NS	-0.5	NS	2011–2013	2017–2019
Sahel	-3	[-4.5; -1]	-0.5	NS	-3	[-4; -2]	-0.5	NS	2013–2015	2017–2019
Guinea G.	-1.5	[-3; -0.14]	-0.2	NS	-1	[-2; 0]	0	NS	2016	2019
Cen. Africa	5	[2; 8]	3	[1; 4.5]	3	[1; 5.5]	2	[1; 3]	2008–2010	2014–2016
Windhoek	2	[1.5; 3]	4	[3; 4.5]	1.5	[1; 2]	3	[2.5; 3.5]	2008–2009	2011–2012
Addis Ababa	0	NS	0	NS	0	NS	0	NS	2011–2013	2015–2017
Jeddah	4.5	[2.5; 6.5]	6	[4; 8.5]	3	[1.5; 5]	4.5	[3; 6]	2011–2013	2017–2019
Caracas	2.5	[0.5; 4.5]	2.5	[1; 3.5]	2	[0.5; 3]	2	[0.5; 3]	2008–2010	2014–2016
Madras	-4	[-6.5; -2]	-0.5	NS	-1.5	[-3; -0.1]	-0.5	NS	2013–2014	2016–2017
South China	-6.5	[-8.5; -4.5]	-1.5	[-2.5; -0.01]	-2.5	[-3.5; -1.5]	-0.5	NS	2011	2016
Bangkok	-1	NS	4	[2.5; 6]	1	NS	3.5	[2; 5]	2013–2015	2017–2019
Thailand G.	4	[2.5; 5.5]	2	[1; 3.5]	1.5	[0.5; 2]	1.5	[0.5; 2]	2012–2013	2015–2016

The largest differences between partial and tropospheric column O₃ change based on IAGOS are found over Madras, South China, Gulf of Thailand (approximately 60 % absolute difference of the O₃ change over the partial and the tropospheric column) and Central Africa (difference of 40 %) (Table 4.4). Differences between tropospheric and partial column O₃ change are also observed by IASI, but their magnitude is much smaller than for IAGOS. For instance, over Central Africa and South China, the O₃ change over the partial column is 30 % smaller than over the tropospheric one. The difference between the columns is even smaller over the Gulf of Thailand (by 25 %). Over Madras, the IASI O₃ change is similar for the two columns.

Figure 4.9 displays the IAGOS vertical profiles of O₃ averaged during the reference and the modern periods for the available sites. The vertical distribution of O₃ in the pressure range between 1000 and 200 hPa can help identify the tropospheric layer that drives the O₃ change for IAGOS. It is clear from Figure 4.9, that the largest change of O₃ over Madras, South

China, the Gulf of Thailand, and Central Africa occur in the lower parts of the troposphere, below 700 hPa. This explains the large differences in IAGOS O₃ change over the tropospheric column and the partial column for the aforementioned sites. On the other hand, IASI O₃ changes over the tropospheric column show minor changes relative to IAGOS when focusing on the partial column over these sites. This indicates that the IASI tropospheric O₃ change is mostly representative of the O₃ change over the partial column where the IASI retrievals are the most sensitive to O₃ (Dufour et al., 2012).

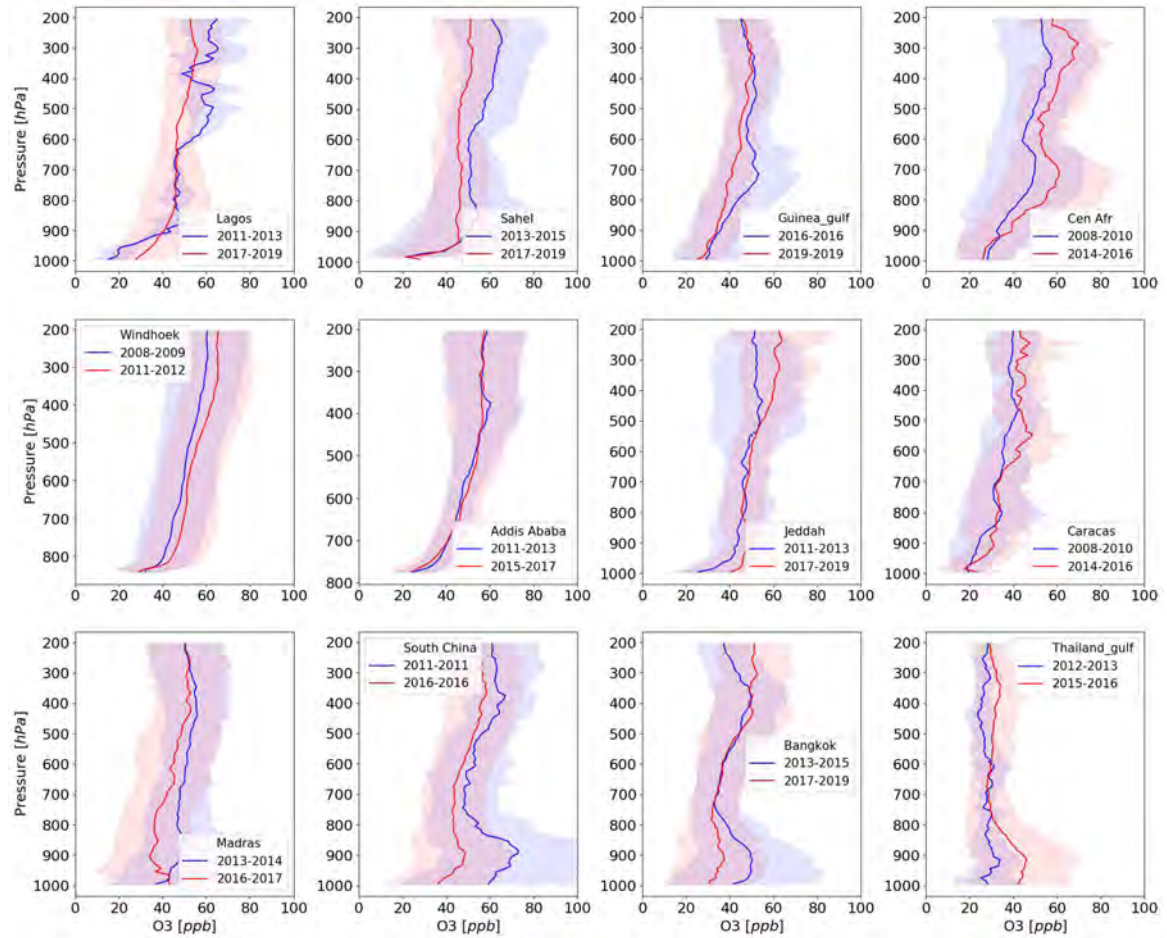


Figure 4.9: IAGOS O₃ vertical distributions (in ppb) averaged for the reference period (blue line) and the modern period (red line). The shadowed part corresponds to ± 1 standard deviation. The time span of the two periods is annotated in the legend.

The comparisons over these four sites (Gulf of Guinea, Madras, South China, and the Gulf of Thailand) show that IASI compares better to IAGOS when the 700–200 hPa is used because of low sensitivity close to the ground. Also, the smaller confidence intervals of the IASI O₃ change over the partial column than the ones over the tropospheric column indicate that the uncertainties of the O₃ change are smaller for the former.

As we mentioned earlier, the poorest agreement between IAGOS and IASI O₃ change in the

tropospheric column is observed over Bangkok, where IAGOS captures a (nonsignificant) negative change (-1 DU), while IASI captures a (significant) positive change (4 DU). According to [Figure 4.9](#), the largest decrease of O_3 between the reference and the modern period is observed below 700 hPa, while the largest increase of O_3 is observed above 400 hPa. Thus, the tropospheric O_3 decrease captured by IAGOS is driven by the decrease in the lower part of the troposphere. This is confirmed by comparing the IAGOS O_3 change over the tropospheric column with the one over the partial column. The absolute difference in O_3 change between the two columns is 200 % ([Table 4.4](#)). In contrast, the comparison of the IASI O_3 change between the two columns shows a minor change of 12 % ([Table 4.4](#)). This indicates that the tropospheric O_3 increase captured by IASI is driven by the increase above 400 hPa. The agreement between IAGOS and IASI is the best for the partial column ([Table 4.4](#)), where both IAGOS and IASI capture a positive O_3 change over Bangkok.

Overall, using IAGOS in situ profiles, we have clearly demonstrated that, as expected from information content analysis (see Barret et al., 2011; 2020; Dufour et al., [2012](#)), IASI documents O_3 changes in the tropics better between 700 and 200 hPa where its sensitivity is high. Focusing on the partial column, IASI captures well the FT O_3 changes mostly seen over the Asian sites (Madras, South China, Bangkok, and the Gulf of Thailand) and the South African sites (Windhoek and Central Africa). Heue et al. ([2016](#)) suggested that the O_3 increase over Central and South Africa is driven by an increase in biomass burning. Thus, IASI is capable of capturing the O_3 changes due to fires, as their injection height reaches the sensitive layer of IASI.

4.3 Free tropospheric O_3 change as seen by IASI

[Figure 4.10](#) displays the O_3 change between 700 and 200 hPa. Based on our evaluation study, this is the column where the confidence in the O_3 change provided by IASI is the highest. The reference and modern periods are defined as the 3-year periods at the beginning (2008–2010) and at the end (2018–2020) of the IASI period respectively, to get the maximum separation between the years. The 3-year average is selected to reduce the impact of the interannual variability on O_3 . We select IASI data between the 60°S to 60°N because the quality of the retrievals is better in this latitudinal band, relative to the polar regions where the sensitivity of the retrieval is lower. The measurements above Northern Africa are erroneous, due to retrieval problems in the presence of desert ground with sand emissivity interfering with the O_3 signature (Boynard et al., [2018](#)).

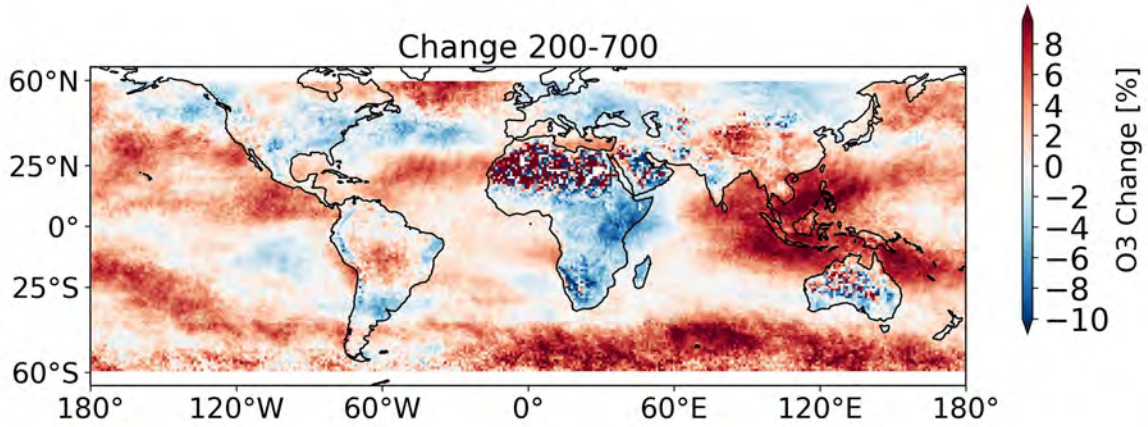


Figure 4.10: Partial column (700–200 hPa) O₃ change (in %) between the reference (2008–2010) and the modern period (2018–2020) based on SOFRID-O₃ retrievals.

The global mean partial column O₃ has increased by approximately 0.4 Dobson units (DU) (or by approx. 1.7 %) in 2018–2020 compared to the 2008–2010 level, with the greatest increase in the tropics (0.32 DU or 2 %) (Figure 4.10). The striking feature of Figure 4.10 is the highest increase of FT O₃ over SouthEast and South Asia (by approx. 10 %). The highest O₃ increase over these regions is also reported by satellite products (Gaudel et al., 2018; Ziemke et al., 2019), chemical transport models (Zhang et al. 2016; 2021; Wang et al., 2022), and IAGOS data in the FT from 1994–2004 to 2005–2014 (Zhang et al., 2016; Gaudel et al., 2018). It is worth noting that SouthEast Asia is the most extensive region in terms of positive trends in Gaudel et al. (2018), as it is the only region where at least five satellite products are in agreement.

According to Zhang et al. (2021), the O₃ increase over South and SouthEast Asia is attributed to increases in anthropogenic emissions of O₃ precursors since 1980. Similar emissions increases were reported over East Asia. However, O₃ increases over the latter are much smaller than over the tropical Asian regions (4 %, Figure 4.10). This highlights the higher efficiency in O₃ production in the tropics due to strong solar radiation, humidity, and NO_x sensitivity compared to mid-latitudes (Zhang et al. 2016; 2021). The relatively high O₃ change over the neighboring oceans indicates that the continental Asian pollutants and advective processes clearly influence the FT O₃ over the oceans. This was also noticed in Beig and Singh (2007), that computed tropospheric O₃ trends based on satellite (TOMS) and model (MOZART) data from 1979 to 2005. Previous studies (Liang et al., 2004; Cooper et al., 2010) showed the impact of trans-Pacific transport of polluted Asian air masses on FT O₃ over western North America. Asian pollution is exported to the Pacific via frontal lifting in warm conveyor belts or convection to the FT (e.g. Bey et al., 2001a; Liu et al., 2003; Lin et al., 2010). This is followed by westerly transport in the FT (Heald et al., 2003). This O₃ transport pathway explains the observed O₃ increase over the Pacific, as a result of the O₃ increase over tropical and East Asia (Figure 4.10).

Over South America, a moderate O_3 increase of 5 % is observed (Figure 4.10). The positive increase is in agreement with the satellite products in Gaudel et al. (2018). The main source of O_3 enhancement over South America is the local BB emissions (Section 5.2.3.2). The peak of the BB coincides with the beginning of the wet season when strong convection moves over the fires (Liu et al., 2010). As a result, O_3 and precursors are uplifted at higher altitudes where O_3 's lifetime is longer, and its accumulation is favoured. Although for a different period (1979–2005), Beig and Singh (2007) have also reported increasing O_3 trends over South America, attributed to BB. Recent studies (e.g. Andela et al., 2017) have found declining global burned area over the past decades, mostly driven by decreasing fires over savannas. In contrast, forest fire emissions are rising and have the potential to counter the negative fire trends in savannas (Zheng et al., 2021). As discussed by Zheng et al. (2021), the intensity of fire emissions over South America decreased from 2005 to 2013, followed by an increase through 2019. The decrease in 2005–2013 resulted from the slowing of Amazonian deforestation due to the application of strict policies (Nepstad et al., 2014). Deforestation has accelerated since then due to the rollback of the policies. In addition, the increase in fire incidences during drought years also contributes to the variability of the fire emissions from Amazonian forests (e.g. Aragão et al., 2018).

Over Africa, we observe a moderate O_3 decrease of 4 % on average. The largest decline is observed over the strong fires regions of SH Africa, while a small positive change of up to 2 % is observed over the West African coast (Figure 4.10). However, some studies contradict our results. Ziemke et al. (2019) show weak positive O_3 change over Africa over the tropospheric column for the period 2005–2016. Using a merged O_3 dataset from multiple satellite instruments, Heue et al. (2016) found an increase in tropospheric O_3 over Africa from 1995–2015. The majority of satellite products in Gaudel et al. (2018) show a general increase in tropospheric O_3 over Africa. As discussed in Section 4.2, trend detection is sensitive to the sampling period and the vertical sensitivity of the sensor. Therefore, the discrepancies between our results with the aforementioned studies can be attributed to the different sampling periods and the different sensitivities among the satellite products. Also, our computations are focused on the partial column where IASI is best suited to document tropical O_3 changes (Section 4.2). Nevertheless, two products show a decrease over South Africa (TOST for 2003–2012 and IASI-SOFRID for 2008–2016), in agreement with our results. Based on the GEOS–chem transport model, Wang et al. (2022) computed the tropospheric O_3 change between 2013–2017 and 1995–1999. Similar to our results, they found mostly negative changes for the tropospheric O_3 over Africa (their Figure 12). As mentioned before, global fire emissions have been decreasing over the past decades, mostly due to decreasing fires over savannas (e.g. Andela et al., 2017). According to Hickman et al. (2021), the NO_x burden has declined over Africa, due to a reduction in BB area extent. This leads to an O_3 decrease over Africa, as the O_3 production is characterised by a NO_x -limited regime (Zhang et al., 2016). The only region where the NO_x burden is increasing is the West African coast, due to an increase in the AN emissions in the proximity of Nigeria, leading to

an O₃ enhancement. This explains the slight increase over West Africa on the coast of the Guinea Gulf (by 2%) captured by IASI ([Figure 4.10](#)).

Concerning the mid-latitudes, over Europe and North America, we mostly observe a decrease of approximately 4 % in O₃, related to reductions in precursor emissions. These reductions are due to emissions controls related to: i) motor vehicles (for CO Granier et al., [2011](#) and NO_x Duncan et al., [2016](#)), and ii) thermal power plants (for NO_x Duncan et al., [2016](#)).

CHAPTER 5

Tropical distributions

5.1 Introduction

Tropospheric O_3 acts to control the oxidizing capacity of the atmosphere, but also as a harmful pollutant for humans and plants in the LT and as greenhouse gas in the UT. CO impacts the oxidation capacity of the atmosphere, by removing OH (Lelieveld et al., 2016), and by influencing the budget of O_3 . Also, it impacts the climate indirectly by contributing to an increase in greenhouse gases such as CO_2 and O_3 (IPCC, 2021). Due to its long lifetime, CO is considered a pollution tracer of combustion processes (Logan et al., 1981). The relation between O_3 and CO is used to constrain our understanding of the factors controlling O_3 . Tropics show particular interest regarding O_3 and CO. They receive maximum sunshine leading to active photochemistry, responsible for ozone production. This photochemistry is associated with many sources of emissions from fires, and the activities of megacities constantly increasing, causing critical pollution. Natural sources (e.g. lightning, soil emissions) can also contribute to changes in the distribution of chemical compounds. Even though the tropics may play an essential role in global warming, the region is poorly documented.

In this chapter, we investigate the distribution and seasonal variability of O_3 and CO for several regions over the tropics. To do so, we take advantage of the high accuracy and resolution of in situ aircraft data (IAGOS) since 1994 (for O_3) and 2002 (for CO). Measurements during the ascend and descend phases are used to study in detail the vertical distribution of 22 tropical sites including megacities such as Rio de Janeiro and Bangkok. Measurements during the cruise phase are used to examine interregional and seasonal differences between 9 and 12km. Further, global distributions provided by IASI-SOFRID O_3 and CO retrievals since 2008 allow us to explore intercontinental connections such as transatlantic transport of biomass burning products in the low troposphere. To investigate further the large IAGOS CO dataset, we use the SOFT-IO tool which couples backward Lagrangian FLEXPART simulations with anthropogenic and fire emission inventories. It allows us to estimate the drivers (anthropogenic and fire sources, regions, and transport) responsible for observed CO anomalies.

5.2 Article

“Tropical tropospheric ozone and carbon monoxide distributions: characteristics, origins and control factors, as seen by IAGOS and IASI”

Tsivlidou, M., Sauvage, B., Barret, B., Wolff, P., Clark, H., Bennouna, Y., Blot, R., Boulanger, D., Nédélec, P., Le Flochmoën, E., and Thouret, V.: Tropical tropospheric ozone and carbon monoxide distributions: characteristics, origins, and control factors, as seen by IAGOS and IASI, *Atmos. Chem. Phys. Discuss.* [preprint], <https://doi.org/10.5194/acp-2022-686>, in review, 2022.

Abstract

The characteristics and seasonal variability of the tropical tropospheric distributions of O₃ and CO were analysed based on in situ measurements provided by the IAGOS program since 1994 and 2002 respectively, combined with observations from the IASI instrument on board the Met-op A satellite since 2008. The SOFT-IO model, which couples back trajectories with CO emissions inventories, was used to explore the origins and sources of the tropical CO observed by IAGOS.

The highest tropical O₃ and CO maxima occur over Northern Tropical (NTr) Africa in the low troposphere (LT; surface to 750 hPa) during the dry season (75 ppb of O₃ at 2.5 km and 850 ppb of CO at 0.3 km over Lagos in January). Despite the active local fires, local anthropogenic (AN) emissions (58 %) are dominant for the CO. The importance of the local AN emissions are highlighted over Central Africa, as they cause a persistent polluted surface layer during the transition seasons (40 % in October and 86 % in April).

The second highest O₃ and CO maxima are observed over Asia. Local or regional Asian AN emissions cause the CO maximum in the LT (at 0.5 km) in January, and the O₃ maximum in above 6 km in the post-monsoon season (April). South China is the only Asian site where O₃ peaks in the LT (75 ppb at 2.5 km), due to local fires (30 %) in addition to the local (52 %) and regional (15 %) AN emissions.

The highest amount of transported CO originates from Africa. The main transport pathway is from the dry-season African regions towards the wet-season ones. Contributions from Northern Hemisphere Africa are found over Arabia and Eastern Africa (up to 70 %) during the dry season and over South America all year long in the mid (MT; 750–300 hPa) and upper troposphere (UT; 300–200

hPa)(18–38 % over Caracas on annual basis).

In contrast, the impact of the Asian emissions in the LT and MT is limited on a local or regional scale. Export of polluted Asian air masses is important in the UT during the Asian summer monsoon and post-monsoon seasons, when convection is active. The AN Asian contributions are mostly found over Arabia and Eastern Africa (up to 80 %) during the Asian summer monsoon. During the post-monsoon, CO impacted by the Indonesian fires (resp. SouthEast Asian AN emissions) are transported towards Eastern Africa (64% and 16%) due to the Tropical Easterly Jet.

The lowest O₃ and CO levels are observed over South America, due to less strong local emissions in comparison to Asia and Africa. The only important CO and O₃ enhancement is observed in the MT during the local fires (October), when O₃ and precursors impacted by the local AN and fire emissions are trapped in an anticyclone and transported towards Southern Africa (5–10 ppb from Northern and Southern Hemisphere South America respectively).

5.2.1 Introduction

Tropospheric O_3 and CO are key components in the atmosphere. O_3 has a significant impact on human health close to the surface (Curtis et al., 2006; Jerrett et al., 2009) and on climate by being a powerful greenhouse gas (Gauss et al., 2003; IPCC, 2021). O_3 is a secondary pollutant produced by photochemical oxidation of precursors such as CO and VOCs in the presence of NO_x (Logan et al., 1981). Its distribution is controlled by: stratospheric transport (Stevenson et al., 2013); transport processes at intercontinental and hemispheric scales (Wild et al., 2004); emissions of precursors (natural and anthropogenic) and destruction processes (photochemical and depositional) (Monks et al., 2015). CO impacts the oxidation capacity of the atmosphere, by removing the cleansing agent of the atmosphere, the hydroxyl radical (OH) (Lelieveld et al., 2016), and by influencing the budget of O_3 . Also, it impacts the climate indirectly by contributing to an increase in several greenhouse gases such as CO_2 , CH_4 , and O_3 (IPCC, 2021). The distribution of CO in the troposphere is controlled by physical and chemical processes including emissions, deposition, and transport. CO is directly (resp. indirectly) produced by anthropogenic and natural emissions (resp. oxidation of methane and VOCs).

The relation between O_3 and CO is used to constrain our understanding of the factors controlling O_3 . Due to its long lifetime, CO is considered a pollution tracer of combustion processes (Logan et al., 1981). The correlation between O_3 and CO indicates that a region has experienced photochemical O_3 production from its precursors (including CO) (Voulgarakis et al., 2011 and references therein). Positive O_3 –CO correlations were observed in aged pollution and biomass burning plumes and were used to explain O_3 production efficiency and continental export (Parrish et al., 1993; Jaffe and Wigder, 2012). In contrast, the anticorrelation between O_3 and CO indicates deposition and O_3 destruction (e.g. via NO titration is favoured when pollution increases). In some cases, the relation between O_3 and CO is not driven by chemistry. Observations from aircraft and remote mountain sites show that O_3 –CO correlations extend into the free troposphere and on intercontinental scales, reflecting the mixing of air masses and chemistry (e.g. Andreae et al., 1994). Also, when stratospheric intrusions occur, O_3 and CO are anti correlated, as stratospheric air is rich in O_3 and poor in CO (Parrish et al., 1998).

Recent studies (Gaudel et al., 2018; Gaudel et al., 2020; Zhang et al., 2016) have shown increasing tropospheric O_3 burden in the second half of the 20th century mostly due to the increase of precursors in the tropical regions. However, the global O_3 distribution and sources of precursors remain uncertain due to inadequate observations in the remote FT, especially over developing countries in the tropics (Gaudel et al., 2018; Tarasick et al., 2019).

The tropical region is of particular interest regarding tropospheric O_3 and CO. It combines: i) intense photochemistry due to high UV radiation and humidity, ii) large active natural sources of CO and other O_3 precursors through biomass burning (Ziemke et al., 2009), biogenic (Aghedo et al., 2007) and lightning emissions (Sauvage et al., 2007c; Sauvage et al.,

2007b), iii) increasing anthropogenic emission due to rapid industrialisation (Granier et al., 2011; Duncan et al., 2016), iv) large O_3 net production potential because deep convection can transport surface emissions to higher altitudes, where their lifetime is increased due to lack of surface deposition and dilution with unpolluted background (Pickering et al., 1995) and v) dynamic processes capable of redistributing chemical species in a regional and global scale (Zhang et al., 2016). Thus, the tropics are a region where O_3 production is favoured.

Satellite observations from the OMI and MLS sensors (Ziemke et al., 2019) and simulations from the GEOS-Chem chemical transport model (Zhang et al., 2016; Zhang et al., 2021) display the highest O_3 burden increase in the tropical region – mostly over India, East Asia, and SouthEast Asia. Most studies tend to confirm an increase of O_3 in the tropics but they are mostly based on model simulations, sparse ground observations, or satellite data with little consistency, and it is not clear what can cause such O_3 increase. Indeed, the trends are attributed to different factors such as biomass burning (Heue et al., 2016), dynamics (Lu et al., 2019a; Thompson et al., 2021) or anthropogenic (Zhang et al., 2016; Gaudel et al., 2020). Thus, further investigation based on *in situ* observations is required to better constrain models, validate satellite retrievals, and reduce the uncertainties in the quantification of O_3 and CO trends and source attribution over the tropics.

Measurements of tropical O_3 and CO are available by satellite observations, but they have a coarse vertical resolution (e.g. Barret et al., 2008; Thompson et al., 2001). Several field campaigns have been carried out in the tropics (Table 5.1). However, they provide sparse measurements in terms of temporal and spatial coverage. The SHADOZ program (Thompson et al., 2003a) provides long-term O_3 observations over the tropics using ozonesondes since 1998. Even though these measurements offered a better understanding of the vertical distribution of tropical O_3 , they are mostly limited to remote observing sites such as Ascension and Reunion Island, and they under-represent the tropical upper troposphere. In addition, it is difficult to provide additional constraints regarding the relation between O_3 and CO in the tropics, due to a lack of simultaneous CO *in situ* observations.

Table 5.1: Field campaigns providing *in situ* gas and aerosol measurements in the tropics.

Campaign	Reference	Place	Period
Cite-1	Chameides et al. (1989)	Atlantic and Brazil	Spring 1984
Cite-2	Hoell Jr et al. (1990)		Aug–Sept 1986
Cite-3	Hoell Jr et al. (1993)		Aug–Sept 1989
ABLE-2A	Harriss et al. (1988)	Amazon	Dry season 1985
ABLE-2B	Garstang et al. (1990)		Wet season 1987
TROPOZ I	Jonquière et al. (1998)	West Africa	Dec 1987
TROPOZ II			Jan–Febr 1991
PEM-WEST-A	Liu et al. (1996)	Western Pacific	Sept–Oct 1991
PEM-WEST-B	Blake et al. (1997)		Febr–Mar 1994
SAFARI-92	Lindesay et al. (1996)	S. Africa to Brazil	Sept–Oct 1992
TRACE-A 1992	Fishman et al. (1996)		
PEM-Tropics-A	Hoell et al. (1999)	Tropical Pacific	Aug–Oct 1996
PEM-Tropics-B	Pickering et al. (2001)		Mar–Apr 1999
EXPRESSO	Delmas et al. (1999)	Central Africa	Nov–Dec 1996
Aerosols99	Thompson et al. (2000)	Virginia to Mauritius	Jan–Febr 1999
INDOEX	Lelieveld et al. (2001)	Tropical Indian Ocean	Jan–Mar 1999
SAFARI-2000	Swap et al. (2003)	Southern Africa	Aug–Sept 1999–2001
TRACE-P	Kondo et al. (2004)	Pacific	Febr–Apr 2001
HIPPO	Wofsy et al. (2011)		2009–2011
TROCCINOX	Mari et al. (2006)	SouthEast Brazil	Febr–Mar 2004
AMMA	Redelsperger et al. (2006)	West Africa	2005–2006
INTEX-B	Singh et al. (2009)	Gulf of Mexico; Pacific	Mar–May 2006
DACCIWA	Knippertz et al. (2017)	Southern West Africa	Jun–Jul 2014–2015
ATom	Bourgeois et al. (2020)	Tropical Atlantic and Pacific	2016–2018
AQABA	Friedrich et al. (2021)		Boreal summer 2017
CLARIFY	Haywood et al. (2021)	SouthEast Atlantic	Aug–Sept 2017
EMeRGe-Asia	Wolf et al. (2020)	East Asia	Mar–Apr 2018
CAFE-Africa	Tadic et al. (2021)	C. Atlantic and W. Africa	Aug–Sept 2018

In a complementary way to all these datasets, the IAGOS ((Marenco et al., 1998; Petzold et al., 2015; Thouret et al., 2022) program has provided continuous and consistent O₃ (Thouret et al., 1998; Blot et al., 2021) and CO (Nédélec et al., 2015) observations over the tropics for the last 26 and 18 years respectively. It measures vertical profiles over remote (e.g. Madras) and megacities (e.g. Lagos, Hong Kong), along with the lower part of the upper tropical troposphere. Previous studies have documented the tropical composition

over Africa (Sauvage et al., 2005; Sauvage et al., 2007a; Sauvage et al., 2007d; Lannuque et al., 2021), South America (Yamasoe et al., 2015) and South Asia (Sahu et al., 2014; Sheel et al., 2014). However, they are focused on specific regions of the tropics and have limited temporal coverage, especially for CO as fewer measurements were available at this time. Thus, the O₃ and CO distributions and their interlocking in the entire tropics are still not well documented.

The SOFT-IO model (Sauvage et al., 2017) has been developed to supplement the analysis of the IAGOS dataset by estimating anthropogenic (AN) and biomass burning (BB) contributions to the observed CO measurements. These measurements, along with the SOFT-IO output allow us to trace the CO origin, and establish connections with the O₃ origin over the tropics. Further, global distributions provided by IASI-SOFRID (Barret et al., 2011; De Wachter et al., 2012) retrievals since 2008 complement the O₃ and CO distributions provided by IAGOS. They allow us to understand the spatial extent of pollution plumes, and explore intercontinental transport patterns.

In this article we take advantage of the unique IAGOS database to (i) document the characteristics and seasonal variability of these two atmospheric species over the whole tropical band for the last decade for the first time, (ii) explore the origin of the observed CO anomalies, (iii) investigate transport processes driving the CO and O₃ distribution in the tropics.

The observational (IAGOS and IASI) and model-based (SOFT-IO) datasets, and methodology are introduced in Sect. 5.2.2. In Section 5.2.3, the IAGOS observations are analysed to document O₃/CO vertical profiles, along with the UT composition over the tropics. In addition, the sources of observed CO are explored with SOFT-IO.

5.2.2 Data and Methods

5.2.2.1 IAGOS observations

The Research Infrastructure IAGOS (Petzold et al., 2015; Thouret et al., 2022) provides *in situ* measurements of trace gases (O₃, CO, water vapour, NO_y between 2001 and 2005 (e.g. Gressent et al., 2014), and more recently NO_x, CH₄, CO₂, and cloud particles, see <https://www.iagos.org/iagos-data/>) and meteorological parameters (temperature and winds), using equipped commercial aircraft. A full description of the instruments can be found in Nédélec et al. (2015). O₃ (resp. CO) is measured using a dual-beam ultraviolet absorption monitor (infrared analyser) with an accuracy of 2 ppb (resp. 5 ppb), a precision of 2 % (resp. 5 %), and a time resolution of 4 (resp. 30) seconds (Thouret et al., 1998; Nédélec et al., 2003). IAGOS measures vertical profiles during ascend and descend phases, and the upper troposphere (between 9 and 12 km; 300–185 hPa) during cruise phases. Considering the aircraft speed (7–8 m s⁻¹ during ascent/descent; 900 km h⁻¹ during cruise), the time resolution of the instruments corresponds to a vertical resolution of 30 m (resp. 225 m) and a horizontal resolution of 1 km (resp. 7.5 km) for O₃ (resp. CO).

O₃ (resp. CO) observations have been collected since 1994 (resp. 2002) in the frame of the IAGOS Research Infrastructure and its predecessor MOZAIC (Marenco et al., 1998) program, based on the same instrument technologies. Good consistency in the measurements between the two programs (hereafter referred to as IAGOS) (Nédélec et al., 2015; Blot et al., 2021) leads to IAGOS temporal coverage of 26 (resp. almost 20) years for O₃ (resp. CO). IAGOS data provides robust O₃ and CO climatologies, allowing studies of long-term trends (e.g. Cohen et al., 2018) along with validation of chemistry transport models (e.g. Sauvage et al., 2007c; Gressent et al., 2016) and satellite data retrievals (e.g. De Wachter et al., 2012) on a global scale. To complement the IAGOS observations, we use the potential vorticity (PV) field, which is part of the ancillary data (<https://doi.org/10.25326/3>) from the IAGOS database. The PV is calculated from the ECMWF operational fields (horizontal resolution 1°, time resolution 3 hours), interpolated along the IAGOS trajectories.

5.2.2.2 Data treatment

The tropical zone can be defined in several ways, such as by meteorological characteristics (e.g. location of the subtropical jets), climatic elements (e.g. precipitation rates), or geographical extent. Following the latter way, in the Tropospheric Ozone Assessment Report, Phase II (TOAR-II; <https://igacproject.org/activities/TOAR/TOAR-II>) Ozone and Precursors in the Tropics working group, the tropics are defined between 20° S and 20° N. In our study, we consider the extended area between 25° S and 25° N, to investigate interactions of pollution and the transport of air masses between the tropics and the subtropics. IAGOS observations are used to document O₃/CO vertical profiles and the (lower part of) UT. Only tropospheric measurements are taken into account, by applying a PV filter of 2 PV units (pvu) for each measurement during the cruise phase, and for the measurements between 20–25° N/S during ascend/descend. The UT climatologies are derived by averaging the cruise data (300–185 hPa) on a 2 x 2.5° grid, for the period 1994–2020 (resp. 2002–2020) for O₃ (resp. CO). For the same periods, the climatologies over the vertical are derived by averaging the data into 10 hPa pressure bins from the surface up to the upper limit of the profile. The upper limit is based on a distance criterion of a 300-km radius around the IAGOS observational site, similar to Petetin et al. (2016). This way we reduce uncertainties due to possible horizontal heterogeneity in the measurements, as the aircraft keeps moving in the horizontal plane during ascent and descent. The cut-off radius is set in alignment with a coarser global model resolution, to limit the potential heterogeneity inside a single grid box.

To determine a reliable climatological profile, we need to assess the statistical significance of the data. Similar to Logan (1999) and Sauvage et al. (2005), we compute the relative standard error (RSE) of the O₃ (CO) monthly mean, versus the number of flights per month. The RSE is defined as the fraction between the standard error ($SE = \frac{\sigma}{\sqrt{N}}$, with σ the square root of the sample variance and N the number of flights) and the O₃ (CO) monthly mean. The minimum number of flights required for statistical significance corresponds to the number above which $RSE \leq 10\%$. We choose RSE less than 10 % because RSE depends not

only on the number of measurements but also on the O_3 (CO) variability which is high over the tropics (Thompson et al., 2003b). For each site with an adequate number of flights per month, we consider an individual profile of O_3 (CO). Otherwise, we combine sites in clusters (see Table 5.2), to increase the amount of data and get significant climatological profiles. Besides, the clusters can be useful for the validation of models with a coarse horizontal resolution, because they represent a wider area as resolved by the models, which are not expected to capture small-scale variations in the O_3 field (e.g. Emmons et al., 2010). For clustering, the sites should be: i) at a relatively close distance from each other, ii) governed by similar meteorological conditions, and iii) display similar characteristics in the vertical distribution of O_3 (CO) (see Sect. 5.2.3.2).

The meteorological conditions in the tropics are peculiar, with different seasonal patterns depending on the region. For instance, in Africa the main seasons are two (dry and wet) with two intermediate seasons passing from wet to dry and vice versa (Sauvage et al., 2005; Lannuque et al., 2021). On the other hand, in Asia the seasons are defined by the Asian monsoon phases: Asian summer monsoon (wet season); Asian winter monsoon (dry season), and post-monsoon. Thus, we considered it more appropriate for our analysis to deviate from the classical definition of the seasons, which fits better to studies concerning higher latitudes. Instead, we analyse the O_3 /CO profiles and horizontal distributions over the intermediate months of the tropical seasons (January, April, July, and October), to highlight seasonal patterns.

5.2.2.3 SOFT-IO model

The SOFT-IO tool (Sauvage et al., 2017; <http://dx.doi.org/10.25326/2>) has been developed to investigate the origin of the observed IAGOS-CO, by coupling FLEXPART 20-days backward transport simulations with emission inventories. For each point of the IAGOS trajectory, SOFT-IO estimates the CO contribution coming from 14 different geographical regions (see Fig. 5.1), for AN and BB origin separately. We use CEDS2 AN emissions (McDuffie et al., 2020) and the GFAS BB emissions (Kaiser et al., 2012) which include fire injection heights, to discriminate sources of CO anomalies over different regions of interest. For the calculations, the AN (resp. BB) emissions are updated on a monthly (resp. daily) basis.

SOFT-IO estimates the contribution to CO anomalies emitted by primary sources during the last 20 days, while it does not calculate the background CO. The background CO can be emitted by primary sources older than 20 days, and by secondary sources such as oxidation of methane and non-methane volatile organic compounds. The meteorological fields are based on $1^\circ \times 1^\circ$ ECMWF analysis and forecast with a time resolution of 6 and 3h respectively.

Several studies (e.g. Cussac et al., 2020; Lannuque et al., 2021; Petetin et al., 2018b) have used SOFT-IO to track back the sources of CO measured by IAGOS. Sauvage et al. (2017) validated SOFT-IO performance against IAGOS CO observations for several regions and tropospheric

Table 5.2: Description of individual sites and clusters used in this study. The location of the sites is displayed in Fig. 5.1

Individual sites/Clusters		IAGOS sites
South America	South Brazil	Rio de Janeiro (Brazil), São Paulo (Brazil)
	Caracas	Caracas (Venezuela)
	Bogota	Bogota (Colombia)
Northern	Lagos	Lagos (Nigeria)
Tropical	Sahel	Abuja (Nigeria), Ouagadougou (Uganda), Niamey (Niger)
Africa	Gulf of Guinea	Lome (Togo), Yaounde (Cameroon), Douala (Cameroon), Libreville (Gabon), Accra (Ghana), Cotonou (Benin), Port Harcourt (Nigeria), Abidjan (Ivory Coast), Malabo (Equatorial Guinea)
	Central Africa	Kinshasa (Democratic Republic of Congo), Brazzaville (Congo), Luanda (Angola),
	Windhoek	Windhoek (Namibia)
	AbuDhabi	Abu Dhabi (United Arab Emirates), Muscat (Oman)
Arabia and Eastern Africa (AEA)	Khartoum	Khartoum (Sudan)
	Addis Ababa	Addis Ababa (Ethiopia)
	Jeddah	Jeddah (Saudi Arabia)
Asia	South China	Hong Kong (China), Guangzhou (China), Xiamen (China)
	Gulf of Thailand	Kuala Lumpur (Malaysia), Singapore (Singapore)
	Madras	Madras (India)
	Hyderabad	Hyderabad (India)
	Mumbai	Mumbai (India)
	Manila	Manila (Philippines)
	Bangkok	Bangkok (Thailand)
	Ho Chi Minh City	Ho Chi Minh City (Vietnam)

levels. As detailed in their study, SOFT-IO uncertainties and biases are mostly due to uncertainties in emission inventories, and to a lesser extent to uncertainties concerning the meteorological fields and FLEXPART transport parameterizations (turbulence, convection). Their results show that SOFT-IO can simulate 95 % of the observed number of anomalies, without any strong dependence on altitude or region of the CO plume. SOFT-IO captures the intensity of CO anomalies with bias lower than 10-15 ppb for most of the regions and tropospheric levels. The bias is higher in extreme pollution events and might be related to uncertainties in the emissions inventories.

In our study, CO anomalies are defined as the positive difference between the observed and the background CO mixing ratio. Background CO mixing ratio represents a reference value, not affected by surface emission or pollution events. For this reason, it is computed as the monthly climatological median CO of a remote area away from polluted regions, in the UT (during the whole study period 2002–2020). The selection of the background is rather subjective (Parrish et al., 2012). The median is generally used to assess baseline concentrations of atmospheric species that are not influenced by recent pollution as they have the characteristics of well-mixed air masses from different origins (Gressent et al., 2014). We performed an evaluation of SOFT-IO for the lower troposphere (LT, surface–750 hPa), the mid troposphere (MT, 750–350 hPa), and upper troposphere (UT, 300–200 hPa). Our simulations detect CO anomalies at the same rates as Sauvage et al. (2017). On average, SOFT-IO underestimates the observed CO anomalies by 10 ppb in the MT and UT, and by 45 ppb in the LT. A sensitivity test has shown absolute differences of 27% in the LT, 16% in the MT and 10% in the UT between SOFT-IO simulations using AN emissions from MACCity and from CEDS2. This clearly highlights the large uncertainty stemming from uncertainties in AN emissions. Another source of uncertainty comes from the definition of background CO. In order to assess this source of uncertainty, we used the 600–300 hPa median CO mixing ratio as background for each site. The differences between the two backgrounds are within 2.5-60 ppbv. Nevertheless, using the alternative background did not make any difference in the anomaly source attribution and in the relative contributions.

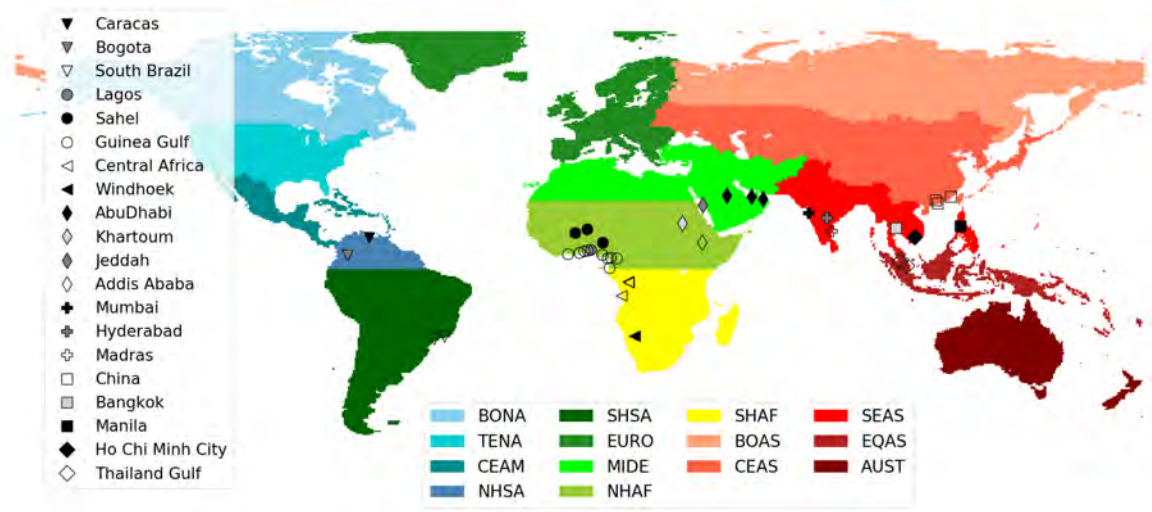


Figure 5.1: Locations of tropical sites served by IAGOS, and geographical source regions used in SOFT-IO model. BONA: Boreal North America; TENA: Temperate North America; CEAM: Central America; NHSA: Northern Hemisphere South America; SHSA: Southern Hemisphere South America; EURO: Europe; MIDE: Middle East; NHAf: Northern Hemisphere Africa; SHAF: Southern Hemisphere Africa; BOAS: Boreal Asia; CEAS: Central Asia; SEAS: Southeast Asia; EQAS: Equatorial Asia; AUST: Australia and New Zealand.

5.2.2.4 IASI-SOFRID observations

The IASI sensor onboard MetOp-A (launched in 2006) has a 12 km footprint at nadir and a 2200 km swath allowing an overpass twice daily at 9:30 and 21:30 local solar time. IASI provides information for the atmospheric composition e.g. content of trace gases such as O_3 (Eremenko et al., 2008; Barret et al., 2011; Boynard et al., 2016), CO (George et al., 2009; De Wachter et al., 2012) and N_2O (Barret et al., 2021). We use O_3 (v3.5) and CO (v2.1 up to 2014, and v2.2 up to 2019) IASI retrievals performed with SOFRID (Barret et al., 2020; De Wachter et al., 2012).

SOFRID- O_3 v3.5 retrievals use a dynamical a priori profile based on latitude, season, and tropopause height (Barret et al., 2020). In the tropics, where the surface temperature, thermal contrast and tropopause height are the highest, SOFRID- O_3 retrievals allow two independent pieces of information, one in the troposphere and one in the UTLS (Barret et al., 2020). Comparisons with ozonesonde measurements for the period 2007–2017, showed that SOFRID- O_3 is biased low in the tropical troposphere and UTLS, by $3 \pm 16 \%$ and $12 \pm 33 \%$ respectively in the Northern Tropics ($0-30^\circ N$), and by $8 \pm 14 \%$ and $21 \pm 30 \%$ in the Southern Tropics ($0-30^\circ S$) (Barret et al., 2020). Comparisons between SOFRID- O_3 retrievals using a single a priori profile and a dynamical a priori profile showed improvements (e.g. a general increase in the correlation coefficients and the amplitude of the retrieved variability) mostly in the troposphere. The change of the a priori profile leads to minor differences in the UTLS, indicating the highest sensitivity of IASI to this layer (Barret et al., 2020).

For SOFRID-CO v(2.1 and 2.2 after 2014), two independent pieces of information are provided in the lower (surface–480 hPa) and upper (480–225 hPa) troposphere (De Wachter et al., 2012). IASI correctly captures the seasonal variability of CO over southern Africa (Windhoek) and European mid-latitudes (Frankfurt) in lower (resp. upper) troposphere relative to IAGOS data (resp. correlation coefficients of 0.85 (0.70)). At Windhoek, SOFRID-CO is biased low in the lower (resp. upper) troposphere by 13 ± 20 % (resp. 4 ± 12 %).

We use monthly averaged SOFRID-CO and O₃ retrievals on a $1^\circ \times 1^\circ$ grid from 2008–2019. We focus on pressure levels corresponding approximately to the independent pieces of information, and on daytime measurements when larger thermal contrast between the surface and the atmosphere results in increased sensitivity of the instrument (Clerbaux et al., 2009).

5.2.3 Results

5.2.3.1 O₃ and CO over the Northern and Southern Tropics

Figure 5.2 displays the tropical IASI LT CO (a) and MT O₃ (b) annual distributions averaged over the 2008–2019 period. The pressure ranges differ for CO and O₃ because they are adjusted to the sensitivity of the instrument for each compound (see Sect. 5.2.2.4). For O₃, the stripes along the 10° latitude bands are due to the use of a dynamical a priori profile (Sect. 5.2.2.4), resulting in discontinuities between adjacent latitude bands with different a priori profiles. Nevertheless, the stripes are a minor issue, as the use of a dynamical a priori profile largely improves the retrieved O₃ profiles in terms of variability and correlation in most latitude bands, relative to the previous version which uses a single a priori profile (Barret et al., 2020).

Northern Tropical (NTr) CO and O₃ mixing ratios are generally higher than the Southern Tropical (STr) ones (Fig. 5.2 and Table 5.3). Geographically, the largest CO (165 ppb) and O₃ (60 ppb) maxima are found over Northern Africa (Table 5.3), followed by comparable CO and O₃ mixing ratios over Southern Africa and East Asia (145–150 ppb of CO and 50 ppb of O₃) (Table 5.3). The smallest magnitude of O₃ and CO maxima are observed over South America.

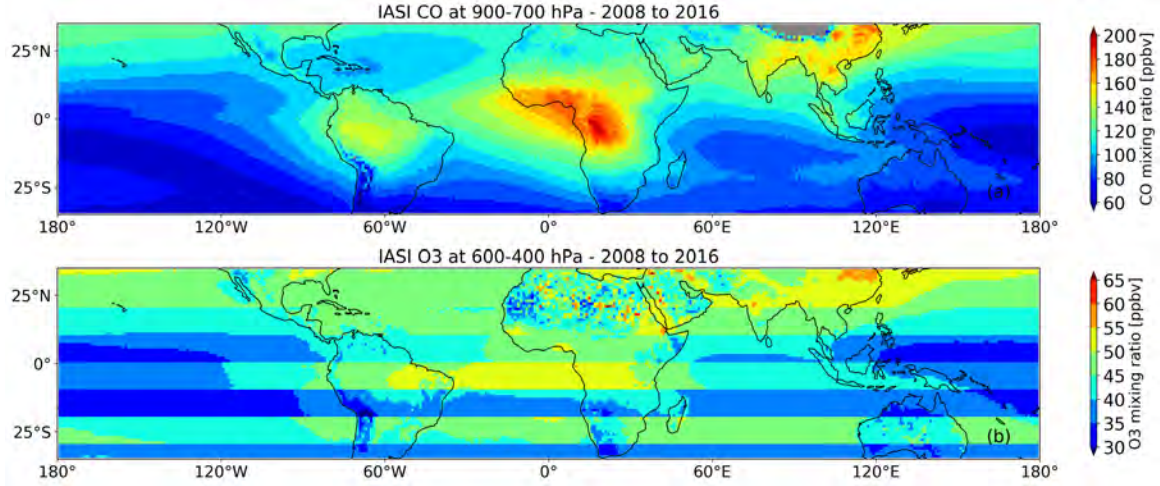


Figure 5.2: IASI LT CO (between 900–700 hPa) (a) and MT O₃ (between 600–400 hPa) (b) mixing ratios averaged from 2008 to 2019 on a 1x1 grid.

Table 5.3: Annual mean LT CO and O₃ mixing ratio (in ppb) over the Northern Tropics (0–25° N), Southern Tropics (0–25° S), Northern Africa (10° W–12.5° E; 0–12.5° N), Southern Africa (10–35° E; 2.5–20° S), East Asia (92.5–110° E; 10–27° N) and South America (35–50° W; 0–20° S) based on IASI data (Fig. 5.2).

	NTr	STr	Northern Africa	Southern Africa	East Asia	South America
CO	115	100	165	145	150	110
O ₃	75	45	60	50	50	45

Figures S1 and S2 show the monthly mean CO flux due to BB and AN emissions respectively. The BB emissions in both hemispheres show strong seasonal variability, as a consequence of the annual shift of the ITCZ, and the alternance of the rainy and dry seasons. In contrast, AN emissions are located mostly in the northern tropics and have weaker seasonal variability. The differences in CO abundances between the two hemispheres could be related to the spatial distribution of the AN emissions and the seasonality of the fires. The main emissions of STr CO are the annual dry-season fires, while NTr CO is related to the larger population and AN activities (Fig. S2) (Edwards et al., 2004).

The CO, and consequently the O₃ maxima over Northern Africa could be related to the strong AN emissions over the Western African coast (Fig. S2a–d). During the dry season, local BB emissions are also active and could contribute to the CO and O₃ maxima (Fig. S1a). High CO and O₃ over East Asia are likely related to anthropogenic emissions (Fig. S2a–d), in contrast to the STr regions (Southern Africa and South America) where the local dry-season BB emissions are significantly stronger than AN (Fig. S1c–d).

The persistent African CO and O₃ maxima are exported over the South Atlantic (Fig. 5.2a–b), contributing to the wave-one O₃ pattern. The wave-one is associated with systematic high

O_3 (60–65 ppb) above the South Atlantic and low O_3 (30–40 ppb) above the western Pacific. Similar asymmetry in the O_3 pattern is observed in the NTr, but with a smaller magnitude because both sides of the equatorial Pacific show similarly low O_3 abundance, while O_3 above the North Atlantic is lower than above the South Atlantic (10–15 ppb difference on average) (Fig. 5.2b).

In this Section, we have shown that the CO and O_3 maxima over the Northern and Southern Tropics are related to AN and BB emissions, as well as transport in the tropical troposphere. We will therefore focus on the following questions: what are the contributions of the AN and BB emissions to the O_3 and CO abundances in the tropics? Are regional or local emissions responsible for the O_3 and CO observed enhancements? To answer these questions, in the next section, we analyse the O_3 and CO tropical profiles to quantify their persistent and repetitive characteristics. Using the SOFT-IO tool, we aim to establish connections between these characteristics and local or regional AN and BB emissions.

5.2.3.2 Regional characteristics of tropical O_3 and CO

In this Section, we focus on the tropical CO and O_3 distributions based on IAGOS and IASI data. The combination of the high vertical resolution of IAGOS (Figs. 5.4, 5.6, 5.7, 5.8 panels 1 and 2), and the high spatial and temporal coverage of IASI 2-D global distributions (Fig. 5.3 a–l), allows us to investigate in detail data-sparse regions like the tropics, and monitor their atmospheric composition.

The results shown in Fig. 5.3 (a–d) motivated our choice in combining IAGOS sites in clusters when it is necessary to increase the number of measurements. The LT CO maxima, like over the Gulf of Guinea, cover a wide area. Thus, cities located close to each other are likely to experience similar air masses. According to the wind maps they are also affected by similar meteorological conditions (Fig. S3).

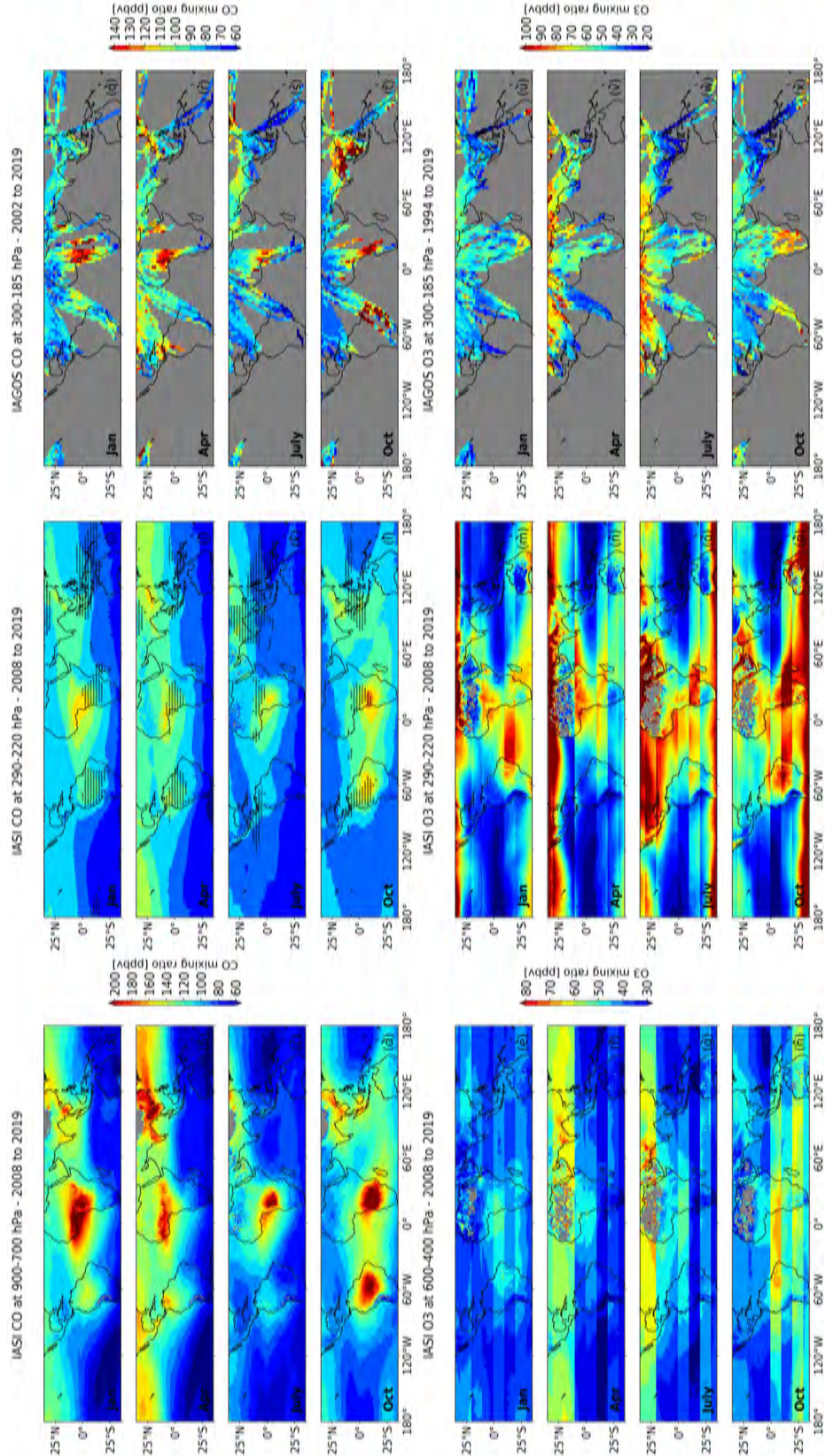


Figure 5.3: Monthly mean LT CO distributions (a–d), MT O₃ distributions (e–h), UT CO distributions based on IASI (i–l) and IAGOS (q–t), UT O₃ distributions based on IASI (m–p) and IAGOS (u–x).

Figures 5.4, 5.6, 5.7 and 5.8 (panels 1 and 2) display the monthly average vertical distributions of O_3 and CO based on IAGOS data, since 1994 and 2002 respectively, for the African, Asian, South American, Arabian and Eastern African clusters. Panels 3 to 5 represent the mean contribution to these CO mixing ratios from AN and BB emissions as estimated by SOFT-IO, with information about their geographical origin (see Sect. 5.2.2.3 and Fig. 5.1). To better understand O_3 and CO anomalies, Fig. 5.5 displays the CO contributions in three tropospheric layers related to different dynamical regimes: lower troposphere below 750 hPa corresponding roughly to planetary boundary layer (PBL); mid troposphere above up to 300 hPa, and upper troposphere above up to 200 hPa corresponding to the beginning of maximum convective detrainment.

5.2.3.2.1 Africa (NTr Africa: Lagos -Nigeria-, Sahel and Gulf of Guinea; STr Africa: Central Africa, Windhoek-Namibia-)

The striking feature of CO and O_3 over the NTr African clusters (Sahel, Gulf of Guinea, and Lagos) is the LT maxima during the dry season (January) (Fig. 5.4 panels 1–2). CO maximises close to the surface, with larger mixing ratios over Lagos (850 ppb) than Sahel (500 ppb) and Gulf of Guinea (400 ppb), mainly due to local AN emissions (58 % over Lagos and Sahel)(Figs. 5.4 panel 3a; 5.12 panel 1a; 5.5a; 5.13a), despite the active local fires (Fig. S1a). This is consistent with the increasing AN emissions (Lioussé et al., 2014) and decreasing BB area extent (Hickman et al., 2021) over NTr Africa. The O_3 gradient close to the surface (Fig. 5.4 panels 1a–1c) is likely related to surface deposition and titration by highly concentrated nitrogen oxide (NO) (Monks, 2005) which is expected along with high CO emissions. The O_3 maximum and the elevated CO levels (exceeding 300–500 ppb) at 2.5 km over the three clusters, likely indicate chemically processed air masses where O_3 has been produced by precursors. The air masses above the Gulf of Guinea and Sahel are transported from the continent (Fig. S3a) by the north–easterly Harmattan flow (Sauvage et al., 2005). AN emissions are the dominant source of CO at 2.5 km over Lagos and Sahel (Figs. 5.4 panel 3a and 5.12 panel 3a). The enhanced O_3 and CO are confined in the LT due to the stability of the Harmattan flow and Saharan anticyclone which prevent vertical mixing (Sauvage et al., 2005). The stability is due to a temperature inversion which characterises the trade current, as moist cooler air above the surface is capped by dry warmer air above, resulting from advection by the Harmattan flow or subsidence in the anticyclone.

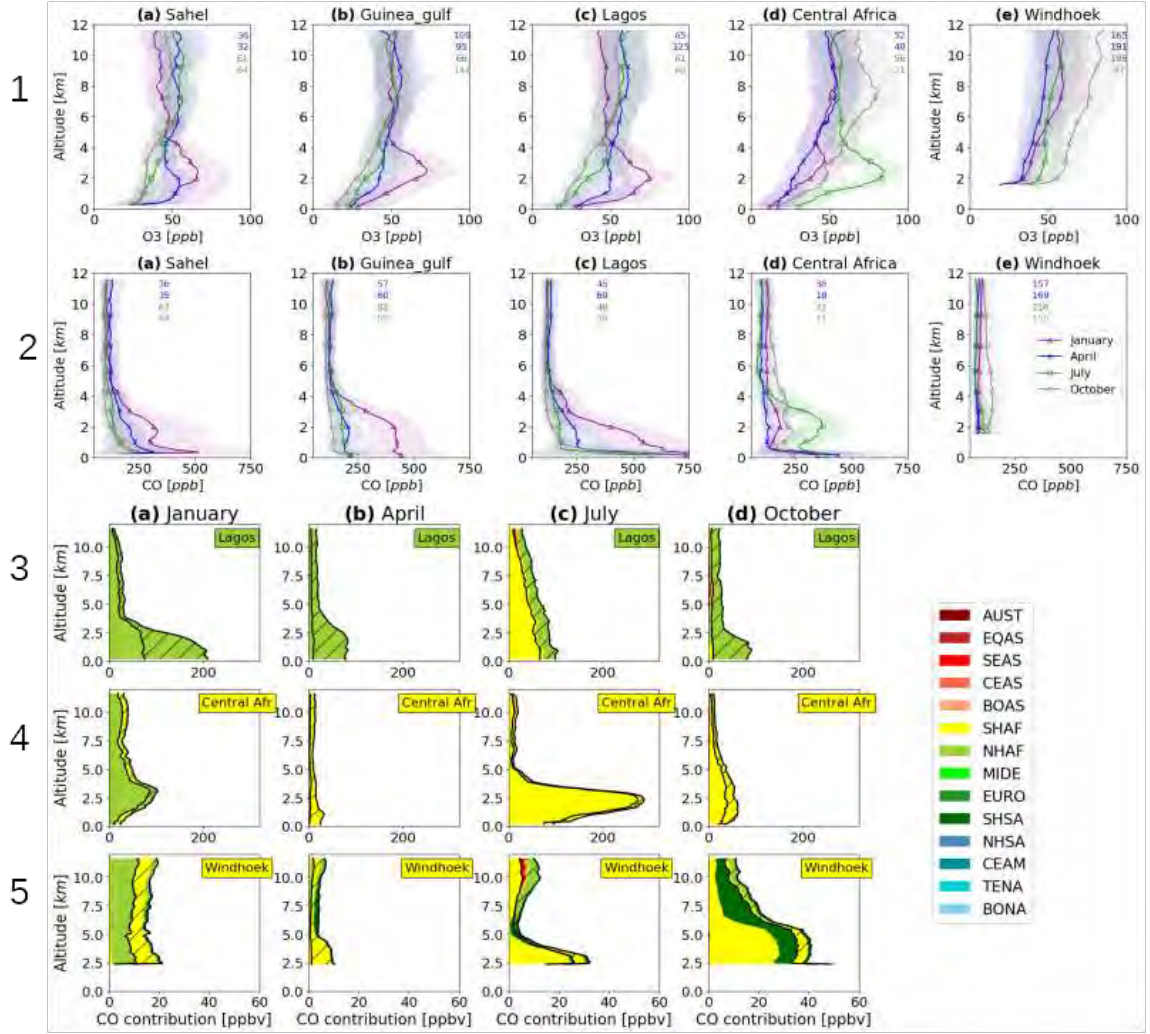


Figure 5.4: IAGOS monthly mean O_3 (panel 1) and CO (panel 2) vertical distributions for the African clusters and sites. The annotated numbers correspond to the number of flights per month, given in the same colour as in the legend. The shadowed part corresponds to \pm one standard deviation. The location of the clusters and sites is displayed in Fig. 5.1. Vertical distribution of CO contributions (in ppb), averaged over all the positive CO anomalies observed in the IAGOS vertical profile (panels 3 to 5). The geographic origin of CO emissions is indicated by the different colours, with the hatched part showing AN contribution, and the non-hatched part BB contribution. Note that the source region where the site belongs is indicated by the colour of the box.

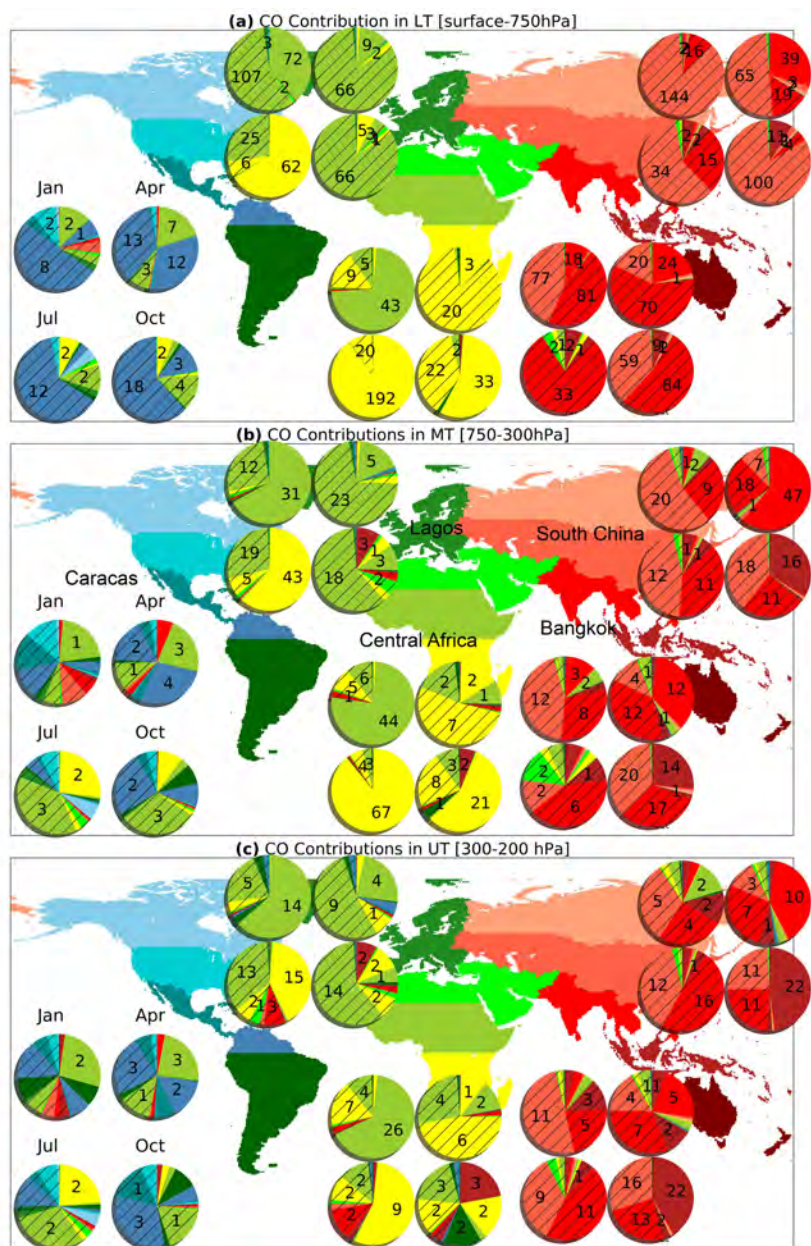


Figure 5.5: Mean SOFT-IO contributions (in ppb), averaged over all the positive CO anomalies for the tropical sites (Caracas, Lagos, Central Africa, South China, and Bangkok) for low (a), mid (b), and upper (c) troposphere. The geographic CO origin of CO is indicated by the colours, for the AN (hatched) and BB (unhatched) contributions. Each pie corresponds to a different month and each group of four pies refers to a different site (see panel b).

Elevated LT CO levels (below 4 km) are observed all year long over the NTr African clusters (Fig. 5.4 panels 2a–2c) except in October. During the transition from the NH dry to wet season (April) when the fires are suppressed (Fig. S1b), CO mainly comes from local AN emissions (Figs. 5.4 panel 3b; 5.12 panels 1b and 2b), located over Ethiopia and Nigeria (Fig. S2b). The fact that SOFT-IO attributes approximately 80 ppbv of CO to local AN emissions (Figs. 5.4 panel 3b; 5.12 panels 1b and 2b), while the observed anomaly reaches

200–250 ppbv, indicates an underestimation of the NHAF AN emissions. Nevertheless, these high CO concentrations in April are detected by IASI in the LT (Fig. 5.3b) over the whole of West Africa indicating the large-scale extent of the impact of these emissions. The enhanced LT O₃ over the three clusters in April (Figs. 5.4a–c) indicates possible O₃ formation during the transport of the aforementioned emissions towards Sahel and the Gulf of Guinea. A small O₃ enhancement is also detected by IASI in the mid-troposphere (400–600 hPa) over West Africa (Fig. 5.3f). During the dry season, nitrogen is accumulated in soils (Jaeglé et al., 2004). The beginning of rains activates the bacterial nitrification leading to significant release of NO which is rapidly converted into NO₂ via oxidative processes. Thus, enhanced NO_x concentrations also contribute to the O₃ increase over NTr Africa in April (Saunois et al., 2009). The O₃ enhancement is larger over Sahel relative to Lagos and the Gulf of Guinea (Fig. 5.4 panel 1a–c) because of higher NO₂ concentrations above dry savannas (Sahel) compared to wet savannas and forests (Southern Western Africa) (Adon et al., 2010). After excess nitrogen is consumed, the wet-season NO emissions decrease, contributing less to the local O₃ (Adon et al., 2010).

During the NH wet season (July), CO close to the surface over Lagos is mostly attributed to southern African (SHAF) emissions (70 ppb) (Fig. 5.5a). This result is clearly consistent with the IASI LT CO July distribution (Fig. 5.3c) which suggests transport from the fire region where the highest concentrations are detected towards the Gulf of Guinea and southern West Africa. The contribution of SHAF emissions is relatively constant from the surface to about 5 km (Fig. 5.4 panel 3c). This suggests the transport of chemically mature air masses from the STr African fires towards Lagos, via the south easterly trade winds turning to the monsoon westerly flow (Sauvage et al., 2007a; Barret et al., 2010). The lower O₃ mixing ratio close to the surface is likely attributed to rapid deposition on forested areas and photochemical destruction in the moist monsoon air (Reeves et al., 2010). Similar to Lagos, CO over the Gulf of Guinea and Sahel originate from local AN and SHAF BB emissions (Fig. 5.12 panels 1c and 2c).

Below about 4km, the annual O₃ minimum occurs in October over the three clusters (Fig. 5.4 panel 1a–c). The CO maximum mixing ratio below 1 km is due to local AN emissions (Figs. 5.4 panel 3d; 5.12 panels 1d and 2d). In contrast with the other months, the CO mixing ratio above the surface maximum decreases sharply with altitude showing low CO concentrations from 2 km to 12 km. Indeed, in October, the monsoon flow disappeared and West Africa is impacted by the north easterly trade winds which block the transport of air masses impacted by BB from SHAF as is clearly visible in the LT CO distribution from IASI (Fig. 5.3d). This is confirmed by the predominant local (NHAF) origin of CO over Lagos which is almost not impacted by SHAF BB in October (Fig. 5.4 panel 3d). The similar O₃ profile close to the surface with the one in July (Fig. 5.4 panel 1c), indicates significant O₃ chemical and depositional sinks as in July. The influence of the moist air over Lagos and Guinea Gulf responsible for the photochemical destruction of O₃ below 2.5 km is confirmed

by high levels of relative humidity (Fig. not shown).

The classical increase of O_3 from the surface to the MT in October (and July) is because the role of photochemistry changes from a net sink to a net source of O_3 above 6km, depending on the NO_x concentration (Jacob et al., 1996). In the tropics, photochemical O_3 destruction dominates the lower troposphere (Archibald et al., 2020), where water vapour concentrations are high, and in highly polluted regions where there is direct removal by titration with NO (Monks et al., 2015). The vegetation can also act as a rapid sink for O_3 via dry deposition (Cros et al., 2000). The lack of these sinks in the FT, coupled with lower water vapour concentrations leads to an increase of O_3 with altitude (Archibald et al., 2020). Lightning can also increase O_3 mixing ratios in the MT and UT (Barret et al., 2010).

O_3 and CO distribution over Central Africa in the SH dry season (July) is very similar to NTr Africa in the respective dry season (Fig. 5.4 panels 1d and 2d). CO is characterised by two distinct maxima close to 400 ppb close to the surface and between 2 and 4 km, exclusively due to local emissions (SHAF) (Fig. 5.4 panel 4c). This is visible on the IASI LT CO distribution with a strong isolated maximum over the whole central African region (Fig. 5.3c). The contribution of local fires is lower close to the surface (80 ppb) than in the upper layer (280 ppb). The O_3 gradient close to the surface is due to the influence of the southern monsoon flow (Sauvage et al., 2005) (high relative humidity below 1.5 km; Fig. not shown). CO emitted above the fires (over Angola, Zambia, and Dem. Rep. of Congo Fig. S1c) is transported towards the IASI CO maximum over Central Africa via the south easterly winds (Fig. 5.3c). During the transport, O_3 is formed (Sauvage et al., 2005; Sauvage et al., 2007a). As in NTr Africa, O_3 and CO enhancements over Central Africa in the dry season are confined below 4 km, because of the stability of the layers below 5 km due to strong temperature inversions.

In October, 3 maxima at the surface, 2 and 4 km visible over Central Africa are due to local emissions (SHAF AN and BB). The lower CO concentrations between the surface and 2 km are probably resulting from the enhancement of the contribution of these emissions with altitude (Fig. 5.4 panel 4d). In January the vertical distribution of CO is characterised by two maxima, at the surface and at 2km. Below 1 km, the main contributions are local AN, and NHAF BB emissions. The contribution from the NHAF fires intensifies and becomes the only important one between 2 and 4 km. During transport from NH Africa, the air masses impacted by BB emissions are chemically processed resulting in the formation of an O_3 secondary maximum of 50 ppb coincident with the CO maximum (Fig. 5.4 panel 1d and 2d) as described in Sauvage et al. (2005).

Interestingly, the annual CO surface maximum in Central Africa Occurs in April, before the beginning of the SH fires. It is due to local AN emissions (SHAF) (Fig. 5.4 panel 4b). The measured CO maximum reaches 350 ppb, while SOFT-IO attributes 40 ppb above the background levels to the aforementioned sources. This means that SHAF AN emissions

are likely underestimated. Above 1km, in the absence of fire contributions, CO remains constant at 100 ppb which is the annual minimum, and the O₃ profile is characterised by a steep gradient and the lowest annual concentrations. IASI LT CO distribution (Fig. 5.3b) indicates that the CO minimum measured by IAGOS above 1km over Central Africa in April extends over the whole central and southern Africa. The maximum close to the surface is indeed not detectable by IASI.

At Windhoek, O₃ and CO maximise in October after SH dry season (July) (Fig. 5.4 panels 1e and 2e). This CO peak has the smallest magnitude among the African clusters (150 ppb at 4 km), while the O₃ peak is among the largest, reaching 80 ppb in the UT (11.5 km).

The LT CO anomalies over Windhoek in October are mainly caused by local BB emissions (68 % BB versus 12 % AN) (Fig. 5.13a). Interestingly, the contribution from the local fires is larger than in July (by 7 ppb in the LT; Fig. 5.4 panel 5c), when the peak of the fire emissions occurs (Fig. S1c–d). These high CO concentrations in October are detected by IASI in the LT (Fig. 5.3d) over the whole of South Africa reflecting the large extent of the impact of these emissions. Using MOPITT CO and MODIS fire count data, Edwards et al. (2006) also noticed the time lag between the peak of the fires and the CO concentration over South Africa. They attributed the lag to smouldering fires at the end of the burning season. The CO emissions, and thus the concentrations, are larger over the savanna fires during October, because of the low combustion efficiency of the smouldering fires resulting in increased CO emissions factors (Zheng et al., 2018b). In addition, there is a non-negligible influence from Southern Hemisphere South America (SHSA) emissions (20 % mostly BB) (Figs. 5.4 panel 5d and 5.13a). The SHSA BB contribution increases with height (30 % contribution in MT and 50 % in UT) contributing to the O₃ maximum observed in the UT (Fig. 5.13b and c) (Sauvage et al., 2006). The absence of a strong CO maximum at the height of the O₃ maximum suggests an additional source of O₃ over Windhoek's UT. As already mentioned (Sect. 5.2.3.1), the high O₃ over South Africa is associated with the South Atlantic O₃ maximum which intensifies in October due to the strong LiNO_x production over southern Africa and South America (Sauvage et al., 2007b; 2007c).

It is noteworthy that an O₃ enhancement of 80 ppb is also observed over Central Africa at 8 km in October (Fig. 5.4 panel 1d). This highlights that the stronger seasonal variability of MT and UT O₃ in STr than in NTr Africa is due to the intense lightning activity in the SH. The IASI UT O₃ distribution clearly shows that the O₃ maximum covers the entire region from South America to Africa south of the Equator (Fig. 5.3l).

The annual minimum of O₃ and CO over Windhoek occurs in April (Fig. 5.4 panels 1e and 2e), the transition period from SH wet to dry season, when the local fires are suppressed (Fig. S1b). The CO mixing ratio is less than 100 ppb over the whole tropospheric column and comes from local AN emissions. In comparison to Central Africa, Windhoek is less influenced by SHAF emissions due to its remote location away from sources (Petetin et al.,

2018b). The O_3 minimum of less than 30 ppb probably results from titration by NO above the surface.

5.2.3.2.2 Asia: Mumbai, Hyderabad, Madras-India-, Ho Chi Minh City-Vietnam-, Manila-Philippines-, Bangkok-Thailand-, Gulf of Thailand, South China

Over the Asian clusters, the CO profiles display the highest mixing ratios in the surface layer (below 1km) all year long (Fig. 5.6 panel 2). The annual maximum occurs in January (except over Manila and the Gulf of Thailand) due to the lowest boundary layer height during winter. The winter surface CO maximum ranges from 300 ppb over oceanic sites (Madras) to 700 ppb over megacities (Ho Chi Minh and Mumbai), and is mainly attributed to local or regional AN emissions (Figs. 5.6 panels 3a to 5a; 5.12 panels 3a to 5a). Over the Indian and South China clusters in January, local emissions (SEAS and CEAS resp.) are dominant, with contributions in the range of 85 to 95 % (Figs. 5.6 panel 3a and 4a; 5.12 panel 3a and 4a and 5.5a). The impact of these Chinese emissions (CEAS) is not limited to a local scale, as they dominate the LT CO anomalies over the rest of the Asian clusters (except Bangkok) with contributions in the range of 52 % (over the Gulf of Thailand) to 75 % (over Manila) (Figs. 5.5a, 5.13a and 5.14a). Their advection is favoured due to the northeasterly trade winds. Bangkok is also impacted by CEAS emissions (42 %), but the local AN (45 %) and BB (10 %) contributions are more important (Fig. 5.5a).

In winter, elevated CO mixing ratios below 2.5 km are related to O_3 enhancements (Figs. 5.6 panel 1). During winter the chemical ageing of the air masses in the LT is favoured by: i) the confinement of the CO-rich air masses due to the large-scale subsidence preventing upward vertical motions (Lelieveld et al., 2001) and ii) the cloud-free conditions promoting O_3 formation. This O_3 enhancement has been described in Barret et al. (2011) for South Asia during the post-monsoon based on IASI O_3 data for 2008. It is also visible on the climatological IASI MT O_3 map (Fig. 5.3f). The accumulation of CO and O_3 in the LT over the Asian clusters is observed in lower altitudes than in the NTr African ones (see Sect. 5.2.3.2.1). This is due to the lower PBL height in DJF over tropical Asia than in Africa as suggested by Kalmus et al. (2022).

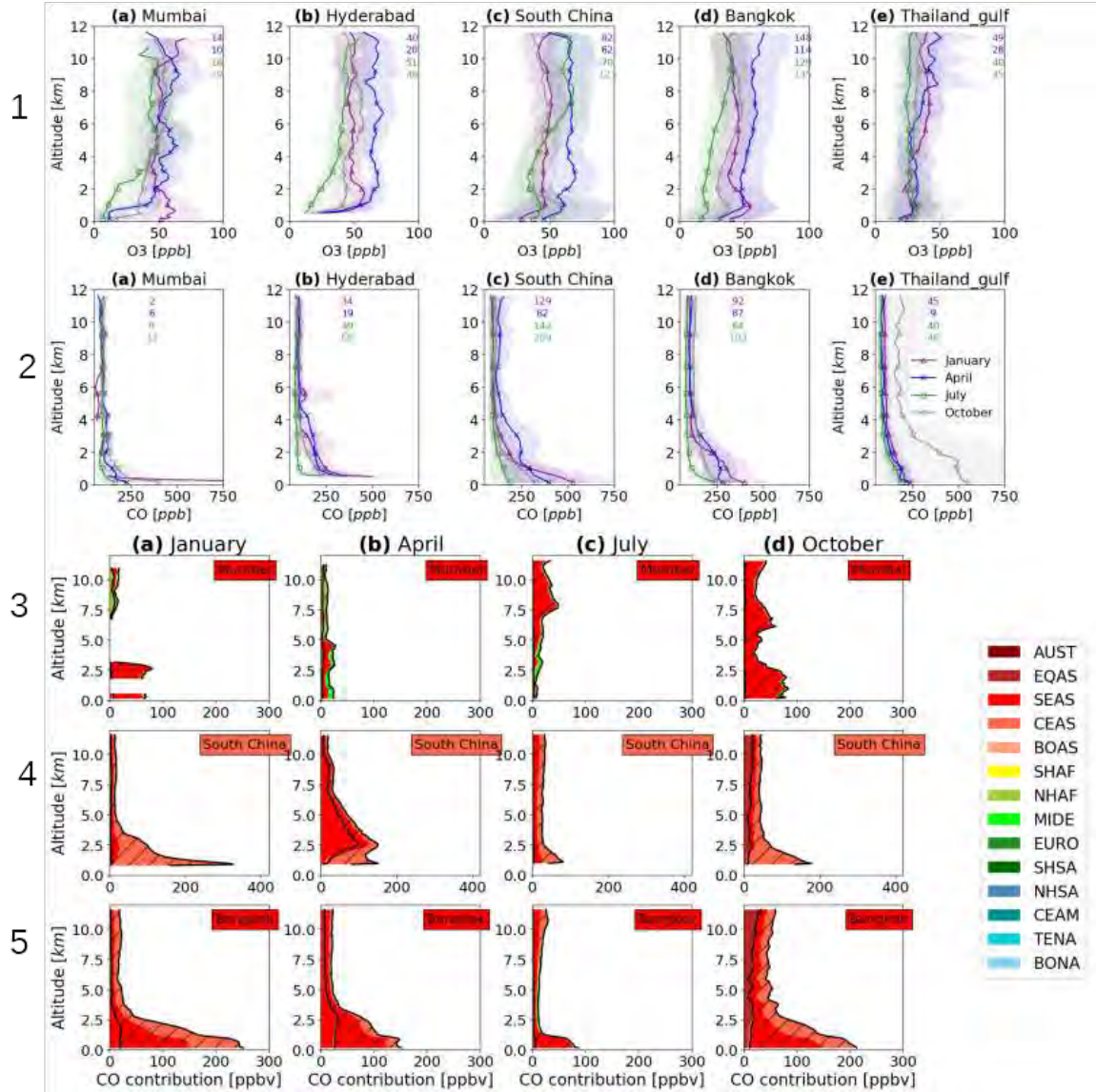


Figure 5.6: Same as Fig. 5.4 for the Asian clusters.

During the pre-monsoon season (April) CO and O₃ are both enhanced above the PBL and below 4 to 6 km over most sites of the Asian clusters. Local AN emissions control the CO anomalies over the majority of the Asian sites (Figs. 5.6 panels 3b–5b; 5.12 panels 3b–7b), while spring SEAS fires significantly impact South China and Bangkok, but also Ho Chi Minh City and Manila. The contributions of the SEAS fires in this cluster are in a range of 20 and 30 % in the LT and MT (Figs. 5.5a and b; 5.14a and b). In spring, the fires are mostly located above East Asia and especially the region of Myanmar, Northern Thailand, and Laos (Fig. S1b), and the corresponding large CO concentrations are captured by IASI (Fig. 5.3b). The westward LT and MT winds above the fires explain the BB outflow towards South China and the Pacific Ocean (Figs. 5.3b and S3b and S3f). The enhanced MT O₃ is attributable to the intense solar radiation associated with the important amounts of precursors from

AN and BB emissions which were previously evidenced. This is in agreement with the observed O_3 maximum in spring over South China (e.g. Dufour et al. (2010) using IASI data) and Bangkok (Sahu et al. (2013) using IAGOS data). Using observational (IAGOS and IASI) and model (Model for OZone And Related chemical Tracers–version–4 model) data, Yarragunta et al. (2019) found that local AN emissions are responsible for the CO and O_3 abundances over South India during the pre-monsoon season. This is in accordance with the SOFT-IO contributions over the Indian clusters (Figs. 5.6 panels 3b; 5.12 panels 3b and 4b; 5.14a). However, it is worth noticing that CO anomalies over Mumbai are also caused by the transport of AN emissions from MIDE (36 %) in the LT, and NHAF (30 %) in the MT (Fig. 5.14a and b). In the UT, where the transport of air masses is favoured, the impact of NHAF emissions dominates over Mumbai (54 %) and Hyderabad (50 %). The UT CO and O_3 transport from NHAF towards the Arabian Sea and South India is also captured by the IASI maps (Figs. 5.3j and 5.3n), indicating O_3 photochemical production during the transport.

The BB contribution is also important during the post-monsoon season (October) because of active fires over Indonesia (Fig. S1). The Gulf of Thailand cluster is the most affected, from the surface (600 ppb), to the UT (Fig. 5.6 panel 1e). Interestingly, the CO mixing ratio at 6–12 km is approximately 200 ppb over the Gulf of Thailand cluster, the highest CO abundance in the MT and UT among the Asian clusters. IASI CO data (Fig. 5.3d) and wind fields (Fig. S3d) show that the LT CO-rich air masses impacted by the fires (Fig. S1d) are advected towards the SE Asian coast (South China, Gulf of Thailand, Bangkok, and Manila), as confirmed by the SOFT-IO contributions (10 % EQAS contribution on average) in addition to the local AN influence (Figs. 5.6 panels 4d and 5d; 5.12 panels 6d and 7d; 5.5a; 5.13a and 5.14a). The collocated O_3 enhancement (below 2 km) over the SEAsian coastal clusters (Figs. 5.6 panels 1c–1e) indicates O_3 production by BB and AN precursors.

The contribution of the EQAS BB intensifies in the UT in October, reaching 40–57 % over the SE Asian coastal clusters, and 33 % (resp. 50%) over Hyderabad (resp. Madras) (Figs. 5.5c; 5.13c and 5.14c). The UT CO maximum above the fires is also captured by IASI and IAGOS UT data (Figs. 5.3l; 5.3p and S1d). Based on MLS CO data, Livesey et al. (2013) also found an UT CO maximum over Indonesia and attributed it to episodically strong convection, in agreement with the low outgoing longwave radiation in Fig. 5.3p. In contrast, the UT and MT O_3 distributions show a SE–NW gradient (Figs. 5.3l and 5.3h) with lower O_3 -levels over the Maritime continent and the southern Indian Ocean and higher ones over India and the Arabian Sea. This was reported by Barret et al. (2011) as a result of convection over the first region and subsidence of precursor-enriched air masses over the second one.

The LT O_3 and CO mixing ratios over the Asian clusters minimise during the summer monsoon (July) (Fig. 5.6 panels 1–2). The reversal of the north-easterly trades to the monsoon flow (Fig. S3c) results in the advection of O_3 - and CO-poor air masses from the

Indian Ocean towards Asia. The lowest O_3 levels close to the surface are observed over Mumbai due to the stronger oceanic influence (high relative humidity close to the surface compared to the other clusters, Fig. not shown). Furthermore, convective clouds result in cloudy conditions, and rain scavenges O_3 precursors resulting in lower O_3 production than in clear sky conditions (Mari et al., 2000; Safieddine et al., 2016). The steep CO gradient close to the surface (below 1 km) clearly indicates the convective uplift of polluted PBL air masses towards the UT. The resulting enhancement of CO in the UT within the AMA analysed by Park et al. (2008) and Barret et al. (2016) is clear from IASI (Fig. 5.3k). In contrast, the positive south-north O_3 gradient between the Maritime continent and north SAsia and the Middle East (Figs. 5.3o and w) is associated with: i) the photochemical ageing of air masses while they are recirculating towards the Middle East, allowing sufficient O_3 production during transport (Lawrence and Lelieveld, 2010) and ii) the high insolation over Middle East favouring O_3 photochemical production ((Barret et al., 2016).

5.2.3.2.3 South America: Caracas -Venezuela-, Bogota -Colombia- and South Brazil

Over Caracas and Bogota, the concentrations of CO in the troposphere are maxima in April and minima in January, while the highest concentrations occur in October over SBrazil (Fig. 5.7 panel 2). In April, CO concentrations exceed 400 ppb over Bogota below 1 km above the surface, and 200 ppb up to 2 km over Caracas. The CO concentrations detected by IASI over northern Venezuela and Colombia are also maxima in April (Fig. 5.3b). This is clearly related to the large vertical extent of the high concentrations which improves the detection by IASI. In terms of CO, Bogota is the most polluted cluster over South America throughout the year.

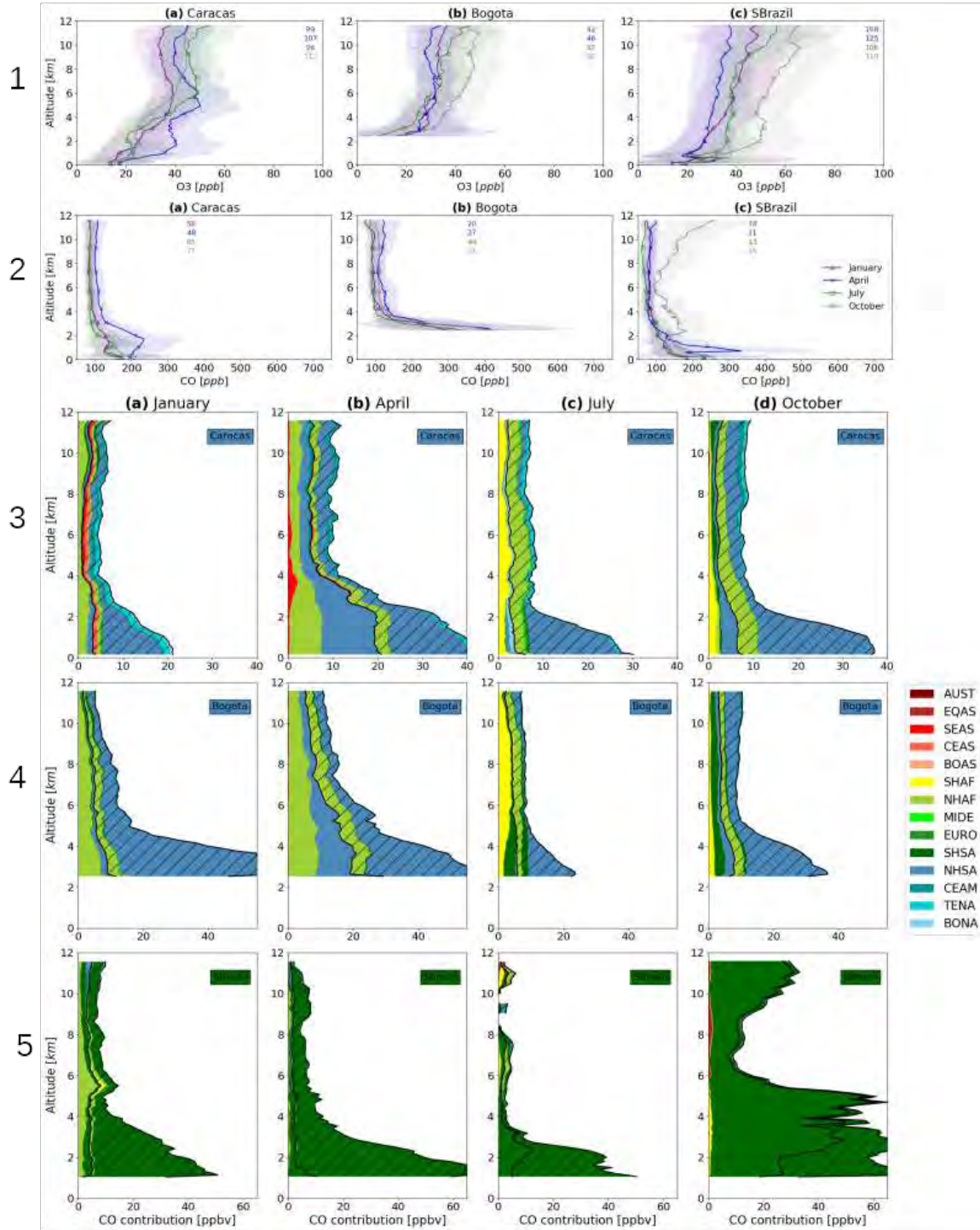


Figure 5.7: Same as Fig. 5.4 for the South American clusters.

In January, CO concentrations are below 300 ppb (resp. 180 ppb) over Bogota (resp. Caracas and SBrazil) below 1km a.s.s.(Fig. 5.7 panel 2). The CO mixing ratios decrease below 100 ppb above the polluted layers all year long, except for South Brazil, where a first maximum (150–200 ppb) occurs in the MT (2–4 km) and a second one (200–250 ppb) is observed above

8 km in October. IASI clearly detects the MT (Fig. 5.3d) and UT (Fig. 5.3p) maxima over most tropical South America in October.

The O₃ profiles over South America generally display the classical increase from the surface to the MT (Fig. 5.7 panel 1). The increase of O₃ with altitude is attributed to the lack of depositional and chemical sinks in the FT, in combination with lower water vapour concentrations, and lightning emissions, as discussed in Sec. 5.2.3.2.1.

Over Caracas, tropospheric CO is maximum in April (250 ppbv) and the profile displays one maximum of O₃ (40 ppb) in the LT and one in the MT (50 ppb). Over Bogota and SBrazil O₃ is maximum in October over the whole troposphere with mixing ratios reaching 45 and 60 ppb in the UT. For Bogota (resp. SBrazil) the tropospheric O₃ annual minimum occurs in July (resp. April). As IAGOS over SBrazil below 6 km, the IASI distributions over tropical South America (Fig. 5.3 e to h) display lower tropospheric O₃ in January and April than in July and October.

From SOFT-IO we can see that, over SBrazil in October, CO enhancement below 1 km is caused by local AN (52 %) and BB (44 %) emissions (Fig. 5.7 panel 5d). In the MT and the UT, the BB contribution exceeds 80 % because of the strong convection moving over the BB regions (Liu et al., 2010). This is also indicated by low outgoing longwave radiation (Fig. 5.3l) which is used as a convection proxy (Park et al., 2007). The uplifted BB products are trapped in an anticyclonic circulation developed over Central South America (Fig. S3l). CO from SHSA fires are transported over Bogota, at the edge of the anticyclone, but does not reach Caracas which lies outside of the anticyclone (Fig. 5.7 panels 3d and 4d). Their photochemical processing contributes to the seasonal O₃ enhancement over South America which is the western part of the wave-one pattern (Thompson et al., 2003b; Sauvage et al., 2006). This is highlighted by the collocation of IASI UT CO (Fig. 5.3l) and O₃ (Fig. 5.3p) maxima within the anticyclone. Nevertheless, as described by Sauvage et al. (2007b) the lightning activity over South America and Africa in October is the most important cause of the O₃ wave-one pattern.

Below 1km, the annual CO maximum over SBrazil in April is due to local AN emissions (Fig. 5.7 panel 5b) located over the southern part of Brazil (Fig. S2b). The observed CO enhancement reaches approximately 350 ppb (Fig. 5.7c), while SOFT-IO attributes 65 ppb above the background levels to the aforementioned emissions. This indicates that SHSA AN emissions are underestimated by the SOFT-IO calculations. The observed CO enhancement at 1.5 km is a new CO feature compared to Yamasoe et al. (2015) which studied CO climatology over SBrazil for the period 1994–2013. The CO enhancement is due to additional data that were collected for the year 2014. SOFT-IO shows increased local AN contributions for March–April–May 2014 relative to the previous years. This is in agreement with the CEDS2 inventory, which shows a peak in AN emissions over South Brazil (18–29° S and 35–52° W) for the year 2014, mostly coming from the transportation sector (Fig. not

shown).

Over Caracas, the annual CO maximum below 2 km in April mostly comes from local AN (35 %) and BB (32 %) emissions (NHSA) (Figs. 5.13, and 5.7 panel 5b). This local origin of emissions is corroborated by the elevated IASI LT CO mixing ratios (Fig. 5.3b) collocated with the strong AN emissions above Colombia and Venezuela, and active fires above the latter (Figs. S1b and S2b). Transport also plays an important role with 20 % of the anomalies caused by BB NHAF emissions (Fig. 5.5a). The O₃ maximum collocated with the CO one at 2 km (Fig. 5.7 panels 1a and 2a), indicates O₃ production during transport of NHAF air masses impacted by BB. The second O₃ maximum above 5 km is also noticed by Yamasoe et al. (2015). Using the GEOS-chem model, they identified local anthropogenic sources followed by lightning, as the main sources of O₃ precursors over Caracas in April. In addition, the O₃ maximum at around 6 km in October was attributed to local anthropogenic sources and lightning from Africa. This transport pathway from Africa to Caracas in October is confirmed by SOFT-IO (Fig. 5.7 panel 3d).

It is interesting to note that the CO mixing ratio between 2 and 4 km over Caracas is elevated (≥ 150 ppb) compared to the free tropospheric background (≈ 100 ppb) all year long. The January–July and October maxima are lower than the April one with dominant CO sources being local AN and African (SHAF or NHAF depending on the season) emissions with contributions of 30 % each. In January there is also a small (15 %) influence from AN central and equatorial Asian emissions (CEAS and EQAS). In Bogota, local (71 %) and NHAF (26 %) emissions control the CO annual maxima close to the surface in April, (Fig. 5.7 panel 4b). During the rest of the year, local AN emissions (≥ 60 %) control the LT CO anomalies. Emissions from Africa are also contributing to LT CO in Bogota with 15 % in July (SHAF and NHAF) and 27 % in January (NHAF). In contrast to Caracas, emissions from SHSA also contribute to LT CO anomalies over Bogota, with 31% in July and 10 % in October.

5.2.3.2.4 Arabia and Eastern Africa (AEA): Khartoum -Sudan-, Addis Ababa -Ethiopia-, Jeddah -Saudi Arabia-, Abu Dhabi

The striking feature of the AEA clusters is the elevated O₃ in the FT (70 ppb on average centred at around 8 km) for all the clusters during April and for the northern clusters of Jeddah and Abu Dhabi during July (Fig. 5.8 panel 1 a–d). The particularly low CO mixing ratio accompanying the O₃ enhancements around 8 km over the AEA clusters (Fig. 5.8 panel 2a–d) points to a dynamical origin of O₃. The O₃ enhancements over the 4 sites of AEA and the anti correlation with CO, are also detected by IASI in the UT and MT (Fig. 5.3j, k, n and o).

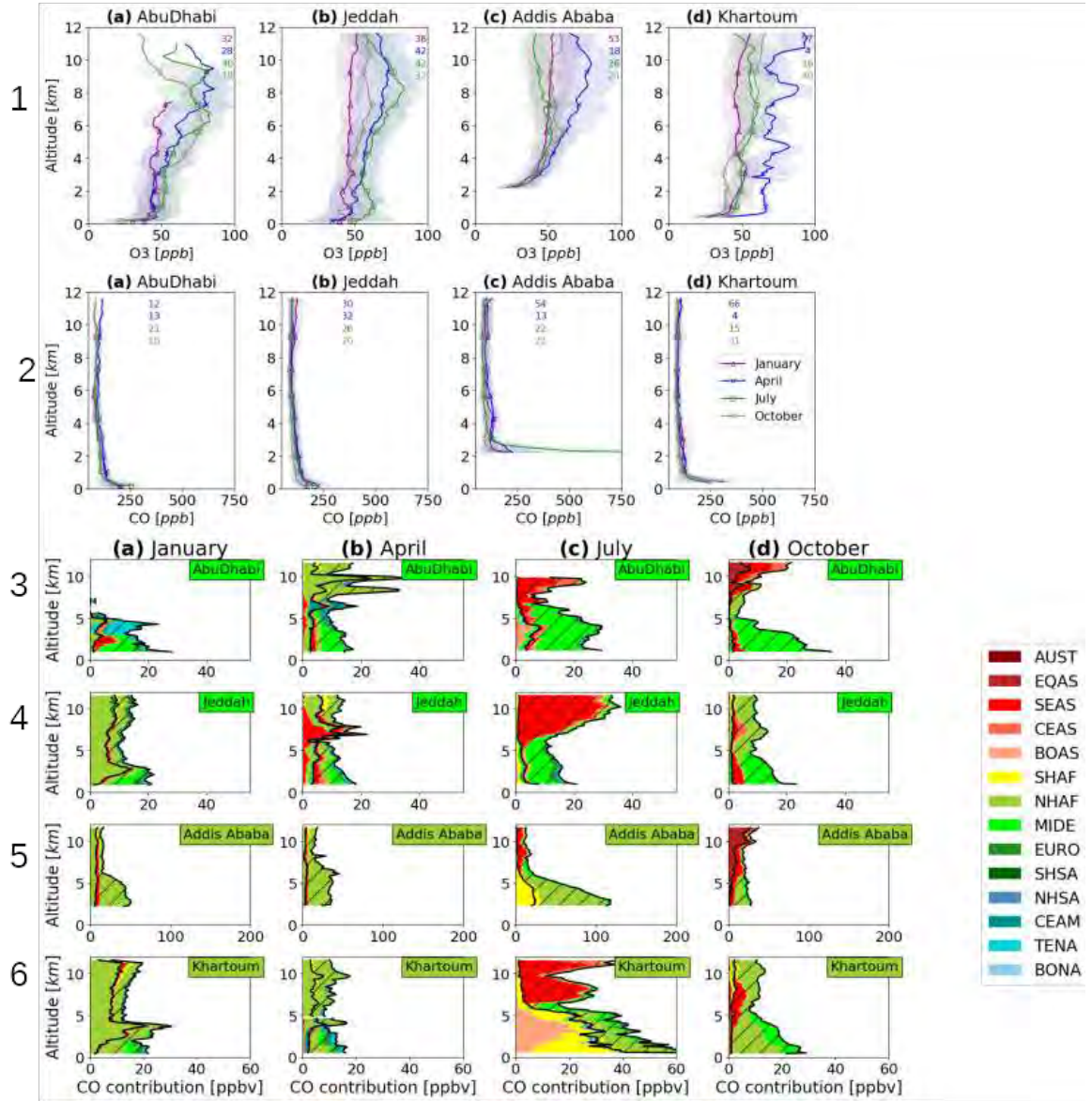


Figure 5.8: Same as Fig. 5.4 for the Arabian and Eastern African clusters.

Tropopause foldings in the vicinity of the subtropical jet stream are associated with downward transport of stratospheric O₃ (Stohl et al., 2003; Lelieveld et al., 2009; Safieddine et al., 2014) resulting in a tropospheric O₃ enhancement. The O₃ flux from the stratosphere to the troposphere in the vicinity of the NH subtropical jet peaks during spring and summer (Tang et al., 2011). This is in agreement with Cohen et al. (2018) that found the maximum O₃ to CO ratio over the Arabian peninsula during spring and summer (their Fig. A1), using IAGOS data for the period 1994 to 2013. This indicates higher occurrence of O₃-rich and CO-poor air masses, reflecting a stronger stratospheric influence. Nevertheless, large O₃ regional enhancements are detected by IASI over the Arabian sea similarly to Jia et al. (2017) based on TOC from OMI/MLS. Jia et al. (2017) attributed these O₃ enhancements

to emissions from India (50 %), with smaller contributions from the Middle East and Africa (30 %). This is in agreement with SOFT-IO, which shows a significant contribution from SEAS over Jeddah (29 %) and a lower one over Addis Ababa (7%) (Figs. 5.8 panels 4b and 5b, and 5.13a). SOFT-IO also attributes large contributions from NHAF AN and BB emissions over Abu Dhabi and to a lesser extent over Khartoum (Fig. 5.8 panels 3b and 6b). The contribution of American sources over Abu Dhabi indicates eastward transport, which is not present in the rest of the AEA clusters. Due to its northern position, Abu Dhabi is affected by the subtropical westerly jet in the UT. In contrast the rest of the AEA clusters are affected by the TEJ which brings CO from Asian regions.

In July, the Middle East summer O₃ maximum is also partly related to subsidence of AMA air masses which brings O₃ produced from South Asian AN and LiNO_x emissions (Barret et al., 2016). The polluted air masses from South and SouthEast Asia uplifted by monsoon deep convection are trapped in the AMA which extends westward to Northeast Africa and the Middle East (Barret et al., 2016; Park et al., 2007). Over Khartoum and Jeddah (resp. Addis Ababa and Abu Dhabi) 20 ppb (resp. 10 ppb) of CO originates from SEAS at 6–12 km. The impact of the SEAS emissions is stronger over Jeddah (78 %) than over Khartoum (60 %) and Addis Ababa (46 %) (Fig. 5.13c). Addis Ababa and Khartoum, further to the south, are outside of the AMA and therefore characterised by lower levels of O₃ in the UT (Fig. 5.8 panel 1). Furthermore, the O₃ minimum over Addis Ababa (45–50 ppb) is related to the ITCZ located between 5° N and 10° N during the NH wet season (Lannuque et al., 2021). The UT O₃ enhancement over Arabia and the Arabian sea, and the transition to lower concentrations south of the tip of Arabia are also clear with the IASI map (Fig. 5.3c). The O₃ minimum over Africa is caused by uplift of local African O₃-poor air masses from the surface in the ITCZ (Fig. 5.3c). The increase of O₃ northwards (such as over Khartoum with 60 ppb) is due to the O₃ production within uplifted CO-rich air masses, transported away from the ITCZ by the upper branches of the Hadley cell (Lannuque et al., 2021).

One common characteristic among the AEA clusters is the elevated CO mixing ratio in the surface layer (below 1km) all year long (Fig. 5.8 panel 2). The surface maximum is larger over Addis Ababa (700 ppb in July) and Khartoum (350 ppb in April), than in Jeddah and Abu Dhabi (<250 ppb). Over the East African sites (Khartoum and Addis Ababa), a layer of enhanced CO is observed in the FT, in January and April. This winter to spring high CO layer in the FT over Eastern Africa is detected by IASI which clearly shows that it does not reach Arabia (Fig. 5.3a–b). IASI data (Fig. 5.3i–l) also displays little annual UT CO variability over this region.

In January, the surface CO maximum is mostly controlled by local AN emissions over the AEA clusters (Figs. 5.8 panels 3a to 6a). Above the surface layer, strong Ethiopian AN emissions (Fig. S2) control the CO anomalies over Addis Ababa with contribution of 71 % in the LT and 58 % in the MT (Fig. 5.13a). Influence from the NHAF fires is also evident (12 % in the LT and 20 % in the MT) (Fig. 5.13a). The impact from the NHAF

fires intensifies over Khartoum and Jeddah between 2 and 4 km with contributions of 58 % and 53 % respectively (Fig. 5.13a). The effect of the NHAf emissions towards eastern Africa (Khartoum and Addis Ababa) and Jeddah is also detected by IASI (Fig. 5.3a), which shows a negative eastward CO gradient. As expected, the fire contribution is stronger in the western African clusters such as Lagos, due to the prevailing north easterly winds (Fig. S3a) (see Sect. 5.2.3.2.1). The co-occurring O₃ enhancement over Khartoum and Jeddah below 4 km reflects O₃ formation during transport from the fires (Fig. 5.8 panels 1b and 1d). The small enhancement of O₃ is also captured by IASI in the MT (Fig. 5.3e).

In July, the CO surface maximum is again caused by local AN emissions (Fig. 5.8 panels 3c–5c), except over Khartoum where air masses from SHAF fires are the dominant source of CO (Fig. 5.8 panel 6c). The combination of local AN (70 %) and SHAF BB (23 %) emissions is responsible for the annual CO maximum at the surface over Addis Ababa in July (Figs. 5.8 panel 5c, and 5.13a). Interestingly, the impact of the SHAF fires below 4km over Khartoum and Addis Ababa is stronger than the impact of local fires during the respective dry season (Figs. 5.8 panels 5ac and 6ac). The O₃ enhancement below 4 km over the Jeddah, Khartoum and Addis Ababa indicates O₃ production during the transport of CO-rich air masses impacted by the SHAF fires (Fig. 5.8 panels 1 j to l). In contrast, over Abu Dhabi the O₃ enhancement in the FT (Fig. 5.8 panel 1a) is likely related to transport of CO-rich air masses from the MIDE and BOAS regions (Fig. 5.8 panel 3c).

In October, long range transport from Asia (SEAS AN and EQAS BB) plays a significant role in CO anomalies over the AEA sites (Figs. 5.8 panels 3d–6d), especially over Addis Ababa and Jeddah. In the LT, the northeasterlies (Fig. S3d), transport CO-rich air masses from Asia towards eastern Africa. This transport of CO from Asia over the Arabian sea is well captured by IASI (Fig. 5.3d).

Above 4km in October, O₃ enhancements are observed over the AEA sites especially over Abu Dhabi which is the easternmost site of the AEA region (Fig. 5.8 panel 1). IASI detects a MT O₃ increase above the Arabian sea and Northern India (Fig. 5.3h). The O₃ enhancement in the MT over the Arabian sea detected with O₃ soundings during the INDOEX campaign (1999–2000) has been attributed to Indian sources uplifted over the marine boundary layer by the sea breeze circulation in Lawrence and Lelieveld (2010). It was further analysed and documented with IASI O₃ data by Barret et al. (2011) who already highlighted the MT O₃ enhancement over northern India and the northern part of the Arabian sea during the post-monsoon season. The O₃-rich air masses are further transported towards Eastern Africa by the prevailing northeasterlies (Fig. S3h) as documented by the predominant SEAS origin of FT CO over the AEA sites (Figs. 5.8 panels 3d and 6d).

5.2.3.3 Control factors of tropical O₃ and CO

In this Section we present the main features of the tropical O₃ and CO distributions. Figure 5.9 displays the annual maximum/minimum of O₃ (a) and CO (b) mixing ratios and their

corresponding mean height. The annual maxima/minima are calculated based on monthly averaged mixing ratios over vertical layers with 40 hPa thickness. Figure 5.10 displays the transport pathways of CO emissions from the African, South American and Asian source regions, towards the 20 tropical sites in the LT (a), MT (b) and UT (c). We show the source regions and the months corresponding to the largest amounts of transported CO (in ppb). Figure 5.11 displays the AN and BB contribution to CO anomalies (in ppb) over the tropical UT (300–185 hPa).

Overall, the CO profiles above all tropical clusters display an annual maximum above the surface layer (approximately at 0.5 km) (Fig. 5.9b). This is also valid for Caracas, Bogota, Windhoek and Addis Ababa which are located at high altitude above the sea surface (with a mean elevation of 0.9 km, 2.6 km, 1.6 km and 2.3 km respectively). For all the clusters located in the NH tropics (African, Asian and South American), the CO-polluted boundary layer, is mainly attributed to local AN emissions, even for clusters such as over West Africa, where BB is expected to be of great importance (Reeves et al., 2010; Mari et al., 2008; Sauvage et al., 2005) (Figs. 5.5a; 5.13a; 5.14a). This finding confirms the key role of the AN emissions in the NH, related to larger population compared to the SH, and enhanced AN urban and industrial activity, as discussed in Edwards et al. (2004). Concerning the SH, the surface-layer pollution is predominantly caused by BB over STr Africa (Central Africa and Windhoek) during the dry season (Figs. 5.5, 5.13), and by AN over the SBrazil (Fig. 5.13). Interestingly, the CO maxima over the latter occurs before the burning season. This is in accordance with previous studies suggesting fossil fuels as the main CO source over São Paulo and Rio de Janeiro (Alonso et al., 2010), and decreasing BB over South America (Andela et al., 2017; Deeter et al., 2018). The decrease of BB CO emissions is due to the long-term declining deforestation rates, especially over forested areas ($\approx 54\%$) and over savanna and shrublands ($\approx 39\%$) (Naus et al., 2022). The importance of the AN emissions is also evident over Central Africa with non negligible contributions during dry season (10 %) (Fig. 5.5). Also, the polluted surface layer over Central Africa is present all year long, with large AN contributions of 40 % and 86 % during the transition seasons, when the fires are suppressed (Fig. 5.5a). Thus, the impact of the AN emissions is also important in the STr.

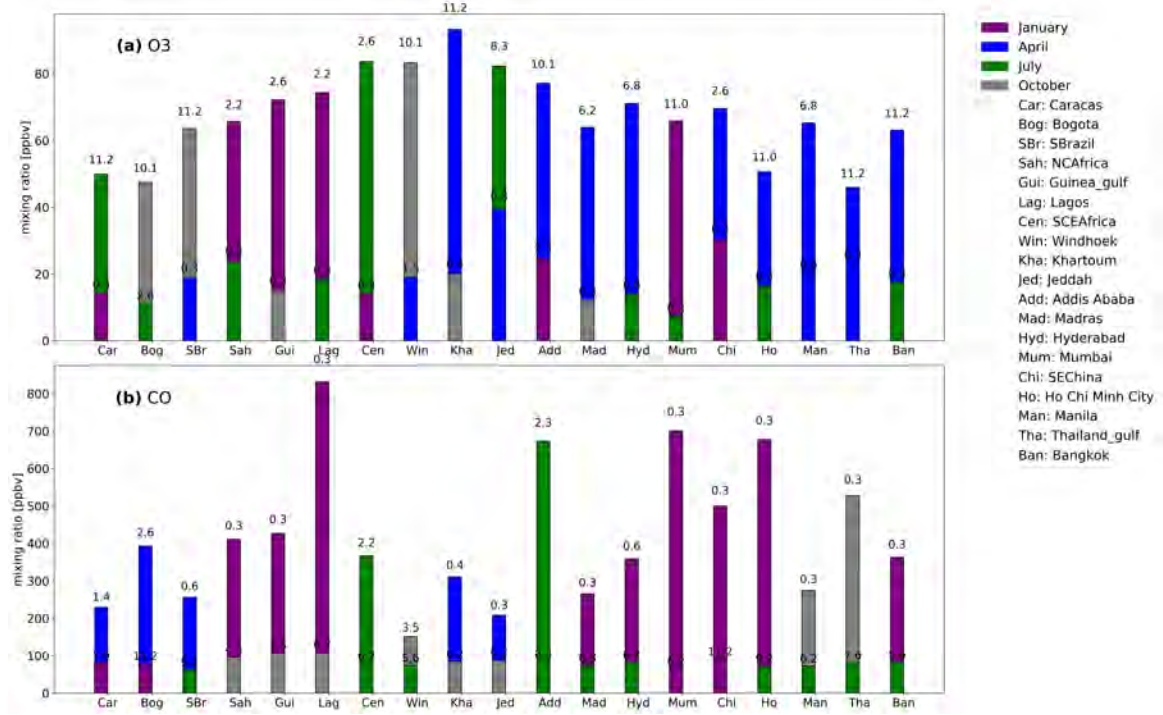


Figure 5.9: O₃ (a) and CO (b) annual maximum (higher bar) and minimum (lower bar) mixing ratio observed over the tropical clusters. The annotated number on top of each bar indicates the altitude (in km) of the observed annual maximum/minimum mixing ratio. The colour in the bar indicates the month of the maximum/minimum.

Table 5.4: Total (AN + BB) CO emission rates (in $10^{-10} \text{ kg m}^{-2} \text{ s}^{-1}$) based on CEDS2 and GFAS emission inventories over West Africa (10° W – 12.5° E ; 0 – 12.5° N), Central Africa (10 – 35° W ; 2.5 – 20° S), East Asia (92.5 – 110° E ; 10 – 27° N), Maritime Continent (93 – 121° E ; 10° S – 10° N), South Brazil (35 – 50° W ; 0 – 20° S) and Arabia and Eastern Africa (30 – 60° E ; 5 – 25° N).

	W. Africa	C. Africa	E. Asia	India	Maritime Continent	S. Brazil	AEA
January	6	1	4	3	1.5	1	1.5
April	3	1	11	3.5	1.5	0.5	1
July	2.5	10	3	3	2	1	0.5
October	2.5	3	3	3	6	4	1
Annual	3.5	3.7	5.5	3.1	3	1.5	1

The CO maxima show strong variations in terms of magnitude and season among the tropical clusters. This is because they are mostly caused by local emissions with varying intensity and seasonal pattern, depending on the region. In contrast, the CO minima are uniform in terms of intensity levels of mixing ratios, close to the CO background levels of 100 ppb, due to mixing and transport over the lifetime of CO. As expected, they occur in the FT, in the absence of the emissions and where CO is chemically destroyed. As for the CO maxima, their

strong seasonality is related to the seasonality of the surface emissions and the meteorological conditions, which differ over each region. Further discussions on the magnitude and the seasonality of the CO maxima and minima will follow later.

Because of its complex chemistry, the situation for O_3 is more complicated. Africa is the only region where the annual O_3 maximum occurs in the LT (2.5 km) during the dry season (Fig. 5.9a Sahel, Guinea Gulf, Lagos and Central Africa). The co-occurrence of maximum O_3 with the maximum in CO over Africa during the local fires indicates stronger dependency of O_3 on the surface BB CO emissions for these regions, in agreement with Sauvage et al. (2007c). South China is the only Asian cluster where the annual O_3 maximum is observed in the LT during the active local fires (April), but it is not accompanied by the annual CO maximum (Fig. 5.9), suggesting that the O_3 maximum has been formed differently. In contrast, over the other regions, the annual O_3 maximum is observed in the FT above 6 km (Fig. 5.9a). This likely indicates that O_3 is formed by photochemical processes, and is associated with larger O_3 production efficiency (Sauvage et al., 2007b). In regions such as Arabia (Jeddah and Abu Dhabi), the lack of CO enhancement in the UT indicates dynamical origin of O_3 (e.g. stratospheric influence and transport of O_3 and precursors from Asia; see Sect. 5.2.3.2.4). In contrast, in regions such SBrazil and Windhoek in October, the co-occurrence of O_3 and CO enhancement in the MT and UT indicates tropospheric origin for O_3 (e.g. fires and $LiNO_x$ emissions; Secs. 5.2.3.2.1 and 5.2.3.2.3). The annual O_3 minima for all the tropical clusters are observed close to the surface (below 0.5 km on average) (Fig. 5.9a). This is related to the chemical and deposition sinks of O_3 located in the LT (see Sect. 5.2.3.2.1 for more details).

The highest CO and O_3 maxima among all the tropical clusters occur over NTr Africa in the LT during the dry season (January) mostly due to local AN emissions. According to IASI (Fig. 5.3), the CO-rich and O_3 -rich air masses due to the African emissions show a large extend along the tropical Equatorial Africa, and accumulate in the LT due to the stability of the Harmattan winds (Sauvage et al., 2005). Table 5.4 displays the total (AN and BB) CO emissions rates over several regions of interests based on the sum of CEDS2 and GFAS emission inventories. Indeed, the O_3 and CO maxima co-occur with the highest emissions over Western Africa in January, confirming their strong dependency on the surface emissions. The NO_x -limited O_3 production regime over Western Africa (Sauniois et al., 2009; Zhang et al., 2016) likely explains the O_3 maxima when the local emissions, and thus the NO_2 concentration (Jaeglé et al., 2004), intensify in the region. The largest O_3 and CO mixing ratio over Lagos (Fig. 5.9) is due to its proximity to the strong Nigerian AN emissions, as confirmed by SOFT-IO (see Sect. 5.2.3.2.1). As expected, the impact on CO is higher in the proximity of the emissions, while the CO mixing ratio decreases downwind (towards Sahel and Gulf of Guinea) (Fig. 5.9) because of physical processes, such as dilution by mixing and entrainment (Martin et al., 2017), and CO consumption in O_3 build-up in fires (Chatfield et al., 1996). The O_3 maxima show smaller variations (of approximately 10 ppb) among the

NTr African clusters. In contrast to CO, the O₃ enhancement does not strongly depend on the proximity to emissions, as it is produced during the transport and chemical ageing of air masses rich in precursors (Sauvage et al., 2007c).

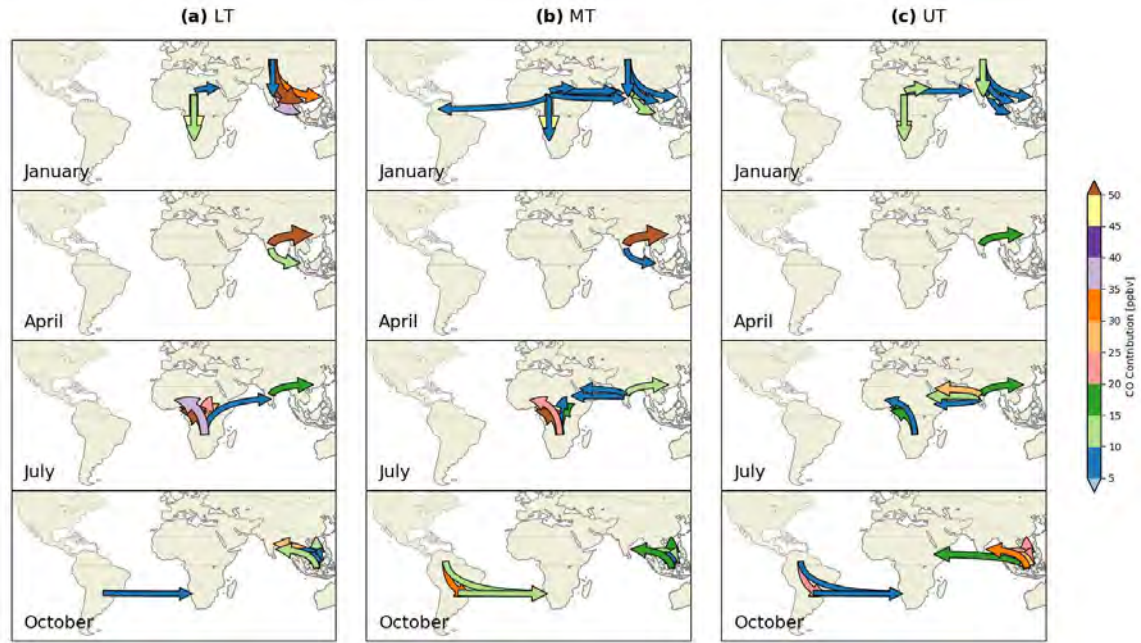


Figure 5.10: Transport of CO (AN+BB) emissions from the African, South American and Asian source regions towards the 20 tropical sites taken into account for this study. The colour bar shows the amount of CO transported in ppb.

The second highest CO and O₃ maxima over the tropical regions are observed over Asia (Fig. 5.9). As in NTr Africa, the CO maximum occurs in January, when the stability of the trade wind results in accumulation of CO-rich air masses in the LT. The surface-layer CO maximum is attributed to local AN emissions over Indian and South China clusters (85–95 %). In the rest of the Asian cluster, there are non-negligible contributions from regional AN sources of the Asian cluster in addition to the dominant local ones. According to Table 5.4, the CO emissions over East Asia and India are lower than the ones over Western Africa in January. This explains the lower CO mixing ratio over Asia than over Lagos. SOFT-IO seems to represent better the Asian contributions relative to the Africa ones. As mentioned in Sect. 5.2.3.2.1, the AN emissions over NH and SH Africa are likely underestimated by the SOFT-IO computations (Fig. 5.4 panels 3b and 4b). This is confirmed by that fact that CO mixing ratio is higher over Africa than over Asia, in contrast to the CO contributions estimated by SOFT-IO. Thus, the impact of the African AN emissions is likely underestimated.

Previous studies have already found concentrations of pollutants in West Africa (e.g. Lagos, Abidjan, Cotonou) comparable to those observed over Asian megacities (Assamoi and Liousse, 2010; Adon et al., 2016; Sauvage et al., 2007c). Indeed, the rapid growth over African

megacities is responsible for increasing emissions from diffuse and inefficient combustion sources (Marais and Wiedinmyer, 2016). This increase is mostly attributed to the growing residential source mainly for cooking and heating (Zheng et al., 2019), but also to traffic emissions (related to large number of two-stroke vehicles, poor fuel quality and poorly-maintained engines) (Assamoi and Lioussé, 2010). In contrast, Eastern China has had one of the largest decreases in CO emissions (Hedelius et al., 2021) due to technological changes with improved combustion efficiency and emission control measures (Zheng et al., 2018a). Using MOPITT data for the period 2002–2018, Buchholz et al. (2021) found the largest reduction in CO concentrations over China. This reduction is attributed to declines in local CO emissions since 2002, related to replacing residential coal use with electricity and natural gas, and to the implementation of Clean Air Policies (A et al., 2017) around 2010. In India, on the other hand, there are no regulation in the emissions, and this explains the highest CO mixing ratios among the Asian clusters (Fig. 5.9). Previous studies have already reported increasing CO emissions over India from 1996–2015, due to several factors such as increases in residential and agricultural sources (Pandey et al., 2014) and to power production and transport activities (Sadavarte and Venkataraman, 2014).

As in NTr Africa, the CO-rich air masses accumulated in the LT over the Asian clusters in January result in a secondary LT O₃ maximum. However, these maxima are significantly lower (40–60 ppb) (Sect. 5.2.3.2.2) than the NTr African ones (65–75 ppb) (Fig. 5.9a; Sect. 5.2.3.2.1), even for clusters with similar LT CO mixing ratios (e.g. Sahel and South China) (Fig. 5.9a). This is because: i) the CO emissions are less strong over the Asian clusters, as mentioned before, and ii) the O₃ enhancement over Asia is caused by AN-polluted air, while in NTr Africa by mixed (AN and BB) polluted air. During the Atom campaign, Bourgeois et al. (2021) found that O₃ levels are more enhanced in mixed air pollution, because they are associated with greater NO_x and peroxy acyl nitrates (a NO_x reservoir compound), and thus increased O₃ production, in comparison to BB- or AN-polluted air alone. This is in agreement with the O₃ annual maximum in April over East Asia (Fig. 5.9a), over clusters such as South China and Bangkok, which are affected by the local fires.

Unlike Africa, the highest emission rates over East Asia and India are observed in April (Table 5.4). In the absence of the stability of the north easterlies, the air masses are not confined close to the surface like in January, and thus the secondary CO maxima above the surface is also captured by IASI (Fig. 5.3f). Over East Asia, the contribution of the local fires is also present in addition to the local AN emissions. The impact of the fires dominates in clusters such as South China and Bangkok, and is evident over Manila and Ho Chi Minh City (see Sect. 5.2.3.2.2). Interestingly, the NH African fires in January correspond to 72 % of the global burned area, whereas the NH Asian fires only to the 2.5 % (Werf et al., 2010). However, both regions contribute significantly to the global CO concentrations (44 % for Africa and 22 % for Asia) because of more complete oxidation, and thus reduced CO production, over grass fires (Africa savannas), relative to fires in forests and peat-lands

(deforestation and peatland fires over Asia) (Werf et al., 2010). The large extent of the impact of the NH Asian fires is displayed in IASI map, with an outflow towards SE Asian coast and the Pacific (Fig. 5.3f). The stronger winds in April than in January, which does not favour the accumulation of the pollution, and the eastwards transport pathway (Fig. 5.10 panel 1 a–b) leads to lower CO mixing ratio in April than January, despite the higher emission rates (Table 5.4).

Concerning India, local AN emissions are responsible for the CO enhancement in April, with negligible BB contribution (Figs. 5.6 panel 3a and 5.12 panels 3a and 4a). The CO emissions rates over India are high during the whole year, showing weak seasonal variability (Table 5.4). The LT CO distribution over India shows strong seasonal variability which is not explained by the seasonality of the emissions. The LT CO is rather linked with seasonal changes in the meteorological circulation. Similarly to East Asia, during January the air masses are transported southward due to the north easterlies, while the reversal of the winds to southwesterlies in July results in northward transport (Figs. 5.3 and S3) (Lawrence and Lelieveld, 2010). Because of this circulation pattern in July, the oceanic influence brings clean air masses over the Asian clusters resulting in an annual CO minimum during the Asian summer monsoon (Fig. 5.9). The CO-rich air masses for the surface are uplifted in the upper troposphere due to deep convection over the area (Sect. 5.2.3.2.2).

As for CO, O₃ seasonality is also linked with the seasonality of the meteorological conditions and dynamics over Asia. The O₃ maximum in April is attributed to the intense solar radiation associated with important amount of precursors from mostly AN emissions, except for South China where BB emissions dominate. The O₃ minimum occurs during the Asian summer monsoon (July), because of lower O₃ production in the presence of convective clouds relative to clear sky conditions (Sect. 5.2.3.2.2).

Despite the CO emissions reductions over South China, the O₃ levels remain relatively high (Fig. 5.9a). This is because the O₃ production regime over South China is VOC-limited (Li et al., 2013), and the total NMVOCs emissions increased in China by a factor of 3.5 (1997–2017) because of activity increases in the solvent, energy, and industry sectors (Zheng et al., 2018a). As discussed in Wang et al. (2017), despite the successful controls of NO_x emissions from coal fired power plants since 2010 over Eastern China, it is recommended to apply controls over VOCs emissions as they control the local O₃ distribution. In contrast, over India the O₃ production regime is NO_x-limited (Kumar et al., 2012), as the local emissions are mostly associated with incomplete combustion processes by biofuel burning, and thus higher NMHC to NO_x emission ratio as compared to other regions of the Northern Hemisphere (Lawrence and Lelieveld, 2010).

Concerning Central Africa, the O₃ and CO maximum in the LT during the dry season, indicates the strong dependence of the CO and O₃ distribution on the surface emissions, as over NTr Africa. The CO magnitude over Central Africa is similar to the one over Sahel and

Guinea Gulf during the respective dry season, even though the emissions rates are higher over the former (Table 5.4). This is because higher amount of CO impacted by the SH African fires is transported towards the NTr Africa due to the trade winds, relative to the respective southward transport during the NH dry season (Fig. 5.10). In addition, the O₃ mixing ratio is slightly higher over Central Africa (85 ppb) likely indicating rapid photochemical O₃ production by BB precursors (Singh et al., 1996) during the SH fires. Concerning Windhoek, the O₃ maximum in the FT (85 ppb at 10 km) (Fig. 5.9) indicates that O₃ production is controlled by LiNO_x emissions at higher altitude (Sauvage et al., 2007c) during the peak of the lightning activity over South Africa (Fig. not shown).

The smallest LT CO maximum over the NTr are observed over Arabia and East Africa clusters and South America (Fig. 5.9) because of the smallest emissions rates among the tropics (Table 5.4). The CO emissions over Middle East are mainly related to electricity generation, water desalination, and industry supplied by oil and gas deposits with cheap but relatively clean fuels (Krotkov et al., 2016). In addition, because of its location between the two highest emitters (Asia and Africa), transport plays a significant role in CO enhancements over AEA, especially in the MT and UT where long range transport of emissions is favoured (Figs. 5.10 panels 1 b–c; 2 a–c and 2b–c). This transport from Asia and Africa over AEA clusters determines the O₃ maxima over the AEA clusters (Sect. 5.2.3.2.4). Similarly, over NTr South America, the local AN contributions are much smaller than the respective local Asian or African ones, indicating lower pollution levels over South America than Asia and Africa. The O₃ maximum is controlled by LiNO_x emissions at higher altitudes.

From the previous analysis, all the tropical clusters and the associated CO source regions exhibit primarily local influence, in the proximity of the region where they are emitted. However, CO transport plays also an important role in the CO distribution over the tropics. CO sources located over Africa show the maximum influence on the regional tropical CO. The highest impact of the African emissions is found at an inter-hemispheric scale, where CO from the dry-season African regions is transported towards the wet-season African (Fig. 5.10 panels 1 and 2). As a result, CO contributions of 45–50 ppb (resp. over 50 ppb) from NHAF (resp. SHAF) is found over SHAF (resp. NHAF) during the respective dry season in the LT and MT. This transport of precursors results in a secondary O₃ maximum, as can be seen by IASI maps (Fig. 5.3e and g).

Impact of the SHAF BB in July is also found in the LT over India with contributions of 5–10 ppb (Fig. 5.10 panel 2a). Similarly, NHAF AN and BB contributions in January are found over South America (5–10 ppb in the MT) and India (5–10 ppb in the MT and UT) (Fig. 5.10 panel 1a). The impact of the NHAF emissions towards South America (10–15 ppb in MT; 5–10 ppb in the rest) is increased in April (Fig. not shown) and significantly contributes to the local South American annual maximum (30 % and 50 % of CO anomalies over Caracas (LT and MT resp.) (Fig. 5.5a–b).

During the transport of the SHAF (resp. NHAF) emissions towards the ITCZ location in the North (resp. South) Africa, the air masses reach convective regions and are injected in the North African (resp. South African) upper troposphere (Fig. 5.11). This explains why the SHAF (resp. NHAF) emissions are dominant in the wet-season hemisphere during July (resp. January) (Figs. 5.11 and resp. 5.17 and 5.15). Nevertheless, the NHAF contribution in the UT CO anomalies is present on a local scale all year long, above NTr Africa and South Atlantic. During the dry season, the impact of the NHAF emissions is stronger and extends to a wider area over South America, Middle East, South Asia (Figs. 5.15 NHAF).

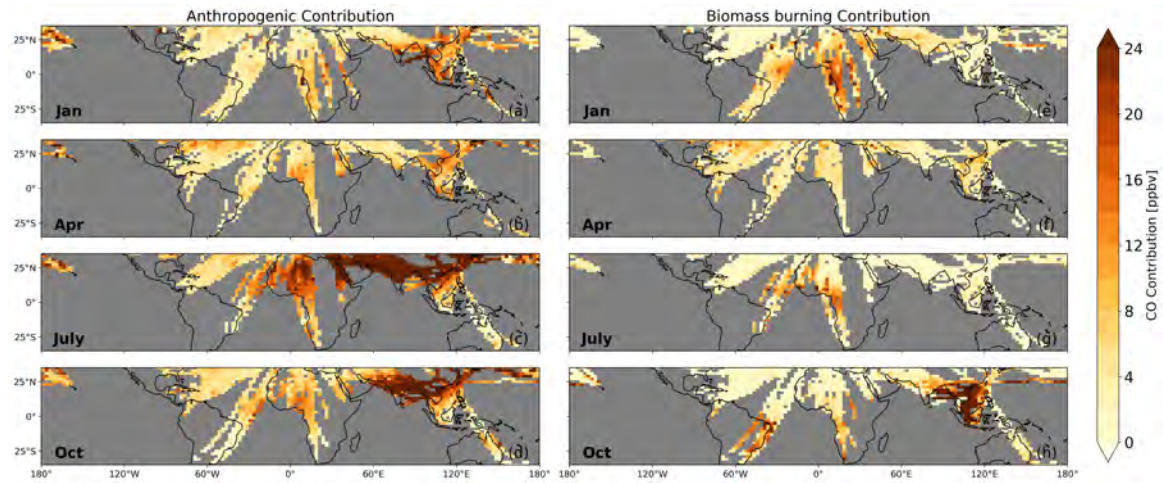


Figure 5.11: Mean AN (a–d) and BB (e–h) contributions in ppb over the tropical upper troposphere (300–185 hPa) from 2002–2019.

The impact of CO emissions from South America is extended over South Africa during October. This is because of the anticyclone over Central South America which traps the CO emitted locally, and transports it towards the east by westerlies (see Sect. 5.2.3.2.3). The highest transport in terms of CO amount from NHSA and SHSA occurs in the MT (10–15 ppb each). IASI maps show an O_3 and CO enhancement over the tropical South Atlantic (Figs. 5.3 d and h, 5.3l and p). Thus, the South American emissions mostly coming from BB (Figs. 5.11, 5.18 SHSA and NHSA) contributes to the wave-one pattern. Nevertheless, the most important source of O_3 over the tropical South Atlantic is $LiNO_x$ emissions from South America and South Africa, as highlighted by previous studies (Sauvage et al., 2007c; Sauvage et al., 2007b).

The contribution of Asian emissions in the tropical LT is limited to a regional or local scale, as they are mostly impact neighbour Asian regions (Fig. 5.10a)(see Sect. 5.2.3.2.2 for more details). CO export from Asia is favoured during the Asian summer monsoon and post-monsoon (July and October) in the UT, where the transport is favoured due to stronger winds relative to the surface (Fig. S3).

During the Asian summer monsoon, the CO-rich (and O_3 -poor) air masses from the PBL

(Fig. 5.3c and g) are convectively uplifted in the UT (Figs. 5.11c and 5.17), and trapped in the AMA circulation (see Sect. 5.2.3.2.2). The impact of the Asian emissions on the UT CO anomalies is extended over Arabia (25–30 ppb) and Eastern Africa (25–30 ppb) (Figs. 5.11c; 5.10 panel 3c and 5.17 SEAS and CEAS). Interestingly, subsidence of air masses from AMA above Arabia are responsible for an O₃ maximum above AEA (Fig. 5.9a) (Sect. 5.2.3.2.4). During the post-monsoon season (October), sporadic convection uplifts CO emitted by EQAS fires (Figs. 5.11g, 5.18 EQAS) (see Sect. 5.2.3.2.2). At the same time, convection over continental Asia uplifts SEAS AN emissions (Figs. 5.11d and 5.18 SEAS) in the UT. As a result, CO from the Asian emissions impacts CO anomalies in the UT over Eastern Africa with EQAS contribution of 15–20 ppb, and SEAS contribution of 5–10 ppb (Fig. not shown).

5.2.4 Summary and conclusions

IAGOS O₃ and CO observations since 1994 and 2002 respectively, were used in order to analyse vertical profiles over 20 tropical sites, along with the (lower part) of the upper tropical troposphere. According to Petetin et al. (2018a), a few hundreds meters above the ground, IAGOS measurements are representative of the urban background and of the regional scale at higher altitudes in the lower troposphere. Furthermore, IASI, which provides global daily O₃ and CO distributions with a coarse vertical resolution, allows us to complement IAGOS observations on the global scale over the data sparse tropical band. Throughout the paper we have shown that the anomalies detected by IAGOS are often also detected by IASI at the regional scale.

In the LT, the CO anomalies over the tropics are caused by a combination of AN and BB emissions. In the majority of the clusters, local AN contributions are dominant all year long. The BB contribution increases or dominates over some clusters, when the regional or local fires are active. Local AN emissions have greatest impact over Asia where they account for more than 80 % of the CO. The BB impact increases over South China (35 % in April), and dominates over the Gulf of Thailand (90 % in October) during the local fires (SEAS and EQAS resp.). Over NTr Africa, local AN contributions are in the range of 60–85 % all year, except July. During the SH dry season, CO impacted by the SHAF fires is transported northwards contributing significantly to LT CO anomalies over NTr Africa (53–66 % over Lagos and Guinea Gulf). Similar impact of the SHAF fires is found over Khartoum in July. In contrast, the rest of the Arabian and Eastern Africa clusters are impacted by local AN emissions all year long (70–95 %). Over South America, stronger AN contribution are found over the STR (81–94 % over SBrazil) than in the NTr (75–80 % Caracas and Bogota), while the contributions from the local fires are similar (51 % over Caracas in April and 53 % over SBrazil in October). The highest BB impact is found over STR Africa during the NH and SH dry season with contributions of 60 and 90 % respectively. As expected, the local BB dominate the LT CO anomalies during the local fires, however there is important transport from the NHAf. Despite the fact that BB dominates over STR Africa during the dry seasons,

the AN emissions are important during the transition periods (46 and 80 %). Our results highlight the importance of the AN emissions over the tropics, even in the STr. This is in accordance with the global decreasing trends of BB (Andela et al., 2017) and the increasing AN emissions (Granier et al., 2011).

In the MT and UT, the BB contributions are increased compared to the LT, and their effect dominates over more clusters. Also, the contribution of the transport is more important than in the LT, where mostly local emissions dominate. Over NTr Africa, the BB dominates twice a year, during the NH and SH dry seasons, because of local and SHAF fires respectively. In STr Africa, as in the LT, BB dominates all year long except April. In addition to the African BB, AN SEAS and BB SHSA contributions are found in the MT and UT. Over Asia, BB from SEAS in April, exceeds the AN contribution over the SE Asian coast (South China, Manila, Ho Chi Minh City) in the MT. In contrast, the EQAS BB effect is stronger in the UT, extending over SE Asian coast (China, Ho Chi Minh City, Manila) and India (Madras), but also Eastern Africa (Addis Ababa).

Over Africa, the O_3 and CO maxima are observed in the low troposphere during the respective dry season. The role of the local AN emissions are more important than previously noted (Reeves et al., 2010; Mari et al., 2008; Sauvage et al., 2005) as: i) local AN emissions define the O_3 and CO anomalies over NTr Africa, and ii) the persistent CO-rich surface layer is caused by local AN emissions (40 and 86 %) in the absence of the local fires. Africa is also the most important tropical region in terms of export of emissions in the tropical troposphere. According to IASI horizontal distributions, the main export pathway is the inter-hemispheric transport of O_3 and precursors from the dry-season African regions to the wet-season ones (≈ 50 ppb), confirmed by SOFT-IO contributions. During the dry season, the NHAF (resp. SHAF) fires are the dominant source of CO over AEA (resp. Khartoum and Jeddah) in the MT and UT, and they also reach India accounting for 5–10 ppb in the MT and UT. Transport of mostly BB emissions from NHAF and SHAF occurs all year round towards northern South America in all tropospheric layers. The highest NHAF regional impact is found over Caracas in the MT and UT (30 % on average). In contrast, the impact of Asian emissions, is mostly limited on a regional or local scale, especially in the LT and MT. The transport of the Asian emissions is important only during the Asian summer monsoon in the UT towards Arabia and Eastern Africa.

The highest abundances of the O_3 (75 ppb) and CO mixing ratio (800 ppb) among the tropical clusters are found over Northern Hemisphere Africa at about 2.5 km altitude. This is largely a result of the local AN emissions as suggested by the co-occurrence of the peaks of O_3 and CO in the LT. In contrast over Asia, the second most polluted region, the distributions are mostly controlled by meteorological conditions associated with the Asian monsoon phase. The CO maximum occurs in the LT during January, due to the stability of the northeasterlies which confine the CO-rich air masses to the LT. In contrast, annual maximum of O_3 occurs during the pre-monsoon season (April) when the increased

solar radiation favours O_3 production. During the Asian summer monsoon, O_3 and CO mixing ratio minimize in the low troposphere because of : i) transport of clean oceanic air above continental Asia, ii) reduced photochemical O_3 production due to cloudy conditions, and iii) convective uplift of CO-rich air masses from the surface towards the Asian upper troposphere.

Over Asia, the LT and MT CO and O_3 anomalies are mostly impacted by regional or local Asian emissions of AN origin. The BB contribution is important during April and significantly contributes to O_3 and CO anomalies over South China. According to IASI, the BB impact extends over the tropical Pacific. The impact of the AN Asian emissions is important only in the UT during the Asian monsoon and post-monsoon season (July and October). According to IASI, the polluted air masses from the surface are uplifted in the UT in July and are trapped in the AMA. These air masses are transported over Arabia and Northern Africa (CO contributions of 25–30 ppb) causing the annual O_3 maxima due to subsidence and high isolation over the regions. This highlights the importance of long range transport for the air quality in the UT over Arabia, which shows the lowest CO local contribution and the highest O_3 levels among the tropical clusters. The CO transport towards Eastern Africa in the UT by the TEJ, is found in October when the air masses impacted by the Indonesian fires, and the AN continental source are uplifted in the UT, and transported towards Eastern Africa (CO contributions of 15–20 ppb and 5–10 ppb respectively).

Last, over South America the local CO contributions at the surface level are as low as over Arabia and Eastern Asia. During the dry season (October), when the convection moves over the South American fires, CO and precursors are trapped in an anticyclonic circulation developed over Central South America, resulting in the annual local maxima of O_3 and CO. The transatlantic transport of O_3 and precursors over the Atlantic can be seen by IASI and this contributes to the O_3 wave-one pattern (Sauvage et al., [2007b](#)). This is confirmed by SOFT-IO which calculates contribution of 10–15 ppb from SHSA and 10–15 ppb NHSA, in the altitude of the anticyclone (MT).

5.2.5 Appendix

5.2.5.1 SOFT-IO CO contributions

Vertical profiles

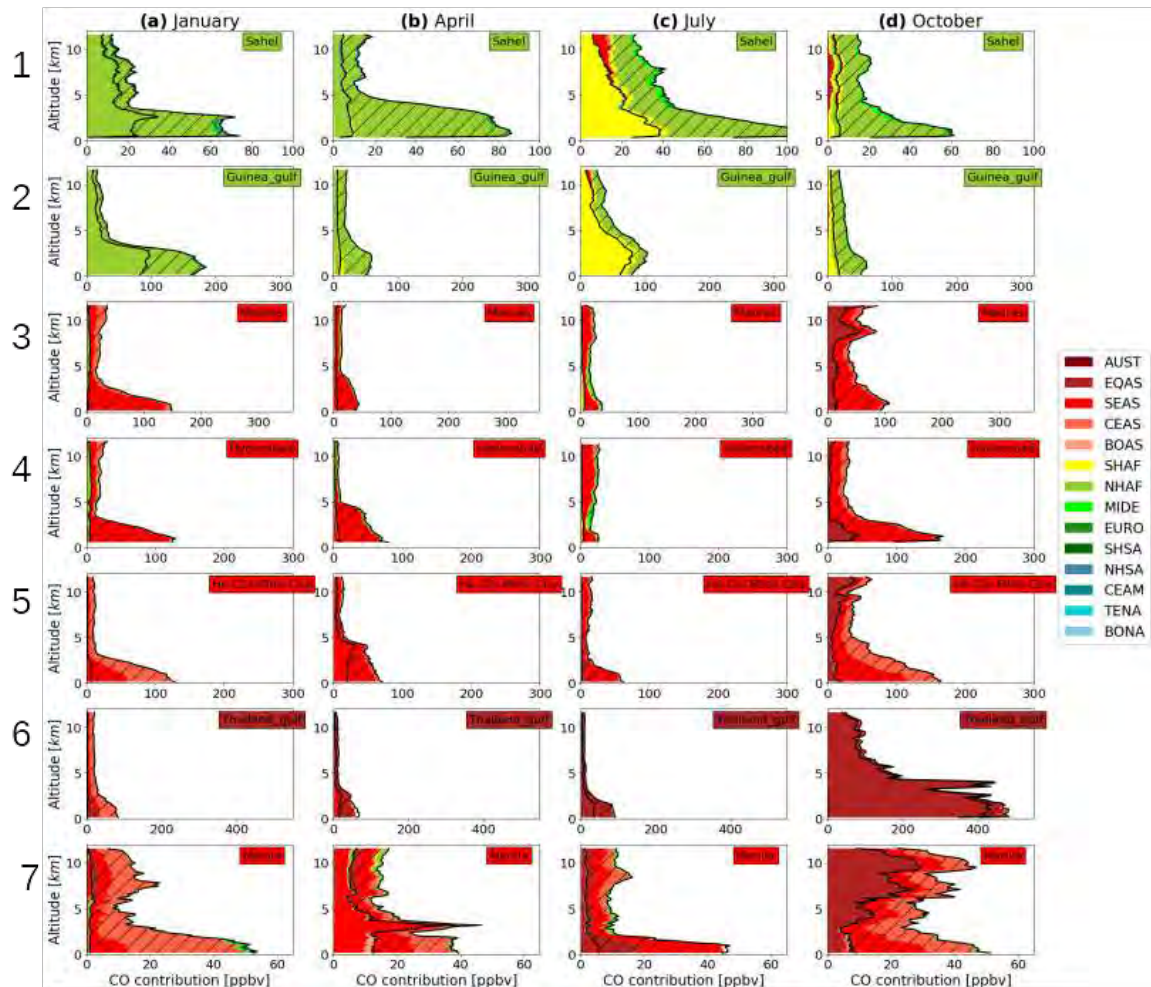


Figure 5.12: Same as Fig. 5.4 (panel 3) for CO contributions over Sahel (1), Gulf of Guinea (2), Madras (3), Hyderabad (4), Ho Chi Minh City (5), Gulf of Thailand (6) and Manila (7).

Low, mid and upper troposphere

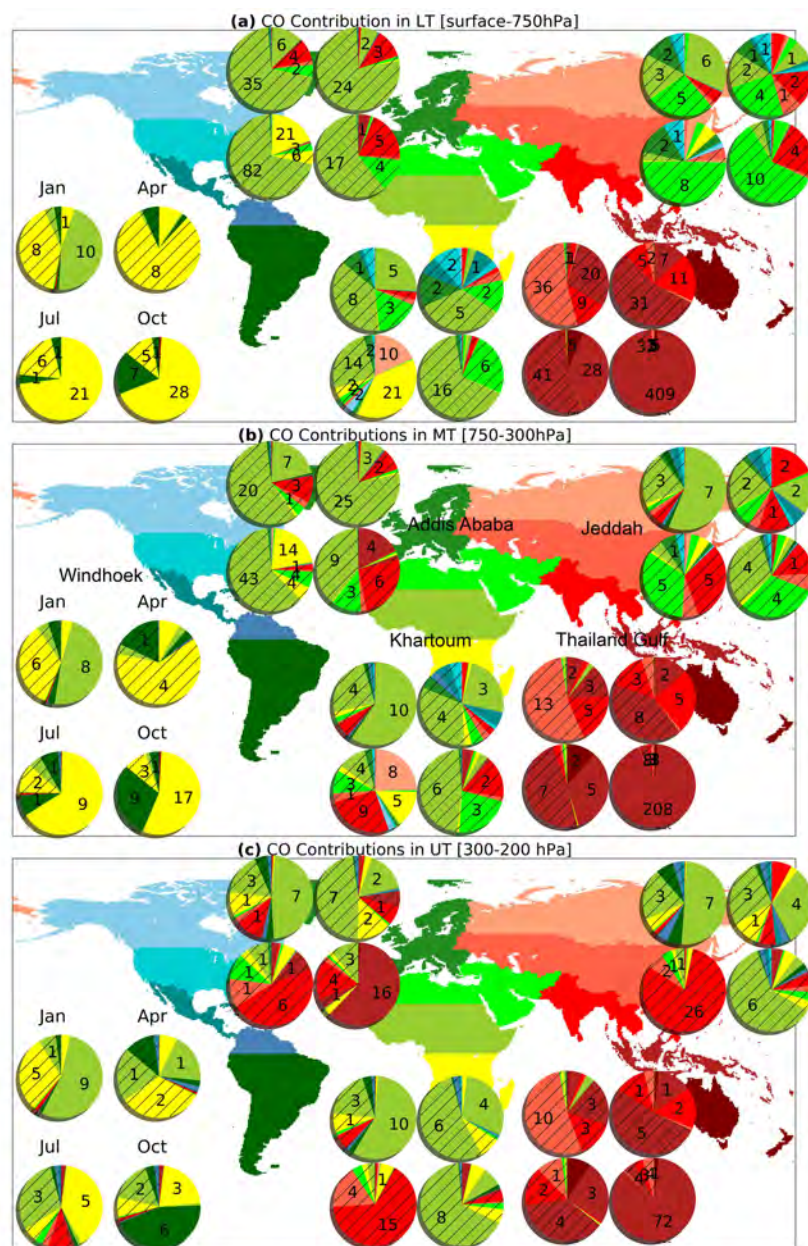


Figure 5.13: Same as Fig. 5.5 for CO contributions over Windhoek, Addis Ababa, Khartoum, Jeddah and Gulf of Thailand.

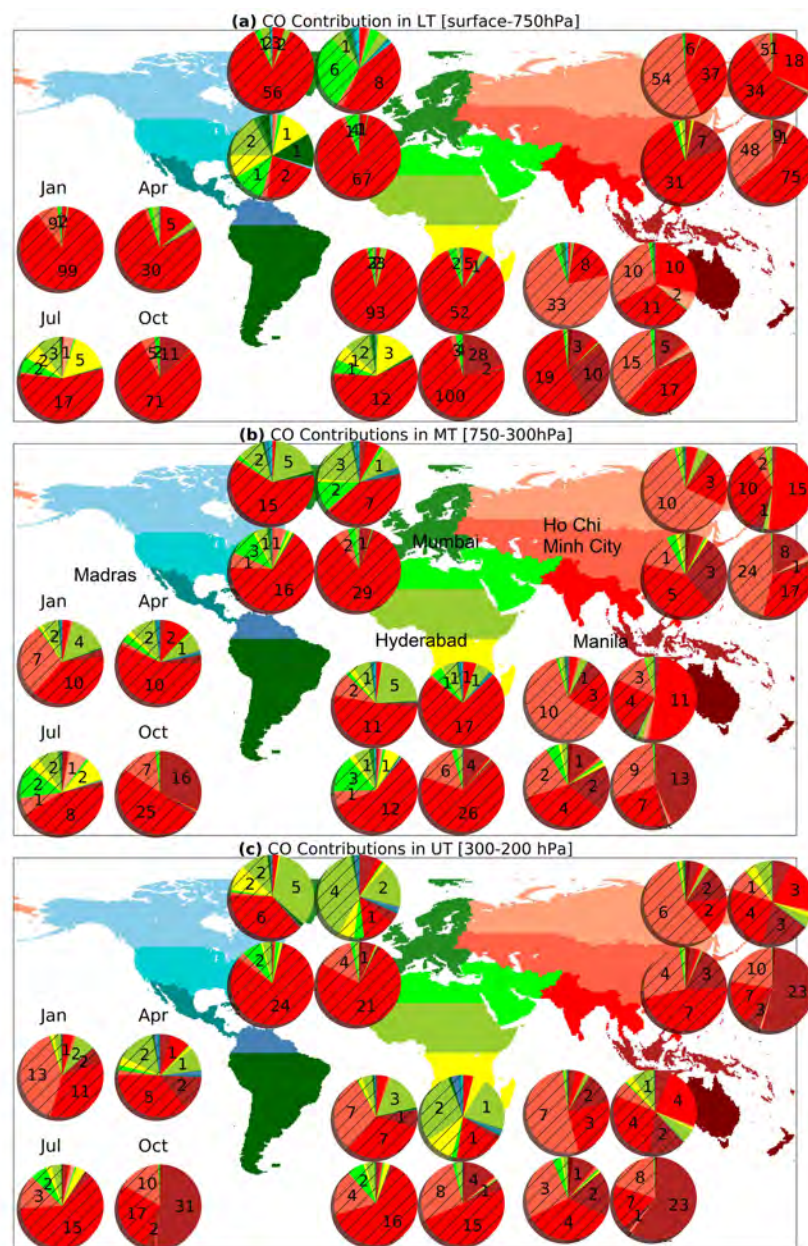


Figure 5.14: Same as Fig. 5.5 for CO contributions over Madras, Mumbai, Hyderabad, Ho Chi Minh City and Manila.

Upper troposphere

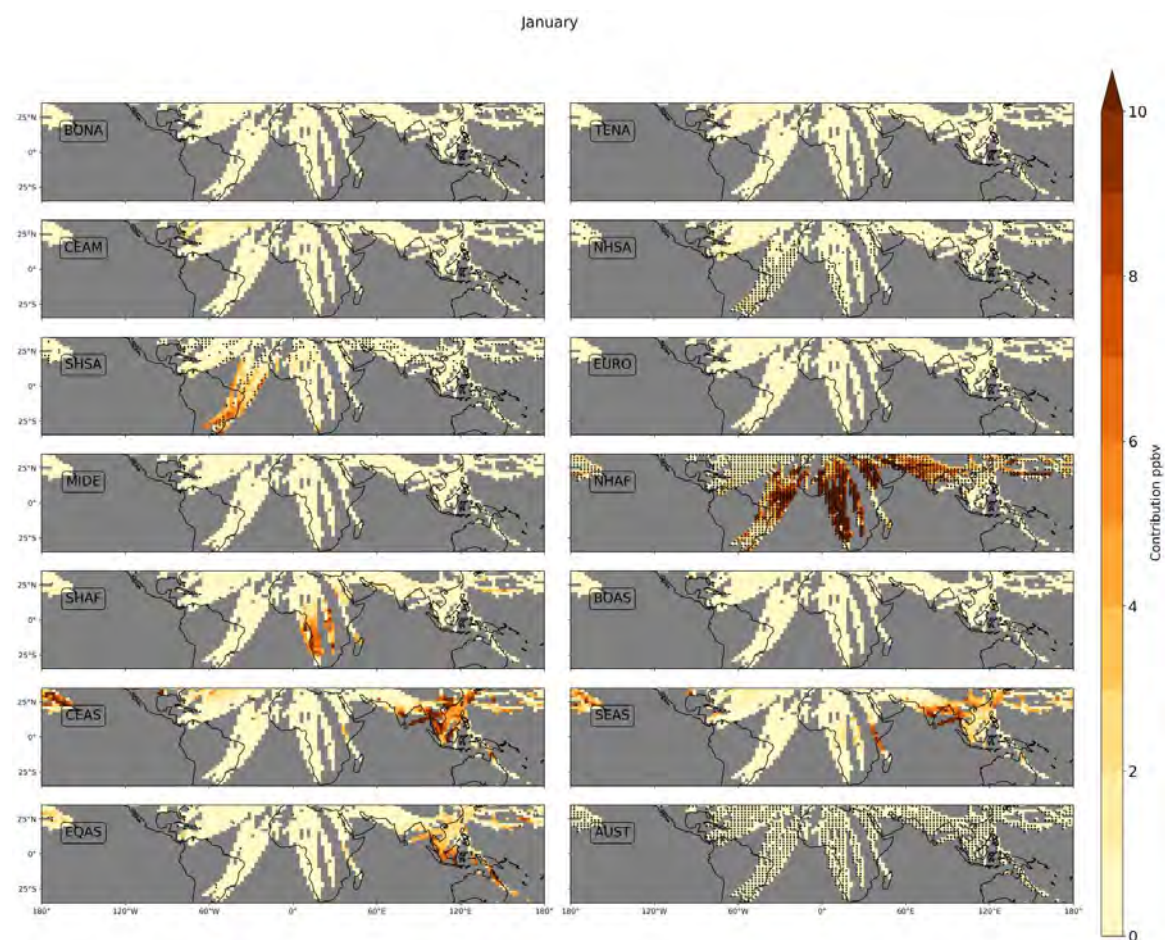


Figure 5.15: Mean CO contribution (in ppb) per source region in the tropical UT (300–185 hPa) averaged from 2002–2019 for January. The hatched part indicates BB as the dominant source of CO.

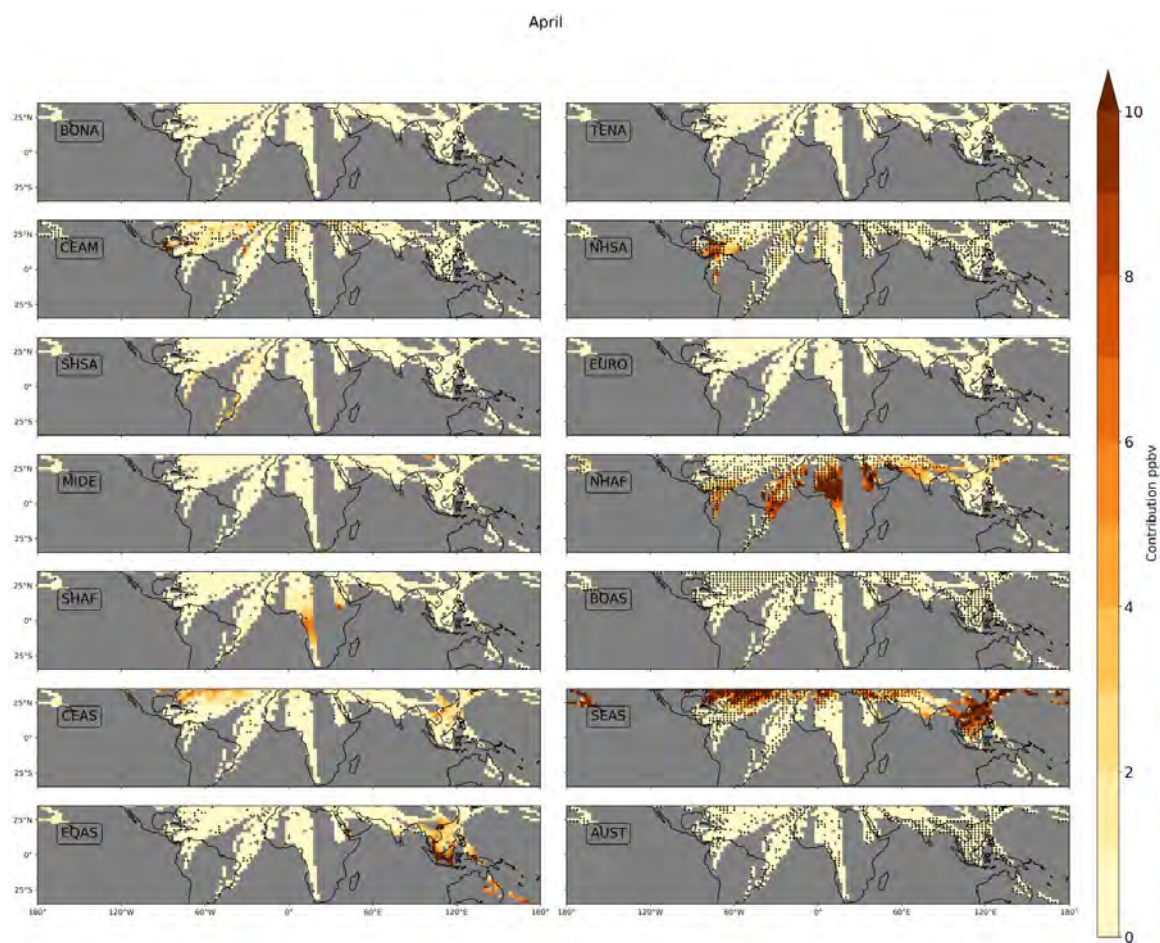


Figure 5.16: Same as Fig. 5.15 for April.

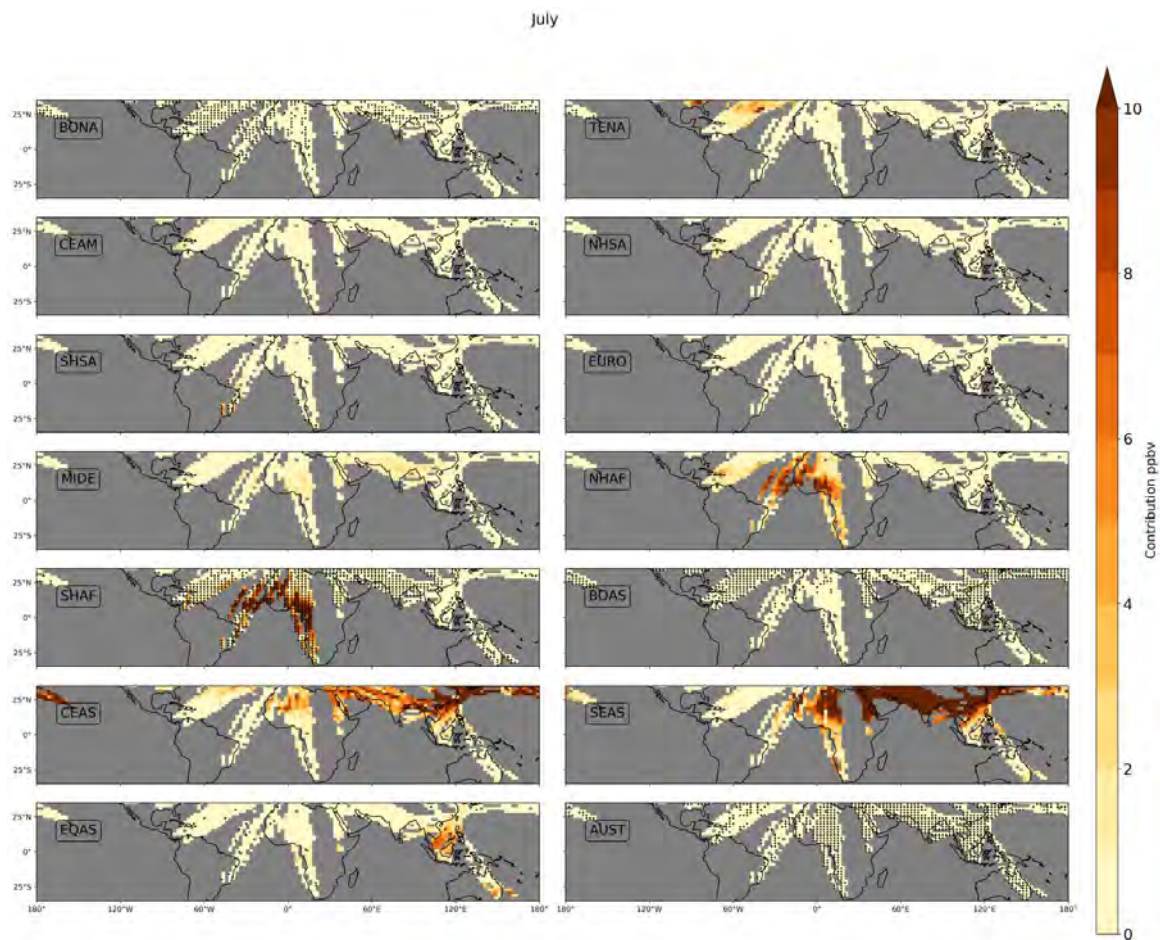


Figure 5.17: Same as Fig. 5.15 for July.

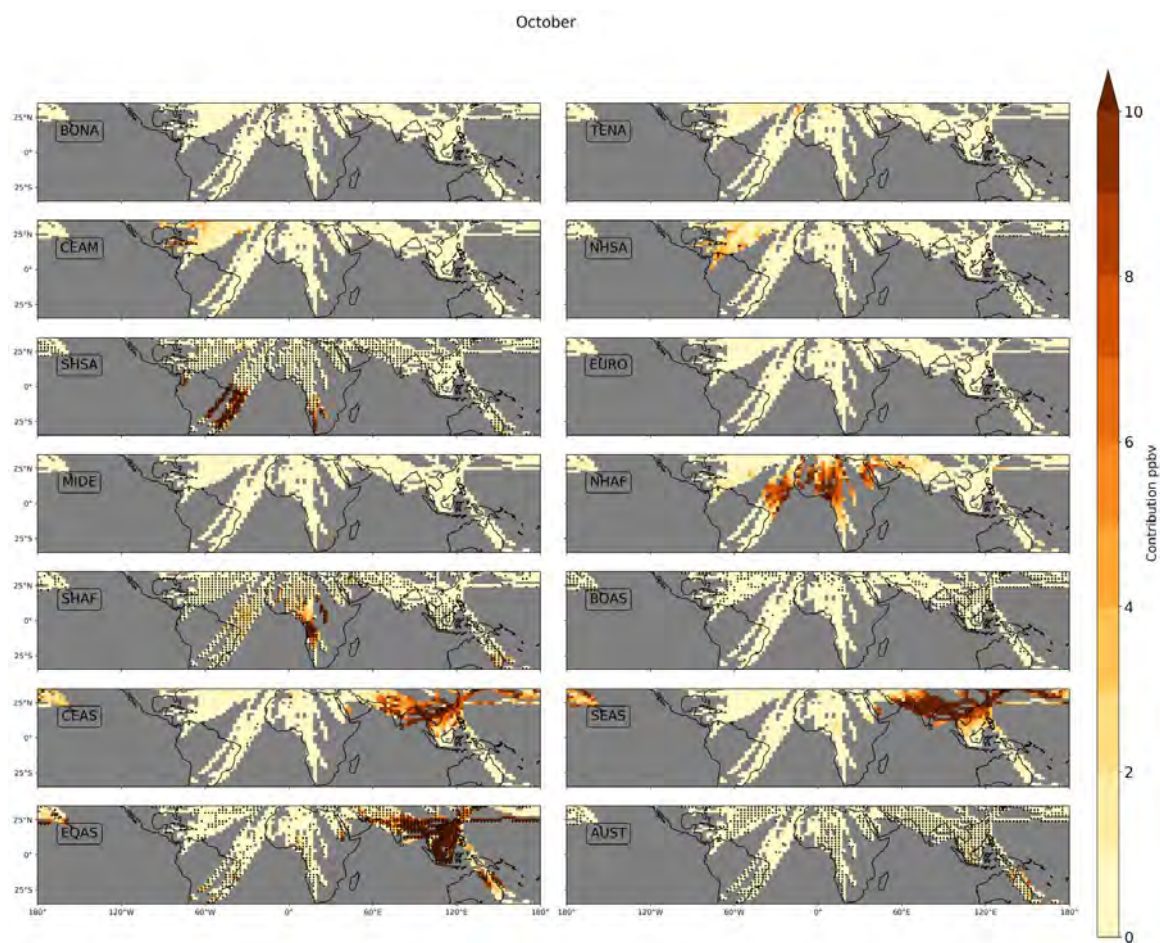


Figure 5.18: Same as Fig. 5.15 for October.

Data availability. The IAGOS data are available on the IAGOS data portal (<https://doi.org/10.25326/20>). The SOFT-IO v1.0 products are part of the ancillary products of IAGOS central database (<https://doi.org/10.25326/2>; <https://doi.org/10.25326/3>). The SOFRID-O₃ data are freely available on the IASI-SOFRID website (<http://thredds.sedoo.fr/iasi-sofrid-o3-co/>, last access: 8 June 2022; SEDOO, 2014).

Author contribution. MT, BS and BB designed the research. All the co-authors contributed to acquisition of data. MT analysed the data. MT, BS and BB interpreted the data. MT drafted the article. MT, BS and BB revised the article. VT and HC commented the article. ELF and BB are responsible for the SOFRID retrieval software. ELF is in charge of the production and quality control of SOFRID data.

Competing interests. The authors declare that they have no conflict of interest.

Acknowledgements We acknowledge the strong support of the European Commission, Airbus and the airlines (Deutsche Lufthansa, Air France, Austrian, Air Namibia, Cathay Pacific, Iberia, China Airlines and Hawaiian Airlines) that have carried the MOZAIC or IAGOS equipment and performed the maintenance since 1994. IAGOS has been funded by the European Union projects IAGOS-DS and IAGOS-ERI. Additionally, IAGOS has been funded by INSU-CNRS (France), Météo-France, Université Paul Sabatier (Toulouse, France) and Research Center Jülich (FZJ, Jülich, Germany). The IAGOS database is supported in France by AERIS (<https://www.aeris-data.fr>). IASI is a joint mission of EUMETSAT and the Centre National d'Etudes Spatiales (CNES, France). The authors acknowledge the CNES for financial support for the IASI activities.

Financial support. This research has been supported by Bonus Stratégique programme at Université Paul Sabatier Toulouse III who funded the first author's doctoral position.

5.2.6 Supplement

5.2.6.1 CO emissions

Biomass burning

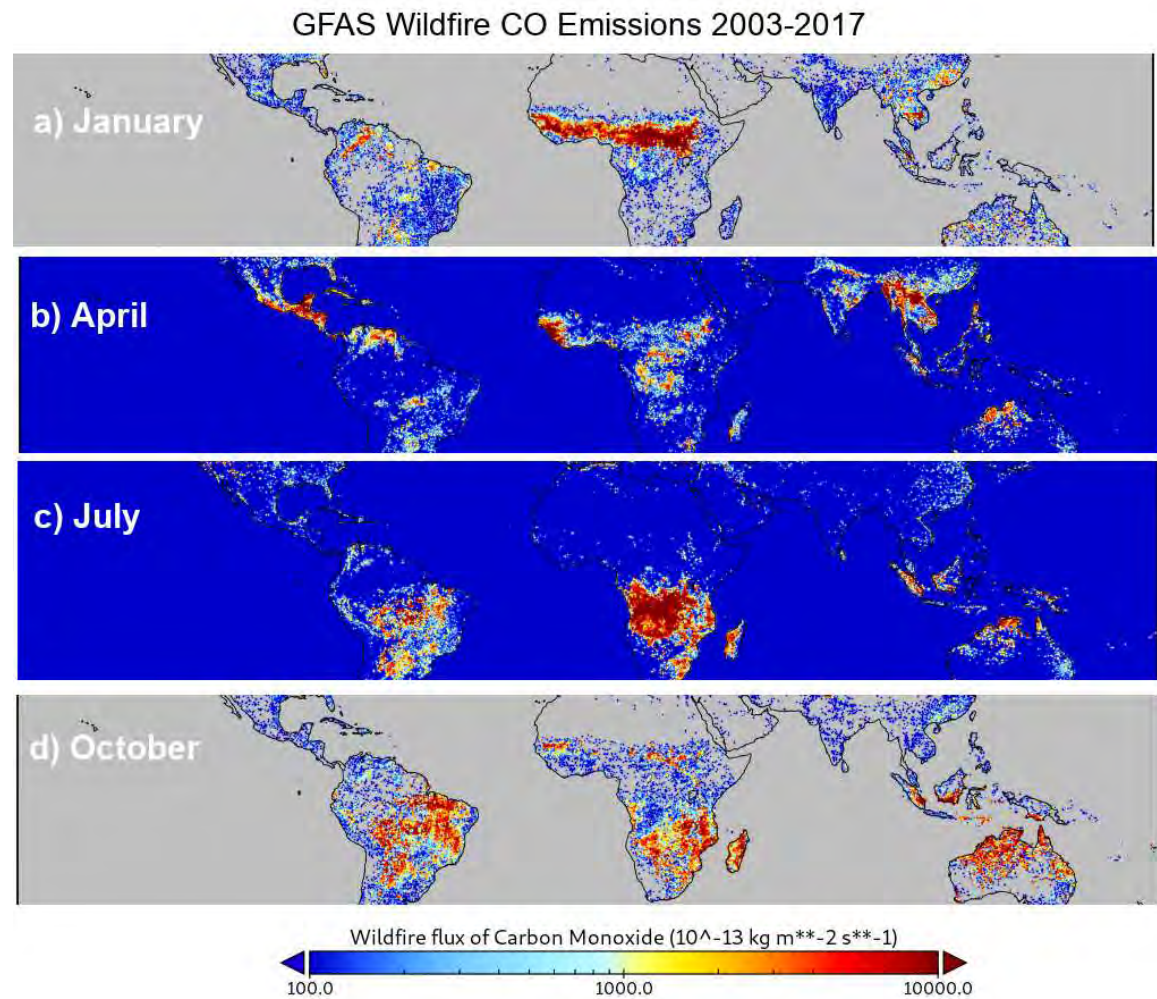
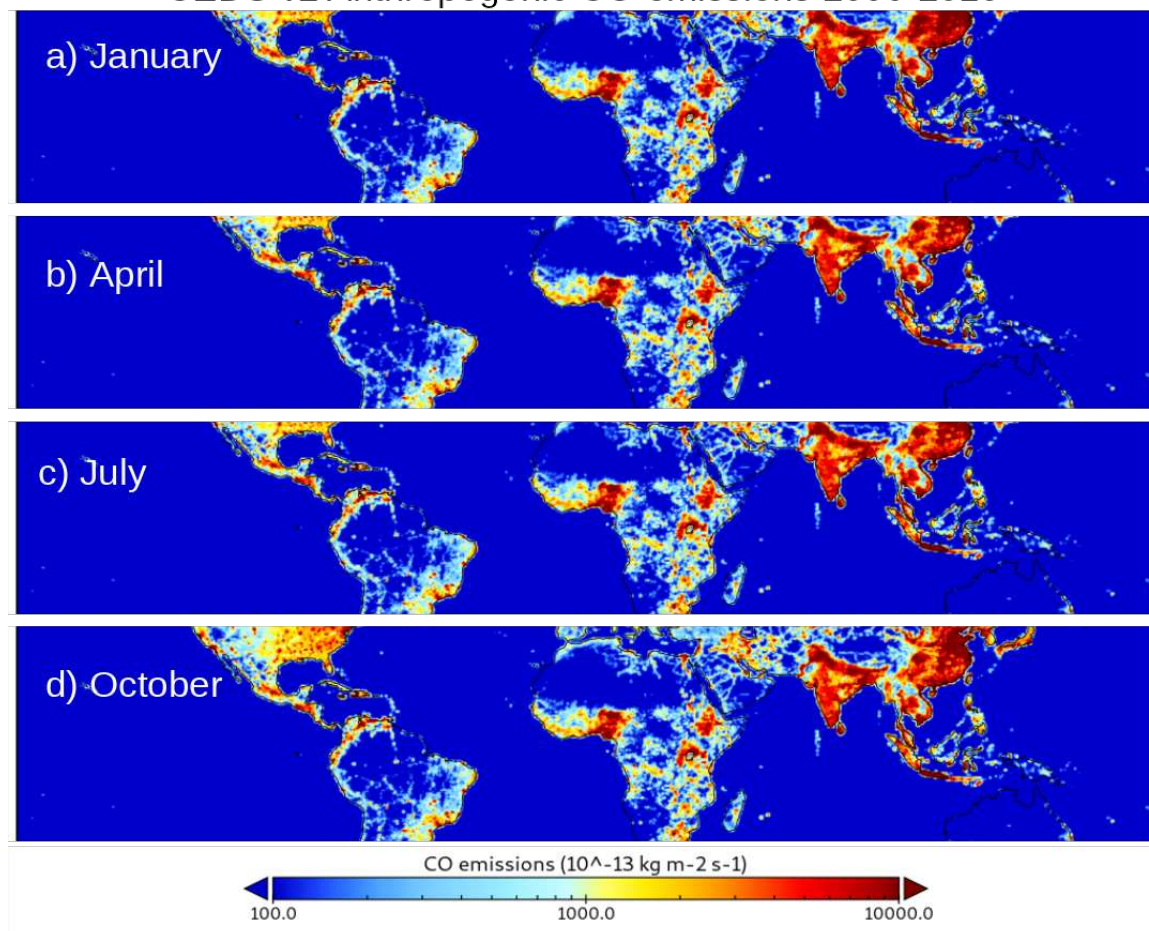


Figure 5.19: GFAS BB CO emissions (in $\text{kg m}^{-2} \text{ s}^{-1}$) averaged from 2003 to 2017.

Anthropogenic

CEDS v2 Anthropogenic CO emissions 2000-2019

**Figure 5.20:** CEDS2 AN CO emissions (in $\text{kg m}^{-2} \text{ s}^{-1}$) averaged from 2000 to 2019.

Winds

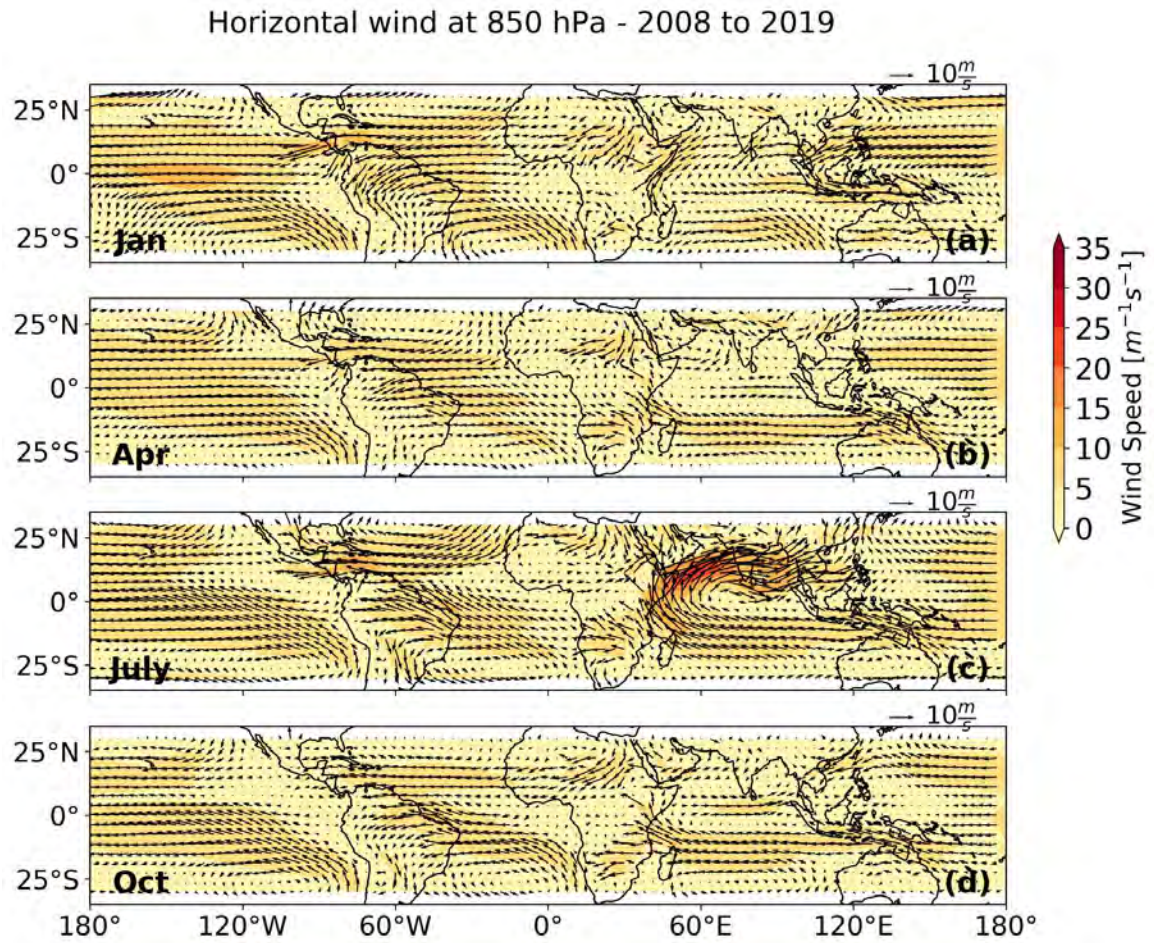


Figure 5.21: ECMWF Reanalysis 5th Generation (ERA5) wind vectors at 850 (a–d), 550 (e–h) and 250 (i–l) hPa averaged from 2008 to 2020 at $0.25 \times 0.25^\circ$ resolution.

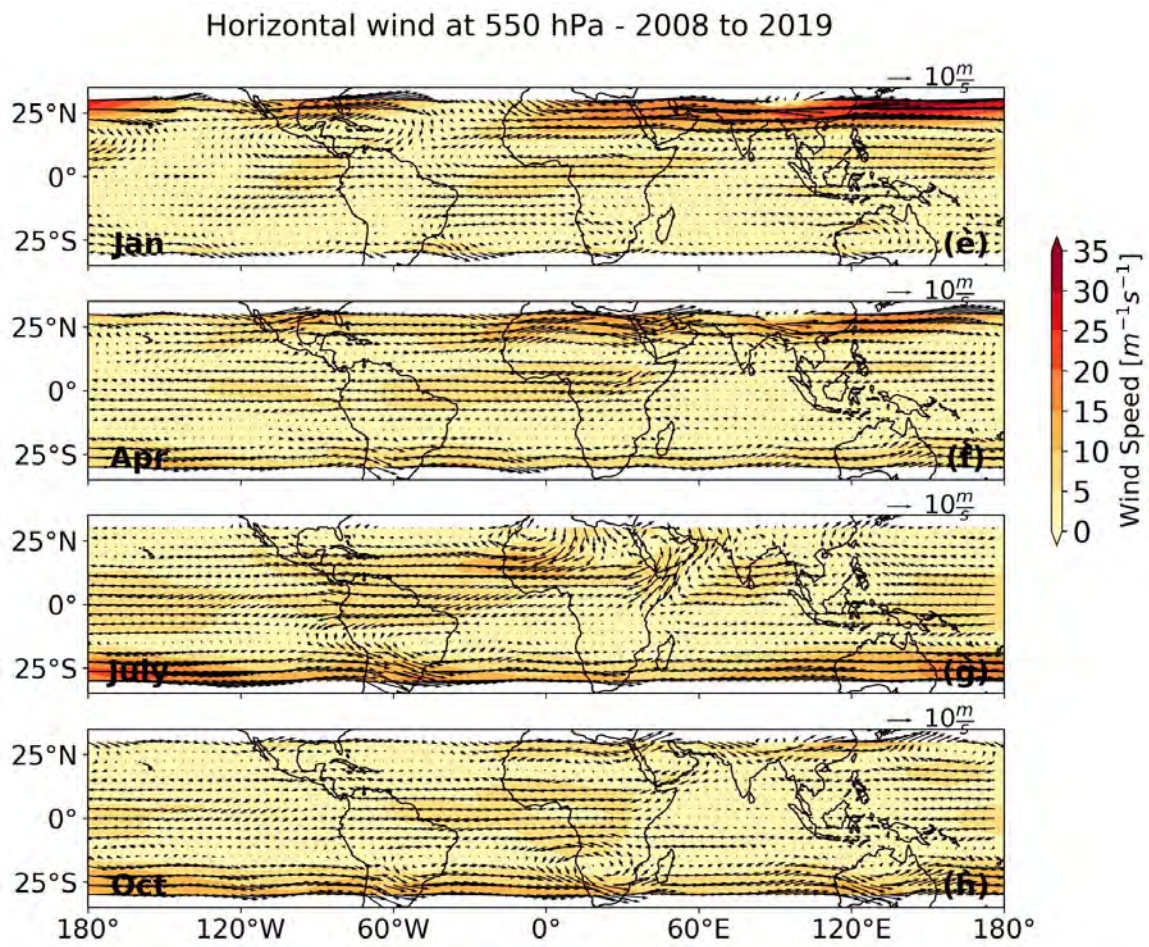


Figure 5.21: Continued.

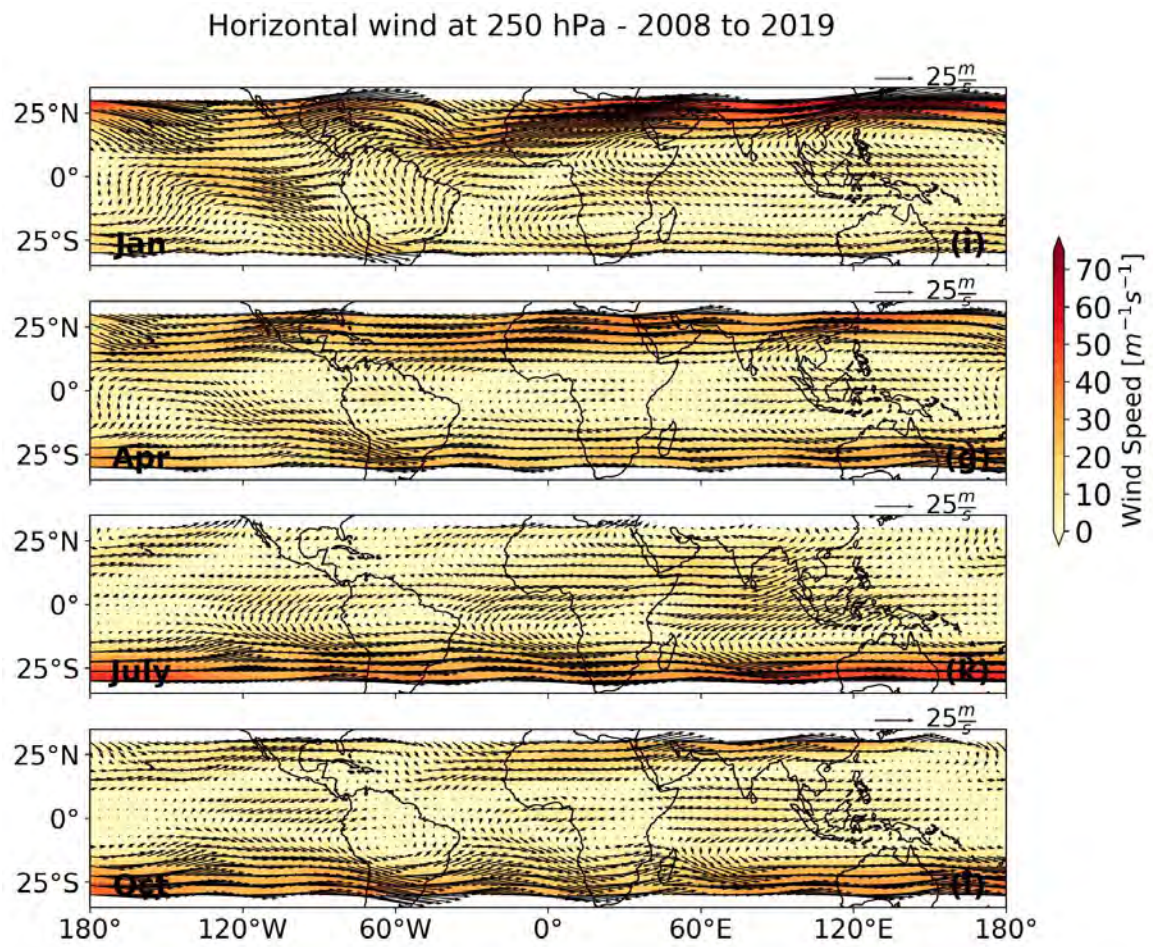


Figure 5.21: Continued.

CHAPTER 6

Conclusions and Perspectives

6.1 Conclusions

O₃ and CO are harmful pollutants, strongly impacting the oxidizing capacity of the troposphere and influencing the climate in a direct (O₃) and an indirect (O₃ and CO) way. The tropics are a key region for O₃ and CO, as they are associated with intense photochemistry and strong natural sources (biomass burning, lightning, and soil emissions). Also, the fast increase in inhabitants results in enhanced anthropogenic emissions, causing air quality issues. Dynamical processes such as deep convection favour the redistribution of the polluted tropical air masses on a local and global scale. Despite the importance of the region, the tropical troposphere and its evolution remain little documented in comparison with the northern mid-latitudes, due to the limited available in situ observations.

The overall objective of this thesis is to document the characteristics of the tropical O₃ and CO distributions and to characterise the tropical ozone change. To do so, we took advantage of in situ aircraft measurements provided by the IAGOS program since 1994 for O₃, and 2002 for CO, characterised by high accuracy and fine vertical resolution. Further, global distributions from IASI-SOFRID retrievals were used to complement IAGOS data and study intercontinental transport pathways of tropical air masses.

In the first part of the thesis, two validation studies have been performed for IASI-SOFRID using IAGOS data. The first one focuses on the evaluation of UT O₃ and CO climatologies. The validation focuses on the tropics, where deep convection can transport chemical species at higher altitudes, where their lifetime is enhanced due to lack of depositional sinks. To do so, we computed the UT CO and O₃ meridional transects based on IAGOS and SOFRID data, over regions where IAGOS showed the highest spatial coverage (Atlantic, North Atlantic, Africa, South Asia, and SouthEast Asia) from 2008–2019. For O₃, on average we find a correlation coefficient of 0.70 with a mean of 9 ± 18 %, not significant positive bias. The ranges of the correlation coefficients (0.66 to 0.84) and the biases (-3 to 20 % resp.) for the different transects indicate high consistency between IAGOS and SOFRID spatiotemporal variabilities. Concerning CO, the agreement between IAGOS and SOFRID is good (correlation coefficient of 0.75, and a mean negative bias of 6 ± 10 %). All transects display high correlation coefficients (0.75–0.90) except the SEAsia one and negative biases

from 0 up to 9 %.

Overall, IAGOS and SOFRID meridional transects and horizontal distributions are fairly consistent in the qualitative representation of O_3 and CO patterns in the tropical UT. SOFRID captures well the seasonal variability of O_3 and CO in the tropical UT, and the minima and maxima are well collocated relative to IAGOS. The discrepancies between SOFRID and IAGOS (e.g. the underestimation of the CO seasonal maxima over Africa and Brazil, and the O_3 overestimation towards the extratropics) are mainly due to differences in the nature of the observing systems. The smoothing of the O_3 and CO profile due to the coarser resolution of the satellite explained part of the discrepancies. Another difference of the systems is that IAGOS sees the lower part of the UT in the tropics and subtropics, while SOFRID is more sensitive to the UTLS in the extratropics, and the TTL in the tropics.

The second study aimed to evaluate tropospheric (1000–200 hPa) O_3 trends from IASI using IAGOS vertical profiles and determine the impact of the vertical sensitivity of IASI upon the documented trends. To do so, we computed the tropospheric O_3 change between a modern and reference period. Because of the sparsity of IAGOS data in space and time, we adjusted the aforementioned period to the IAGOS data availability.

The comparisons between IASI monthly with IAGOS data revealed big discrepancies in the observed tropospheric O_3 change. For IASI, the majority of the O_3 changes were non-statistically significant and close to zero, in contrast to IAGOS. The comparisons between IASI and IAGOS data only for the specific days when IAGOS are available improved the agreement in the observed tropospheric O_3 change (in terms of sign and magnitude). Thus, our results indicate that the O_3 change is sensitive to the sampling.

The comparisons between the tropospheric column and the partial (700–200 hPa) column O_3 change using IASI and IAGOS data (for their overlapping days) showed that their agreement is the best when we account for the partial column, due to the higher sensitivity of the retrievals in this layer. This validation study proves that we can rely on IASI data for O_3 trends in the region of its highest sensitivity.

As a next step, we used IASI data in the partial column, to assess the free tropospheric O_3 changes between 2018–2020 and 2008–2010. We selected these periods because of their maximum separation in the IASI period. Our results showed an increase in the global partial O_3 average by approximately 0.4 DU (or 1.7 %), with the greatest increase in the tropics (0.32 DU or 2 %). In accordance with previous studies, the largest O_3 increase is observed over South and SouthEast Asia (approximately 10 %) probably due to increased emissions. Small O_3 increases over West Africa (by 2%), likely due to increases in anthropogenic emissions. In contrast, O_3 decreases over South Africa (by 4%) probably associated with a decline in biomass burning. Previous studies based on satellite (TOST for 2013–2017 and IASI for 2008–2016; Gaudel et al., 2018) and chemical transport model (from 2013–2015 to 1995–2015) confirm the decrease in O_3 over South Africa.

The second part of the thesis focuses on the tropical CO and O₃ distributions and aims to offer a better understanding of their seasonal characteristics and control factors. To do so, we analysed IAGOS measurements for the whole IAGOS period (since 1994 for O₃ and 2002 for CO), and satellite data based on IASI-SOFRID retrievals (since 2008). We also used the SOFT-IO tool, which provides auxiliary information for the IAGOS-CO measurements, such as its geographic origin and its type of emissions (AN or BB).

The main findings are the following:

- The AN emissions are of great importance in the LT CO enhancement in the tropics, even in the SH. AN emissions dominate the CO maxima above the surface over all clusters (except Central Africa and the Gulf of Thailand). The role of AN emissions over Central Africa is highlighted by a persistent CO enhancement above the surface on an annual basis.
- In the MT and UT, the BB contribution is increased relative to the contribution from AN. Also, the contribution from transported CO emissions is more important than in the LT, where local emissions dominate. This is because, at such altitudes, long-range transport is favoured by stronger winds, allowing the redistribution of the plumes on an intercontinental scale (e.g. Liang et al., 2004; Barret et al., 2008). Over NH Africa, BB dominates in the MT during NH (January) and SH (July) fire seasons. The SouthEast Asian fires in April mainly cause the MT CO anomalies over the SE Asian coast (South China, Ho Chi Minh City, Bangkok, and Manila). In contrast, during the Equatorial Asian fires in October, the impact of BB in the UT has a larger spatial extent, over the SE Asian coast reaching India and Africa.
- The highest CO and O₃ maxima among the tropical clusters are observed over NH Africa in the LT during the dry season (80 ppb of O₃ at 2.5 km and 850 ppb of CO at 0.3 km over Lagos in January). Despite the active fires, the CO and consequently the O₃ maxima are mostly attributed to local AN emissions (approximately 60 %).
- The second highest O₃ and CO maxima are observed over Asia. O₃ peaks in the FT (at 6km) in the post-monsoon season (April), while CO maximises in the LT (0.5 km) in January due to local AN emissions. The only cluster with O₃ maxima in the LT is South China (75 ppb at 2.6 km), during the Central Asian fires (April). These fires also contribute to LT CO anomalies, in addition to local and regional AN emissions.
- The smallest LT CO maxima are observed over South America, due to lower CO emissions relative to Africa and Asia. The only significant CO and O₃ enhancement is observed in the MT during the local fires season (October) when O₃ and precursors impacted by the local AN and fire emissions are trapped in an anticyclone and transported toward South Africa.
- Africa is the most important tropical region in terms of export of emissions in the

troposphere. The main transport pathway is from the dry-season African regions towards the wet-season ones. Contributions from NH Africa are found over Arabia and Eastern Africa, and India during the dry season and towards NH South America all year long.

- The impact of the Asian emissions in the LT and MT is limited on a regional or local scale. In the UT, the export of Asian emissions intensifies during the Asian summer monsoon (July). The polluted air masses from the surface are uplifted in the Asian UT and trapped in the AMA. These air masses are transported over Arabia and Eastern Africa causing the annual O₃ maxima due to subsidence and high isolation over these regions.

6.2 Limitations and Perspectives

Observations in the Tropics

As we mentioned in [Section 3.1](#), the IAGOS program provides a rich database of atmospheric compounds on a global scale. This is the first time that IAGOS observations were analysed thoroughly to study the climatological O₃ and CO distributions over the tropics. As a next step, it could be interesting to document the interannual variability of these atmospheric compounds. Previous studies (e.g. Voulgarakis et al., [2015](#)) have found that CO interannual variability on a global scale is almost entirely attributed to BB emissions. Thus, we could testify the impact of BB emissions and their changes, on O₃ and CO over the tropics, where the strongest BB emissions occur (see [Section 2.2](#)). In addition, we could analyse the impact of nonseasonal variation of the circulation such as the ENSO oscillation ([Section 2.1](#)) on the tropical O₃ and CO distributions.

One limitation of our study is that IAGOS data are provided over selected locations, mostly in proximity to tropical megacities. To deal with the sparsity of data coverage in the tropics, we could account for other networks and campaigns (e.g. SHADOZ, Atom) providing measurements over this region to complement our knowledge regarding the tropical composition.

Except for O₃ and CO, other atmospheric compounds have been measured by IAGOS over the tropics, such as NO_x (since 2015), NO_y (between April 2001 and May 2005), and NO (with IAGOS-CARIBIC since 1997). These Nitrogen species (especially NO_x) play a key role in O₃ formation (see [Section 1.1.2](#)), emitted among others from soils and lightning emissions, which are mostly active in the tropics (see [Section 2.2](#)). Thus, studying tropical NO_x based on in situ observations in combination with simultaneous O₃ measurements could help understand better O₃ photochemistry. In the same scope, using a global transport chemical model could help to interpret the characteristics of O₃ and CO distributions in the tropics, by quantifying their sources and sinks. Further details on the model will follow later.

Trends in the Tropics

Our study provided some insights into the impact of the sampling of IAGOS and the vertical sensitivity of IASI on the observed O₃ change (Section 4.2). However, uncertainties remain in the quantification of O₃ trends based on satellite products. In addition, one limitation of our study is that the O₃ change has not been addressed by IAGOS data in the tropics as a whole. Because of the sparse measurements in time over the tropical sites, it was not possible to define the same reference and modern periods for the computations of the O₃ change. For these reasons, it would be interesting to estimate the trends based on IAGOS measurements using the quantile regression method. This method predicts trends for distribution by taking into consideration the quantiles of the distribution instead of the condition means. An advantage of this method is that it can tolerate missing values and outliers, making it appropriate for datasets with gaps in time and space like IAGOS and ozonesondes.

Previous studies have already used in situ data such as IAGOS (e.g Gaudel et al., 2020; Wang et al., 2022) and ozonesondes (Christiansen et al., 2022) for O₃ trends computations on a global scale. However, these studies do not focus on the tropics and lack documenting the trends of CO. Cohen et al. (2018) computed the trends for O₃ and CO using IAGOS, but over the upper troposphere in the northern mid-latitudes. Tropical O₃ trends have been documented by Thompson et al. (2021) over the SHADOZ sites, mostly located in the southern tropics. Thus, we could complement this study by providing O₃ trends for additional sites, as well as CO trends. The O₃ and CO trends provided by IAGOS would be useful for evaluating satellite products and the performance of chemical models used for interpreting trend attributions in the tropics.

One limitation of IAGOS measurements is that they under-sample the tropical troposphere because the high tropopause (12–18 km Gettelman et al., 2002) is higher than the IAGOS cruise altitude (9–12 km). To make fair comparisons with satellite trends, and sample the full tropospheric column, it would be necessary to complete IAGOS profiles using the appropriate data such as MLS profiles.

Attribution of trends in the tropics

Our results highlight the largest increase of free tropospheric O₃ over the tropics. This is in accordance with recent studies reporting that the tropics are responsible for the greatest increase in tropospheric O₃ (Zhang et al., 2016; Gaudel et al., 2018). However, the positive O₃ trends are attributed to different factors such as biomass burning (Heue et al., 2016), anthropogenic emissions (Zhang et al., 2016), and dynamics (Lu et al., 2019a; Thompson et al., 2021). Therefore, the chemical and physical mechanisms responsible for the O₃ increase are not clear yet and need further investigation.

To have a better understanding of the evolution of tropical O₃ and precursors, it would be necessary to use a global **Chemistry Transport Model (CTM)**. Modelling studies (e.g. Zhang et al., 2016; 2021, Lu et al., 2019a) attributing O₃ trends lack an updated evaluation of the

anthropogenic and climate factors, as they are focused on rather limited periods up to 2010. Also, the coarse horizontal resolution of the simulations ($4^\circ \times 5^\circ$, Lu et al., 2019a; Wang et al., 2022) limits the ability of the model to capture the fine-scale characteristics of O_3 trends, especially near the surface where the lifetime of O_3 and precursors is shorter (e.g. Young et al., 2018).

In this context, we could take advantage of the new generation of the global GEOS-Chem CTM (Bey et al., 2001b), the **GEOS-Chem High Performance (GCHP)** (Eastham et al., 2018; Martin et al., 2022). In contrast to GEOS-Chem, the GCHP allows the parallel execution of the model and thus it achieves greater accuracy in simulating transport (Eastham et al., 2018). GCHP also enables the simulations to be performed at high resolution ($0.5^\circ \times 0.625^\circ$), with 72 vertical layers extending from the surface up to 0.01 hPa. GCHP represents the complete chemistry of NO_x -VOCs- O_3 -aerosols by coupling the troposphere to the stratosphere (Eastham et al., 2014). It is driven by the MERRA-2 meteorological fields from the NASA Global Modelling and Assimilation Office (GMAO), with a native horizontal resolution of $0.5^\circ \times 0.625^\circ$ (Gelaro et al., 2017).

The simulations should represent the evolution of the atmospheric composition over a period accounting for demographic and climate changes (e.g. 1997–2020). The AN emissions could be driven by the latest version of CEDS2 (McDuffie et al., 2020), which is the most up-to-date AN emission inventory and is provided at a monthly $0.5^\circ \times 0.5^\circ$ resolution. Concerning the BB emissions, we could use the GFED4 emission inventory (Giglio et al., 2013), which is available at a monthly $0.25^\circ \times 0.25^\circ$ resolution. The burned area and fire emissions provided by GFED4 are based on satellite information on fire activity and vegetation productivity. Natural emissions of O_3 precursors which are sensitive to the climate, such as biogenic emissions of non- CH_4 VOCs, soil, and lightning emissions of NO_x , can be calculated online in the model.

In this frame, we could perform a series of simulations using GCHP, to calibrate the model and then develop sensitivity tests on the processes related to O_3 chemistry:

- The reference simulation should be conducted at a $0.5^\circ \times 0.625^\circ$ resolution, using year-specific meteorology and emissions for the period 1997–2020. The validation of the reference simulation could be done by comparisons with IAGOS and IASI measurements in the tropics.
- The sensitivity simulations could quantify the impact of changes in: i) anthropogenic emissions, ii) biomass burning emissions, iii) lightning emissions, iv) soil emissions, v) aircraft emissions, vi) methane concentration, and v) meteorology on O_3 and precursors trends in the tropics. This can be achieved by fixing a specific source or meteorology at the 1997 conditions in the model simulations. The contribution of each factor could be estimated as the difference of ozone trends estimated in the reference simulation and the sensitivity tests.

The reference and sensitivity simulations could be useful to assess the controlling factors of the tropical O₃ and precursors trends, as well as their impact on a global scale.

CHAPTER 7

Conclusions and Perspectives in french

7.1 Conclusions in french

L'O₃ et le CO sont des polluants nocifs, qui ont un impact important sur la capacité d'oxydation de la troposphère et influencent le climat de manière directe (O₃) et indirecte (O₃ et CO). Les tropiques sont une région clé pour le O₃ et le CO, car ils sont associés à une photochimie intense et à de fortes sources naturelles (combustion de la biomasse, foudre et émissions du sol). En outre, l'augmentation rapide du nombre d'habitants entraîne une augmentation des émissions anthropiques, ce qui pose des problèmes de qualité de l'air. Les processus dynamiques tels que la convection profonde favorisent la redistribution des masses d'air tropical pollué à l'échelle locale et mondiale. Malgré l'importance de la région, la troposphère tropicale et son évolution restent peu documentées par rapport aux moyennes latitudes nord, en raison du peu d'observations in situ disponibles.

L'objectif global de cette thèse est de documenter les caractéristiques des distributions tropicales de O₃ et de CO et de caractériser l'évolution de l'ozone tropical. Pour ce faire, nous avons profité des mesures in situ par avion fournies par le programme IAGOS depuis 1994 pour O₃, et 2002 pour CO, caractérisées par une haute précision et une fine résolution verticale. De plus, les distributions globales issues des récupérations IASI-SOFRID ont été utilisées pour compléter les données IAGOS et étudier les voies de transport intercontinentales des masses d'air tropicales.

Dans la première partie de la thèse, deux études de validation ont été réalisées pour IASI-SOFRID en utilisant les données IAGOS. La première se concentre sur l'évaluation des climatologies UT O₃ et CO. La validation se concentre sur les tropiques, où la convection profonde peut transporter des espèces chimiques à des altitudes plus élevées, où leur durée de vie est accrue en raison du manque de puits de dépôt. Pour ce faire, nous avons calculé les transects méridiens UT CO et O₃ basés sur les données IAGOS et SOFRID, sur les régions où IAGOS a montré la plus grande couverture spatiale (Atlantique, Atlantique Nord, Afrique, Asie du Sud et Asie du Sud-Est) de 2008 à 2019. Pour O₃, nous trouvons en moyenne un coefficient de corrélation de 0.70 avec un biais positif moyen de 9 ± 18 %, non significatif. Les plages des coefficients de corrélation (0.66 à 0.84) et des biais (-3 à 20 % respectivement) pour les différents transects indiquent une grande cohérence entre les

variabilités spatio-temporelles de IAGOS et SOFRID. Concernant le CO, la concordance entre IAGOS et SOFRID est bonne (coefficient de corrélation de 0.75, et un biais négatif moyen de 6 ± 10 %). Tous les transects présentent des coefficients de corrélation élevés (0.75–0.90), à l’exception du transect SEAsia, et des biais négatifs allant de 0 à 9 %.

Dans l’ensemble, les transects méridiens et les distributions horizontales de IAGOS et SOFRID sont assez cohérents dans la représentation qualitative des patrons de O₃ et de CO dans l’UT tropicale. SOFRID capture bien la variabilité saisonnière de O₃ et CO dans l’UT tropicale, et les minima et maxima sont bien colocalisés par rapport à IAGOS. Les divergences entre SOFRID et IAGOS (par exemple la sous-estimation des maxima saisonniers de CO sur l’Afrique et le Brésil, et la surestimation de O₃ vers les extratropiques) sont principalement dues aux différences dans la nature des systèmes d’observation. Le lissage du profil de O₃ et de CO dû à la résolution plus grossière du satellite explique une partie des divergences. Une autre différence entre les systèmes est que IAGOS voit la partie inférieure de l’UT dans les tropiques et les subtropiques, tandis que SOFRID est plus sensible à l’UTLS dans les extratropiques, et au TTL dans les tropiques.

L’objectif de la seconde étude était d’évaluer les tendances de l’O₃ troposphérique (1000–200 hPa) à partir de l’IASI en utilisant les profils verticaux de l’IAGOS, et de déterminer l’impact de la sensibilité verticale de l’IASI sur les tendances documentées. Pour ce faire, nous avons calculé le changement de O₃ troposphérique entre une période moderne et une période de référence. En raison de la rareté des données IAGOS dans l’espace et le temps, nous avons ajusté la période susmentionnée à la disponibilité des données IAGOS.

Les comparaisons entre les données mensuelles de l’IASI et celles de l’IAGOS ont révélé de grandes divergences dans le changement observé de l’O₃ troposphérique. Pour IASI, la majorité des changements de O₃ n’étaient pas statistiquement significatifs et proches de zéro, contrairement à IAGOS. Les comparaisons entre les données IASI et IAGOS uniquement pour les jours spécifiques où IAGOS est disponible ont amélioré la concordance dans le changement O₃ troposphérique observé (en termes de signe et de magnitude). Ainsi, nos résultats indiquent que le changement O₃ est sensible à l’échantillonnage.

Les comparaisons entre la colonne troposphérique et le changement partiel (700–200 hPa) de la colonne O₃ en utilisant les données IASI et IAGOS (pour leurs jours de chevauchement) ont montré que leur accord est le meilleur lorsque nous tenons compte de la colonne partielle, en raison de la plus grande sensibilité des récupérations dans cette couche. Cette étude de validation prouve que nous pouvons nous fier aux données IASI pour les tendances de O₃ dans la région de sa plus grande sensibilité.

Comme étape suivante, nous avons utilisé les données IASI dans la colonne partielle, pour évaluer les changements de l’O₃ de la troposphère libre entre 2018–2020 et 2008–2010. Nous avons choisi ces périodes en raison de leur séparation maximale dans la période IASI. Nos résultats ont montré une augmentation de la moyenne globale de l’O₃ partiel d’environ 0.4

DU (soit 1.7 %), la plus grande augmentation se situant dans les tropiques (0.32 DU ou 2 %). Conformément aux études précédentes, la plus forte augmentation de O_3 est observée sur l'Asie du Sud et du Sud-Est (environ 10 %), probablement en raison de l'augmentation des émissions. De faibles augmentations de O_3 sont observées sur l'Afrique de l'Ouest (de 2 %), probablement dues à l'augmentation des émissions anthropiques. En revanche, l' O_3 diminue sur l'Afrique du Sud (de 4 %) probablement associé à une baisse de la combustion de la biomasse. Des études antérieures basées sur le satellite (TOST pour 2013–2017 et IASI pour 2008–2016 ; Gaudel et al., 2018) et le modèle de transport chimique (de 2013–2015 à 1995–2015) confirment la diminution de O_3 au-dessus de l'Afrique du Sud.

La deuxième partie de la thèse se concentre sur les distributions tropicales de CO et O_3 , et vise à offrir une meilleure compréhension de leurs caractéristiques saisonnières et des facteurs de contrôle. Pour ce faire, nous avons analysé les mesures IAGOS pour toute la période IAGOS (depuis 1994 pour O_3 et 2002 pour CO), et les données satellitaires basées sur les récupérations IASI-SOFRID (depuis 2008). Nous avons également utilisé l'outil SOFT-IO, qui fournit des informations auxiliaires pour les mesures IAGOS-CO, telles que son origine géographique et son type d'émissions (AN ou BB).

Les principaux résultats sont les suivants :

- Les émissions de nitrate d'ammonium sont d'une grande importance dans l'augmentation du CO à long terme dans les tropiques, même dans le sud-est. Les émissions de nitrate d'ammonium dominent les maxima de CO au-dessus de la surface dans tous les groupes (sauf en Afrique centrale et dans le Golfe de Thaïlande). Le rôle des émissions de nitrate d'ammonium sur l'Afrique centrale est mis en évidence par une augmentation persistante du CO au-dessus de la surface sur une base annuelle.
- Dans les régions MT et UT, la contribution de BB est accrue par rapport à la contribution de AN. De même, la contribution des émissions de CO transportées est plus importante que dans le LT, où les émissions locales dominent. Cela s'explique par le fait qu'à ces altitudes, le transport à longue distance est favorisé par des vents plus forts, permettant la redistribution des panaches à une échelle intercontinentale (e.g Liang et al., 2004; Barret et al., 2008). Au-dessus de l'Afrique du Nord, le BB domine dans le MT pendant la saison des feux du NH (janvier) et du SH (juillet). Les feux d'Asie du Sud-Est en avril sont principalement à l'origine des anomalies de CO sur la côte sud-est de l'Asie (Chine du Sud, Ho Chi Minh Ville, Bangkok et Manille). En revanche, pendant les incendies d'Asie équatoriale en octobre, l'impact du BB dans l'UT a une plus grande portée spatiale, sur la côte de l'Asie du Sud-Est jusqu'en Inde et en Afrique.
- Les maxima de CO et de O_3 les plus élevés parmi les groupes tropicaux sont observés au-dessus de l'Afrique du Nord dans la LT pendant la saison sèche (80 ppb de O_3 à 2.5 km et 850 ppb de CO à 0.3 km au-dessus de Lagos en janvier). Malgré les incendies

actifs, les maxima de CO et par conséquent de O₃ sont principalement attribués aux émissions locales d'AN (environ 60 %).

- Les deuxièmes maxima les plus élevés de O₃ et de CO sont observés au-dessus de l'Asie. L'O₃ atteint son maximum dans le FT (à 6 km) pendant la saison post-mousson (avril), tandis que le CO est maximal dans le LT (0.5 km) en janvier en raison des émissions locales de nitrate d'ammonium. Le seul groupe présentant des maxima de O₃ dans le LT est la Chine du Sud (75 ppb à 2.6 km), pendant les feux d'Asie centrale (avril). Ces incendies contribuent également aux anomalies de CO dans les LT, en plus des émissions locales et régionales d'AN.
- Les plus petits maxima de LT CO sont observés au-dessus de l'Amérique du Sud, en raison d'émissions de CO plus faibles par rapport à l'Afrique et à l'Asie. La seule augmentation significative du CO et de l'O₃ est observée dans le MT pendant la saison des incendies locaux (octobre), lorsque l'O₃ et les précurseurs impactés par les émissions locales de l'AN et des incendies sont piégés dans un anticyclone et transportés vers l'Afrique du Sud.
- L'Afrique est la région tropicale la plus importante en termes d'exportation d'émissions dans la troposphère. La principale voie de transport est celle des régions africaines de saison sèche vers les régions de saison humide. Les contributions de l'Afrique du Nord se trouvent au-dessus de l'Arabie, de l'Afrique de l'Est et de l'Inde pendant la saison sèche et vers l'Amérique du Sud du Nord tout au long de l'année.
- L'impact des émissions asiatiques dans les régions LT et MT est limité à une échelle régionale ou locale. Dans l'UT, l'exportation des émissions asiatiques s'intensifie pendant la mousson d'été asiatique (juillet). Les masses d'air pollué de la surface sont soulevées dans l'UT asiatique et piégées dans l'AMA. Ces masses d'air sont transportées au-dessus de l'Arabie et de l'Afrique de l'Est, provoquant les maxima annuels de O₃ en raison de la subsidence et de l'isolement élevé de ces régions.

7.2 Limitations and Perspectives in french

Observations dans les tropiques

Comme nous l'avons mentionné dans [Section 3.1](#), le programme IAGOS fournit une riche base de données sur les composés atmosphériques à l'échelle mondiale. C'est la première fois que les observations IAGOS ont été analysées en profondeur pour étudier les distributions climatologiques de O₃ et de CO au-dessus des tropiques. Dans une prochaine étape, il pourrait être intéressant de documenter la variabilité interannuelle de ces composés atmosphériques. Des études antérieures (e.g. Voulgarakis et al., [2015](#)) ont montré que la variabilité interannuelle du CO à l'échelle mondiale est presque entièrement attribuée aux émissions de BB. Ainsi, nous pourrions témoigner de l'impact des émissions de BB et de leurs changements, sur O₃ et CO sur les tropiques, où les émissions de BB les plus fortes se produisent (voir [Section 2.2](#)).

En outre, nous pourrions analyser l'impact des variations non saisonnières de la circulation telles que l'oscillation ENSO (Section 2.1) sur les distributions tropicales de O_3 et de CO.

L'une des limites de notre étude est que les données IAGOS sont fournies sur des sites sélectionnés, principalement à proximité des mégapoles tropicales. Pour faire face à la rareté de la couverture des données dans les tropiques, nous pourrions tenir compte d'autres réseaux et campagnes (par exemple SHADOZ, Atom) fournissant des mesures sur cette région pour compléter nos connaissances sur la composition tropicale.

A part O_3 et CO, d'autres composés atmosphériques ont été mesurés par IAGOS au-dessus des tropiques, tels que NO_x (depuis 2015), NO_y (entre avril 2001 et mai 2005) et NO (avec IAGOS-CARIBIC depuis 1997). Ces espèces azotées (notamment NO_x) jouent un rôle clé dans la formation de O_3 (voir Section 1.1.2), émises entre autres par les sols et les émissions de foudre, qui sont surtout actives sous les tropiques (voir Section 2.2). Ainsi, l'étude des NO_x tropicaux basée sur des observations in-situ en combinaison avec des mesures simultanées de O_3 , pourrait aider à mieux comprendre la photochimie de O_3 . Dans le même ordre d'idées, l'utilisation d'un modèle chimique de transport global pourrait aider à interpréter les caractéristiques des distributions de O_3 et de CO dans les tropiques, en quantifiant leurs sources et leurs puits. De plus amples détails sur le modèle seront fournis ultérieurement.

Tendances dans les tropiques

Notre étude a fourni quelques indications sur l'impact de l'échantillonnage de IAGOS et de la sensibilité verticale de IASI sur le changement observé de O_3 (Section 4.2). Cependant, des incertitudes subsistent dans la quantification des tendances de l' O_3 basée sur les produits satellitaires. En outre, une des limites de notre étude est que le changement de O_3 n'a pas été abordé par les données IAGOS dans l'ensemble des tropiques. En raison des mesures éparses dans le temps sur les sites tropicaux, il n'a pas été possible de définir les mêmes périodes de référence et modernes pour les calculs du changement O_3 . Pour ces raisons, il serait intéressant d'estimer les tendances à partir des mesures IAGOS en utilisant la méthode de régression par quantile. Cette méthode prédit les tendances d'une distribution en prenant en compte les quantiles de la distribution au lieu des moyennes de l'état. Un avantage de cette méthode est qu'elle peut tolérer les valeurs manquantes et les valeurs aberrantes, ce qui la rend appropriée pour les ensembles de données avec des lacunes dans le temps et l'espace comme IAGOS et les ozonesondes.

Des études antérieures ont déjà utilisé des données in situ telles que IAGOS (e.g Gaudel et al., 2020; Wang et al., 2022) et ozonesondes (Christiansen et al., 2022) pour le calcul des tendances de O_3 à l'échelle mondiale. Cependant, ces études ne se concentrent pas sur les tropiques et ne documentent pas les tendances du CO. Cohen et al. (2018) ont calculé les tendances de l' O_3 et du CO à l'aide d'IAGOS, mais sur la haute troposphère aux moyennes latitudes nord. Les tendances tropicales de l' O_3 ont été documentées par Thompson et al. (2021) sur les sites SHADOZ, principalement situés dans les tropiques du

sud. Nous pourrions donc compléter cette étude en fournissant les tendances de l'O₃ pour des sites supplémentaires, ainsi que les tendances du CO. Les tendances de O₃ et de CO fournies par IAGOS seraient utiles pour évaluer les produits satellitaires et les performances des modèles chimiques utilisés pour interpréter les attributions de tendances dans les tropiques.

Une limitation des mesures IAGOS est qu'elles sous-échantillonnent la troposphère tropicale, parce que la haute tropopause (12–18 km Gettelman et al., 2002) est plus élevée que l'altitude de croisière IAGOS (9–12 km). Afin de faire des comparaisons justes avec les tendances des satellites, et d'échantillonner la colonne troposphérique complète, il serait nécessaire de compléter les profils IAGOS en utilisant les données appropriées telles que les profils MLS.

Attribution des tendances dans les tropiques

Nos résultats mettent en évidence la plus forte augmentation de l'O₃ troposphérique libre au-dessus des tropiques. Ceci est en accord avec des études récentes rapportant que les tropiques sont responsables de la plus grande augmentation de l'O₃ troposphérique (Zhang et al., 2016; Gaudel et al., 2018). Cependant, les tendances positives de l'O₃ sont attribuées à différents facteurs tels que la combustion de la biomasse (Heue et al., 2016), les émissions anthropiques (Zhang et al., 2016) et la dynamique (Lu et al., 2019a; Thompson et al., 2021). Par conséquent, les mécanismes chimiques et physiques responsables de l'augmentation de l'O₃ ne sont pas encore clairs et doivent être étudiés plus en profondeur.

Afin de mieux comprendre l'évolution de l'O₃ tropical et de ses précurseurs, il serait nécessaire d'utiliser un **Chemistry Transport Model (CTM)** global. Les études de modélisation (par exemple, Zhang et al., 2016; 2021; Lu et al., 2019a) attribuant les tendances de l'O₃ manquent d'une évaluation actualisée des facteurs anthropiques et climatiques, car elles se concentrent sur des périodes plutôt limitées jusqu'en 2010. En outre, la résolution horizontale grossière des simulations (4° × 5°, Lu et al., 2019a; Wang et al., 2022) limite la capacité du modèle à saisir les caractéristiques à fine échelle des tendances de l'O₃, en particulier près de la surface où la durée de vie de l'O₃ et des précurseurs est plus courte (e.g. Young et al., 2018).

Dans ce contexte, nous pourrions tirer parti de la nouvelle génération de la MCT globale GEOS-Chem (Bey et al., 2001b), de la **GEOS-Chem High Performance (GCHP)** (Eastham et al., 2018; Martin et al., 2022). Contrairement à GEOS-Chem, le GCHP permet l'exécution parallèle du modèle et atteint ainsi une plus grande précision dans la simulation du transport (Eastham et al., 2018). Le GCHP permet également de réaliser les simulations à haute résolution (0.5° × 0.625°), avec 72 couches verticales s'étendant de la surface jusqu'à 0.01 hPa. Le GCHP représente la chimie complète des NO_x–VOCs–O₃–aérosols en couplant la troposphère à la stratosphère (Eastham et al., 2014). Il est piloté par les champs météorologiques MERRA-2 du Global Modeling and Assimilation Office (GMAO) de la NASA, avec une résolution horizontale native de 0.5° × 0.625° (Gelaro et al., 2017).

Les simulations doivent représenter l'évolution de la composition de l'atmosphère sur une période tenant compte des changements démographiques et climatiques (par exemple, 1997–

2020). Les émissions AN pourraient être déterminées par la dernière version de CEDS2 (McDuffie et al., 2020), qui est l'inventaire d'émissions AN le plus à jour et qui est fourni à une résolution mensuelle de $0.5^\circ \times 0.5^\circ$. En ce qui concerne les émissions BB, nous pourrions utiliser l'inventaire des émissions GFED4 (Giglio et al., 2013), qui est disponible à une résolution mensuelle de $0.25^\circ \times 0.25^\circ$. La surface brûlée et les émissions dues aux incendies fournies par GFED4 sont basées sur des informations satellitaires sur l'activité des incendies et la productivité de la végétation. Les émissions naturelles de précurseurs de l' O_3 qui sont sensibles au climat, telles que les émissions biogéniques de COV non- CH_4 , les émissions de NO_x provenant du sol et des éclairs, peuvent être calculées en ligne dans le modèle.

Dans ce cadre, nous pourrions effectuer une série de simulations à l'aide du GCHP, pour calibrer le modèle et ensuite développer des tests de sensibilité sur les processus liés à la chimie de O_3 :

- La simulation de référence devrait être réalisée à une résolution de $0,5$ degré \times $0,625$ degré, en utilisant la météorologie et les émissions spécifiques à l'année pour la période 1997–2020. La validation de la simulation de référence pourrait être effectuée par des comparaisons avec les mesures IAGOS et IASI dans les tropiques.
- Les simulations de sensibilité pourraient quantifier l'impact des changements dans : i) les émissions anthropiques, ii) les émissions de la combustion de la biomasse, iii) les émissions de la foudre, iv) les émissions du sol, v) les émissions des avions, vi) la concentration de méthane, et v) la météorologie sur les tendances de O_3 et des précurseurs dans les tropiques. Ceci peut être réalisé en fixant une source ou une météorologie spécifique aux conditions de 1997 dans les simulations du modèle. La contribution de chaque facteur pourrait être estimée comme la différence entre les tendances de l'ozone estimées dans la simulation de référence et dans les tests de sensibilité.

Les simulations de référence et de sensibilité pourraient être utiles pour évaluer les facteurs de contrôle des tendances de l' O_3 tropical et des précurseurs, ainsi que leur impact à l'échelle mondiale.

Bibliography

- A, R. J. van der, Mijling, B., Ding, J., Koukouli, M. E., Liu, F., Li, Q., Mao, H., and Theys, N. (2017). “Cleaning up the air: effectiveness of air quality policy for SO₂ and NO_x emissions in China”. In: *Atmospheric Chemistry and Physics* 17.3, pp. 1775–1789. DOI: [10.5194/acp-17-1775-2017](https://doi.org/10.5194/acp-17-1775-2017).
- Adon, M., Galy-Lacaux, C., Yoboué, V., Delon, C., Lacaux, J., Castera, P., Gardrat, E., Pienaar, J., Al Ourabi, H., Laouali, D., et al. (2010). “Long term measurements of sulfur dioxide, nitrogen dioxide, ammonia, nitric acid and ozone in Africa using passive samplers”. In: *Atmospheric Chemistry and Physics* 10.15, pp. 7467–7487. DOI: [10.5194/acp-10-7467-2010](https://doi.org/10.5194/acp-10-7467-2010).
- Adon, M., Yoboué, V., Galy-Lacaux, C., Lioussé, C., Diop, B., Gardrat, E., Ndiaye, S. A., Jarnot, C., et al. (2016). “Measurements of NO₂, SO₂, NH₃, HNO₃ and O₃ in West African urban environments”. In: *Atmospheric Environment* 135, pp. 31–40. DOI: [10.1016/j.atmosenv.2016.03.050](https://doi.org/10.1016/j.atmosenv.2016.03.050).
- Aghedo, A. M., Schultz, M. G., and Rast, S. (2007). “The influence of African air pollution on regional and global tropospheric ozone”. In: *Atmospheric Chemistry and Physics* 7.5, pp. 1193–1212. DOI: [10.1016/j.atmosenv.2016.03.050](https://doi.org/10.1016/j.atmosenv.2016.03.050).
- Akimoto, H. (2003). “Global air quality and pollution”. In: *Science* 302.5651, pp. 1716–1719. DOI: [10.1126/science.1092666](https://doi.org/10.1126/science.1092666).
- Alonso, M. F., Longo, K. M., Freitas, S. R., Fonseca, R. M. da, Marécal, V., Pirre, M., and Klenner, L. G. (2010). “An urban emissions inventory for South America and its application in numerical modeling of atmospheric chemical composition at local and regional scales”. In: *Atmospheric Environment* 44.39, pp. 5072–5083. DOI: [10.1016/j.atmosenv.2010.09.013](https://doi.org/10.1016/j.atmosenv.2010.09.013).
- Andela, N., Morton, D. C., Giglio, L., Chen, Y., Werf, G. R. van der, Kasibhatla, P. S., DeFries, R. S., Collatz, G., Hantson, S., Kloster, S., et al. (2017). “A human-driven decline in global burned area”. In: *Science* 356.6345, pp. 1356–1362. DOI: [10.1126/science.aal4108](https://doi.org/10.1126/science.aal4108).
- Andreae, M. O., Artaxo, P., Fischer, H., Freitas, S., Grégoire, J.-M., Hansel, A., Hoor, P., Kormann, R., Krejci, R., Lange, L., et al. (2001). “Transport of biomass burning smoke to the upper troposphere by deep convection in the equatorial region”. In: *Geophysical Research Letters* 28.6, pp. 951–954. DOI: [10.1029/2000GL012391](https://doi.org/10.1029/2000GL012391).
- Andreae, M., Anderson, B., Blake, D., Bradshaw, J., Collins, J., Gregory, G., Sachse, G., and Shipham, M. (1994). “Influence of plumes from biomass burning on atmospheric chemistry over the equatorial and tropical South Atlantic during CITE 3”. In: *Journal of Geophysical Research: Atmospheres* 99.D6, pp. 12793–12808. DOI: [10.1029/94JD00263](https://doi.org/10.1029/94JD00263).

- Aragão, L. E., Anderson, L. O., Fonseca, M. G., Rosan, T. M., Vedovato, L. B., Wagner, F. H., Silva, C. V., Silva Junior, C. H., Arai, E., Aguiar, A. P., et al. (2018). “21st Century drought-related fires counteract the decline of Amazon deforestation carbon emissions”. In: *Nature communications* 9.1, pp. 1–12. DOI: [10.1038/s41467-017-02771-y](https://doi.org/10.1038/s41467-017-02771-y).
- Archibald, A., Neu, J., Elshorbany, Y., Cooper, O., Young, P., Akiyoshi, H., Cox, R., Coyle, M., Derwent, R., Deushi, M., et al. (2020). “Tropospheric Ozone Assessment Report A critical review of changes in the tropospheric ozone burden and budget from 1850 to 2100”. In: *Elementa: Science of the Anthropocene* 8.1. DOI: [10.1525/elementa.2020.034](https://doi.org/10.1525/elementa.2020.034).
- Assamoi, E.-M. and Lioussé, C. (2010). “A new inventory for two-wheel vehicle emissions in West Africa for 2002”. In: *Atmospheric Environment* 44.32, pp. 3985–3996. DOI: [10.1016/j.atmosenv.2010.06.048](https://doi.org/10.1016/j.atmosenv.2010.06.048).
- Avnery, S., Mauzerall, D. L., Liu, J., and Horowitz, L. W. (2011). “Global crop yield reductions due to surface ozone exposure: 2. Year 2030 potential crop production losses and economic damage under two scenarios of O₃ pollution”. In: *Atmospheric Environment* 45.13, pp. 2297–2309. DOI: [10.1016/j.atmosenv.2011.01.002](https://doi.org/10.1016/j.atmosenv.2011.01.002).
- Barret, B., Emili, E., and Le Flochmoen, E. (2020). “A tropopause-related climatological a priori profile for IASI-SOFRID ozone retrievals: improvements and validation”. In: *Atmospheric Measurement Techniques* 13.10, pp. 5237–5257. DOI: [10.5194/amt-13-5237-2020](https://doi.org/10.5194/amt-13-5237-2020).
- Barret, B., Gouzenes, Y., Le Flochmoen, E., and Ferrant, S. (2021). “Retrieval of Metop-A/IASI N₂O profiles and validation with NDACC FTIR data”. In: *Atmosphere* 12.2, p. 219. DOI: [10.3390/atmos12020219](https://doi.org/10.3390/atmos12020219).
- Barret, B., Le Flochmoen, E., Sauvage, B., Pavelin, E., Matricardi, M., and Cammas, J.-P. (2011). “The detection of post-monsoon tropospheric ozone variability over south Asia using IASI data”. In: *Atmospheric Chemistry and Physics* 11.18, pp. 9533–9548. DOI: [10.5194/acp-11-9533-2011](https://doi.org/10.5194/acp-11-9533-2011).
- Barret, B., Ricaud, P., Mari, C., Attié, J.-L., Bousserez, N., Josse, B., Le Flochmoën, E., Livesey, N., Massart, S., Peuch, V.-H., et al. (2008). “Transport pathways of CO in the African upper troposphere during the monsoon season: a study based upon the assimilation of spaceborne observations”. In: *Atmospheric Chemistry and Physics* 8.12, pp. 3231–3246. DOI: [10.5194/acp-8-3231-2008](https://doi.org/10.5194/acp-8-3231-2008).
- Barret, B., Sauvage, B., Bennouna, Y., and Le Flochmoen, E. (2016). “Upper-tropospheric CO and O₃ budget during the Asian summer monsoon”. In: *Atmospheric Chemistry and Physics* 16.14, pp. 9129–9147. DOI: [10.5194/acp-16-9129-2016](https://doi.org/10.5194/acp-16-9129-2016).
- Barret, B., Williams, J., Bouarar, I., Yang, X., Josse, B., Law, K., Pham, M., Le Flochmoën, E., Lioussé, C., Peuch, V., et al. (2010). “Impact of West African Monsoon convective transport and lightning NO_x production upon the upper tropospheric composition: a multi-model study”. In: *Atmospheric Chemistry and Physics* 10.12, pp. 5719–5738. DOI: [10.5194/acp-10-5719-2010](https://doi.org/10.5194/acp-10-5719-2010).

- Beig, G. and Singh, V. (2007). “Trends in tropical tropospheric column ozone from satellite data and MOZART model”. In: *Geophysical research letters* 34.17. DOI: [10.1029/2007GL030460](https://doi.org/10.1029/2007GL030460).
- Bey, I., Jacob, D. J., Logan, J. A., and Yantosca, R. M. (2001a). “Asian chemical outflow to the Pacific in spring: Origins, pathways, and budgets”. In: *Journal of Geophysical Research: Atmospheres* 106.D19, pp. 23097–23113. DOI: [10.1029/2001JD000806](https://doi.org/10.1029/2001JD000806).
- Bey, I., Jacob, D. J., Yantosca, R. M., Logan, J. A., Field, B. D., Fiore, A. M., Li, Q., Liu, H. Y., Mickley, L. J., and Schultz, M. G. (2001b). “Global modeling of tropospheric chemistry with assimilated meteorology: Model description and evaluation”. In: *Journal of Geophysical Research: Atmospheres* 106.D19, pp. 23073–23095. DOI: [10.1029/2001JD000807](https://doi.org/10.1029/2001JD000807).
- Blake, N. J., Blake, D. R., Chen, T.-Y., Collins Jr, J. E., Sachse, G. W., Anderson, B. E., and Rowland, F. S. (1997). “Distribution and seasonality of selected hydrocarbons and halocarbons over the western Pacific basin during PEM-West A and PEM-West B”. In: *Journal of Geophysical Research: Atmospheres* 102.D23, pp. 28315–28331. DOI: [10.1029/97JD02538](https://doi.org/10.1029/97JD02538).
- Blot, R., Nedelec, P., Boulanger, D., Wolff, P., Sauvage, B., Cousin, J.-M., Athier, G., Zahn, A., Obersteiner, F., Scharffe, D., et al. (2021). “Internal consistency of the IAGOS ozone and carbon monoxide measurements for the last 25 years”. In: *Atmospheric Measurement Techniques* 14.5, pp. 3935–3951. DOI: [10.5194/amt-14-3935-2021](https://doi.org/10.5194/amt-14-3935-2021).
- Bourgeois, I., Peischl, J., Neuman, J. A., Brown, S. S., Thompson, C. R., Aikin, K. C., Allen, H. M., Angot, H., Apel, E. C., Baublitz, C. B., et al. (2021). “Large contribution of biomass burning emissions to ozone throughout the global remote troposphere”. In: *Proceedings of the National Academy of Sciences* 118.52, e2109628118. DOI: [10.1073/pnas.2109628118](https://doi.org/10.1073/pnas.2109628118).
- Bourgeois, I., Peischl, J., Thompson, C. R., Aikin, K. C., Campos, T., Clark, H., Commane, R., Daube, B., Diskin, G. W., Elkins, J. W., et al. (2020). “Global-scale distribution of ozone in the remote troposphere from the ATom and HIPPO airborne field missions”. In: *Atmospheric Chemistry and Physics* 20.17, pp. 10611–10635. DOI: [10.5194/acp-20-10611-2020](https://doi.org/10.5194/acp-20-10611-2020).
- Boynard, A., Hurtmans, D., Garane, K., Goutail, F., Hadji-Lazaro, J., Koukouli, M. E., Wespes, C., Vigouroux, C., Keppens, A., Pommereau, J.-P., et al. (2018). “Validation of the IASI FORLI/EUMETSAT ozone products using satellite (GOME-2), ground-based (Brewer–Dobson, SAOZ, FTIR) and ozonesonde measurements”. In: *Atmospheric Measurement Techniques* 11.9, pp. 5125–5152. DOI: [10.5194/amt-11-5125-2018](https://doi.org/10.5194/amt-11-5125-2018).
- Boynard, A., Hurtmans, D., Koukouli, M. E., Goutail, F., Bureau, J., Safieddine, S., Lerot, C., Hadji-Lazaro, J., Wespes, C., Pommereau, J.-P., et al. (2016). “Seven years of IASI ozone retrievals from FORLI: validation with independent total column and vertical profile measurements”. In: *Atmospheric Measurement Techniques* 9.9, pp. 4327–4353. DOI: [10.5194/amt-9-4327-2016](https://doi.org/10.5194/amt-9-4327-2016).
- Brenninkmeijer, C. A. M., Crutzen, P. J., Fischer, H., Güsten, H., Hans, W., Heinrich, G., Heintzenberg, J., Hermann, M., Immelmann, T., Kersting, D., Maiss, M., Nolle, M.,

- Pitscheider, A., Pohlkamp, H., Scharffe, D., Specht, K., and Wiedensohler, A. (1999). “CARIBIC–Civil Aircraft for Global Measurement of Trace Gases and Aerosols in the Tropopause Region”. In: *J. Atmos. Ocean Tech.* 16.10, pp. 1373–1383. DOI: [10.1175/1520-0426\(1999\)016<1373:CCAFGM>2.0.CO;2](https://doi.org/10.1175/1520-0426(1999)016<1373:CCAFGM>2.0.CO;2).
- Bruhn, D., Albert, K. R., Mikkelsen, T. N., and Ambus, P. (2013). “UV-induced carbon monoxide emission from living vegetation”. In: *Biogeosciences* 10.12, pp. 7877–7882. DOI: [10.5194/bg-10-7877-2013](https://doi.org/10.5194/bg-10-7877-2013).
- Buchholz, R. R., Worden, H. M., Park, M., Francis, G., Deeter, M. N., Edwards, D. P., Emmons, L. K., Gaubert, B., Gille, J., Martínez-Alonso, S., et al. (2021). “Air pollution trends measured from Terra: CO and AOD over industrial, fire-prone, and background regions”. In: *Remote Sensing of Environment* 256, p. 112275. DOI: [10.1016/j.rse.2020.112275](https://doi.org/10.1016/j.rse.2020.112275).
- Chameides, W., Davis, D.-D., Gregory, G., Sachse, G., and Torres, A. (1989). “Ozone precursors and ozone photochemistry over eastern North Pacific during the spring of 1984 based on the NASA GTE/CITE 1 airborne observations”. In: *Journal of Geophysical Research: Atmospheres* 94.D7, pp. 9799–9808. DOI: [10.1029/JD094iD07p09799](https://doi.org/10.1029/JD094iD07p09799).
- Chang, K.-L., Schultz, M. G., Lan, X., McClure-Begley, A., Petropavlovskikh, I., Xu, X., and Ziemke, J. R. (2021). “Trend detection of atmospheric time series: Incorporating appropriate uncertainty estimates and handling extreme events”. In: *Elem Sci Anth* 9.1, p. 00035. DOI: [10.1525/elementa.2021.00035](https://doi.org/10.1525/elementa.2021.00035).
- Chapman, S. (1930). “A theory of upperatmospheric ozone”. In: *Mem. Roy. Meteor.* 3, pp. 103–125.
- Chatfield, R. B., Vastano, J. A., Singh, H., and Sachse, G (1996). “A general model of how fire emissions and chemistry produce African/oceanic plumes (O₃, CO, PAN, smoke) in TRACE A”. In: *Journal of Geophysical Research: Atmospheres* 101.D19, pp. 24279–24306.
- Chen, W.-T., Liao, H., and Seinfeld, J. H. (2007). “Future climate impacts of direct radiative forcing of anthropogenic aerosols, tropospheric ozone, and long-lived greenhouse gases”. In: *Journal of Geophysical Research: Atmospheres* 112.D14. DOI: [10.1029/2006jd008051](https://doi.org/10.1029/2006jd008051).
- Christian, H. J., Blakeslee, R. J., Boccippio, D. J., Boeck, W. L., Buechler, D. E., Driscoll, K. T., Goodman, S. J., Hall, J. M., Koshak, W. J., Mach, D. M., et al. (2003). “Global frequency and distribution of lightning as observed from space by the Optical Transient Detector”. In: *Journal of Geophysical Research: Atmospheres* 108.D1, ACL–4. DOI: [10.1029/2002JD002347](https://doi.org/10.1029/2002JD002347).
- Christiansen, A., Mickley, L. J., Liu, J., Oman, L. D., and Hu, L. (2022). “Multidecadal increases in global tropospheric ozone derived from ozonesonde and surface site observations: Can models reproduce ozone trends?” In: *Atmospheric Chemistry and Physics Discussions*, pp. 1–50. DOI: [10.5194/acp-22-14751-2022](https://doi.org/10.5194/acp-22-14751-2022).
- Clerbaux, C., Boynard, A., Clarisse, L., George, M., Hadji-Lazaro, J., Herbin, H., Hurtmans, D., Pommier, M., Razavi, A., Turquety, S., et al. (2009). “Monitoring of atmospheric

- composition using the thermal infrared IASI/MetOp sounder”. In: *Atmospheric Chemistry and Physics* 9.16, pp. 6041–6054. DOI: [10.5194/acp-9-6041-2009](https://doi.org/10.5194/acp-9-6041-2009).
- Cohen, Y., Petetin, H., Thouret, V., Marécal, V., Josse, B., Clark, H., Sauvage, B., Fontaine, A., Athier, G., Blot, R., et al. (2018). “Climatology and long-term evolution of ozone and carbon monoxide in the upper troposphere–lower stratosphere (UTLS) at northern midlatitudes, as seen by IAGOS from 1995 to 2013”. In: *Atmospheric Chemistry and Physics* 18.8, pp. 5415–5453. DOI: [10.5194/acp-18-5415-2018](https://doi.org/10.5194/acp-18-5415-2018).
- Conte, L., Szopa, S., Séférian, R., and Bopp, L. (2019). “The oceanic cycle of carbon monoxide and its emissions to the atmosphere”. In: *Biogeosciences* 16.4, pp. 881–902. DOI: [10.5194/bg-16-881-2019](https://doi.org/10.5194/bg-16-881-2019).
- Cooper, O. R., Gao, R.-S., Tarasick, D., Leblanc, T., and Sweeney, C. (2012). “Long-term ozone trends at rural ozone monitoring sites across the United States, 1990–2010”. In: *Journal of Geophysical Research: Atmospheres* 117.D22. DOI: [10.1029/2012JD018261](https://doi.org/10.1029/2012JD018261).
- Cooper, O. R., Langford, A. O., Parrish, D. D., and Fahey, D. W. (2015). “Challenges of a lowered US ozone standard”. In: *Science* 348.6239, pp. 1096–1097. DOI: [10.1126/science.aaa5748](https://doi.org/10.1126/science.aaa5748).
- Cooper, O. R., Parrish, D., Stohl, A., Trainer, M., Nédélec, P., Thouret, V., Cammas, J.-P., Oltmans, S., Johnson, B., Tarasick, D., et al. (2010). “Increasing springtime ozone mixing ratios in the free troposphere over western North America”. In: *Nature* 463.7279, pp. 344–348. DOI: [10.1038/nature08708](https://doi.org/10.1038/nature08708).
- Cristofanelli, P., Fierli, F., Marinoni, A., Calzolari, F., Duchi, R., Burkhardt, J., Stohl, A., Maione, M., Arduini, J., and Bonasoni, P. (2013). “Influence of biomass burning and anthropogenic emissions on ozone, carbon monoxide and black carbon at the Mt. Cimone GAW-WMO global station (Italy, 2165 m asl)”. In: *Atmospheric Chemistry and Physics* 13.1, pp. 15–30. DOI: [10.5194/acp-13-15-2013](https://doi.org/10.5194/acp-13-15-2013).
- Cros, B., Delon, C., Affre, C., Marion, T., Druilhet, A., Perros, P., and Lopez, A. (2000). “Sources and sinks of ozone in savanna and forest areas during EXPRESSO: Airborne turbulent flux measurements”. In: *Journal of Geophysical Research: Atmospheres* 105.D24, pp. 29347–29358. DOI: [10.1029/2000JD900451](https://doi.org/10.1029/2000JD900451).
- Crutzen, P. J. and Andreae, M. O. (1990). “Biomass burning in the tropics: Impact on atmospheric chemistry and biogeochemical cycles”. In: *science* 250.4988, pp. 1669–1678. DOI: [10.1126/science.250.4988.1669](https://doi.org/10.1126/science.250.4988.1669).
- Curtis, L., Rea, W., Smith-Willis, P., Fenyves, E., and Pan, Y. (2006). “Adverse health effects of outdoor air pollutants”. In: *Environment international* 32.6, pp. 815–830. DOI: [10.1016/j.envint.2006.03.012](https://doi.org/10.1016/j.envint.2006.03.012).
- Cussac, M., Marécal, V., Thouret, V., Josse, B., and Sauvage, B. (2020). “The impact of biomass burning on upper tropospheric carbon monoxide: a study using MOCAGE global model and IAGOS airborne data”. In: *Atmospheric Chemistry and Physics* 20.15, pp. 9393–9417. DOI: [10.5194/acp-20-9393-2020](https://doi.org/10.5194/acp-20-9393-2020).

- Danielsen, E. F. (1968). “Stratospheric-tropospheric exchange based on radioactivity, ozone and potential vorticity”. In: *Journal of Atmospheric Sciences* 25.3, pp. 502–518. DOI: [10.1175/1520-0469\(1968\)025<0502:STEBOR>2.0.CO;2](https://doi.org/10.1175/1520-0469(1968)025<0502:STEBOR>2.0.CO;2).
- Dayan, U., Ricaud, P., Zbinden, R., and Dulac, F. (2017). “Atmospheric pollution over the eastern Mediterranean during summer—a review”. In: *Atmospheric Chemistry and Physics* 17.21, pp. 13233–13263. DOI: [10.5194/acp-17-13233-2017](https://doi.org/10.5194/acp-17-13233-2017).
- De Wachter, E., Barret, B., Le Flochmoën, E., Pavelin, E., Matricardi, M., Clerbaux, C., Hadji-Lazaro, J., George, M., Hurtmans, D., Coheur, P.-F., et al. (2012). “Retrieval of MetOp-A/IASI CO profiles and validation with MOZAIC data”. In: *Atmospheric Measurement Techniques* 5.11, pp. 2843–2857. DOI: [10.5194/amt-5-2843-2012](https://doi.org/10.5194/amt-5-2843-2012).
- Deeter, M., Martínez-Alonso, S., Andreae, M. O., and Schlager, H. (2018). “Satellite-based analysis of CO seasonal and interannual variability over the Amazon Basin”. In: *Journal of Geophysical Research: Atmospheres* 123.10, pp. 5641–5656. DOI: [10.1029/2018JD028425](https://doi.org/10.1029/2018JD028425).
- Delmas, R., Druilhet, A., Cros, B., Durand, P., Delon, C., Lacaux, J., Brustet, J., Serça, D., Affre, C., Guenther, A., et al. (1999). “Experiment for regional sources and sinks of oxidants (EXPRESSO): An overview”. In: *Journal of Geophysical Research: Atmospheres* 104.D23, pp. 30609–30624. DOI: [10.1029/1999JD900291](https://doi.org/10.1029/1999JD900291).
- Dufour, G., Eremenko, M., Orphal, J., and Flaud, J.-M. (2010). “IASI observations of seasonal and day-to-day variations of tropospheric ozone over three highly populated areas of China: Beijing, Shanghai, and Hong Kong”. In: *Atmospheric Chemistry and Physics* 10.8, pp. 3787–3801. DOI: [10.5194/acp-10-3787-2010](https://doi.org/10.5194/acp-10-3787-2010).
- Dufour, G., Eremenko, M., Griesfeller, A., Barret, B., LeFlochmoën, E., Clerbaux, C., Hadji-Lazaro, J., Coheur, P.-F., and Hurtmans, D. (2012). “Validation of three different scientific ozone products retrieved from IASI spectra using ozonesondes”. In: *Atmospheric Measurement Techniques* 5.3, pp. 611–630. DOI: [10.5194/amt-5-611-2012](https://doi.org/10.5194/amt-5-611-2012).
- Duncan, B. N., Lamsal, L. N., Thompson, A. M., Yoshida, Y., Lu, Z., Streets, D. G., Hurwitz, M. M., and Pickering, K. E. (2016). “A space-based, high-resolution view of notable changes in urban NO_x pollution around the world (2005–2014)”. In: *Journal of Geophysical Research: Atmospheres* 121.2, pp. 976–996. DOI: [10.1002/2015JD024121](https://doi.org/10.1002/2015JD024121).
- Eastham, S. D., Long, M. S., Keller, C. A., Lundgren, E., Yantosca, R. M., Zhuang, J., Li, C., Lee, C. J., Yannetti, M., Auer, B. M., et al. (2018). “GEOS-Chem High Performance (GCHP v11-02c): a next-generation implementation of the GEOS-Chem chemical transport model for massively parallel applications”. In: *Geoscientific Model Development* 11.7, pp. 2941–2953. DOI: [10.5194/gmd-11-2941-2018](https://doi.org/10.5194/gmd-11-2941-2018).
- Eastham, S. D., Weisenstein, D. K., and Barrett, S. R. (2014). “Development and evaluation of the unified tropospheric–stratospheric chemistry extension (UCX) for the global chemistry–transport model GEOS-Chem”. In: *Atmospheric Environment* 89, pp. 52–63. DOI: [10.1016/j.atmosenv.2014.02.001](https://doi.org/10.1016/j.atmosenv.2014.02.001).
- Edwards, D., Emmons, L., Gille, J., Chu, A., Attié, J.-L., Giglio, L., Wood, S., Haywood, J., Deeter, M., Massie, S., et al. (2006). “Satellite-observed pollution from Southern

- Hemisphere biomass burning”. In: *Journal of Geophysical Research: Atmospheres* 111.D14. DOI: [10.1029/2005JD006655](https://doi.org/10.1029/2005JD006655).
- Edwards, D., Emmons, L., Hauglustaine, D., Chu, D., Gille, J., Kaufman, Y., Pétron, G., Yurganov, L., Giglio, L., Deeter, M., et al. (2004). “Observations of carbon monoxide and aerosols from the Terra satellite: Northern Hemisphere variability”. In: *Journal of Geophysical Research: Atmospheres* 109.D24. DOI: [10.1029/2004JD004727](https://doi.org/10.1029/2004JD004727).
- Emili, E., Barret, B., Massart, S., Le Flochmoen, E., Piacentini, A., El Amraoui, L., Pannekoek, O., and Cariolle, D (2014). “Combined assimilation of IASI and MLS observations to constrain tropospheric and stratospheric ozone in a global chemical transport model”. In: *Atmospheric Chemistry and Physics* 14.1, pp. 177–198. DOI: [10.5194/acp-14-177-2014](https://doi.org/10.5194/acp-14-177-2014).
- Emmons, L. K., Walters, S., Hess, P. G., Lamarque, J.-F., Pfister, G. G., Fillmore, D., Granier, C., Guenther, A., Kinnison, D., Laepple, T., et al. (2010). “Description and evaluation of the Model for Ozone and Related chemical Tracers, version 4 (MOZART-4)”. In: *Geoscientific Model Development* 3.1, pp. 43–67. DOI: [10.5194/gmd-3-43-2010](https://doi.org/10.5194/gmd-3-43-2010).
- Eremenko, M., Dufour, G., Foret, G., Keim, C., Orphal, J., Beekmann, M., Bergametti, G., and Flaud, J.-M. (2008). “Tropospheric ozone distributions over Europe during the heat wave in July 2007 observed from infrared nadir spectra recorded by IASI”. In: *Geophysical Research Letters* 35.18. DOI: [10.1029/2008GL034803](https://doi.org/10.1029/2008GL034803).
- Fiehn, A. (2017). “Transport of very short-lived substances from the Indian Ocean to the stratosphere through the Asian monsoon”. PhD thesis. Christian-Albrechts-Universität Kiel.
- Fishman, J., Hoell Jr, J. M., Bendura, R. D., McNeal, R. J., and Kirchhoff, V. W. (1996). “NASA GTE trace a experiment (September–October 1992): Overview”. In: *Journal of Geophysical Research: Atmospheres* 101.D19, pp. 23865–23879. DOI: [10.1029/96JD00123](https://doi.org/10.1029/96JD00123).
- Friedrich, N., Eger, P., Shenolikar, J., Sobanski, N., Schuladen, J., Dienhart, D., Hottmann, B., Tadic, I., Fischer, H., Martinez, M., et al. (2021). “Reactive nitrogen around the Arabian Peninsula and in the Mediterranean Sea during the 2017 AQABA ship campaign”. In: *Atmospheric Chemistry and Physics* 21.10, pp. 7473–7498. DOI: [10.5194/acp-21-7473-2021](https://doi.org/10.5194/acp-21-7473-2021).
- Galloway, J. N., Dentener, F. J., Capone, D. G., Boyer, E. W., Howarth, R. W., Seitzinger, S. P., Asner, G. P., Cleveland, C. C., Green, P., Holland, E. A., et al. (2004). “Nitrogen cycles: past, present, and future”. In: *Biogeochemistry* 70.2, pp. 153–226. DOI: [10.1007/s10533-004-0370-0](https://doi.org/10.1007/s10533-004-0370-0).
- Garstang, M., Ulanski, S., Greco, S., Scala, J., Swap, R., Fitzjarrald, D., Martin, D., Browell, E., Shipman, M., Connors, V., et al. (1990). “The Amazon boundary-layer experiment (ABLE 2B): A meteorological perspective”. In: *Bulletin of the American Meteorological Society* 71.1, pp. 19–32. DOI: [10.1175/1520-0477\(1990\)071<0019:TABLEA>2.0.CO;2](https://doi.org/10.1175/1520-0477(1990)071<0019:TABLEA>2.0.CO;2).
- Gaudel, A., Cooper, O. R., Ancellet, G., Barret, B., Boynard, A., Burrows, J., Clerbaux, C., Coheur, P.-F., Cuesta, J., Cuevas, E., et al. (2018). “Tropospheric Ozone Assessment Report: Present-day distribution and trends of tropospheric ozone relevant to climate and

- global atmospheric chemistry model evaluation". In: *Elementa: science of the anthropocene* 6. DOI: [10.1525/elementa.291](https://doi.org/10.1525/elementa.291).
- Gaudel, A., Cooper, O. R., Chang, K.-L., Bourgeois, I., Ziemke, J. R., Strode, S. A., Oman, L. D., Sellitto, P., Nédélec, P., Blot, R., et al. (2020). "Aircraft observations since the 1990s reveal increases of tropospheric ozone at multiple locations across the Northern Hemisphere". In: *Science Advances* 6.34, eaba8272. DOI: [10.1525/elementa.291](https://doi.org/10.1525/elementa.291).
- Gauss, M., Myhre, G., Pitari, G., Prather, M., Isaksen, I., Bernsten, T., Brasseur, G., Dentener, F., Derwent, R., Hauglustaine, D., et al. (2003). "M uller". In: *JF, Plantevin, P., Pyle, JA, Rogers, HL, Stevenson, DS, Sundet, JK, van Weele, M., and Wild, O.: Radiative forcing in the 21st century due to ozone changes in the troposphere and the lower stratosphere, J. Geophys. Res* 108. DOI: [10.1029/2002JD002624](https://doi.org/10.1029/2002JD002624).
- Gelaro, R., McCarty, W., Suárez, M. J., Todling, R., Molod, A., Takacs, L., Randles, C. A., Darmenov, A., Bosilovich, M. G., Reichle, R., et al. (2017). "The modern-era retrospective analysis for research and applications, version 2 (MERRA-2)". In: *Journal of climate* 30.14, pp. 5419–5454. DOI: [10.1175/JCLI-D-16-0758.1](https://doi.org/10.1175/JCLI-D-16-0758.1).
- George, M., Clerbaux, C., Hurtmans, D., Turquety, S., Coheur, P.-F., Pommier, M., Hadji-Lazaro, J., Edwards, D., Worden, H., Luo, M., et al. (2009). "Carbon monoxide distributions from the IASI/METOP mission: evaluation with other space-borne remote sensors". In: *Atmospheric Chemistry and Physics* 9.21, pp. 8317–8330. DOI: [10.5194/acp-9-8317-2009](https://doi.org/10.5194/acp-9-8317-2009).
- Gettelman, A et al. (2002). "A climatology of the tropical tropopause layer". In: *Journal of the Meteorological Society of Japan. Ser. II* 80.4B, pp. 911–924. DOI: [10.2151/jmsj.80.911](https://doi.org/10.2151/jmsj.80.911).
- Gettelman, A., Holton, J. R., and Rosenlof, K. H. (1997). "Mass fluxes of O₃, CH₄, N₂O and CF₂Cl₂ in the lower stratosphere calculated from observational data". In: *Journal of Geophysical Research: Atmospheres* 102.D15, pp. 19149–19159. DOI: [10.1029/97JD01014](https://doi.org/10.1029/97JD01014).
- Ghude, S. D., Jena, C., Chate, D., Beig, G, Pfister, G., Kumar, R., and Ramanathan, V (2014). "Reductions in India's crop yield due to ozone". In: *Geophysical Research Letters* 41.15, pp. 5685–5691. DOI: [10.1002/2014GL060930](https://doi.org/10.1002/2014GL060930).
- Giglio, L and Kendall, J. (2004). "Commentary on "Improving the seasonal cycle and inter-annual variations of biomass burning aerosol sources" by Generoso et al." In: *Atmospheric Chemistry and Physics* 4.3, pp. 585–587. DOI: [10.5194/acp-4-585-2004](https://doi.org/10.5194/acp-4-585-2004).
- Giglio, L., Csiszar, I., and Justice, C. O. (2006). "Global distribution and seasonality of active fires as observed with the Terra and Aqua Moderate Resolution Imaging Spectroradiometer (MODIS) sensors". In: *Journal of geophysical research: Biogeosciences* 111.G2. DOI: [10.1029/2005JG000142](https://doi.org/10.1029/2005JG000142).
- Giglio, L., Randerson, J. T., and Van Der Werf, G. R. (2013). "Analysis of daily, monthly, and annual burned area using the fourth-generation global fire emissions database (GFED4)". In: *Journal of Geophysical Research: Biogeosciences* 118.1, pp. 317–328. DOI: [10.1002/jgrg.20042](https://doi.org/10.1002/jgrg.20042).
- Granier, C., Bessagnet, B., Bond, T., D'Angiola, A., Gon, H. Denier van der, Frost, G. J., Heil, A., Kaiser, J. W., Kinne, S., Klimont, Z., et al. (2011). "Evolution of anthropogenic

- and biomass burning emissions of air pollutants at global and regional scales during the 1980–2010 period”. In: *Climatic change* 109.1, pp. 163–190. DOI: [10.1007/s10584-011-0154-1](https://doi.org/10.1007/s10584-011-0154-1).
- Gressent, A., Sauvage, B., Cariolle, D., Evans, M., Leriche, M., Mari, C., and Thouret, V. (2016). “Modeling lightning-NO_x chemistry on a sub-grid scale in a global chemical transport model”. In: *Atmospheric Chemistry and Physics* 16.9, pp. 5867–5889. DOI: [10.5194/acp-16-5867-2016](https://doi.org/10.5194/acp-16-5867-2016).
- Gressent, A., Sauvage, B., Defer, E., Pätz, H. W., Thomas, K., Holle, R., Cammas, J.-P., Nédélec, P., Boulanger, D., Thouret, V., et al. (2014). “Lightning NO_x influence on large-scale NO_y and O₃ plumes observed over the northern mid-latitudes”. In: *Tellus B: Chemical and Physical Meteorology* 66.1, p. 25544. DOI: [10.3402/tellusb.v66.25544](https://doi.org/10.3402/tellusb.v66.25544).
- Grewe, V. (2007). “Impact of climate variability on tropospheric ozone”. In: *Science of the total environment* 374.1, pp. 167–181. DOI: [10.1016/j.scitotenv.2007.01.032](https://doi.org/10.1016/j.scitotenv.2007.01.032).
- Hanif, N. M., Hawari, N. S. S. L., Othman, M., Abd Hamid, H. H., Ahamad, F., Uning, R., Ooi, M. C. G., Wahab, M. I. A., Sahani, M., and Latif, M. T. (2021). “Ambient volatile organic compounds in tropical environments: Potential sources, composition and impacts—A review”. In: *Chemosphere* 285, p. 131355. DOI: [10.1016/j.chemosphere.2021.131355](https://doi.org/10.1016/j.chemosphere.2021.131355).
- Harriss, R., Wofsy, S., Garstang, M., Browell, E., Molion, L., McNeal, R., Hoell Jr, J., Bendura, R., Beck, S., Navarro, R., et al. (1988). “The Amazon boundary layer experiment (ABLE 2A): Dry season 1985”. In: *Journal of Geophysical Research: Atmospheres* 93.D2, pp. 1351–1360. DOI: [10.1029/JD093iD02p01351](https://doi.org/10.1029/JD093iD02p01351).
- Haywood, J. M., Abel, S. J., Barrett, P. A., Bellouin, N., Blyth, A., Bower, K. N., Brooks, M., Carslaw, K., Che, H., Coe, H., et al. (2021). “The CLOUD–Aerosol–Radiation interaction and forcing: Year 2017 (CLARIFY-2017) measurement campaign”. In: *Atmospheric Chemistry and Physics* 21.2, pp. 1049–1084. DOI: [10.5194/acp-21-1049-2021](https://doi.org/10.5194/acp-21-1049-2021).
- Heald, C. L., Jacob, D. J., Fiore, A. M., Emmons, L. K., Gille, J. C., Deeter, M. N., Warner, J., Edwards, D. P., Crawford, J. H., Hamlin, A. J., et al. (2003). “Asian outflow and trans-Pacific transport of carbon monoxide and ozone pollution: An integrated satellite, aircraft, and model perspective”. In: *Journal of Geophysical Research: Atmospheres* 108.D24. DOI: [10.1029/2003JD003507](https://doi.org/10.1029/2003JD003507).
- Hedelius, J. K., Toon, G. C., Buchholz, R. R., Iraci, L. T., Podolske, J. R., Roehl, C. M., Wennberg, P. O., Worden, H. M., and Wunch, D. (2021). “Regional and urban column CO trends and anomalies as observed by MOPITT over 16 years”. In: *Journal of Geophysical Research: Atmospheres* 126.5, e2020JD033967. DOI: [10.1029/2020JD033967](https://doi.org/10.1029/2020JD033967).
- Helten, M., Smit, H., Kley, D., Ovarlez, J., Schlager, H., Baumann, R., Schumann, U., Nédélec, P., and Marenco, A. (1999). “In-flight comparison of MOZAIC and POLINAT water vapor measurements”. In: *Journal of Geophysical Research: Atmospheres* 104.D21, pp. 26087–26096. DOI: [10.1029/1999JD900315](https://doi.org/10.1029/1999JD900315).
- Heue, K.-P., Coldewey-Egbers, M., Delcloo, A., Lerot, C., Loyola, D., Valks, P., and Van Roozendaal, M. (2016). “Trends of tropical tropospheric ozone from 20 years of European

- satellite measurements and perspectives for the Sentinel-5 Precursor”. In: *Atmospheric Measurement Techniques* 9.10, pp. 5037–5051. DOI: [10.5194/amt-9-5037-2016](https://doi.org/10.5194/amt-9-5037-2016).
- Hickman, J. E., Andela, N., Dammers, E., Clarisse, L., Coheur, P.-F., Van Damme, M., Di Vittorio, C. A., Ossohou, M., Bauer, S. E., et al. (2021). “Changes in biomass burning, wetland extent, or agriculture drive atmospheric NH₃ trends in select African regions”. In: *Atmospheric Chemistry and Physics* 21.21, pp. 16277–16291. DOI: [10.5194/acp-21-16277-2021](https://doi.org/10.5194/acp-21-16277-2021).
- Hoell, J., Davis, D., Jacob, D. J., Rodgers, M., Newell, R., Fuelberg, H., McNeal, R., Raper, J., and Bendura, R. (1999). “Pacific Exploratory Mission in the tropical Pacific: PEM-Tropics A, August-September 1996”. In: *Journal of Geophysical Research: Atmospheres* 104.D5, pp. 5567–5583. DOI: [10.1029/1998JD100074](https://doi.org/10.1029/1998JD100074).
- Hoell Jr, J. M., Albritton, D. L., Gregory, G. L., McNeal, R. J., Beck, S. M., Bendura, R. J., and Drewry, J. W. (1990). “Operational overview of NASA GTE/CITE 2 airborne instrument intercomparisons: Nitrogen dioxide, nitric acid, and peroxyacetyl nitrate”. In: *Journal of Geophysical Research: Atmospheres* 95.D7, pp. 10047–10054. DOI: [10.1029/JD095iD07p10047](https://doi.org/10.1029/JD095iD07p10047).
- Hoell Jr, J. M., Davis, D. D., Gregory, G. L., McNeal, R. J., Bendura, R. J., Drewry, J. W., Barrick, J. D., Kirchhoff, V. W., Motta, A. G., Navarro, R. L., et al. (1993). “Operational overview of the NASA GTE/CITE 3 airborne instrument intercomparisons for sulfur dioxide, hydrogen sulfide, carbonyl sulfide, dimethyl sulfide, and carbon disulfide”. In: *Journal of Geophysical Research: Atmospheres* 98.D12, pp. 23291–23304. DOI: [10.1029/93JD00453](https://doi.org/10.1029/93JD00453).
- Hoesly, R. M., Smith, S. J., Feng, L., Klimont, Z., Janssens-Maenhout, G., Pitkanen, T., Seibert, J. J., Vu, L., Andres, R. J., Bolt, R. M., et al. (2018). “Historical (1750–2014) anthropogenic emissions of reactive gases and aerosols from the Community Emissions Data System (CEDS)”. In: *Geoscientific Model Development* 11.1, pp. 369–408. DOI: [10.5194/gmd-11-369-2018](https://doi.org/10.5194/gmd-11-369-2018).
- Huijnen, V., Wooster, M. J., Kaiser, J. W., Gaveau, D. L., Flemming, J., Parrington, M., Inness, A., Murdiyarso, D., Main, B., and Weele, M. van (2016). “Fire carbon emissions over maritime southeast Asia in 2015 largest since 1997”. In: *Scientific reports* 6.1, pp. 1–8. DOI: [10.1038/srep26886](https://doi.org/10.1038/srep26886).
- IPCC (2021). *Climate change 2021: The physical science basis*. Tech. rep. URL: <http://www.ipcc.ch/report/ar6/wg1/>.
- Jacob, D. J. (1999). *Introduction to atmospheric chemistry*. Princeton University Press.
- Jacob, D. J., Heikes, E., Fan, S.-M., Logan, J. A., Mauzerall, D., Bradshaw, J., Singh, H., Gregory, G., Talbot, R., Blake, D., et al. (1996). “Origin of ozone and NO_x in the tropical troposphere: A photochemical analysis of aircraft observations over the South Atlantic basin”. In: *Journal of Geophysical Research: Atmospheres* 101.D19, pp. 24235–24250. DOI: [10.1029/96JD00336](https://doi.org/10.1029/96JD00336).

- Jacobson, M. Z. (2012). *Air pollution and global warming: history, science, and solutions*. Cambridge University Press.
- Jaeglé, L., Martin, R., Chance, K., Steinberger, L., Kurosu, T., Jacob, D. J., Modi, A., Yoboué, V., Sigha-Nkamdjou, L., and Galy-Lacaux, C. (2004). “Satellite mapping of rain-induced nitric oxide emissions from soils”. In: *Journal of Geophysical Research: Atmospheres* 109.D21. DOI: [10.1029/2004JD004787](https://doi.org/10.1029/2004JD004787).
- Jaffe, D. A. and Wigder, N. L. (2012). “Ozone production from wildfires: A critical review”. In: *Atmospheric Environment* 51, pp. 1–10. DOI: [10.1016/j.atmosenv.2011.11.062](https://doi.org/10.1016/j.atmosenv.2011.11.062).
- Jerrett, M., Burnett, R. T., Pope III, C. A., Ito, K., Thurston, G., Krewski, D., Shi, Y., Calle, E., and Thun, M. (2009). “Long-term ozone exposure and mortality”. In: *New England Journal of Medicine* 360.11, pp. 1085–1095. DOI: [10.1056/NEJMoa0803894](https://doi.org/10.1056/NEJMoa0803894).
- Jia, J., Ladstätter-Weissenmayer, A., Hou, X., Rozanov, A., and Burrows, J. P. (2017). “Tropospheric ozone maxima observed over the Arabian Sea during the pre-monsoon”. In: *Atmospheric Chemistry and Physics* 17.8, pp. 4915–4930. DOI: [10.5194/acp-17-4915-2017](https://doi.org/10.5194/acp-17-4915-2017).
- Jonquière, I., Marenco, A., Maalej, A., and Rohrer, F. (1998). “Study of ozone formation and transatlantic transport from biomass burning emissions over West Africa during the airborne Tropospheric Ozone Campaigns TROPOZ I and TROPOZ II”. In: *Journal of Geophysical Research: Atmospheres* 103.D15, pp. 19059–19073. DOI: [10.1029/98JD00819](https://doi.org/10.1029/98JD00819).
- Kaiser, J., Heil, A., Andreae, M., Benedetti, A., Chubarova, N., Jones, L., Morcrette, J.-J., Razinger, M., Schultz, M., Suttie, M., et al. (2012). “Biomass burning emissions estimated with a global fire assimilation system based on observed fire radiative power”. In: *Biogeosciences* 9.1, pp. 527–554. DOI: [10.5194/bg-9-527-2012](https://doi.org/10.5194/bg-9-527-2012).
- Kalmus, P., Ao, C. O., Wang, K.-N., Manzi, M. P., and Teixeira, J. (2022). “A high-resolution planetary boundary layer height seasonal climatology from GNSS radio occultations”. In: *Remote Sensing of Environment* 276, p. 113037. DOI: [10.1016/j.rse.2022.113037](https://doi.org/10.1016/j.rse.2022.113037).
- Karl, T., Guenther, A., Yokelson, R. J., Greenberg, J., Potosnak, M., Blake, D. R., and Artaxo, P. (2007). “The tropical forest and fire emissions experiment: Emission, chemistry, and transport of biogenic volatile organic compounds in the lower atmosphere over Amazonia”. In: *Journal of Geophysical Research: Atmospheres* 112.D18. DOI: [10.1029/2007JD008539](https://doi.org/10.1029/2007JD008539).
- Knippertz, P., Fink, A. H., Deroubaix, A., Morris, E., Tocquer, F., Evans, M. J., Flamant, C., Gaetani, M., Lavaysse, C., Mari, C., et al. (2017). “A meteorological and chemical overview of the DACCIIWA field campaign in West Africa in June–July 2016”. In: *Atmospheric Chemistry and Physics* 17.17, pp. 10893–10918. DOI: [10.5194/acp-17-10893-2017](https://doi.org/10.5194/acp-17-10893-2017).
- Kondo, Y., Morino, Y., Takegawa, N., Koike, M., Kita, K., Miyazaki, Y., Sachse, G., Vay, S., Avery, M., Flocke, F., et al. (2004). “Impacts of biomass burning in Southeast Asia on ozone and reactive nitrogen over the western Pacific in spring”. In: *Journal of Geophysical Research: Atmospheres* 109.D15. DOI: [10.1029/2003JD004203](https://doi.org/10.1029/2003JD004203).
- Krotkov, N. A., McLinden, C. A., Li, C., Lamsal, L. N., Celarier, E. A., Marchenko, S. V., Swartz, W. H., Bucsela, E. J., Joiner, J., Duncan, B. N., et al. (2016). “Aura

- OMI observations of regional SO₂ and NO₂ pollution changes from 2005 to 2015”. In: *Atmospheric Chemistry and Physics* 16.7, pp. 4605–4629. DOI: [10.5194/acp-16-4605-2016](https://doi.org/10.5194/acp-16-4605-2016).
- Kumar, R., Naja, M., Pfister, G., Barth, M., Wiedinmyer, C, and Brasseur, G. (2012). “Simulations over South Asia using the Weather Research and Forecasting model with Chemistry (WRF-Chem): chemistry evaluation and initial results”. In: *Geoscientific Model Development* 5.3, pp. 619–648. DOI: [10.5194/gmd-5-619-2012](https://doi.org/10.5194/gmd-5-619-2012).
- Lannuque, V., Sauvage, B., Barret, B., Clark, H., Athier, G., Boulanger, D., Cammas, J.-P., Cousin, J.-M., Fontaine, A., Le Flochmoën, E., et al. (2021). “Origins and characterization of CO and O₃ in the African upper troposphere”. In: *Atmospheric chemistry and physics* 21.19, pp. 14535–14555. DOI: [10.5194/acp-21-14535-2021](https://doi.org/10.5194/acp-21-14535-2021).
- Lawrence, M. and Lelieveld, J (2010). “Atmospheric pollutant outflow from southern Asia: a review”. In: *Atmospheric Chemistry and Physics* 10.22, pp. 11017–11096. DOI: [10.5194/acp-10-11017-2010](https://doi.org/10.5194/acp-10-11017-2010).
- Lelieveld, J. o., Crutzen, P., Ramanathan, V, Andreae, M., Brenninkmeijer, C., Campos, T, Cass, G., Dickerson, R., Fischer, H, De Gouw, J., et al. (2001). “The Indian Ocean experiment: widespread air pollution from South and Southeast Asia”. In: *Science* 291.5506, pp. 1031–1036. DOI: [10.1126/science.1057103](https://doi.org/10.1126/science.1057103).
- Lelieveld, J. and Dentener, F. J. (2000). “What controls tropospheric ozone?” In: *Journal of Geophysical Research: Atmospheres* 105.D3, pp. 3531–3551. DOI: [10.1029/1999jd901011](https://doi.org/10.1029/1999jd901011).
- Lelieveld, J., Gromov, S., Pozzer, A., and Taraborrelli, D. (2016). “Global tropospheric hydroxyl distribution, budget and reactivity”. In: *Atmospheric Chemistry and Physics* 16.19, pp. 12477–12493. DOI: [10.5194/acp-16-12477-2016](https://doi.org/10.5194/acp-16-12477-2016).
- Lelieveld, J., Hoor, P, Jöckel, P, Pozzer, A, Hadjinicolaou, P, Cammas, J.-P., and Beirle, S (2009). “Severe ozone air pollution in the Persian Gulf region”. In: *Atmospheric Chemistry and Physics* 9.4, pp. 1393–1406. DOI: [10.5194/acp-9-1393-2009](https://doi.org/10.5194/acp-9-1393-2009).
- Leventidou, E., Eichmann, K.-U., Weber, M., and Burrows, J. P. (2016). “Tropical tropospheric ozone columns from nadir retrievals of GOME-1/ERS-2, SCIAMACHY/Envisat, and GOME-2/MetOp-A (1996–2012)”. In: *Atmospheric Measurement Techniques* 9.7, pp. 3407–3427. DOI: [10.5194/amt-9-3407-2016](https://doi.org/10.5194/amt-9-3407-2016).
- Li, D (1995). “A 4-dimensional ozone climatology for UGAMP models.” In: *UGAMP Internal Report No. 35*.
- Li, Y., Lau, A. K., Fung, J. C., Zheng, J., and Liu, S. (2013). “Importance of NO_x control for peak ozone reduction in the Pearl River Delta region”. In: *Journal of Geophysical Research: Atmospheres* 118.16, pp. 9428–9443. DOI: [10.1002/jgrd.50659](https://doi.org/10.1002/jgrd.50659).
- Liang, Q., Jaeglé, L., Jaffe, D. A., Weiss-Penzias, P., Heckman, A., and Snow, J. A. (2004). “Long-range transport of Asian pollution to the northeast Pacific: Seasonal variations and transport pathways of carbon monoxide”. In: *Journal of Geophysical Research: Atmospheres* 109.D23. DOI: [10.1029/2003JD004402](https://doi.org/10.1029/2003JD004402).

- Liaskos, C. E., Allen, D. J., and Pickering, K. E. (2015). "Sensitivity of tropical tropospheric composition to lightning NO_x production as determined by replay simulations with GEOS-5". In: *Journal of Geophysical Research: Atmospheres* 120.16, pp. 8512–8534. DOI: [10.1002/2014jd022987](https://doi.org/10.1002/2014jd022987).
- Lin, M., Holloway, T., Carmichael, G., and Fiore, A. (2010). "Quantifying pollution inflow and outflow over East Asia in spring with regional and global models". In: *Atmospheric Chemistry and Physics* 10.9, pp. 4221–4239. DOI: [10.5194/acp-10-4221-2010](https://doi.org/10.5194/acp-10-4221-2010).
- Lindesay, J., Andreae, M., Goldammer, J., Harris, G., Annegarn, H., Garstang, M., Scholes, R., and Van Wilgen, B. (1996). "International geosphere-biosphere programme/international global atmospheric chemistry SAFARI-92 field experiment: Background and overview". In: *Journal of Geophysical Research: Atmospheres* 101.D19, pp. 23521–23530. DOI: [10.1029/96JD01512](https://doi.org/10.1029/96JD01512).
- Liousse, C., Assamoi, E., Criqui, P., Granier, C., and Rosset, R. (2014). "Explosive growth in African combustion emissions from 2005 to 2030". In: *Environmental Research Letters* 9.3, p. 035003. DOI: [10.1088/1748-9326/9/3/035003](https://doi.org/10.1088/1748-9326/9/3/035003).
- Liu, H., Jacob, D. J., Bey, I., Yantosca, R. M., Duncan, B. N., and Sachse, G. W. (2003). "Transport pathways for Asian pollution outflow over the Pacific: Interannual and seasonal variations". In: *Journal of Geophysical Research: Atmospheres* 108.D20. DOI: [10.1029/2002JD003102](https://doi.org/10.1029/2002JD003102).
- Liu, J., Logan, J. A., Jones, D., Livesey, N., Megretskaia, I., Carouge, C., and Nedelec, P. (2010). "Analysis of CO in the tropical troposphere using Aura satellite data and the GEOS-Chem model: insights into transport characteristics of the GEOS meteorological products". In: *Atmospheric Chemistry and Physics* 10.24, pp. 12207–12232. DOI: [10.5194/acp-10-12207-2010](https://doi.org/10.5194/acp-10-12207-2010).
- Liu, S., McKeen, S., Hsie, E.-Y., Lin, X., Kelly, K., Bradshaw, J., Sandholm, S., Browell, E., Gregory, G., Sachse, G., et al. (1996). "Model study of tropospheric trace species distributions during PEM-West A". In: *Journal of Geophysical Research: Atmospheres* 101.D1, pp. 2073–2085. DOI: [10.1029/95JD02277](https://doi.org/10.1029/95JD02277).
- Livesey, N., Logan, J., Santee, M., Waters, J., Doherty, R., Read, W., Froidevaux, L., and Jiang, J. (2013). "Interrelated variations of O₃, CO and deep convection in the tropical/subtropical upper troposphere observed by the Aura Microwave Limb Sounder (MLS) during 2004–2011". In: *Atmospheric Chemistry and Physics* 13.2, pp. 579–598. DOI: [10.5194/acp-13-579-2013](https://doi.org/10.5194/acp-13-579-2013).
- Logan, J., Megretskaia, I., Miller, A., Tiao, G., Choi, D., Zhang, L., Stolarski, R., Labow, G., Hollandsworth, S., Bodeker, G., et al. (1999). "Trends in the vertical distribution of ozone: A comparison of two analyses of ozonesonde data". In: *Journal of Geophysical Research: Atmospheres* 104.D21, pp. 26373–26399. DOI: [10.1029/1999JD900300](https://doi.org/10.1029/1999JD900300).
- Logan, J. A. (1999). "An analysis of ozonesonde data for the troposphere: Recommendations for testing 3-D models and development of a gridded climatology for tropospheric ozone".

- In: *Journal of Geophysical Research: Atmospheres* 104.D13, pp. 16115–16149. DOI: [10.1029/1998JD100096](https://doi.org/10.1029/1998JD100096).
- Logan, J. A., Prather, M. J., Wofsy, S. C., and McElroy, M. B. (1981). “Tropospheric chemistry: A global perspective”. In: *Journal of Geophysical Research: Oceans* 86.C8, pp. 7210–7254. DOI: [10.1029/JC086iC08p07210](https://doi.org/10.1029/JC086iC08p07210).
- Lu, X., Zhang, L., Chen, Y., Zhou, M., Zheng, B., Li, K., Liu, Y., Lin, J., Fu, T.-M., and Zhang, Q. (2019c). “Exploring 2016–2017 surface ozone pollution over China: source contributions and meteorological influences”. In: *Atmospheric Chemistry and Physics* 19.12, pp. 8339–8361. DOI: [10.5194/acp-19-8339-2019](https://doi.org/10.5194/acp-19-8339-2019).
- Lu, X., Zhang, L., and Shen, L. (2019b). “Meteorology and climate influences on tropospheric ozone: a review of natural sources, chemistry, and transport patterns”. In: *Current Pollution Reports* 5.4, pp. 238–260. DOI: [10.1007/s40726-019-00118-3](https://doi.org/10.1007/s40726-019-00118-3).
- Lu, X., Zhang, L., Zhao, Y., Jacob, D. J., Hu, Y., Hu, L., Gao, M., Liu, X., Petropavlovskikh, I., McClure-Begley, A., et al. (2019a). “Surface and tropospheric ozone trends in the Southern Hemisphere since 1990: possible linkages to poleward expansion of the Hadley circulation”. In: *Science Bulletin* 64.6, pp. 400–409. DOI: [10.1016/j.scib.2018.12.021](https://doi.org/10.1016/j.scib.2018.12.021).
- Marais, E. A. and Wiedinmyer, C. (2016). “Air quality impact of diffuse and inefficient combustion emissions in Africa (DICE-Africa)”. In: *Environmental science & technology* 50.19, pp. 10739–10745. DOI: [10.1021/acs.est.6b02602](https://doi.org/10.1021/acs.est.6b02602).
- Marengo, A., Thouret, V., Nédélec, P., Smit, H., Helten, M., Kley, D., Karcher, F., Simon, P., Law, K., Pyle, J., et al. (1998). “Measurement of ozone and water vapor by Airbus in-service aircraft: The MOZAIC airborne program, An overview”. In: *Journal of Geophysical Research: Atmospheres* 103.D19, pp. 25631–25642. DOI: [10.1029/98JD00977](https://doi.org/10.1029/98JD00977).
- Mari, C., Chaboureaud, J.-P., Pinty, J.-P., Duron, J., Mascart, P., Cammas, J.-P., Gheusi, F., Fehr, T., Schlager, H., Roiger, A., et al. (2006). “Regional lightning NO_x sources during the TROCCINOX experiment”. In: *Atmospheric Chemistry and Physics* 6.12, pp. 5559–5572. DOI: [10.5194/acp-6-5559-2006](https://doi.org/10.5194/acp-6-5559-2006).
- Mari, C., Jacob, D. J., and Bechtold, P. (2000). “Transport and scavenging of soluble gases in a deep convective cloud”. In: *Journal of Geophysical Research: Atmospheres* 105.D17, pp. 22255–22267. DOI: [10.1029/2000JD900211](https://doi.org/10.1029/2000JD900211).
- Mari, C., Cailley, G., Corre, L., Saunois, M., Attié, J., Thouret, V., and Stohl, A. (2008). “Tracing biomass burning plumes from the Southern Hemisphere during the AMMA 2006 wet season experiment”. In: *Atmospheric Chemistry and Physics* 8.14, pp. 3951–3961. DOI: [10.5194/acp-8-3951-2008](https://doi.org/10.5194/acp-8-3951-2008).
- Martin, R. V., Eastham, S. D., Bindle, L., Lundgren, E. W., Clune, T. L., Keller, C. A., Downs, W., Zhang, D., Lucchesi, R. A., Sulprizio, M. P., et al. (2022). “Improved Advection, Resolution, Performance, and Community Access in the New Generation (Version 13) of the High Performance GEOS-Chem Global Atmospheric Chemistry Model (GCHP)”. In: *Geoscientific Model Development Discussions*, pp. 1–30. DOI: [10.5194/gmd-2022-42](https://doi.org/10.5194/gmd-2022-42).

- Martin, S. T., Artaxo, P., Machado, L., Manzi, A. O., Souza, R. d., Schumacher, C., Wang, J., Biscaro, T., Brito, J., Calheiros, A., et al. (2017). “The Green Ocean Amazon experiment (GoAmazon2014/5) observes pollution affecting gases, aerosols, clouds, and rainfall over the rain forest”. In: *Bulletin of the American Meteorological Society* 98.5, pp. 981–997. DOI: [10.1175/BAMS-D-15-00221.1](https://doi.org/10.1175/BAMS-D-15-00221.1).
- Martins, L. D. and Andrade, M. d. F. (2008). “Ozone formation potentials of volatile organic compounds and ozone sensitivity to their emission in the megacity of São Paulo, Brazil”. In: *Water, Air, and Soil Pollution* 195.1, pp. 201–213. DOI: [10.1007/s11270-008-9740-x](https://doi.org/10.1007/s11270-008-9740-x).
- Matricardi, M., Chevallier, F., Kelly, G., and Thépaut, J.-N. (2004). “An improved general fast radiative transfer model for the assimilation of radiance observations”. In: *Quarterly Journal of the Royal Meteorological Society* 130.596, pp. 153–173. DOI: [10.1256/qj.02.181](https://doi.org/10.1256/qj.02.181).
- McDuffie, E. E., Smith, S. J., O’Rourke, P., Tibrewal, K., Venkataraman, C., Marais, E. A., Zheng, B., Crippa, M., Brauer, M., and Martin, R. V. (2020). “A global anthropogenic emission inventory of atmospheric pollutants from sector-and fuel-specific sources (1970–2017): an application of the Community Emissions Data System (CEDS)”. In: *Earth System Science Data* 12.4, pp. 3413–3442. DOI: [10.5194/essd-12-3413-2020](https://doi.org/10.5194/essd-12-3413-2020).
- Mills, G., Buse, A., Gimeno, B., Bermejo, V., Holland, M., Emberson, L., and Pleijel, H. (2007). “A synthesis of AOT40-based response functions and critical levels of ozone for agricultural and horticultural crops”. In: *Atmospheric Environment* 41.12, pp. 2630–2643. DOI: [10.1016/j.atmosenv.2006.11.016](https://doi.org/10.1016/j.atmosenv.2006.11.016).
- Miyazaki, K., Eskes, H., Sudo, K., Boersma, K. F., Bowman, K., and Kanaya, Y. (2017). “Decadal changes in global surface NO_x emissions from multi-constituent satellite data assimilation”. In: *Atmospheric Chemistry and Physics* 17.2, pp. 807–837. DOI: [10.5194/acp-17-807-2017](https://doi.org/10.5194/acp-17-807-2017).
- Monks, P. S. (2005). “Gas-phase radical chemistry in the troposphere”. In: *Chemical Society Reviews* 34.5, pp. 376–395. DOI: [10.1039/B307982C](https://doi.org/10.1039/B307982C).
- Monks, P. S., Archibald, A., Colette, A., Cooper, O., Coyle, M., Derwent, R., Fowler, D., Granier, C., Law, K. S., Mills, G., et al. (2015). “Tropospheric ozone and its precursors from the urban to the global scale from air quality to short-lived climate forcer”. In: *Atmospheric Chemistry and Physics* 15.15, pp. 8889–8973. DOI: [10.5194/acp-15-8889-2015](https://doi.org/10.5194/acp-15-8889-2015).
- Murphy, D. and Fahey, D. (1994). “An estimate of the flux of stratospheric reactive nitrogen and ozone into the troposphere”. In: *Journal of Geophysical Research: Atmospheres* 99.D3, pp. 5325–5332. DOI: [10.1029/93JD03558](https://doi.org/10.1029/93JD03558).
- Myhre, G., Samset, B. H., Schulz, M., Balkanski, Y., Bauer, S., Bernsten, T. K., Bian, H., Bellouin, N., Chin, M., Diehl, T., et al. (2013). “Radiative forcing of the direct aerosol effect from AeroCom Phase II simulations”. In: *Atmospheric Chemistry and Physics* 13.4, pp. 1853–1877. DOI: [10.5194/acp-13-1853-2013](https://doi.org/10.5194/acp-13-1853-2013).
- National Research Council (1991). *Rethinking the Ozone Problem in Urban and Regional Air Pollution*. Washington, DC: The National Academies Press. DOI: [10.17226/1889](https://doi.org/10.17226/1889).

- Naus, S., Domingues, L. G., Krol, M., Luijkx, I. T., Gatti, L. V., Miller, J. B., Gloor, E., Basu, S., Correia, C., Koren, G., et al. (2022). “Sixteen years of MOPITT satellite data strongly constrain Amazon CO fire emissions”. In: *European Geoscience Union (EGU) General Assembly 2022*, pp. 1–25. DOI: [10.5194/egusphere-2022-450](https://doi.org/10.5194/egusphere-2022-450).
- Nedelec, P., Cammas, J.-P., Thouret, V., Athier, G., Cousin, J.-M., Legrand, C., Abonnel, C., Lecoecur, F., Cayez, G., and Marizy, C. (2003). “An improved infrared carbon monoxide analyser for routine measurements aboard commercial Airbus aircraft: technical validation and first scientific results of the MOZAIC III programme”. In: *Atmospheric Chemistry and Physics* 3.5, pp. 1551–1564. DOI: [10.5194/acp-3-1551-2003](https://doi.org/10.5194/acp-3-1551-2003).
- Nédélec, P., Blot, R., Boulanger, D., Athier, G., Cousin, J.-M., Gautron, B., Petzold, A., Volz-Thomas, A., and Thouret, V. (2015). “Instrumentation on commercial aircraft for monitoring the atmospheric composition on a global scale: the IAGOS system, technical overview of ozone and carbon monoxide measurements”. In: *Tellus B: Chemical and Physical Meteorology* 67.1, p. 27791. DOI: [10.3402/tellusb.v67.27791](https://doi.org/10.3402/tellusb.v67.27791).
- Nepstad, D., McGrath, D., Stickler, C., Alencar, A., Azevedo, A., Swette, B., Bezerra, T., DiGiano, M., Shimada, J., Motta, R. Seroa da, et al. (2014). “Slowing Amazon deforestation through public policy and interventions in beef and soy supply chains”. In: *science* 344.6188, pp. 1118–1123. DOI: [10.1126/science.1248525](https://doi.org/10.1126/science.1248525).
- Olivier, J. and Berdowski, J. (2001). “Global emissions sources and sinks, The Climate System”. In: *Lisse, The Netherlands: AA Balkema Publishers/Swets & Zeitlinger Publishers* 90 5809.255, p. 0.
- Osterman, G., Kulawik, S., Worden, H., Richards, N., Fisher, B., Eldering, A., Shephard, M., Froidevaux, L., Labow, G., Luo, M., et al. (2008). “Validation of Tropospheric Emission Spectrometer (TES) measurements of the total, stratospheric, and tropospheric column abundance of ozone”. In: *Journal of Geophysical Research: Atmospheres* 113.D15. DOI: [10.1029/2007JD008801](https://doi.org/10.1029/2007JD008801).
- Pandey, A., Sadavarte, P., Rao, A. B., and Venkataraman, C. (2014). “Trends in multi-pollutant emissions from a technology-linked inventory for India: II. Residential, agricultural and informal industry sectors”. In: *Atmospheric environment* 99, pp. 341–352. DOI: [10.1016/j.atmosenv.2014.09.080](https://doi.org/10.1016/j.atmosenv.2014.09.080).
- Park, M., Randel, W. J., Emmons, L. K., Bernath, P. F., Walker, K. A., and Boone, C. D. (2008). “Chemical isolation in the Asian monsoon anticyclone observed in Atmospheric Chemistry Experiment (ACE-FTS) data”. In: *Atmospheric Chemistry and Physics* 8.3, pp. 757–764. DOI: [10.5194/acp-8-757-2008](https://doi.org/10.5194/acp-8-757-2008).
- Park, M., Randel, W. J., Gettelman, A., Massie, S. T., and Jiang, J. H. (2007). “Transport above the Asian summer monsoon anticyclone inferred from Aura Microwave Limb Sounder tracers”. In: *Journal of Geophysical Research: Atmospheres* 112.D16. DOI: [10.1029/2006JD008294](https://doi.org/10.1029/2006JD008294).

- Parrish, D. D., Holloway, J. S., Trainer, M., Murphy, P. C., Fehsenfeld, F. C., and Forbes, G. L. (1993). “Export of North American ozone pollution to the north Atlantic Ocean”. In: *Science* 259.5100, pp. 1436–1439. DOI: [10.1126/science.259.5100.1436](https://doi.org/10.1126/science.259.5100.1436).
- Parrish, D., Trainer, M., Holloway, J., Yee, J., Warshawsky, M., Fehsenfeld, F., Forbes, G., and Moody, J. (1998). “Relationships between ozone and carbon monoxide at surface sites in the North Atlantic region”. In: *Journal of Geophysical Research: Atmospheres* 103.D11, pp. 13357–13376. DOI: [10.1029/98JD00376](https://doi.org/10.1029/98JD00376).
- Paul, J., Fortuin, F., and Kelder, H. (1998). “An ozone climatology based on ozonesonde and satellite measurements”. In: *Journal of Geophysical Research: Atmospheres* 103.D24, pp. 31709–31734. DOI: [10.1029/1998JD200008](https://doi.org/10.1029/1998JD200008).
- Pavelin, E., English, S., and Eyre, J. (2008). “The assimilation of cloud-affected infrared satellite radiances for numerical weather prediction”. In: *Quarterly Journal of the Royal Meteorological Society: A journal of the atmospheric sciences, applied meteorology and physical oceanography* 134.632, pp. 737–749. DOI: [10.1002/qj.243](https://doi.org/10.1002/qj.243).
- Peters, W. (2002). “Ozone in the Tropical Troposphere”. PhD thesis.
- Petetin, H., Jeoffrion, M., Sauvage, B., Athier, G., Blot, R., Boulanger, D., Clark, H., Cousin, J.-M., Gheusi, F., Nédélec, P., et al. (2018a). “Representativeness of the IAGOS airborne measurements in the lower troposphere”. In: *Elementa: Science of the Anthropocene* 6. DOI: [10.1525/elementa.280](https://doi.org/10.1525/elementa.280).
- Petetin, H., Thouret, V., Athier, G., Blot, R., Boulanger, D., Cousin, J.-M., Gaudel, A., Nédélec, P., and Cooper, O (2016). “Diurnal cycle of ozone throughout the troposphere over Frankfurt as measured by MOZAIC-IAGOS commercial aircraftDiurnal cycle of ozone throughout the troposphere”. In: *Elementa: Science of the Anthropocene* 4. DOI: [10.12952/journal.elementa.000129](https://doi.org/10.12952/journal.elementa.000129).
- Petetin, H., Sauvage, B., Parrington, M., Clark, H., Fontaine, A., Athier, G., Blot, R., Boulanger, D., Cousin, J.-M., Nédélec, P., et al. (2018b). “The role of biomass burning as derived from the tropospheric CO vertical profiles measured by IAGOS aircraft in 2002–2017”. In: *Atmospheric Chemistry and Physics* 18.23, pp. 17277–17306. DOI: [10.5194/acp-18-17277-2018](https://doi.org/10.5194/acp-18-17277-2018).
- Petzold, A., Thouret, V., Gerbig, C., Zahn, A., Brenninkmeijer, C. A., Gallagher, M., Hermann, M., Pontaud, M., Ziereis, H., Boulanger, D., et al. (2015). “Global-scale atmosphere monitoring by in-service aircraft—current achievements and future prospects of the European Research Infrastructure IAGOS”. In: *Tellus B: Chemical and Physical Meteorology* 67.1, p. 28452. DOI: [10.3402/tellusb.v67.28452](https://doi.org/10.3402/tellusb.v67.28452).
- Pickering, K. E., Thompson, A. M., Kim, H., DeCaria, A. J., Pfister, L., Kucsera, T. L., Witte, J. C., Avery, M. A., Blake, D. R., Crawford, J. H., et al. (2001). “Trace gas transport and scavenging in PEM-Tropics B South Pacific Convergence Zone convection”. In: *Journal of Geophysical Research: Atmospheres* 106.D23, pp. 32591–32607. DOI: [10.1029/2001JD000328](https://doi.org/10.1029/2001JD000328).

- Pickering, K. E., Thompson, A. M., Tao, W.-K., Rood, R. B., McNamara, D. P., and Molod, A. M. (1995). "Vertical transport by convective clouds: Comparisons of three modeling approaches". In: *Geophysical research letters* 22.9, pp. 1089–1092. DOI: [10.1029/95GL00889](https://doi.org/10.1029/95GL00889).
- Pisso, I., Real, E., Law, K. S., Legras, B., Bousserez, N., Attié, J.-L., and Schlager, H (2009). "Estimation of mixing in the troposphere from lagrangian trace gas reconstructions during long-range pollution plume transport". In: *Journal of Geophysical Research: Atmospheres* 114.D19. DOI: [10.1029/2008JD011289](https://doi.org/10.1029/2008JD011289).
- Randel, W. J., Park, M., Emmons, L., Kinnison, D., Bernath, P., Walker, K. A., Boone, C., and Pumphrey, H. (2010). "Asian monsoon transport of pollution to the stratosphere". In: *Science* 328.5978, pp. 611–613. DOI: [10.1126/science.1182274](https://doi.org/10.1126/science.1182274).
- Raub, J. and Benignus, V. (2002). "Carbon monoxide and the nervous system". In: *Neuroscience & Biobehavioral Reviews* 26.8, pp. 925–940. DOI: [10.1016/S0149-7634\(03\)00002-2](https://doi.org/10.1016/S0149-7634(03)00002-2).
- Ravindrababu, S, Ratnam, M. V., Basha, G., Liou, Y.-A., and Reddy, N. N. (2019). "Large anomalies in the tropical upper troposphere lower stratosphere (UTLS) trace gases observed during the extreme 2015–16 El Niño event by using satellite measurements". In: *Remote Sensing* 11.6, p. 687. DOI: [10.3390/rs11060687](https://doi.org/10.3390/rs11060687).
- Redelsperger, J.-L., Thorncroft, C. D., Diedhiou, A., Lebel, T., Parker, D. J., and Polcher, J. (2006). "African Monsoon Multidisciplinary Analysis: An international research project and field campaign". In: *Bulletin of the American Meteorological Society* 87.12, pp. 1739–1746. DOI: [10.1175/BAMS-87-12-1739](https://doi.org/10.1175/BAMS-87-12-1739).
- Reeves, C., Formenti, P, Afif, C., Ancellet, G., Attié, J.-L., Bechara, J, Borbon, A., Cairo, F, Coe, H, Crumeyrolle, S, et al. (2010). "Chemical and aerosol characterisation of the troposphere over West Africa during the monsoon period as part of AMMA". In: *Atmospheric Chemistry and Physics* 10.16, pp. 7575–7601. DOI: [10.5194/acp-10-7575-2010](https://doi.org/10.5194/acp-10-7575-2010).
- Rodgers, C. D. (2000). *Inverse methods for atmospheric sounding: theory and practice*. Vol. 2. World scientific.
- Sadavarte, P. and Venkataraman, C. (2014). "Trends in multi-pollutant emissions from a technology-linked inventory for India: I. Industry and transport sectors". In: *Atmospheric environment* 99, pp. 353–364. DOI: [10.1016/j.atmosenv.2014.09.081](https://doi.org/10.1016/j.atmosenv.2014.09.081).
- Safieddine, S., Boynard, A., Coheur, P.-F., Hurtmans, D., Pfister, G., Quennehen, B., Thomas, J. L., Raut, J.-C., Law, K. S., Klimont, Z., et al. (2014). "Summertime tropospheric ozone assessment over the Mediterranean region using the thermal infrared IASI/MetOp sounder and the WRF-Chem model". In: *Atmospheric chemistry and physics* 14.18, pp. 10119–10131. DOI: [10.5194/acp-14-10119-2014](https://doi.org/10.5194/acp-14-10119-2014).
- Safieddine, S., Boynard, A., Hao, N., Huang, F., Wang, L., Ji, D., Barret, B., Ghude, S. D., Coheur, P.-F., Hurtmans, D., et al. (2016). "Tropospheric ozone variability during the East Asian summer monsoon as observed by satellite (IASI), aircraft (MOZAIC) and

- ground stations”. In: *Atmospheric Chemistry and Physics* 16.16, pp. 10489–10500. DOI: [10.5194/acp-16-10489-2016](https://doi.org/10.5194/acp-16-10489-2016).
- Sahu, L., Sheel, V., Kajino, M., Deushi, M., Gunthe, S. S., Sinha, P., Sauvage, B., Thouret, V., and Smit, H. G. (2014). “Seasonal and interannual variability of tropospheric ozone over an urban site in India: A study based on MOZAIC and CCM vertical profiles over Hyderabad”. In: *Journal of Geophysical Research: Atmospheres* 119.6, pp. 3615–3641. DOI: [10.1002/2013JD021215](https://doi.org/10.1002/2013JD021215).
- Sahu, L., Sheel, V., Kajino, M., Gunthe, S. S., Thouret, V., Nedelec, P., and Smit, H. G. (2013). “Characteristics of tropospheric ozone variability over an urban site in Southeast Asia: A study based on MOZAIC and MOZART vertical profiles”. In: *Journal of Geophysical Research: Atmospheres* 118.15, pp. 8729–8747. DOI: [10.1002/jgrd.50662](https://doi.org/10.1002/jgrd.50662).
- Saunders, R., Hocking, J., Turner, E., Rayer, P., Rundle, D., Brunel, P., Vidot, J., Roquet, P., Matricardi, M., Geer, A., et al. (2018). “An update on the RTTOV fast radiative transfer model (currently at version 12)”. In: *Geoscientific Model Development* 11.7, pp. 2717–2737. DOI: [10.5194/gmd-11-2717-2018](https://doi.org/10.5194/gmd-11-2717-2018).
- Saunois, M., Reeves, C., Mari, C., Murphy, J., Stewart, D. J., Mills, G., Oram, D., and Purvis, R. (2009). “Factors controlling the distribution of ozone in the West African lower troposphere during the AMMA (African Monsoon Multidisciplinary Analysis) wet season campaign”. In: *Atmospheric Chemistry and Physics* 9.16, pp. 6135–6155. DOI: [10.5194/acp-9-6135-2009](https://doi.org/10.5194/acp-9-6135-2009).
- Sauvage, B., Gheusi, F., Thouret, V., Cammas, J.-P., Duron, J., Escobar, J., Mari, C., Mascart, P., and Pont, V. (2007a). “Medium-range mid-tropospheric transport of ozone and precursors over Africa: two numerical case studies in dry and wet seasons”. In: *Atmospheric Chemistry and Physics* 7.20, pp. 5357–5370. DOI: [10.5194/acp-7-5357-2007](https://doi.org/10.5194/acp-7-5357-2007).
- Sauvage, B., Martin, R. V., Van Donkelaar, A., and Ziemke, J. (2007b). “Quantification of the factors controlling tropical tropospheric ozone and the South Atlantic maximum”. In: *Journal of Geophysical Research: Atmospheres* 112.D11. DOI: [10.1029/2006JD008008](https://doi.org/10.1029/2006JD008008).
- Sauvage, B., Martin, R., Van Donkelaar, A., Liu, X., Chance, K., Jaeglé, L., Palmer, P., Wu, S., and Fu, T.-M. (2007c). “Remote sensed and in situ constraints on processes affecting tropical tropospheric ozone”. In: *Atmospheric Chemistry and Physics* 7.3, pp. 815–838. DOI: [10.5194/acp-7-815-2007](https://doi.org/10.5194/acp-7-815-2007).
- Sauvage, B., Thouret, V., Cammas, J.-P., Brioude, J., Nedelec, P., and Mari, C. (2007d). “Meridional ozone gradients in the African upper troposphere”. In: *Geophysical Research Letters* 34.3. DOI: [10.1029/2006GL028542](https://doi.org/10.1029/2006GL028542).
- Sauvage, B., Thouret, V., Cammas, J.-P., Gheusi, F., Athier, G., and Nédélec, P. (2005). “Tropospheric ozone over Equatorial Africa: regional aspects from the MOZAIC data”. In: *Atmospheric Chemistry and Physics* 5.2, pp. 311–335. DOI: [10.5194/acp-5-311-2005](https://doi.org/10.5194/acp-5-311-2005).
- Sauvage, B., Thouret, V., Thompson, A., Witte, J., Cammas, J.-P., Nédélec, P., and Athier, G. (2006). “Enhanced view of the “tropical Atlantic ozone paradox” and “zonal wave one”

- from the in situ MOZAIC and SHADOZ data”. In: *Journal of Geophysical Research: Atmospheres* 111.D1. DOI: [10.1029/2005JD006241](https://doi.org/10.1029/2005JD006241).
- Sauvage, B., Fontaine, A., Eckhardt, S., Auby, A., Boulanger, D., Petetin, H., Paugam, R., Athier, G., Cousin, J.-M., Darras, S., et al. (2017). “Source attribution using FLEX-PART and carbon monoxide emission inventories: SOFT-IO version 1.0”. In: *Atmospheric Chemistry and Physics* 17.24, pp. 15271–15292. DOI: [10.5194/acp-17-15271-2017](https://doi.org/10.5194/acp-17-15271-2017).
- Scharffe, D., Slemr, F., Brenninkmeijer, C. A. M., and Zahn, A. (2012). “Carbon monoxide measurements onboard the CARIBIC passenger aircraft using UV resonance fluorescence”. In: *Atmos. Meas. Tech.* 5.7, pp. 1753–1760. DOI: [10.5194/amt-5-1753-2012](https://doi.org/10.5194/amt-5-1753-2012).
- Schumann, U. and Huntrieser, H. (2007). “The global lightning-induced nitrogen oxides source”. In: *Atmospheric Chemistry and Physics* 7.14, pp. 3823–3907. DOI: [10.5194/acp-7-3823-2007](https://doi.org/10.5194/acp-7-3823-2007).
- Seinfeld, J. H. and Pandis, S. N. (1998). “From air pollution to climate change”. In: *Atmospheric chemistry and physics* 1326. DOI: [10.1063/1.882420](https://doi.org/10.1063/1.882420).
- Sheel, V., Sahu, L., Kajino, M., Deushi, M., Stein, O., and Nedelec, P. (2014). “Seasonal and interannual variability of carbon monoxide based on MOZAIC observations, MACC reanalysis, and model simulations over an urban site in India”. In: *Journal of Geophysical Research: Atmospheres* 119.14, pp. 9123–9141. DOI: [10.1002/2013JD021425](https://doi.org/10.1002/2013JD021425).
- Shindell, D., Faluvegi, G., Lacis, A., Hansen, J., Ruedy, R., and Aguilar, E. (2006). “Role of tropospheric ozone increases in 20th-century climate change”. In: *Journal of Geophysical Research: Atmospheres* 111.D8. DOI: [10.1029/2005JD006348](https://doi.org/10.1029/2005JD006348).
- Silva, V. B. and Kousky, V. E. (2012). “The South American monsoon system: climatology and variability”. In: *Modern climatology* 123, p. 152.
- Sindelarova, K., Granier, C., Bouarar, I., Guenther, A., Tilmes, S., Stavrakou, T., Müller, J.-F., Kuhn, U., Stefani, P., and Knorr, W. (2014). “Global data set of biogenic VOC emissions calculated by the MEGAN model over the last 30 years”. In: *Atmospheric Chemistry and Physics* 14.17, pp. 9317–9341. DOI: [10.5194/acp-14-9317-2014](https://doi.org/10.5194/acp-14-9317-2014).
- Singh, H., Brune, W., Crawford, J., Flocke, F., and Jacob, D. J. (2009). “Chemistry and transport of pollution over the Gulf of Mexico and the Pacific: spring 2006 INTEx-B campaign overview and first results”. In: *Atmospheric Chemistry and Physics* 9.7, pp. 2301–2318. DOI: [10.5194/acp-9-2301-2009](https://doi.org/10.5194/acp-9-2301-2009).
- Singh, H., Herlth, D., Kolyer, R., Chatfield, R., Viezee, W., Salas, L., Chen, Y., Bradshaw, J., Sandholm, S., Talbot, R., et al. (1996). “Impact of biomass burning emissions on the composition of the South Atlantic troposphere: Reactive nitrogen and ozone”. In: *Journal of Geophysical Research: Atmospheres* 101.D19, pp. 24203–24219. DOI: [10.1029/96JD01018](https://doi.org/10.1029/96JD01018).
- Sinha, B., Singh Sangwan, K., Maurya, Y., Kumar, V., Sarkar, C., Chandra, B., and Sinha, V. (2015). “Assessment of crop yield losses in Punjab and Haryana using 2 years of continuous in situ ozone measurements”. In: *Atmospheric Chemistry and Physics* 15.16, pp. 9555–9576. DOI: [10.5194/acp-15-9555-2015](https://doi.org/10.5194/acp-15-9555-2015).

- Stein, O, Schultz, M. G., Bouarar, I., Clark, H, Huijnen, V, Gaudel, A, George, M., and Clerbaux, C. (2014). “On the wintertime low bias of Northern Hemisphere carbon monoxide found in global model simulations”. In: *Atmospheric chemistry and physics* 14.17, pp. 9295–9316. DOI: [10.5194/acp-14-9295-2014](https://doi.org/10.5194/acp-14-9295-2014).
- Stevenson, D., Dentener, F., Schultz, M., Ellingsen, K, Van Noije, T., Wild, O, Zeng, G, Amann, M, Atherton, C., Bell, N, et al. (2006). “Multimodel ensemble simulations of present-day and near-future tropospheric ozone”. In: *Journal of Geophysical Research: Atmospheres* 111.D8. DOI: [10.1029/2005JD006338](https://doi.org/10.1029/2005JD006338).
- Stevenson, D., Young, P., Naik, V., Lamarque, J.-F., Shindell, D. T., Voulgarakis, A, Skeie, R. B., Dalsoren, S. B., Myhre, G., Berntsen, T. K., et al. (2013). “Tropospheric ozone changes, radiative forcing and attribution to emissions in the Atmospheric Chemistry and Climate Model Intercomparison Project (ACCMIP)”. In: *Atmospheric Chemistry and Physics* 13.6, pp. 3063–3085. DOI: [10.5194/acp-13-3063-2013](https://doi.org/10.5194/acp-13-3063-2013).
- Stohl, A, Bonasoni, P, Cristofanelli, P, Collins, W, Feichter, J., Frank, A, Forster, C, Gerasopoulos, E, Gäggeler, H, James, P, et al. (2003). “Stratosphere-troposphere exchange: A review, and what we have learned from STACCATO”. In: *Journal of Geophysical Research: Atmospheres* 108.D12. DOI: [10.1029/2002JD002490](https://doi.org/10.1029/2002JD002490).
- Stohl, A., Forster, C, Frank, A, Seibert, P, and Wotawa, G (2005). “The Lagrangian particle dispersion model FLEXPART version 6.2”. In: *Atmospheric Chemistry and Physics* 5.9, pp. 2461–2474. DOI: [10.5194/acp-5-2461-2005](https://doi.org/10.5194/acp-5-2461-2005).
- Stohl, A., Klimont, Z., Eckhardt, S., Kupiainen, K., Shevchenko, V. P., Kopeikin, V., and Novigatsky, A. (2013). “Black carbon in the Arctic: the underestimated role of gas flaring and residential combustion emissions”. In: *Atmospheric Chemistry and Physics* 13.17, pp. 8833–8855.
- Swap, R. J., Annegarn, H. J., Suttles, J. T., King, M. D., Platnick, S., Privette, J. L., and Scholes, R. J. (2003). “Africa burning: a thematic analysis of the Southern African Regional Science Initiative (SAFARI 2000)”. In: *Journal of Geophysical Research: Atmospheres* 108.D13. DOI: [10.1029/2003JD003747](https://doi.org/10.1029/2003JD003747).
- Tadic, I., Nussbaumer, C. M., Bohn, B., Harder, H., Marno, D., Martinez, M., Obersteiner, F., Parchatka, U., Pozzer, A., Rohloff, R., et al. (2021). “Central role of nitric oxide in ozone production in the upper tropical troposphere over the Atlantic Ocean and western Africa”. In: *Atmospheric Chemistry and Physics* 21.10, pp. 8195–8211. DOI: [10.5194/acp-21-8195-2021](https://doi.org/10.5194/acp-21-8195-2021).
- Tang, Q, Prather, M., and Hsu, J (2011). “Stratosphere-troposphere exchange ozone flux related to deep convection”. In: *Geophysical Research Letters* 38.3. DOI: [10.1029/2010GL046039](https://doi.org/10.1029/2010GL046039).
- Tanimoto, H., Zbinden, R. M., Thouret, V., and Nédélec, P. (2015). “Consistency of tropospheric ozone observations made by different platforms and techniques in the global databases”. In: *Tellus B: Chemical and Physical Meteorology* 67.1, p. 27073. DOI: [10.3402/tellusb.v67.27073](https://doi.org/10.3402/tellusb.v67.27073).

- Tarasick, D., Carey-Smith, T., Hocking, W., Moeini, O, He, H, Liu, J, Osman, M., Thompson, A., Johnson, B., Oltmans, S., et al. (2019). “Quantifying stratosphere-troposphere transport of ozone using balloon-borne ozonesondes, radar windprofilers and trajectory models”. In: *Atmospheric Environment* 198, pp. 496–509. DOI: [10.1016/j.atmosenv.2018.10.040](https://doi.org/10.1016/j.atmosenv.2018.10.040).
- Thompson, A. M., Doddridge, B. G., Witte, J. C., Hudson, R. D., Luke, W. T., Johnson, J. E., Johnson, B. J., Oltmans, S. J., and Weller, R. (2000). “A tropical Atlantic paradox: Shipboard and satellite views of a tropospheric ozone maximum and wave-one in January–February 1999”. In: *Geophysical Research Letters* 27.20, pp. 3317–3320. DOI: [10.1029/1999GL011273](https://doi.org/10.1029/1999GL011273).
- Thompson, A. M., Stauffer, R. M., Wargan, K., Witte, J. C., Kollonige, D. E., and Ziemke, J. R. (2021). “Regional and Seasonal trends in tropical ozone from SHADOZ profiles: Reference for models and satellite products”. In: *Journal of Geophysical Research: Atmospheres* 126.22, e2021JD034691. DOI: [10.1029/2021JD034691](https://doi.org/10.1029/2021JD034691).
- Thompson, A. M., Witte, J. C., Hudson, R. D., Guo, H., Herman, J. R., and Fujiwara, M. (2001). “Tropical tropospheric ozone and biomass burning”. In: *Science* 291.5511, pp. 2128–2132. DOI: [10.1126/science.291.5511.2128](https://doi.org/10.1126/science.291.5511.2128).
- Thompson, A. M., Witte, J. C., McPeters, R. D., Oltmans, S. J., Schmidlin, F. J., Logan, J. A., Fujiwara, M., Kirchhoff, V. W., Posny, F., Coetzee, G. J., et al. (2003a). “Southern hemisphere additional Ozonesondes (SHADOZ) 1998–2000 tropical ozone climatology 1. Comparison with Total ozone mapping spectrometer (TOMS) and ground-based measurements”. In: *Journal of Geophysical Research: Atmospheres* 108.D2. DOI: [10.1029/2001JD000967](https://doi.org/10.1029/2001JD000967).
- Thompson, A. M., Witte, J. C., Oltmans, S. J., Schmidlin, F. J., Logan, J. A., Fujiwara, M., Kirchhoff, V. W., Posny, F., Coetzee, G. J., Hoegger, B., et al. (2003b). “Southern Hemisphere Additional Ozonesondes (SHADOZ) 1998–2000 tropical ozone climatology 2. Tropospheric variability and the zonal wave-one”. In: *Journal of Geophysical Research: Atmospheres* 108.D2. DOI: [10.1029/2002JD002241](https://doi.org/10.1029/2002JD002241).
- Thouret, V., Marenco, A., Logan, J. A., Nédélec, P., and Grouhel, C. (1998). “Comparisons of ozone measurements from the MOZAIC airborne program and the ozone sounding network at eight locations”. In: *Journal of Geophysical Research: Atmospheres* 103.D19, pp. 25695–25720. DOI: [10.1029/98JD02243](https://doi.org/10.1029/98JD02243).
- Thouret, V., Clark, H., Petzold, A., Nédélec, P., and Zahn, A. (2022). “IAGOS: Monitoring Atmospheric Composition for Air Quality and Climate by Passenger Aircraft”. In: *In Handbook of Air Quality and Climate Change*. Singapore: Springer Nature Singapore, pp. 1–14. DOI: https://doi.org/10.1007/978-981-15-2527-8_57-1.
- Tsivlidou, M., Sauvage, B., Barret, B., Wolff, P., Clark, H., Bennouna, Y., Blot, R., Boulanger, D., Nédélec, P., Le Flochmoën, E., et al. (2022). “Tropical tropospheric ozone and carbon monoxide distributions: characteristics, origins and control factors, as seen by IAGOS and IASI”. In: *Atmospheric Chemistry and Physics Discussions*, pp. 1–50. DOI: [10.5194/acp-2022-686](https://doi.org/10.5194/acp-2022-686).

- Van Der Werf, G. R., Randerson, J. T., Giglio, L., Van Leeuwen, T. T., Chen, Y., Rogers, B. M., Mu, M., Van Marle, M. J., Morton, D. C., Collatz, G. J., et al. (2017). “Global fire emissions estimates during 1997–2016”. In: *Earth System Science Data* 9.2, pp. 697–720. DOI: [10.5194/essd-9-697-2017](https://doi.org/10.5194/essd-9-697-2017), 2017.
- Vinken, G., Boersma, K., Maasakkers, J., Adon, M., and Martin, R. (2014). “Worldwide biogenic soil NO_x emissions inferred from OMI NO₂ observations”. In: *Atmospheric Chemistry and Physics* 14.18, pp. 10363–10381. DOI: [10.5194/acp-14-10363-2014](https://doi.org/10.5194/acp-14-10363-2014).
- Voulgarakis, A., Telford, P., Aghedo, A., Braesicke, P., Faluvegi, G., Abraham, N., Bowman, K., Pyle, J., and Shindell, D. (2011). “Global multi-year O₃-CO correlation patterns from models and TES satellite observations”. In: *Atmospheric Chemistry and Physics* 11.12, pp. 5819–5838. DOI: [10.5194/acp-11-5819-2011](https://doi.org/10.5194/acp-11-5819-2011).
- Voulgarakis, A., Marlier, M. E., Faluvegi, G., Shindell, D. T., Tsigaridis, K., and Mangeon, S. (2015). “Interannual variability of tropospheric trace gases and aerosols: The role of biomass burning emissions”. In: *Journal of Geophysical Research: Atmospheres* 120.14, pp. 7157–7173. DOI: [10.1002/2014JD022926](https://doi.org/10.1002/2014JD022926).
- Wang, H., Lu, X., Jacob, D. J., Cooper, O. R., Chang, K.-L., Li, K., Gao, M., Liu, Y., Sheng, B., Wu, K., et al. (2022). “Global tropospheric ozone trends, attributions, and radiative impacts in 1995–2017: an integrated analysis using aircraft (IAGOS) observations, ozonesonde, and multi-decadal chemical model simulations”. In: *Atmospheric Chemistry and Physics* 22.20, pp. 13753–13782. DOI: [10.5194/acp-22-13753-2022](https://doi.org/10.5194/acp-22-13753-2022).
- Wang, T., Xue, L., Brimblecombe, P., Lam, Y. F., Li, L., and Zhang, L. (2017). “Ozone pollution in China: A review of concentrations, meteorological influences, chemical precursors, and effects”. In: *Science of the Total Environment* 575, pp. 1582–1596. DOI: [10.1016/j.scitotenv.2016.10.081](https://doi.org/10.1016/j.scitotenv.2016.10.081).
- Welch, B. L. (1947). “The generalization of ‘STUDENT’S’ problem when several different population variances are involved”. In: *Biometrika* 34.1-2, pp. 28–35. DOI: [10.1093/biomet/34.1-2.28](https://doi.org/10.1093/biomet/34.1-2.28).
- Weng, H., Lin, J., Martin, R., Millet, D. B., Jaeglé, L., Ridley, D., Keller, C., Li, C., Du, M., and Meng, J. (2020). “Global high-resolution emissions of soil NO_x, sea salt aerosols, and biogenic volatile organic compounds”. In: *Scientific Data* 7.1, pp. 1–15. DOI: [10.6084/m9.figshare.12205379](https://doi.org/10.6084/m9.figshare.12205379).
- Werf, G. R. Van der, Randerson, J. T., Giglio, L., Collatz, G., Mu, M., Kasibhatla, P. S., Morton, D. C., DeFries, R., Jin, Y. v., and Leeuwen, T. T. van (2010). “Global fire emissions and the contribution of deforestation, savanna, forest, agricultural, and peat fires (1997–2009)”. In: *Atmospheric chemistry and physics* 10.23, pp. 11707–11735. DOI: [10.5194/acp-10-11707-2010](https://doi.org/10.5194/acp-10-11707-2010).
- Wespes, C., Hurtmans, D., Clerbaux, C., and Coheur, P.-F. (2017). “O₃ variability in the troposphere as observed by IASI over 2008–2016: Contribution of atmospheric chemistry and dynamics”. In: *Journal of Geophysical Research: Atmospheres* 122.4, pp. 2429–2451. DOI: [10.1002/2016JD025875](https://doi.org/10.1002/2016JD025875).

- WHO (2021). *WHO global air quality guidelines: particulate matter (PM_{2.5} and PM₁₀), ozone, nitrogen dioxide, sulfur dioxide and carbon monoxide*. World Health Organization. DOI: <https://apps.who.int/iris/handle/10665/345329>.
- Wild, O. (2007). “Modelling the global tropospheric ozone budget: exploring the variability in current models”. In: *Atmospheric Chemistry and Physics* 7.10, pp. 2643–2660. DOI: [10.5194/acp-7-2643-2007](https://doi.org/10.5194/acp-7-2643-2007).
- Wild, O., Pochanart, P., and Akimoto, H. (2004). “Trans-Eurasian transport of ozone and its precursors”. In: *Journal of Geophysical Research: Atmospheres* 109.D11. DOI: [10.1029/2003JD004501](https://doi.org/10.1029/2003JD004501).
- Wofsy, S. et al. (2011). “HIAPER Pole-to-Pole Observations (HIPPO): Fine grained, global scale measurements for determining rates for transport, surface emissions, and removal of climatically important atmospheric gases and aerosols”. In: *Philos Trans R Soc Lond A* 369.1943, pp. 2073–2086. DOI: [10.1098/rsta.2010.0313](https://doi.org/10.1098/rsta.2010.0313).
- Wolf, J., Sauer, D., Eirenschmalz, L., Klausner, T., and Schlager, H. (2020). “Aerosol microphysical properties for selected case studies during the EMeRGe-EU and EMeRGe-Asia campaigns”. In: *EGU General Assembly Conference Abstracts*, p. 18315. DOI: [10.5194/egusphere-egu2020-18315](https://doi.org/10.5194/egusphere-egu2020-18315).
- Yamasoe, M. A., Sauvage, B., Thouret, V., Nédélec, P., Le Flochmoen, E., and Barret, B. (2015). “Analysis of tropospheric ozone and carbon monoxide profiles over South America based on MOZAIC/IAGOS database and model simulations”. In: *Tellus B: Chemical and Physical Meteorology* 67.1, p. 27884. DOI: [10.3402/tellusb.v67.27884](https://doi.org/10.3402/tellusb.v67.27884).
- Yan, Y. Y. (2005). “Intertropical convergence zone (ITCZ)”. In: *Encyclopedia of world climatology*, pp. 429–432. DOI: [10.1007/1-4020-3266-8_110](https://doi.org/10.1007/1-4020-3266-8_110).
- Yarragunta, Y., Srivastava, S., Mitra, D., Le Flochmoën, E., Barret, B., Kumar, P., and Chandola, H. (2019). “Source attribution of carbon monoxide and ozone over the Indian subcontinent using MOZART-4 chemistry transport model”. In: *Atmospheric Research* 227, pp. 165–177. DOI: [10.1016/j.atmosres.2019.04.019](https://doi.org/10.1016/j.atmosres.2019.04.019).
- Young, P. J., Naik, V., Fiore, A. M., Gaudel, A., Guo, J., Lin, M., Neu, J., Parrish, D., Rieder, H., Schnell, J., et al. (2018). “Tropospheric Ozone Assessment Report: Assessment of global-scale model performance for global and regional ozone distributions, variability, and trends”. In: *Elementa: Science of the Anthropocene* 6. DOI: [10.1525/elementa.265](https://doi.org/10.1525/elementa.265).
- Young, P., Archibald, A., Bowman, K., Lamarque, J.-F., Naik, V., Stevenson, D., Tilmes, S., Voulgarakis, A., Wild, O., Bergmann, D., et al. (2013). “Pre-industrial to end 21st century projections of tropospheric ozone from the Atmospheric Chemistry and Climate Model Intercomparison Project (ACCMIP)”. In: *Atmospheric Chemistry and Physics* 13.4, pp. 2063–2090. DOI: [10.5194/acp-13-2063-2013](https://doi.org/10.5194/acp-13-2063-2013).
- Zahn, A., Weppner, J., Widmann, H., Schlote-Holubek, K., Burger, B., Kühner, T., and Franke, H. (2012). “A fast and precise chemiluminescence ozone detector for eddy flux and airborne application”. In: *Atmos. Meas. Tech.* 5.2, pp. 363–375. DOI: [10.5194/amt-5-363-2012](https://doi.org/10.5194/amt-5-363-2012).

- Zhang, Y., Cooper, O. R., Gaudel, A., Thompson, A. M., Nédélec, P., Ogino, S.-Y., and West, J. J. (2016). “Tropospheric ozone change from 1980 to 2010 dominated by equatorward redistribution of emissions”. In: *Nature Geoscience* 9.12, pp. 875–879. DOI: [10.1038/ngeo2827](https://doi.org/10.1038/ngeo2827).
- Zhang, Y., West, J. J., Emmons, L. K., Flemming, J., Jonson, J. E., Lund, M. T., Sekiya, T., Sudo, K., Gaudel, A., Chang, K.-L., et al. (2021). “Contributions of world regions to the global tropospheric ozone burden change from 1980 to 2010”. In: *Geophysical Research Letters* 48.1, e2020GL089184. DOI: [10.1029/2020GL089184](https://doi.org/10.1029/2020GL089184).
- Zheng, B., Chevallier, F., Ciais, P., Yin, Y., Deeter, M. N., Worden, H. M., Wang, Y., Zhang, Q., and He, K. (2018a). “Rapid decline in carbon monoxide emissions and export from East Asia between years 2005 and 2016”. In: *Environmental Research Letters* 13.4, p. 044007. DOI: [10.1088/1748-9326/aab2b3](https://doi.org/10.1088/1748-9326/aab2b3).
- Zheng, B., Chevallier, F., Ciais, P., Yin, Y., and Wang, Y. (2018b). “On the role of the flaming to smoldering transition in the seasonal cycle of African fire emissions”. In: *Geophysical Research Letters* 45.21, pp. 11–998. DOI: [10.1029/2018GL079092](https://doi.org/10.1029/2018GL079092).
- Zheng, B., Chevallier, F., Yin, Y., Ciais, P., Fortems-Cheiney, A., Deeter, M. N., Parker, R. J., Wang, Y., Worden, H. M., and Zhao, Y. (2019). “Global atmospheric carbon monoxide budget 2000–2017 inferred from multi-species atmospheric inversions”. In: *Earth System Science Data* 11.3, pp. 1411–1436. DOI: [10.5194/essd-11-1411-2019](https://doi.org/10.5194/essd-11-1411-2019).
- Zheng, B., Ciais, P., Chevallier, F., Chuvieco, E., Chen, Y., and Yang, H. (2021). “Increasing forest fire emissions despite the decline in global burned area”. In: *Science advances* 7.39, eabh2646. DOI: [10.1126/sciadv.abh2646](https://doi.org/10.1126/sciadv.abh2646).
- Ziemke, J. R., Oman, L. D., Strode, S. A., Douglass, A. R., Olsen, M. A., McPeters, R. D., Bhartia, P. K., Froidevaux, L., Labow, G. J., Witte, J. C., et al. (2019). “Trends in global tropospheric ozone inferred from a composite record of TOMS/OMI/MLS/OMPS satellite measurements and the MERRA-2 GMI simulation”. In: *Atmospheric Chemistry and Physics* 19.5, pp. 3257–3269. DOI: [10.5194/acp-19-3257-2019](https://doi.org/10.5194/acp-19-3257-2019).
- Ziemke, J., Chandra, S., Duncan, B., Schoeberl, M., Torres, O., Damon, M., and Bhartia, P. (2009). “Recent biomass burning in the tropics and related changes in tropospheric ozone”. In: *Geophysical Research Letters* 36.15. DOI: [10.1029/2009GL039303](https://doi.org/10.1029/2009GL039303).
- Ziemke, J., Chandra, S., Labow, G., Bhartia, P., Froidevaux, L., and Witte, J. (2011). “A global climatology of tropospheric and stratospheric ozone derived from Aura OMI and MLS measurements”. In: *Atmospheric Chemistry and Physics* 11.17, pp. 9237–9251. DOI: [10.5194/acp-11-9237-2011](https://doi.org/10.5194/acp-11-9237-2011).
- Ziemke, J., Chandra, S., Oman, L., and Bhartia, P. (2010). “A new ENSO index derived from satellite measurements of column ozone”. In: *Atmospheric Chemistry and Physics* 10.8, pp. 3711–3721. DOI: [10.5194/acp-10-3711-2010](https://doi.org/10.5194/acp-10-3711-2010).